DOCTOR OF SCIENCES

Hierarchically porous carbon materials for advanced Lithium selenium battery

LI, Hongyan

Award date:
2022

Awarding institution:
University of Namur

Université de Namur

Faculté des Sciences
DÉPARTEMENT DE CHIMIE
Laboratoire de Chimie des Matériaux Inorganiques

Hierarchically porous carbon materials for advanced Lithium-Selenium battery

Dissertation présentée par
Hongyan Li

en vue de l'obtention du grade
de Docteur en Sciences

Composition du jury:

Prof. Olivier Deparis (UNamur, Président)
Prof. Alexandru Vlad (UCLouvain)
Prof. Laurence Leherte (UNamur)
Dr. Nikolay TUMANOV (UNamur)
Prof. Yu Li (WHUT)
Prof. Bao-Lian Su (UNamur, Promoteur)

November 2022

Université de Namur
FACULTÉ DES SCIENCES
Rue de Bruxelles 61-5000 Namur
Téléphone : +32 498 69 30 69

Matériaux en carbone hiérarchiquement poreux pour une batterie Li-Se avancée

Hongyan Li

Résumé

Les batteries sont devenues un appareil apprécié en raison de leurs caractéristiques propres, efficaces et amovibles. Les batteries Li-ion ont déjà été appliquées avec succès dans les domaines des véhicules, des équipements électroniques, de l'aérospatiale, etc. La demande pour le haut environnement, haute densité d'énergie, faible volume, et large application de la température, à son tour, favorise le développement de nouveaux systèmes de stockage de batterie comme les batteries Li-S, Li-O_2, Na-ion, K-ion, Al-ion, etc. Les batteries Li-Se, en raison de la capacité spécifique élevée (675 mA h g^{-1}) et une conductivité beaucoup plus élevée de Se que de S, sont devenus un candidat prometteur et ont atteint un développement significatif au cours de ces quelques décennies. Malheureusement, la décroissance de la capacité de la batterie par la diffusion des polysséléniures intermédiaires (Se_n^{2-}, $n \geq 4$) et l'expansion volumique de la cathode ont limité la commercialisation des batteries Li-Se. En outre, les problèmes de fuite d'électrolyte et de croissance de dendrites de lithium doivent également être surmontés.

Dans cette thèse, nous allons d'abord parler de la vue d'ensemble des batteries Li-Se. Dans lequel l'historique du développement des batteries, le mécanisme de la batterie Li-Se, les défis auxquels elle est confrontée et les stratégies pour résoudre ces problèmes seront décrits en détail. Notre travail se concentre principalement sur la conception et la structuration de matériaux hôtes de la cathode Se pour supprimer la diminution rapide de la capacité des batteries causée par la diffusion de polysséléniure. La recherche peut être divisée dans les trois parties suivantes:

1. Les matériaux en carbone tridimensionnels hiérarchiquement micro-méso-macroporeux ont été conçus comme matériau hôte du Se. Le confinement et la richesse des sites de réaction de Se par les micropores et l'électrolyte rapide et le transfert des ions par les voies méso-macropores interconnectées, assurent la stabilité de la batterie Li-Se et la capacité de taux élevé. De plus, la taille optimisée de spores de ces trois pores a été explorée et a obtenu les meilleures performances électrochimiques.
2. La forte interaction entre les matériaux hôtes et les espèces Se de la chimisorption pourrait péniblement confiner l'espèce Se dans la cathode, ce qui est bénéfique pour la longue durée de vie de la batterie Li-Se. En combinant les avantages des cadres micro-méso-macroporeux, on a fabriqué un cadre monocristallin métal-organique (MOF)-dérivé de carbone N-dopé ordonné hiérarchiquement poreux. Bénéficiant de la synergie de l'adsorption physique des micropores et de la chimisorption du dopage N, combinée à la conception poreuse optimisée, la capacité de la batterie a encore été améliorée.
3. Afin de briser la limitation du site polaire apportée par le dopage à l'azote, des oxydes bimétalliques amorphes $CoSnO_3$ ont été introduits dans le système hôte du nanotube de carbone interconnecté (CNT). Outre l'adsorption accrue aux polysséléniures, le $CoSnO_3$ introduit a montré un effet catalytique sur les réactions redox au cours du processus de décharge/charge. De plus, la méthode de calcul de la théorie fonctionnelle de la densité (DFT) permet d'accéder au mécanisme catalytique.

Essai soumis pour le diplôme de docteur en sciences
Novembre 2022
Superviseur: Prof. Bao-Lian Su

University of Namur
FACULTY OF SCIENCE
Rue de Bruxelles 61-5000 Namur
Phone:+32 498 69 30 69

Hierarchically porous carbon materials for advanced Lithium-Selenium battery

Hongyan Li

Abstract

Batteries became a welcomed device due to their clean, efficient, removable features. Li-ion batteries have already been successfully applied in the fields of vehicles, electronic equipment, aerospace, etc. The demand for the high environment-friendly, high energy density, small volume, and wide temperature applicability, in turn, promotes the development of new battery storage systems, such as Li-S batteries, Li-O_2 batteries, Na-ion batteries, K-ion batteries, Al-ion batteries, etc. Li-Se batteries, due to their high specific capacity (675 mA h g^{-1}) and much higher conductivity of Se than S, became a promising candidate and have achieved significant development in these few decades. Unfortunately, the capacity decay of the battery by the diffusion of the intermediate polyselenides (Se_n^{2-}, $n \geq 4$) and volume expansion of cathode have limited the commercialization of Li-Se batteries. In addition, the problems of electrolyte leakage and growth of lithium dendrites should also be overcome.

In this thesis, we will first talk about the overview of the Li-Se batteries. In which the development history of batteries, the mechanism of Li-Se battery, the challenges it faces, and the strategies how to solve these problems will be described in detail. Our work mainly focuses on designing and structuring Se cathode host materials to suppress the rapid capacity fading of batteries caused by polyselenide diffusion. The research can be included in the following three parts:

1. The three-dimensional ordered hierarchically micro-meso-macro-porous carbon materials were designed as Se host material. The confinement and rich of reaction sites of Se by the micropores and the rapid electrolyte and ions transfer by the interconnected meso-macropores pathways, ensure the stability of the Li-Se battery and high rate capability. Moreover, the optimized pore size of these three pores range value was explored and achieved the best electrochemical performance.
2. The strong interaction between host materials and Se species of chemisorption tiredly confines the Se species in the cathode, which is beneficial for the long lifespan of Li-Se battery. Combining the advantages of the micro-meso-macroporous frameworks, single-crystal metal-organic framework (MOF)-derived N-doped ordered hierarchically porous carbon was fabricated. Benefiting from the synergy of physical adsorption of micropores and chemisorption of N-doping, combined with the optimized porous design, the capacity of the battery achieved a further improved.
3. In order to break the number of the polar site limitation brought by nitrogen doping, amorphous bimetallic oxides $CoSnO_3$ was introduced to the host system of the interconnected carbon nanotube (CNT). Besides the further enhanced adsorption to polyselenides, the introduced $CoSnO_3$ showed catalytic effect on the redox reactions during the discharge/charge process. The catalytic mechanism was accessed by the density functional theory (DFT) calculation method.

Essay submitted for the degree of Doctor of Science
November 2022
Supervisor: Prof. Bao-Lian Su

List of abbreviations

3D: Three-dimensional

ASSBs: All-solid-state batteries

BET: Brunauer-Emmett-Teller

BJH: Barrett-Joyner-Halenda

BTB: 3,5-bis(trifluoromethyl)thiophenol

CE: Coulomb efficiency

CV: Cyclic voltammetry

DEC: Diethyl carbonate

DFT: Density functional theory

DIB: 1,3-diisopropenylbenzene

DIPE: Diisopropyl ether

DME: 1,2-dimethoxyethane

DMC: Dimethyl carbonate

DOL: 1,3-dioxolane

EC: Ethylene carbonate

EDX: Dispersive X-ray Spectroscopy

FEC: Fluoroethylene carbonate

EIS: Electrochemical impedance spectroscopy

GITT: Galvanostatic intermittent titration technique

GO: Graphene oxide

HFE: Hydrofluoroether

HK: Horvath-Kawazoe

HOMO: Highest Occupied Molecular Orbital

LIB: Lithium-ion battery

LiDFBOP: Lithium difluorobis(oxalato) phosphate

LiDFOB: Difluoro(oxalato)borate

LiODFB: Lithium oxalyldifluoroborate

$LiPF_6$: Lithium hexafluorophosphate

LiPS: Lithium polysulfide

LiPSe: Lithium polyselenide

LiTFSI: Lithium bis(trifluoromethane sulfonyl) imide

LUMO: Lowest unoccupied molecular orbital

MOF: Metal-organic framework

MWCNTs: Multi-walled carbon nanotubes

OHPC: ordered hierarchically porous carbon

PANI: Encapsulating polyaniline

PC: Propylene carbonate

PMMA: Polymethyl methacrylate

PP: Polypropylene

PS: Polystyrene

PVA: Polyvinyl alcohol

PVDF: Polyvinylidene fluoride

PXRD: Power X-ray diffraction

SEI: Solid-electrolyte interphase (SEI) layer

SEM: Scanning electron microscopy

Se_xS_y: Selenium-sulfur solid solution

SHE: Standard hydrogen electrode

S-NMC: Single-crystal MOF-derived N-doped microporous carbon

S-NOHPC: Single-crystal MOF-derived N-doped ordered hierarchically porous carbon

S-NOMMC: Single-crystal MOF-derived N-doped micro-macroporous carbon

TEM: Transmission electron microscopy

TEGDME: Tetraethylene glycol dimethyl ether

TGA: Thermogravimetric analysis

XPS: X-ray photoelectron spectroscopy

Table of Contents

Chapter I

General introduction

Abstract

In recent years, lithium-selenium (Li-Se) batteries have attracted increasing attention due to their high theoretical volumetric capacity, better electrochemical performance and much higher conductivity of selenium compared to sulfur. However, its practical application still faces great challenges in maintaining high capacity stability and the tricky safety hazards. To address these problems, a lot of research and optimization work have been carried out on Li-Se batteries, from selenium cathodes, lithium anodes, and electrolytes to separators. This chapter reviews the current status of Li-Se batteries, focusing on the polyselenides (PSe, Se_n^{2-}, n=4-8) confinement effect to reduce the shuttle effect, high ionic conductivity and stable electrolyte, and the suppression of the lithium dendrites. The future scope for the development of the Li-Se battery is also proposed. Afterwards, the purpose, scientific strategy and main research methods on our research work are described.

Introduction

With increasingly severe energy demands and environmental issues, as well as the rapid development of electronic and electrical equipment, batteries as high-capacity energy storage devices are urgently needed[1]. In 1990, Sony Corporation introduced graphite-based lithium-ion battery (LIB) to market, announcing the arrival of the battery age[2]. Since then, LIB has been widely applied in electronic equipment, electric tools and electric vehicles due to its low self-discharge, absence of memory effect, wide operating temperature range, and long cycle life[3]. However, limited by its low theoretical specific capacity ($LiCoO_2$: 278 mA h g^{-1}) and security risks of electrolyte leakage and self-ignition, LIB is difficult to meet the demand of high-performance portable electronic devices and electric vehicles[4-6]. The next generation metallic battery, especially the Li-S battery, has shown various merits, such as high theoretical capacity (1672 mA h g^{-1}), low cost and environmental friendliness, which leads to remarkable development in recent years[7-9]. Nevertheless, problems of low electrical conductivity of sulfur, polysulfide dissolution in electrolytes, redox shuttle effect as well as deposition of Li_2S on the Li anode hinder the practical application of Li-S battery[10, 11].

Selenium, as another chalcogen element, has recently attracted enormous attention. Compared to sulfur (5×10^{-28} S m^{-1}), selenium has a much higher electrical conductivity (1×10^{-5} S·m^{-1}), which is beneficial for electron transport in batteries. Moreover, the shuttle effect produced by soluble polyselenides (PSe) in Li-Se battery is much weaker than that of polysulfide in the Li-S battery[12]. Li-Se battery has a comparable theoretical volumetric capacity (3253 mA h cm^{-3}) to that of Li-S batteries (3467 mA h cm^{-3}) due to the significantly higher mass density of selenium (4.81 g·cm^{-3}) than that of sulfur (2.07 g·cm^{-3}), which is one of the most important properties to miniaturize batteries for portable devices[13]. These advantages suggest that the Li-Se batteries are promising energy storage devices in the future.

However, the commercial applications of Li-Se batteries are severely hampered by their low practical capacity and poor stability due to the shuttle effect of PSe, low selenium utilization and production of lithium dendrites[14, 15]. To address these problems, considerable efforts have been devoted to research on Li-Se battery, especially in recent years. Research statistics shown in **Fig. 1** indicates that the number of research works on Li-Se battery is growing exponentially and that most of them focus on cathode. Although several excellent review papers for the Li-Se battery have

been published, their focus is made on a single or part aspect of the battery[16, 17]. A complete guide for designing high-performance Li-Se batteries is highly recommended to respond to the urgent need for the rapid development of Li-Se batteries from academia and industry as well. In this review, we provide a comprehensive summary of breakthroughs and innovations, including the construction of novel cathode materials, tuning of the electrolytes, design of separators and anode modification, emphasizing the suppression of shuttle effect and lithium dendrites, the most challenging part of improving battery performance. The strategies and key facts of high-performance Li-Se battery are introduced and discussed in this review. The working mechanism of Li-Se batteries is firstly presented to understand how the reaction is undergoing and know the problems at the source. Then, the improvement strategies are classified according to the different parts of the battery. Finally, a perspective insight of the future research in Li-Se batteries is provided.

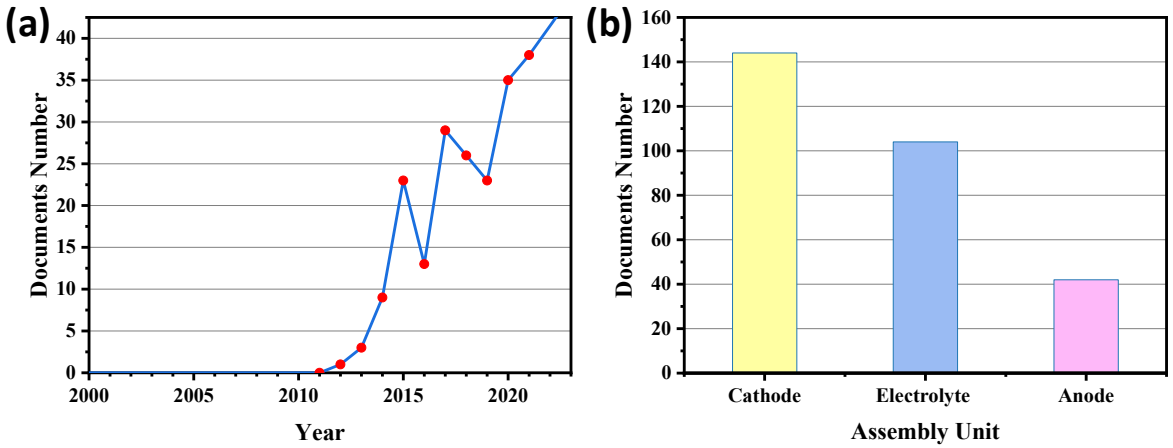

Fig. 1 Papers published till 2022 of Li-Se batteries (a) documents by year, (b) documents by assembly unit.

1 Overview of Li-Se battery

Li-Se battery as an energy storage device realizes the charge/discharge process through the interconversion of electrical energy and chemical energy. **Fig. 2** schematically shows that the Li-Se batteries are composed of selenium cathode, separator, lithium anode and filled with electrolyte in the cells. The reversible electrochemical reaction of Se with Li occurs in the Li-Se battery during discharge/charge process. The parameters of the batteries are essential indicators for judging their performance.

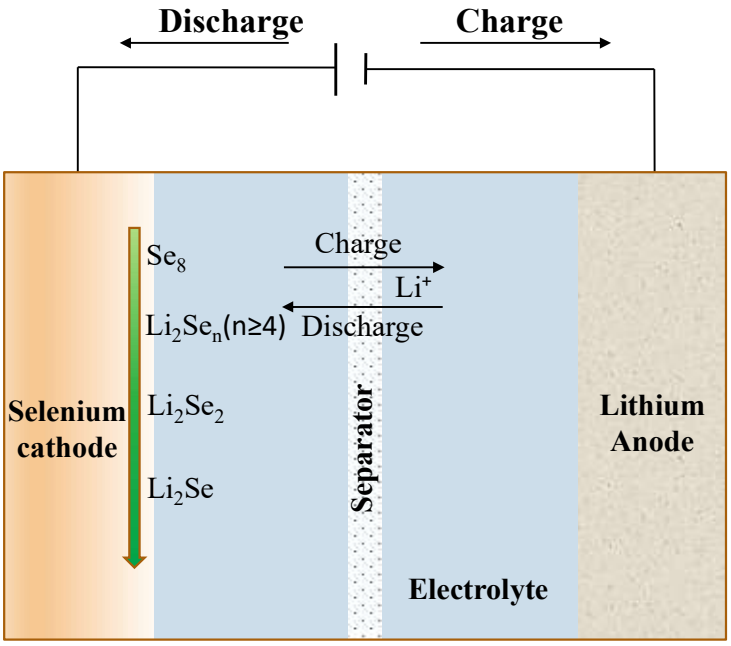

Fig. 2 Schematic diagram of lithium selenium battery.

1.1 Working mechanism for Li-Se battery

Different from the intercalation and deintercalation mechanism of current commercial lithium-ion batteries, lithium-selenium batteries are based on the redox reaction between selenium and lithium. Generally, during discharge process, the lithium anode undergoes an oxidation reaction and releases electrons and lithium ions. Then, the electrons arrive at cathode side through the external circuit, while the lithium ions dissolve in the electrolyte and reach the same side passthrough the separator in the internal circuit. Then, selenium gains electrons and gradually reacts with lithium ions to form Li_2Se[18-20]. In ether-based electrolyte, the discharge process can be derived into four stages, as shown in **Fig. 3**. These four stages reaction are shown below:

(I) In the first stage, the ring Se_8 (Fig. 3) is lithiated to form long chain polyselenide of Li_2Se_8 (Equation 1):

$$Se_8 + 2e^- \rightarrow Se_8^{2-} \qquad (1)$$

(II) Then, Li_2Se_8 reduced to Li_2Se_n (n≥4) and form a reduction platform at voltage of ~2.1 V (Equation 2):

$$Se_8^{2-} + 2e^- \rightarrow Se_n^{2-}\ (n \geq 4) \qquad (2)$$

(III) After, the long chain Li_2Se_n is reduced to Li_2Se_2. Here, the second reduction platform appears at voltage of ~2.0 V, and the capacity increases greatly (Equation 3):

$$Se_n^{2-} + 2e^- \rightarrow Se_2^- \qquad (3)$$

(IV) Finally to Li_2Se (Equation 4),

$$Se_2^- + 2e^- \rightarrow 2Se^- \qquad (4)$$

The charging process is completely opposite to the discharging process from Li_2Se back to Se again. The molecular structure of different PSe are shown in **Fig. 3**. Thus, the reaction in ether-based electrolyte is a multi-step reaction. The start and end products of Se_8 and Li_2Se are solids, while the intermediate products of Li_2Se_n are dissolved in liquid. The reaction is a solid-liquid-solid process.

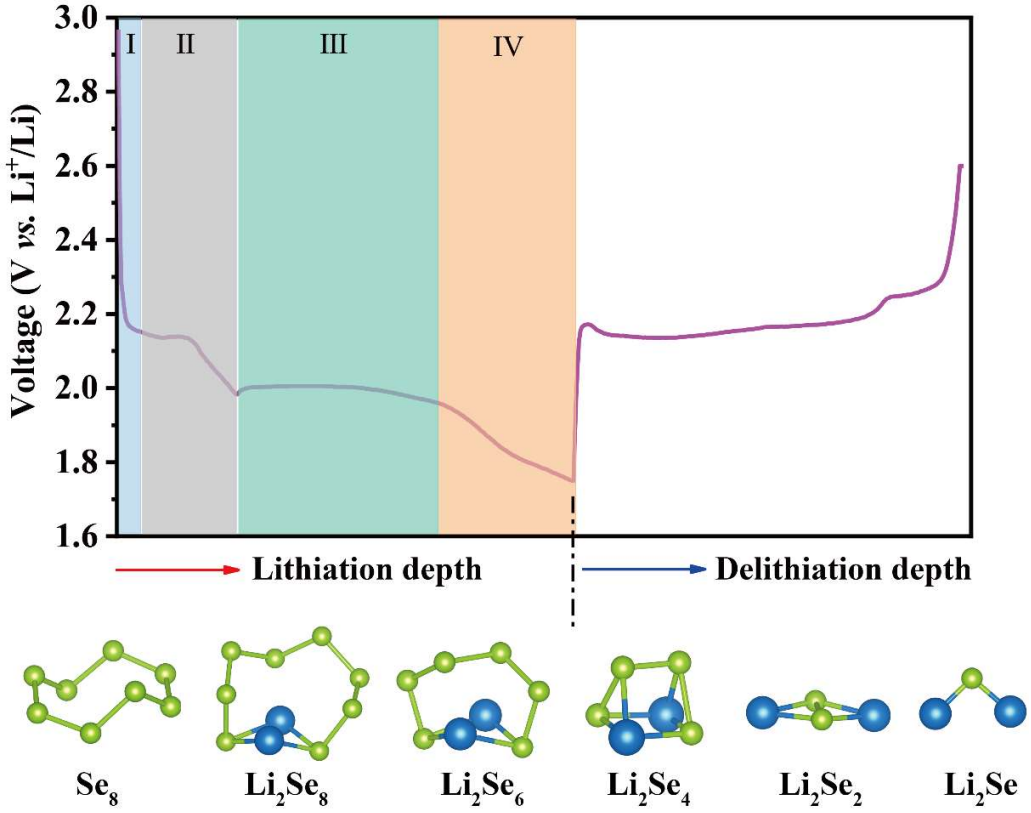

Fig. 3 Reaction mechanism of Li-Se battery and products of Se_8 to Li_2Se. (blue and green balls symbolize lithium and selenium atoms, respectively).

1.2 Performance parameters for Li-Se battery

1) Electromotive force (E^{Θ})

E^{Θ} is the thermodynamic equilibrium voltage under standard conditions (1atm, 298 K). Let us consider the generic electrochemical reaction:

$$\alpha A+\beta B\rightarrow\gamma C+\delta D$$

If all the standard Gibbs free energy of the reaction is transformed into electrical energy, the equilibrium voltage can be calculated by the following formula[21, 22]:

$$\Delta_r G^{\Theta} = \gamma\Delta_f G_C^{\Theta} + \delta\Delta_f G_D^{\Theta} - \alpha\Delta_f G_A^{\Theta} - \beta\Delta_f G_B^{\Theta} = -nFE^{\Theta}$$

$\Delta_r G^{\Theta}$ is the standard Gibbs free energy of the reaction. $\Delta_f G^{\Theta}$ represents the standard Gibbs free energy of a specific material. n is the number of electrons (mol) transferred in the redox reaction. F is Faraday's constant, which represents the charge carried by each mole of electrons, which is the product of Avogadro's number (N_A=6.02214×10^{23} mol^{-1}) and the elementary charge (e=1.602176×10^{-19} C), F=96485.3383 C mol^{-1}.

2) Theoretical capacity (C_0)

In the theoretical case, all of reactants participate in the electrochemical reaction to provide capacity. The detailed derivation can be found in many other papers[22, 23]. Its value is calculated by the following formula:

$$C_0\left(\frac{mA\ h}{g}\right) = F\left(\frac{C}{mol}\right) \times n \times \frac{1}{M}\left(\frac{mol}{g}\right) \times \frac{1}{3.6}\left(\frac{mA\ h}{C}\right)$$

M is the molar mass of the reactant and 1 mA h=0.001A×3600 S=3.6 C.

For Se cathode, n=2, M=78.971 g mol^{-1}, thus the theoretical capacity of Se is:

C_0(Se)=nF/3.6M=678 mA h g^{-1}

3) Volume energy and mass energy density (E_V and E_m)

The energy released per unit volume (L) or unit mass (KG) of battery[24]:

$$E_V\left(\frac{Wh}{L}\right) = \frac{Capacity(mA\ h) \times E^{\Theta}(V)}{Volume\ of\ battery}$$

$$E_m\left(\frac{Wh}{KG}\right) = \frac{Capacity(mA\ h) \times E^{\Theta}(V)}{weight\ of\ battery}$$

4) Power density (P_E)

Power density refers to the output power per unit mass or unit volume of the battery, and specific power is an important indicator to evaluate whether the battery meets the acceleration performance of electric vehicles.

$$P_E(\frac{W}{L} or \frac{W}{KG}) = \frac{E_V \ or \ E_m}{T(h)}$$

Here, T is the time consumed in charge or discharge of the battery.

5) Battery discharge/charge rate (C-rate)

The C-rate is a measure of the speed of discharge. Discharge rate refers to the current value required to discharge its rated capacity value within a specified time. For example, 1 C means the current strength of the battery when it is fully discharged in 1 h.

$$C = \frac{\text{Charge and discharge current (A)}}{\text{Rated capacity (Ah)}}$$

For Se cathode battery, at C-rate of 0.1 C, the battery finishes the discharge/charge process at the constant current of 678 mA×0.1=67.8 mA in 10 h.

6) Coulombic efficiency (CE)

Coulombic efficiency refers to the ratio of battery discharge capacity to charging capacity during the same cycle, that is, the percentage of discharge capacity to charging capacity.

For the positive electrode material,

$$CE_P = \frac{C_{lithiation}}{C_{delithiation}} = \frac{C_{Discharge}}{C_{Charge}}$$

For negative electrode material,

$$CE_N = \frac{C_{delithiation}}{C_{lithiation}} = \frac{C_{Charge}}{C_{Discharge}}$$

1.3 Key factors for Li-Se battery

Li-Se batteries, as one of the most attractive next generation energy storage devices, have been attracted significant attention, but it also undergoes some critical challenges:

1) Se cathode undergoes volume expansion when reacting with lithium. The density of the discharge product Li_2Se is lower than that of Se, which leads to the expansion of the active Se particles, finally leading to the active Se pieces peeled off and loss.

2) Se and discharge products Li_2Se and Li_2Se_2 have low electrical conductivity and are not conductive to the transport of electrons in the electrode material, leading to the low reaction activity between Se and Li.

3) The "shuttle effect" deceases the stability of the capacity of Li-Se battery. During discharge, the produced long-chains PSe dissolve in the electrolyte and diffuse to the negative electrode with the assistance of the concentration gradient, where the PSe products directly react with lithium metal to form short-chain lithium polyselenides or Li_2Se. Part of the remaining PSe will then diffuse back to the positive electrode under the effect of potential difference, and return to long-chain PSe in charging. The phenomenon of repeated back-and-forth diffusion is called the "shuttle effect"[25-27]. The shuttle effect eventually leads to irreversible loss of active Se, resulting in rapid capacity degradation, battery life decay and poor Coulombic efficiency.

4) Due to the excessive local current, lithium dendrites grow on the surface of Li foil and pierce separator and induce an internal short-circuit of batteries, which leads to the explosion and self-ignition of the battery.

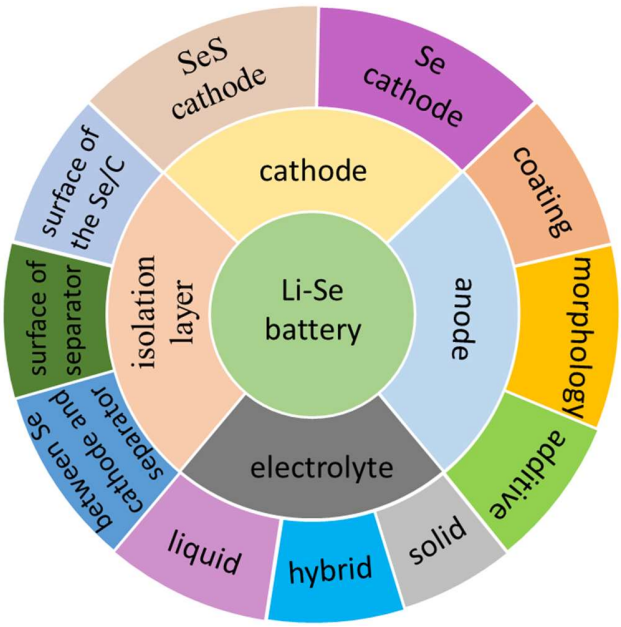

Fig. 4 The resolution strategies of Li-Se batteries.

To overcome the above shortcomings, various strategies have been explored for each part of the battery, **Fig. 4** summaries the widely conducted strategies: 1) Designing and preparing novel cathode materials with modified morphology and composition, which not only effectively improve electron and ion transportation but also significantly inhibit the shuttle effect of PSe; 2) Adding active materials to optimize the electrolyte or preparing solid electrolytes; 3) Treating the surface of existing commercial separators to prevent the passage of PSe; 4) Modifying the lithium anode of the battery to avoid the formation of lithium dendrites. These efforts effectively suppress the shuttle effect of PSe, improve the utilization of active substances and reduce the generation of dendrites, thereby improving the electrochemical performance of Li-Se battery.

2 Se cathode

Se cathode is the most critical part of the Li-Se battery where the active Se exists. Unfortunately, here is also the place where the above-mentioned shuttle effect, active Se loss, and volume expansion happen. Although compared with S, the conductivity of Se has a significant improvement, the electron transfer is still limited. It is important to modify the selenium electrode. Increasing the surface area of active Se by reducing Se particle size or morphology design is the most direct method. The problem of volume expansion can be alleviated, and at the same time, more reaction sites can be exposed. Another feasible method is to confine Se inside of conductive framework materials. Besides the improved conductivity of the cathode, framework materials with porous structure and high specific surface area exhibit strong adsorption to PSe, which can trap the PSe inside the selenium electrode, thereby reducing the dissolution of the PSe. To avoid the dissolution of PSe and loss of Se, the atoms of Se can bind with some polystructure to form hybrid sulfur-selenium co-polymers to fix the Se. Moreover, adjusting the electrolyte to decrease the solubility of PSe to convert the solid-liquid-solid reaction into a solid-solid reaction is another direction to avoid the shuttle effect. Further, SeS cathode could achieve a high capacity and improved electrical conductivity, showing an excellent property. In addition, freestanding and binder-free Se-host cathode could greatly decrease the weight of the battery, thus can significantly increase the energy density. The method to be executed is shown in **Fig. 5**.

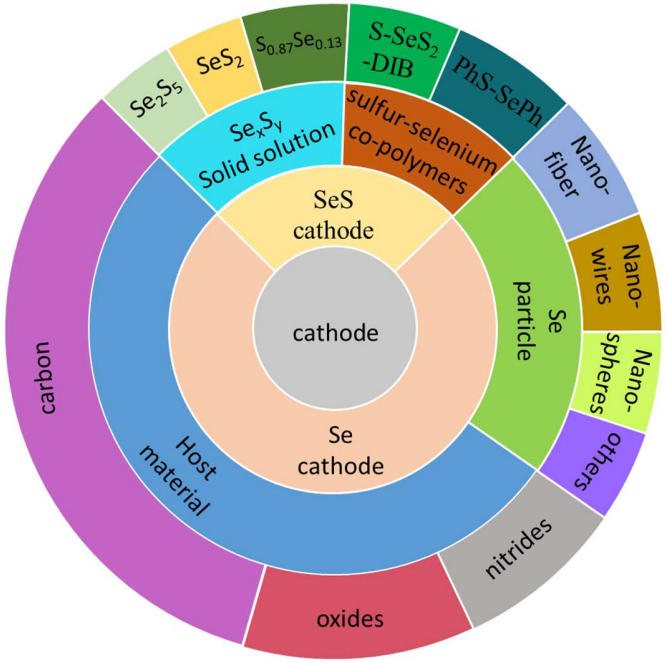

Fig. 5 The resolution strategies developed in cathode of Li-Se batteries.

2.1 Modification of the active Se nanoparticles

Selenium, being worked as active material, its content and utilization have a direct influence on the energy density of the Li-Se battery. Se particles directly used as the active materials is a simple method for their application. However, the electrolyte transfer, conductivity of electrode as well as the Se particle expansion limit the full utilization of Se, leading to quick capacity drop. Thus, morphology modification of selenium to get a high surface area is a good strategy to solve the above problems.

The synthesis of Se particles can be realized by solution route[28], mechanical method[29], and template methods[30]. Liu *et al.* synthesized a kind of nanoporous selenium (NP-Se) and directly used it as active material[29], as is shown in **Fig. 6a**. Compared with commercial Se particles (CP-Se, only 0.3 m^2 g^{-1}), the BET surface area of the NP-Se (40.9 m^2 g^{-1}) enlarged obviously. The reversible capacity of the NP-Se retained 206 mA h g^{-1} in the 20th cycle, which is much higher than that of CP-Se. Kundu *et al.* fabricated trigonal selenium (t-Se) nanofibers (**Fig. 6b**) and used in Li-Se battery[31]. In **Fig. 6c**, the electrochemical performance of pure t-Se fibers electrode exhibited high specific capacity of 678 mA h g^{-1} at the current of C/120, but the capacity greatly decreases at high rate current density because of the collapse of the trigonal structure of selenium and the limitation of the electrons/ions transfer. By coating a protective layer of polypyrrole or graphene,

the obtained t-Se/-polypyrrole and t-Se/-graphene composites achieve improved electrochemical performance due to the reduced polarization and the enhanced electron transport. Moreover, Se nanowires@Al_2O_3 core-shell nanowires were fabricated with the help of anodic aluminum oxide (AAO) template[30]. Fan *et al.* synthesized hollow Se nanospheres and encapsulated them with 3D graphene hydrogels[28]. With the protection coating layer, the electrochemical performance of the battery has some degree of improvement in capacity and stability. In order to tightly confine Se

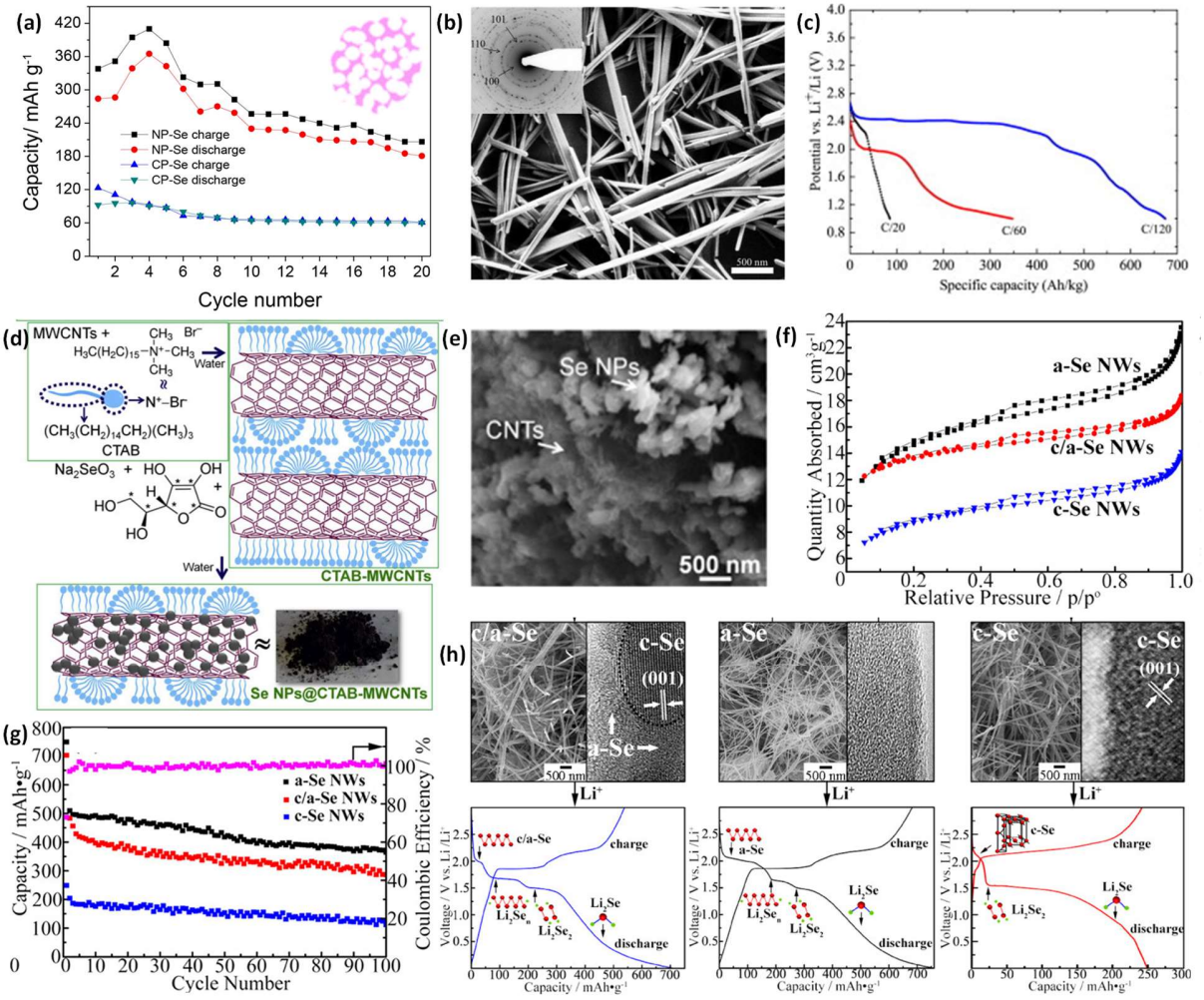

Fig. 6 (a) Cycling performance of nanoporous Se (NP-Se: image inserted) and commercial Se (CP-Se)[29], (b) SEM image of the t-Se nanofibers with a TEM ED pattern that has been recorded of the fibers, shown in the inset, (c) Galvanostatic discharge curves of pristine t-Se electrode at different current rate[31], (d) The synthesis process and (e) SEM image of Se NPs@CTAB-MWCNTs composite[32], (f) N_2 adsorption desorption isotherms, (g) Cycle performance and (h) Initial charge–discharge behavior of the a-Se, c/a-Se, and c-Se nanowires, respectively[20].

particles in cathode,Mukkabla *et al. in-situ* integrated the selenium nanoparticles (NPs) with CTAB decorated MWCNTs and fabricated Se NPs@CTAB-MWCNTs with the process indicated in **Fig. 6d**[32]. The Se NPs@CTAB-MWCNTs (**Fig. 6e**) composite cathode delivered a high initial discharge capacity of 570.4 mA h $g^{-1}$and the capacity retained at 171.8 mA h g^{-1} after 500 cycles. It should be noted that when the Se particle is broken into pieces, the fix function by the *in-situ* connection will be greatly discounted.

Through unique morphology design of high surface area Se particles, the electrochemical performance of Li-Se batteries has achieved obvious improvement. However, the expansion problem of crystalline Se still exists. In order to clarify the (De)Lithiation mechanisms at different Se crystalline states, Zhou *et al.* prepared amorphous, crystalline and crystalline/amorphous selenium nanowires (NWs), labelled as a-Se NWs, c/a-Se NW and c-Se NW, respectively[20]. As shown in **Fig. 6f**, amorphous Se nanowires (a-Se NWs) have a further increased surface area than crystalline Se nanowires. The amorphous material is in a metastable state with more active sites due to the "dangling bonds" and a higher surface-bulk ratio. The a-Se NWs achieved better performance than c/a-Se NW and c-Se NW, with a reversible capacity of 755 mA h g^{-1} and 350 mA h g^{-1} after 100 cycles (**Fig. 6g**). The a-Se NW and c/a-Se NW are reduced to polyselenides Li_2Se_n ($n \geq 4$), Li_2Se_2, and Li_2Se sequentially during the lithiation, while c-Se NWs cathode was fast reduced to Li_2Se (**Fig. 6h**).

Selenium with larger surface area morphology could improve the cycle stability and specific capacity performance of Li-Se battery. That is beneficial from more active Se reaction sites, the shorten pathways of electrons and lithium ions, accommodate volume expansion, and promote efficient penetration of the electrolyte inside. In addition, compared with crystalline Se, the amorphous Se achieved higher performance in Li-Se battery. That is due to the abundant active sites present in amorphous Se. Guided by this conclusion, the research attention in Li-Se batteries was paid on searching for a simple method to prepare amorphous selenium. Confining Se inside of porous framework to keep its amorphous state is a simple and efficient method.

2.2 Se confinement in host materials

Porous frameworks can have large space for Se loading. Moreover, the dispersed Se inside of framework host can stay in amorphous state or very small crystalline Se particles, which is beneficial for the electrochemical reaction. Besides the high ability of Se loading, the framework

usually with high conductivity is beneficial for the transport of electrons. In addition, the enhanced adsorption of lithium polyselenides by the introduced host materials will depress the shuttle effect. As a carrier for active selenium, the host materials must have the following characteristics: 1) good conductivity to compensate for the low conductivity of selenium; 2) sufficient space to load selenium; 3) ability to prevent the diffusion of polyselenide. After intensive research, it was proven that carbon hosts with high surface areas, high electrical conductivities and large pore volumes are ideal framework materials to encapsulate the active selenium[33-35]. In addition, some oxides and nitrides also showed high potential in Li-Se battery[36].

2.2.1 Carbon-based host materials

For the selenium cathode, the confined selenium inside of porous carbon material can effectively improve the performance of the Li-Se battery[37]: 1) the conductivity of the carbon material can improve the electron transport in the cathode, 2) the high specific surface area of the carbon material can provide a larger electrode reaction area and improve the electrochemical activity of selenium, 3) the pores in carbon material have a strong adsorption effect on PSe to reduce the shuttle effect. Moreover, heteroatoms doped carbon materials can effectively prevent the dissolution of PSe *via* the enhanced chemisorption. Thus, using physical confinement effects and chemisorption to inhibit the dissolution and diffusion of PSe is the effective approach to suppress the shuttle effect.

2.2.1.1 Carbon materials with physical confinement effects (porous structure design)

The physical confinement effects (van der Waals adsorption) can effectively inhibit the dissolution and diffusion of polyselenides. Since the porous structure and pore size affect the strength of the adsorption, the structural design of the carbon material has a great influence on the physical confinement effects. Carbon materials of various dimensions are used as conductive carriers of selenium in the cathode, which improves the performance of the Li-Se battery. The common carbon host materials can be categorized as carbon spheres[38], one-dimensional materials (such as carbon nanotubes, carbon fiber)[39], two-dimensional materials (such as graphene, graphene oxide), and three-dimensional materials[40].

Carbon Spheres

Spherical nano-materials, due to their advantages of uniform dispersion, tunable pore size distribution, high specific surface area and enhanced strong adsorption capacity for PSe, have

aroused extensive research enthusiasm to prepare carbon spheres as Se host materials using different methods[41]. For instance, Yan *et al.* prepared monodisperse carbon spheres (RFCS) as Se host material[42]. The pore size distribution of RFCS mainly ranges in micropores (**Fig. 7a**). The introduced Se occupied the pores of RFCS and stayed in amorphous state. The Li-Se battery based on RFCS/Se-50 composite exhibited a high reversible capacity of 643.9 mA h g^{-1} in the 100th cycle at 0.2 C (**Fig. 7b**). Li *et al.* prepared microporous carbon nanospheres (PCNs) by a hydrothermal route[43]. The carbon material had a high specific surface area of 853 m^2 g^{-1} and the selenium content in the corresponding Se/C composites was 70.5 wt.%. The battery exhibited a volumetric capacity density of 3150 mA h cm^{-3}.

However, high viscosity liquid electrolytes cannot effectively penetrate the carbon spheres with only micropores. Therefore, carbon microspheres with developed mesopores and micropores and high pore volume have been prepared. For instance, Hong *et al.* designed graphitic carbon (GC) microspheres with well-developed mesopores[44], resulting in a longer cycle life and excellent rate performance (584 mA h g^{-1} at 0.5 C after 850 cycles). Park *et al.* synthesized well-developed micropores and mesopores carbon microspheres (**Fig. 7c**)[45]. The carbon/Se electrodes exhibited initial charge capacities of 632 mA h g^{-1} and a stable reversible capacity of 582 mA h g^{-1} after 500 cycles at a current density of 0.5 A g^{-1}. Even at a high current density of 2.0 A g^{-1}, the capacity achieved a value of 343 mA h g^{-1} after 2000 cycles, which is much higher than similar microspheres having only micropores.

Introducing hollow structure into the carbon sphere cores can further improve the battery performance due to the obtained thin wall that facilitate the electron and Li-ion transport, provide sufficient void space to accommodate the volume expansion, and hinder the dissolution of the PSe[47]. Hollow carbon materials such as hollow carbon spheres (HCPSs)[48] and porous hollow carbon spheres (PHCSs)[49] were synthesized. Hong *et al.* synthesized micro- and mesoporous hollow carbon microspheres, as shown in **Fig. 7d**[46]. The Se-impregnated hollow carbon (C-Se) microspheres perform a good stability, with a discharge capacity of 525 mA h g^{-1} after 1000 cycles at a constant current density of 0.5 A g^{-1}, and 87% capacity retained compared with the 2nd cycle capacity of 603 mA h g^{-1}. Moreover, Pongilat *et al.* synthesized hollow carbon spheres (HCSs) with tunable sizes to explore their size-dependent charge storage behavior[50]. Se@HCS200 with a sphere size of 200 nm achieved optimized electrochemical performance due to the advantages in improving diffusion kinetics and correspondingly enhancing electrochemical performance.

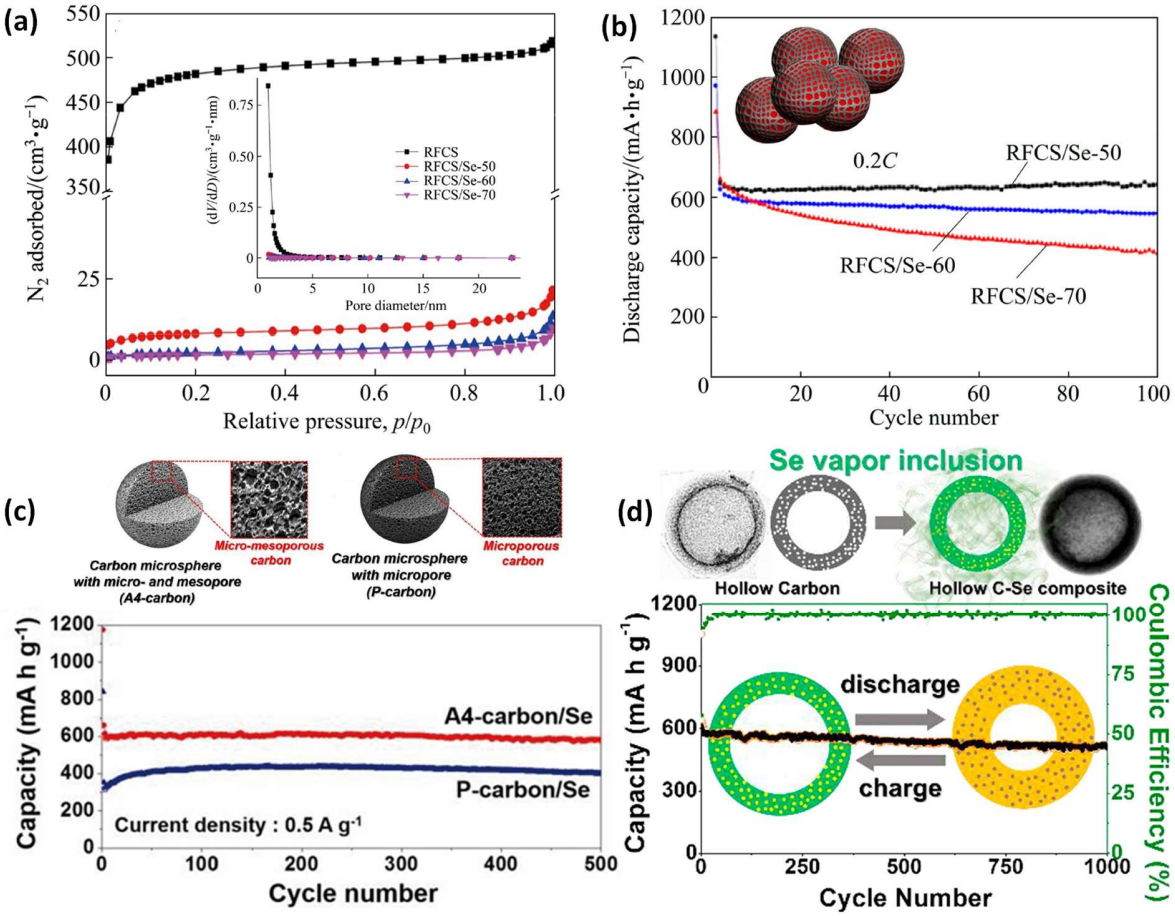

Fig. 7 (a) N_2 adsorption−desorption isotherms of RFCS and RFCS/Se composite with different mass ratios (inserted is pore size distribution)[42], (b) cycling performance of RFCS/Se electrodes, (c) P- and A4-carbon structure and their cycling performances[45], (d) Hollow C-Se composite and its cycling performances[46].

Carbon spheres have an isotropic structure, which is beneficial for their uniform dispersion in the system. High surface area microporous carbon spheres contain enough space for active Se and reaction sites, however, the mass transfer in the micropores will be limited. Introduction of mesopores in microporous carbon sphere can solve this problem and achieve a better rate capability. In addition, confining Se in the hollow carbon is also an effective method to suppress the shuttle effect and volume expansion, leading to a stable performance in the Li-Se battery.

One-dimensional carbon materials

One-dimensional carbon materials have a high aspect ratio, which can form an interconnected network, enabling the Se/C composites to have long-range conductivity and thus efficient utility in

Li-Se battery. Commonly, one-dimensional carbon materials include carbon nanotubes and carbon fibers.

Carbon nanotubes with a hollow innertube have the characteristics of high conductivity, high lithium-ion and electron mobility, and active Se loading space, which help to improve the capacity of the Li-Se battery. Wang *et al.* loaded small sizes of selenium particles into multi-walled carbon nanotubes (MWCNTs), and the obtained Se/C electrodes delivered a high initial discharge capacity (645.7 mA h g^{-1}) and cycling stability (355.5 mA h g^{-1} at 0.5 C after 100 cycles)[51]. To block the diffusion of PSe, Balakumar *et al.* synthesized Tube-in-Tube carbon (TTC) material with the assistance of SiO_2 as hard template (**Fig. 8a**)[52]. The MWCNTs (core) backbone provided the facile electron transfer path while the surrounding porous carbon (shell) prevented the loss of active material. The Se@TTC cathode delivered an initial capacity of 625 mA h g^{-1} at 0.2 C and retained at 403 mA h g^{-1} after 800 cycles. Due to the long distance of the CNTs for Se loading, there are still a lot of non-loaded regions in CNT. Dutta *et al.* used pressure-induced capillary encapsulation protocol to confine sulfur and selenium inside the open-ended CNTs[53]. In **Fig. 8b**, the concave Se meniscus and the small contact angle of confined Se (θc) inside the inner cavity of the CNT indicate the small vapor-Se surface tension. In this method, the S/Se mass ratio in S/Se-CNTs reached nearly 85%.

Carbon fiber with a cross-linked network structure facilitates electron transport. For a better application in Li-Se batteries, carbon fibers rich in pores with high specific surface area are required for selenium incorporation, and PSe capture. Wang *et al.*[54] and Zeng *et al.*[55] respectively fabricated polyacrylonitrile–selenium (PAN–Se) fibers by electrospinning technique, and obtained CPAN/Se mixtures after carbonization. In the composite, Se clusters are chemically bonded and physically encapsulated by carbonized PAN-CNT composite (**Fig. 8c**), which suppresses the shuttle effect of the battery. The CPAN/Se composite cathode delivered a high capacity of nearly 600 mA h g^{-1} in the 500^{th} cycle. To further increase the Se loading and inhibit the shuttle effect, Zhang *et al.*[56] and Liu *et al.*[57] activated cross-linked porous carbon nanofiber webs (PCNFWs) and microporous carbon nanofibers (MCNF) with KOH to introduce micropores. The interconnected fiber structure, which displays the highly desirable characteristics of abundant porous nanostructure, interconnected channel structure, and high specific surface area, achieved superior electrochemical performance in Li-Se battery (414.5 mA h g^{-1} after 100 cycles at 0.2 C and 400 mA h g^{-1} after 2000 cycles at 1 C). To further improve the battery cyclability, Mukkabla

et al. coated conducting polycarbazole (PCZ) layer on the surface of Selenium@Conical Carbon Nanofibers electrode[58]. The coating acted as a barrier to restrict the dissolution and crossover of PSe, thereby minimizing the capacity decay of the battery. As shown in **Fig. 8d**, the cathode with PCZ coating displays a very slow capacity decay, eventually maintaining a reversible capacity of 640 mA h g^{-1} after 100 cycles at 0.1 C.

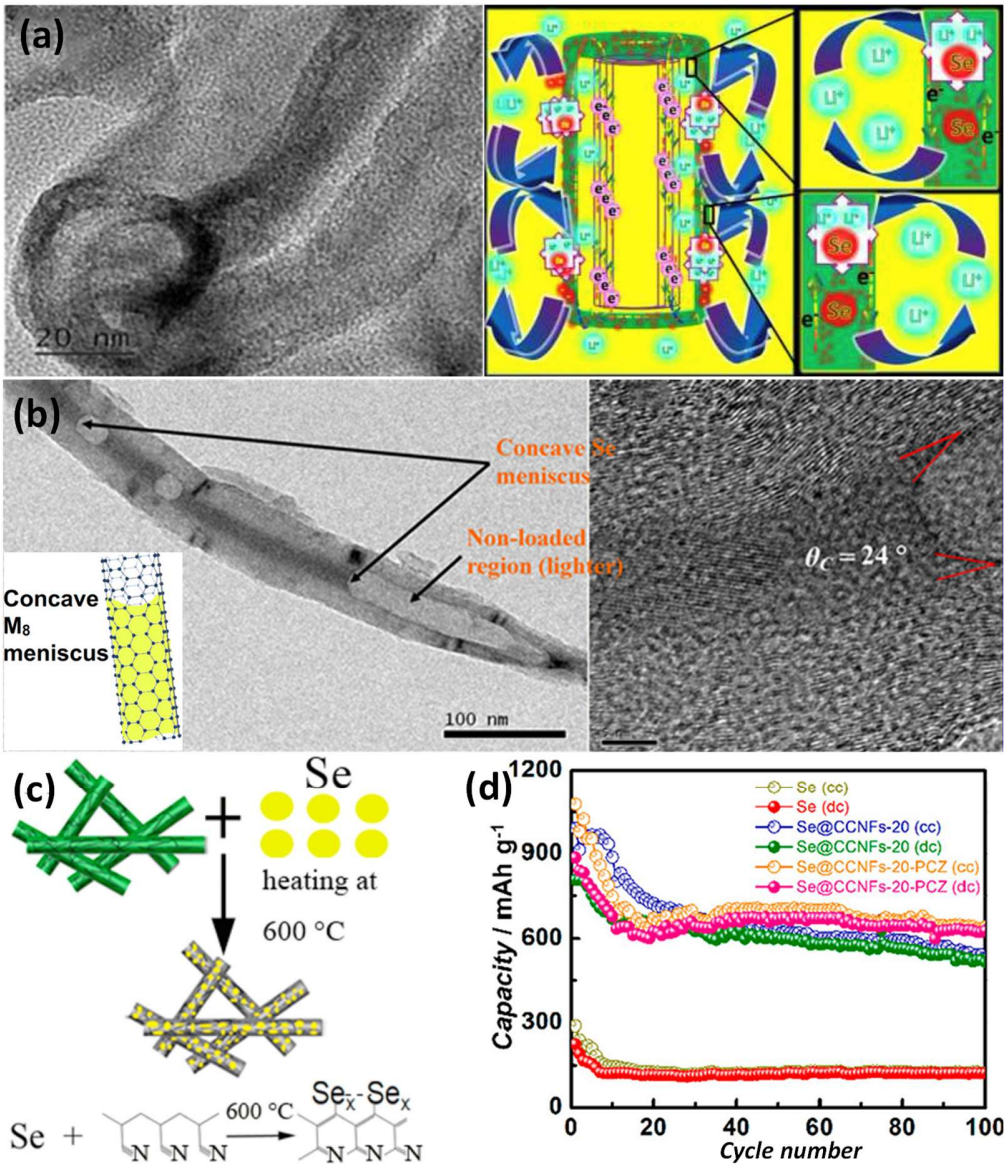

Fig. 8 (a) HRTEM image of TTC/Se-50 and reaction inside[52], (b) Bright-field TEM and HRTEM images of Se-CNT showing concave meniscus of Se filament in the interior core of CNT[53], (c) Schematic illustration of the synthesis process for Se@CNFs-CNT electrode[55], (d) Cycling stability of different cells at 0.1 C-rate over a voltage range of 1.65–3 V (cc and dc represent charge and discharge capacities)[58].

One-dimensional carbon host materials exhibit a very good electron conductivity; the carbon nanotubes or fibers are thus commonly used in Li-Se batteries. High Se loading and suppression of shuttle effect are always the unchanged challenges to address. These problems can be alleviated by enriched porous structure design or protection layer.

Two-dimensional carbon materials

Carbon nanomaterials with two-dimensional (2D) structures have high specific surface area, excellent conductivity and stability. 2D nanomaterials are composed of thin layers and even can reach to one atomic layer. In this case, the Li^+ ion is easy to connect with the host material reaction sites; coupled with the high electron transfer of the high graphitized structure, the 2D carbon achieved high performance.

Graphene is the most widely studied 2D nanomaterial due to its excellent electrical conductivity and ease of functionalization. Youn *et al.* synthesized a novel graphene-selenium hybrid microballs (G-SeHMs) by wrapping around micro-sized Se particles with graphene sheets[59]. The hybrid microballs are well encapsulated by graphene sheets, which served as confinement matrices for selenium fixing, thereby suppressing the dissolution of polyselenide during the charging/discharging process, meanwhile, providing an electrically conductive path for increasing the rate of electron transfer. The hybrid materials as a cathode in Li-Se batteries exhibited a high specific capacity, good rate capability, and stable cycling performance. Zhang *et al.*[60] synthesized porous carbon nanosheets (CNS) and Zhao *et al.*[61] prepared carbon nanoplate for Se loading by calcination of potassium citrate. The optimal Se/CNSs composite achieved a reversible capacity of 672 mA h g^{-1}, and remained at 376 mA h g^{-1} after 1000 cycles at 0.5 C. The porous carbon nanoplate/Se composite exhibited a discharge capacity of 589.2 mA h g^{-1} at 0.2 C and good rate capability of 415.2 mA h g^{-1} at 4 C. The superior electrochemical performance was attributed to the rich content of micro/mesopores, nanoplate structure and a high graphitization degree of the carbon host.

Although these 2D carbon sheet based materials have improved the performance of Li-Se batteries, the application of sheet structure in lithium selenium batteries is still limited, and there still exists great scope for future work. Due to the high aspect ratio (surface-area-to-volume ratio), heteroatoms are easier to decorate on their surface. Thus, introducing other polar particles or heteroatoms on its surface could further enhance the adsorption of PSe.

Three-dimensional (3D) carbon materials

3D carbon materials generally have high specific surface area and a rich pore structure, which can provide more contact between the active materials and conductive carbon, and enhance active Se loading[62]. Besides, the 3D porous conductive network facilitates the transport of electrons. Under the capillary effect, the electrolyte can also be fully infiltrated in the pores, which facilitates the transportation of lithium ions. At the same time, the abundant pores have a stronger physical adsorption effect on the PSe, which can effectively suppress the shuttling effect. The 3D carbon materials can be either artificially designed or directly derived from natural biomass materials.

1) Artificially designed 3D carbon materials

Artificially designed 3D carbon material can take advantage of every building block by selecting appropriate nanostructures. Due to its advantages, 3D carbon materials were applied in many devices, such as supercapacitors[63, 64], photoelectric conversion devices[65, 66], energy storage batteries[67], electrochemical sensors[68, 69], and other fields[70]. For the lithium battery, the 3D interconnected structure provides not only a high surface area for loading more active material but also a large pore volume to reduce the structural damage caused by volume expansion. Besides, its highly conductive framework is beneficial for electron transfer and offers a pathway for transport of Li-ions during electrochemical cycling[71]. The 3D porous carbon materials exhibit good performance in Li-Se battery.

Structured 3D carbon material with 1D and 2D materials as building blocks will be a good choice. As we mentioned above, 1D carbon nanotubes have a rapid electron transfer ability, 2D graphene layers could provide rich reaction sites and prevent the dissolution of polyselenide. Therefore, carbon nanotubes and graphene are commonly used together to build 3D composites. There are a lot of work in this field. For example, Li *et al.* synthesized a series of Se/G-xCNTs composites as cathode material for Li-Se battery[72]. The strongly bonded interfaces between graphene sheets and CNTs stabilized the 3D CNTs@graphene network composite (G-CNTs), as shown in **Fig. 9a**. Compared with pure CNT or graphene host, the optimized Se/G-18CNTs cathode delivered a much higher initial capacity of 575 mA h g^{-1} at 0.5 A g^{-1} and a retained of 479 mA h g^{-1} at 2.0 A g^{-1}. The achieved good rate capability and cycling stability were due to the 3D hierarchical porous framework and excellent electron transfer channels at the interfaces between

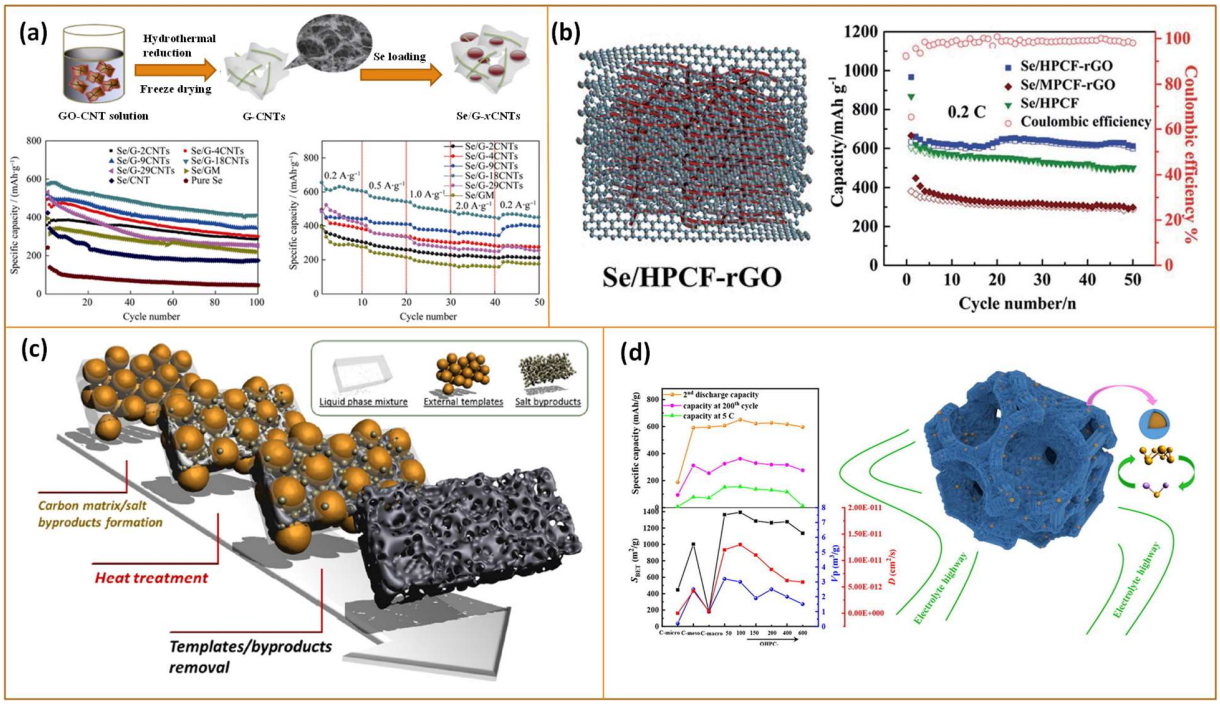

Fig. 9 Preparation scheme of Se/G-xCNTs composites and their cycling stability and rate capacity[72], (b) Structure of the Se/HPCF–rGO composite and its cycle performance[73], (c) Scheme of SPC synthesis route[74], (d) The structure of hierarchically ordered porous carbon and size depended performance[75].

graphene and CNTs. Zeng *et al.* fabricated Se/HPCF-rGO composite by coating reduced graphene oxide (rGO) on the surface of hierarchical porous carbon fiber (HPCF) and selenium composite to suppress the shuttle effect[73]. With the protection of the GO coating layer, Se/HPCF-rGO cathode exhibited excellent reversible capacity and high rate performance for Li-Se batteries (**Fig. 9b**).

The pore size distribution has a significant influence on the performance of the Li-Se battery. Under capillary condensation, the Se prefers to be loaded in the micropores, where the reaction takes place and the produced PSe can be confined inside by physical adsorption. While the mesopores and macropores form structured highway for electrolyte and ions transfer. Thus, the 3D carbon materials with three levels of pore size exhibit a good performance in Li-Se battery. Dai *et al.* synthesized a 3D hierarchically porous carbon structure with a high level of micro-, meso- and macro-level porosities using SiO_2 as template (**Fig. 9c**)[74]. The hierarchical electrode architectures enabled loading of 57.5wt.% of the active Se material, tight encapsulation of both the small and long-chain polyselenide species, inhibition of SEI reaction, and increase of mass transfer of the electrolyte. At higher area selenium loading (~3-3.5 mg_{Se} cm^{-2}), the Se/C electrode showed an

initial specific discharge capacity of 592 mA h g^{-1} at a current density of 0.2 C. Our group synthesized a 3D ordered hierarchically porous carbon with the help of SiO_2 and polystyrene spheres[75]. As shown in **Fig. 9d**, the cathode materials following the concept of the generalized Murray's law maximize the performance of advanced Li-Se battery.

3D carbon materials are promising host for Se, which can combine all the advantages of different materials together, leading to the wonderful electrochemical performance. However, the 3D synthesis process with designed structure is a complex process, which is hard to realize as commercial application. Looking for an easy and green method to get the 3D carbon will be a direction of the future efforts.

2) Naturally derived 3D carbon material

It is a recognized fact that 3D porous carbon materials are beneficial to improve the performance of Li-Se batteries[76, 77]. Generally, the synthesis of materials with complicated structures is not only difficult and complex but also expensive. Thus, fabricating carbon materials with lower prices and higher performance is highly desirable. Biomaterials are a good choice due to their rich carbon elements (protein, fats, carbohydrates), natural abundance, low cost, environmentally friendly and easy accessibility. In reasonable dehydration carbonization, 3D carbon materials can be fabricated. Because of their unique advantages, carbon materials derived from biomass, such as fruit peel[78, 79], cereal shell[80], plant straw[81], animal bones[82], silk[83], etc., have been widely used in Li-Se batteries, as is shown in **Fig. 10**. However, due to the fact that these kinds of carbon lack enough micropores for Se loading, further chemical activation treatment to bio-carbon is necessary.

Fruit peel, discarded as useless to increased bio-waste, can be served as a good carbon precursor. Therefore, different kinds of fruit peels have been employed as raw materials to prepare highly porous and partially graphitized carbon materials. Jia *et al.* synthesized three-dimensional hierarchical porous tubular carbon (HPTCs) using coconut shells[84]. The HPTCs activated by KOH have a large BET surface area of 1786.0 m^2 g^{-1}. Benefiting from the unique 3D hierarchically porous channel structure and high surface area, the prepared HPTCs/Se composite electrode exhibited a high capacity of ~515 mA h g^{-1} at 0.2 C and remained at 317 mA h g^{-1} after running over 900 cycles at high rate of 2 C. With the similar process, 3D porous carbon host materials derived from pomelo peel were synthesized by Zhang *et al.*[85] and Sun *et al.*[86], respectively. The

interconnected micro-macropores, good conductivity, and surface functional group modification enable the battery to exhibit good cycle and rate performance.

Plant by-products are also the main raw materials for the preparation of carbon materials. For example, Jia *et al.* obtained porous carbon from sunflower sponge, and the selenium loading in the porous carbon/Se composite was 63 wt.%[87]. Li-Se battery with the porous carbon/Se composite electrode delivered a high specific initial capacity of 319 mA h g^{-1} and maintained 290 mA h g^{-1} after 840 cycles at 1 C, representing an extremely high capacity retention of 90.9%. Similarly, based on plant by-products loofah sponge, nitrogen-doped loofah sponge carbon (N-LSC) has been synthesized via a simple calcination process and then applied as a blocking layer for Li-Se batteries[88]. Rice husks can also be used as the carbon source for 3D porous SiOC with the help of a supercritical CO_2 (SC-CO_2) technique[89]. In addition, there are many other sources that come from animals, such as silk cocoons[90], animal bone[82] can be used as precursors of porous carbon materials. And even the abandoned paper cup was found to be worked well as Se loading carbon material[91]. There are millions of natural resources from animals, plants, algae, etc., which could be potentially used as the precursors of carbon supports for selenium in lithium batteries, which provides a promising avenue for the future development of batteries.

Fig. 10 The source of biological carbon.

2.2.2 Polar sites host materials

Porous carbon host materials could suppress the dissolution of polyselenide intermediates by physical adsorption. However, the weak interaction between the non-polar carbon material and the polar polyselenide is unfavorable for the binding and capture of the soluble PSe. In addition to changing the porosity of the carbon materials, improving the polarity of the host materials is another effective solution to address the problem of shuttle effect[92].

O, N, and S elements have a higher electronegativity than that of C, and thus have a better lithophilicity. These heteroatoms in carbon host materials will have a strong interaction with PSe, known as "chemisorption". Moreover, the introduction of such heteroatom dopants (B, O, N, et al.) in carbon materials improve the conductivity and stiffness of the material, generate surface polarization by changing the surface environment of the material. These changes enhance the interaction between carbon matrix and polyselenide, providing strong chemisorption while promoting electron and ion transfer, thereby inhibiting the shuttle effect and extending the cycle lifespan. Besides, the polar nanostructures such as oxide, nitride, and sulfide can be directly used as Se host materials or as polar sites introduced to carbon host frameworks. Thus, the polar sites can be realized by heteroatom doping or by incorporating polar nanostructures rich in O, S, N elements into the host system.

2.2.2.1 Heteroatom (B, O, S, N, et al.) doped carbon materials

B, O, and N atoms are commonly used in doping treatment of carbon materials because of their similar atomic size to carbon atoms and higher electronegativity. Carbonization N, P, or O-rich precursor to form heteroatom doped carbon is one of the most simple and common methods. Jia *et al.* synthesized chitosan derived porous carbon framework (CPC) for Li-Se battery[93]. The SEM images of the obtained porous CPC are shown in **Fig. 11a** and **b**. The EDX mapping in **Fig. 11c** indicates that the heteroatoms O and N successfully doped in the C/Se composite. The Se-50.2/CPC composite cathode delivered a reversible capacity of 673.1 mA h g^{-1} in the 2nd cycle and maintained at a high value of 633.9 mA h g^{-1} after 100 cycles at 0.1 C, showing a good cycling performance. Zhao *et al.* synthesized a heteroatom (N and O) double-doped hierarchical porous carbon (HDHPC) utilizing polydopamine as precursor[94]. Pyrrolic-N and ketonic-O codoped carbon possessed a strong binding to Li_2Se with binging energy of -3.04 eV (**Fig. 11d**), which is much higher than that of pure carbon (-0.96 eV). The result indicates that heteroatom doping (N,

O) can effectively enhance the interaction between selenium/PSe guests and carbon host. Thus, the composite delivered a good electrochemical performance with a stable reversible capacity of 545 mA h g^{-1} at 0.5 C after 1500 cycles (**Fig. 11e**). Many other heteroatom doped carbons were synthesized from different raw precursors, such as polypyrrole[95, 96], polyaniline[97], amino acid-rich gelatin[98], cyanuric chloride[99], melamine[100, 101], pyrrole[102, 103], nitrogen-containing flame retardant MELANIC MC (MCA)[104] and polyacrylonitrile[105], etc.

Metal-organic frameworks (MOFs) are another type of precursor material to produce heteroatom-doped carbon[106, 107]. MOFs, a class of porous material assembled by metal ions and organic connectors, have a vast variety in structure and diversity in chemical compositions[108]. In MOFs structure, the metal sites can be ions of transition metals, alkaline earth metals, or

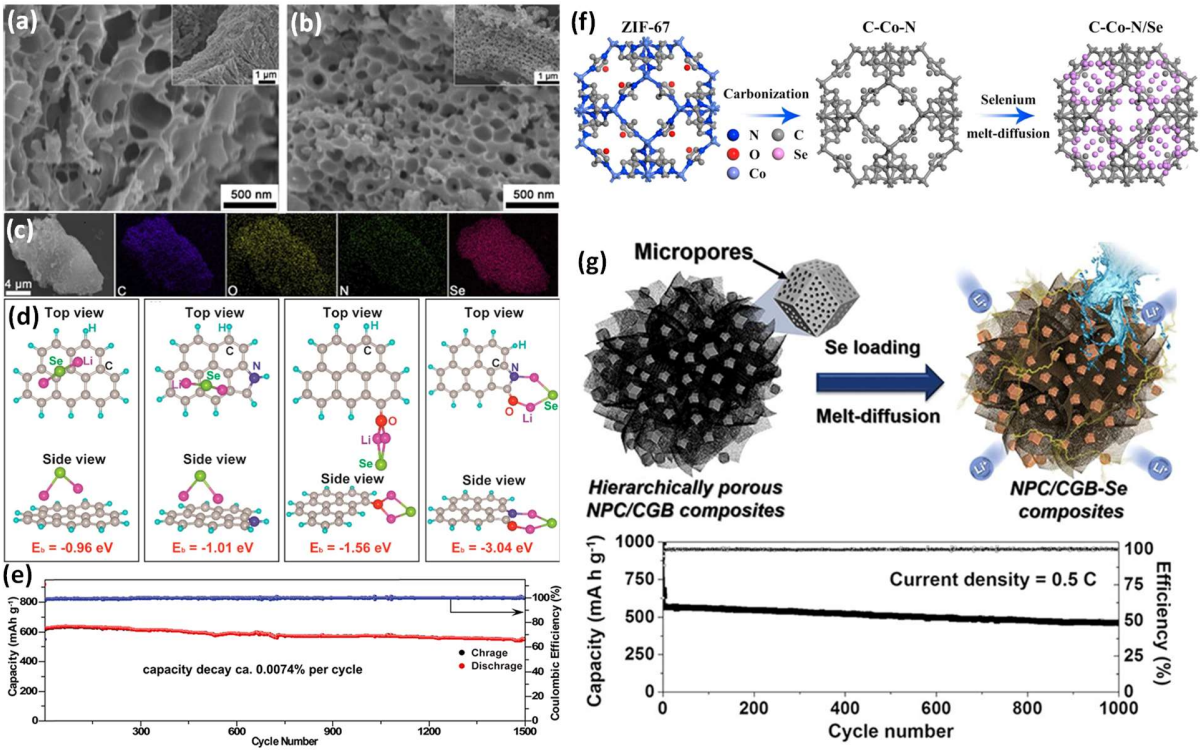

Fig. 11 (a, b) SEM images of framework CPC and composite Se-50.2/CPC, and an inset in each panel is the relatively low-resolution picture. (c) corresponding C, O, N and Se elemental mapping images of Se-50.2/CPC composite[93], (d) Schematic adsorption configuration of Li_2Se on prinstine carbon framework, carbon only with pyrrolic-N, carbon only with kenotic-O, and pyrrolic-N and kenotic-O codoped carbon, respectively. (e) Cycling performance of Se50/HDHPC at a current density of 0.5 C[94], (f) Schematic illustration of the synthetic process for C-Co-N/Se[109], (g) Formation Mechanism of Se-Nanoparticle-Filled Hierarchically Porous NPC/CGB Composite and cycle performances of NPC/CGB-Se[110].

lanthanides, while the organic linkers are typically multidentate molecules with N- or O- donor atoms, such as pyridyl, polyamines, carboxylates, etc.[111] Therefore, the MOF itself contains heteroatoms such as oxygen and nitrogen. In the past decade, MOFs have been regarded as promising carbon precursors due to their easy fabrication of different MOFs networks with various pore sizes, shapes, volumes and chemistries by properly selecting different combinations of metal ions and organic ligands.[112, 113] So far, more than 20,000 MOFs with diverse compositions, crystal structures, and morphologies have been reported.[114, 115] N-doped graphitic C-Co scaffold (C-Co-N) derived from ZIF-67 was synthesized by He's group and used for the impregnation of Se and SeS_2[109, 116]. The schematic illustration of the synthetic process for C-Co-N/Se is shown in **Fig. 11f**, the pores constructed in the ZIF-67 and heteroatom distribution can be observed. Moreover, the N-doped porous carbon derived from MOF-Al[117] and MOF-Ni[118] were fabricated by Li *et al.* and Liu *et al.*, respectively. These N-doped porous carbons exhibit excellent cycling stability, superior rate capability and high Coulombic efficiency. Song *et al.* designed nitrogen-doped core-shell hierarchical porous carbon derived from ZIF-8 and ZIF-67[119]. Liu *et al.* synthesized irregular bubbles-rich porous carbon microcubes (CMCs) derived from Zn/Ni-MOF2 microcubes[120]. Besides the advantage of N-doping adsorption, the core-shell and the structure rich in bubbles also greatly increase selenium loading and buffers volume expansion. These corresponding Se/C composites exhibited an ultrahigh initial discharge specific capacity and cyclic stability. To increase the electron conductivity of the host, Park *et al.* introduced MOF in graphene[110] and porous carbon nanofibers[121]. As shown in **Fig. 11g**, the rich pore structure from MOF provides enough space for selenium loading, and high conductivity of graphene is favorable for ion/electron transport, and most importantly the nitrogen doping enhances chemical adsorption and thereby prevents the diffusion of PSe. Thus, the N-doped carbon polyhedrons anchored on crumpled graphene balls (NPC/CGB)-Se composite achieved superior high specific capacity of 998 and 462 mA h g^{-1} at the 1st and 1000th cycles and excellent rate capability of 409 mA h g^{-1} at an extremely high rate of 15 C.

2.2.2.2 Introducing polar nanostructures

Metal oxide, metal nitrides, and metal selenides are beneficial to inhibit the shuttle effect owing to the presence of O, N, S elements forming chemisorption bonds with soluble PSe[122-124]. Moreover, these polar particles can be used as efficient catalysts to facilitate the polysulfide redox

reactions and transform soluble lithium polysulfide Li_2Se_n ($8 \geq n \geq 4$) to Li_2Se_2 and Li_2Se, thereby significantly improving battery performance.

Metal oxides have strong affinity toward the highly polarized PSe for their polarized structure. Wu *et al.* synthesized hollow spherical α-MoO_3 used for both electrocatalyst and adsorbent of PSe in Li-Se batteries[125]. From the Li_2Se_6 solution adsorption experiment in **Fig. 12a**, the solution with α-MoO_3 changed to colorless after the adsorption, suggesting that the α-MoO_3 has the most strong interaction with PSe. The catalyst and strong adsorption function lead to the lower overpotential for the reaction, as shown in **Fig. 12b**. Zhang *et al.* confined Se within TiO_2 to reduce the dissolution of PSe by the hydrophilic Ti-O bonds[36]. The TiO_2–Se composite cathode exhibited a higher initial discharge capacity of 481 mA h g^{-1} than that of the pure selenium cathode with capacity of 343 mA g^{-1}, displaying a higher utilization of active materials. Ye *et al.* coated 5 nm MnO_2 nanoparticles on the surface of ZIF-67@Se to form a MOF@Se@MnO_2 structure composite[126]. The obtained MOF@Se@MnO_2 sandwich structure provided more active sites for tethering the selenium so that the shuttle effect and the dissolution of PSe in the electrolyte are reduced, thereby showing an excellent electrochemical performance in Li-Se battery. Jayan *et al.* used MXenes as an effective PSe immobilizer for Li-Se Battery[127]. In **Fig. 12c**, compared with graphene, the electron transfer from the PSe to all the $Ti_3C_2X_2$ (X=S, O, F, and Cl) increases, leading to the stronger chemical interactions between polyselenides and $Ti_3C_2O_2$. In **Fig. 12d**, the calculated Li_2Se_n adsorption strength provided by S and O terminated Ti_3C_2 is stronger than the commonly used ether based electrolyte (DME and DOL), indicating the effective suppression of the Li_2Se_n shuttling. For different MXenes, the adsorption energy in $Ti_3C_2S_2$ and $Ti_3C_2O_2$ are higher than other MXenes and graphene, which demonstrates stronger chemical interactions of Li_2Se_n with S and O terminated surfaces.

Metal selenides are also used in the Se cathode to reduce the shuttle effect. The strong interfacial interaction between metal selenide and adsorbate enables the adsorbate to be effectively anchored on the surface of the metal selenide. Wang *et al.* analyzed the adsorption strength influence on the catalyst working process in Li-S battery[128]. By adding $CoSe_2$, the bond length of S-S in Li_2S_4 and S-Li in Li_2Se becomes longer due to the strong adsorption between the substrate and polysulfide, as is shown in **Fig 12e**, indicating that the anion N doping in $CoSe_2$ composites (N-$CoSe_2$) could more effectively weaken the S−S bridged bond. In this case, as shown in **Fig. 12f**, Li_2S_4 is easily broken to Li_2S- and finally gradually converted to shorter PSe, which is beneficial

for the discharge reaction. While for Li_2S, the weakened Li-S bond also has a lower barrier to form LiS- and Li-, the Li_2S is thus easily charged back to sulfur. Yang *et al.* applied the $CoSe_2$-porous carbon ($CoSe_2$-PC) to Li-Se battery and explored its function on PSe[129]. The $CoSe_2$ served as an effective electro-catalyst and dynamically facilitated the redox reaction kinetics of polyselenide and suppressed the dissolution of Li_2Se_n intermediates into the electrolyte, thus mitigating the shuttle effect. Se@$CoSe_2$-PC achieved a high reversible capacity of 408 mA $h \cdot g^{-1}$ at the current rate of 1 C after 100 charge-discharge cycles. Sun *et al.* coated Ag_2Se on the surface of Se/nitrogen-doped mesoporous carbon (NMC) composite by in-situ reaction to achieve Ag_2Se@Se/NMC cathode material[101]. The highly conductive Ag_2Se coating within which the selenium is completely encapsulated, leads to the faster electron transport to the interconnected carbon framework, achieving greatly improved cycle stability and rate performance of the battery. Xiao *et al.* synthesized a series of two-dimensional selenides ($TiSe_2$, VSe, VSe_2, CrSe, FeSe, CoSe, $NbSe_2$, $MoSe_2$, InSe, SnSe, $SnSe_2$, and WSe_2) and analyze their anchoring function and redox reaction kinetics for LiPSs/S_8[130]. As shown in **Fig. 12g**, compared with isolated LiPSs/S_8, the free energy plots of conversion reactions of LiPSs/S_8 activated by 2D selenides become lower, which reflects the decreased reaction barrier, proving their catalytic effect on reaction conversion. Among these 2D selenides, CoSe and SnSe achieved the best performance. Strong adsorption of polar particles to PSe is helpful for the suppression of the shuttle effect and can catalyze the reaction conversion. However, it does not mean that the stronger the adsorption is, the higher electrochemical performance will be. Cui *et al.* proved that the moderate interaction between polar particles and PSe should be considered in cathode materials, as shown in **Fig. 12h**[131]. Both chemical and physical interaction make a strong synergistic contribution to anchoring polysulfides, extremely alleviating shuttle effect and reducing capacity decay rate. The strong interaction between anchoring materials and lithium weakens the Li−S bond and even induces the thorough separation between sulfur and lithium atoms, promoting the dissolution of sulfur molecules in electrolytes. While, for highly metallic anchoring materials, the strong bond formed between substrate and polysulfide can break the S−S bond of Li_2S_n molecules and cause sulfur to lose its electrochemical activity. Tao *et al.* fabricated various nonconductive metal-oxide nanoparticle (MgO, Al_2O_3, CeO_2, La_2O_3, and CaO) anchored on porous carbon nanoflakes[132]. As shown in **Fig. 12i** and **j**, MgO has the medium adsorption strength to Li_2S_8, which achieved the best performance in Li-S battery.

Although the rule is obtained from the Li-S battery, due to the very similar properties of Se to S, it will give guidance for the Li-Se battery.

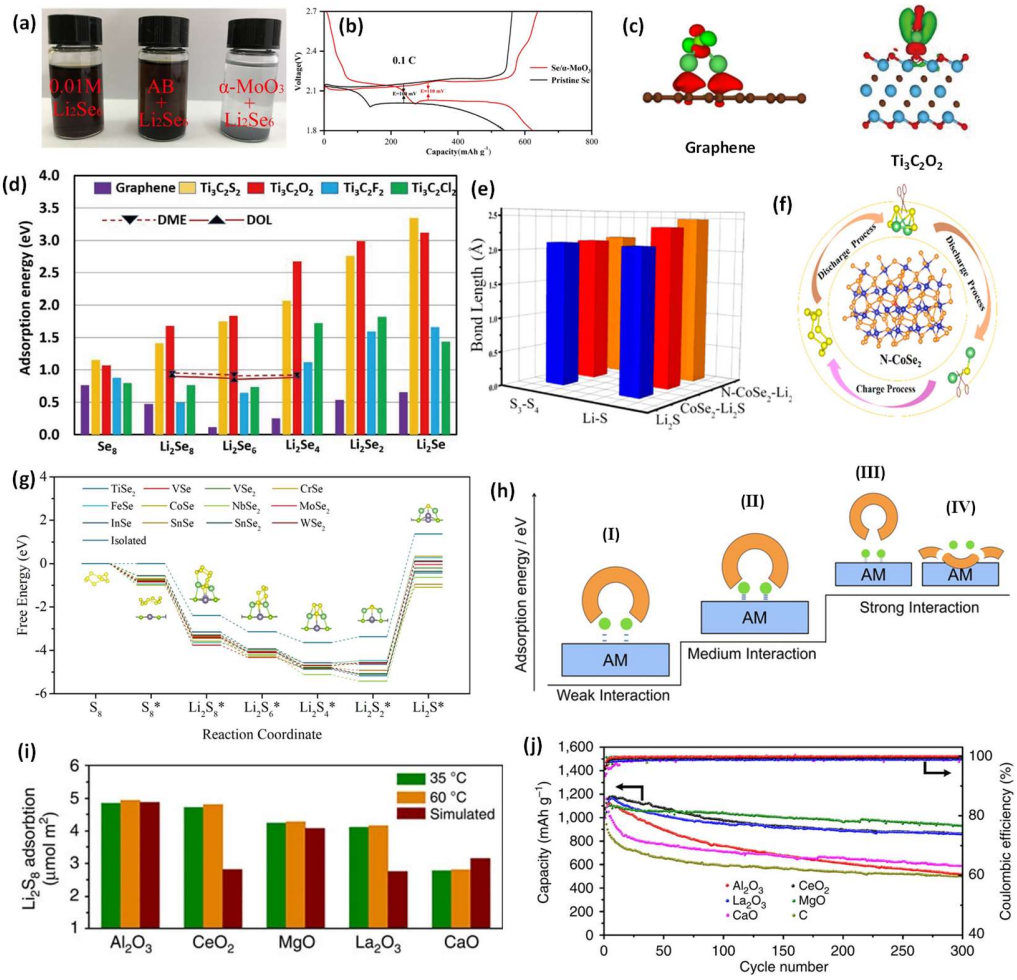

Fig 12 (a) Adsorption experiment after standing for 1 h, (b) Initial charge/discharge curve of Se/α-MoO_3 and pristine Se electrodes at 0.1 C[125], (c) Side views of charge density difference of Li_2Se on $Ti_3C_2O_2$ and graphene (The green and red colors denote charge accumulation and depletion, respectively), (d) Adsorption energies of Se_8 and Li_2Se_n on graphene and $Ti_3C_2X_2$ (X = S, O, F, and Cl) and the binding energies of PSe with electrolyte solvent molecules of DME and DOL[127], (e) The detailed bond lengths of S–S of Li_2S_4 and Li–S of Li_2S on the surface of $CoSe_2$ and N-$CoSe_2$, (f) Bond lengths effect on the electrochemical reaction[128], (g) Free energy plots of conversion reactions of isolated LiPSs/S_8 and LiPSs/S_8 activated by 2D selenides[130], (h) of polysulfides anchored on anchoring materials (AMs) on different interaction strength[131], (i) Experimental and simulated adsorption amount of Li_2S_8 on different metal oxides. (j) Specific capacity and the corresponding Coulombic efficiency of the composite electrodes upon prolonged 300 charge/discharge cycles at 0.5 C[132].

The introduction of functional inorganic additives in the cathode contributes to effectively improve the battery performance. However, the weight density of the inorganic materials should be optimized, otherwise the energy density of the battery could decrease. Moreover, some inorganic material is semiconductor, which limits the transfer of the electron, thereby reducing the utilization of active Se. Most importantly, not all the polar particles will accelerate the reaction, only an appropriate adsorption strength can be helpful. How to choose the appropriate particles is still challenging. Thus, introducing an appropriate amount of inorganic additives and preparation of small size inorganic nanomaterial with optimized adsorption strength is necessary to get high electrochemical performance in Li-Se battery.

2.3 SeS cathode

Li-S batteries have a high theoretical energy density (~2,600 Wh kg^{-1}) and low cost, but S exhibits low conductivity. In contrast, the specific capacity of Li-Se battery is lower than that of a Li-S battery (675 mA h g^{-1}), also the cost of Se is relatively higher, but its conductivity is 20 order magnitude higher than S. Thus, introducing a certain amount of S into the Se cathode is an effective method to improve the capacity of the Li-Se battery[133]. Therefore, much research work on lithium-selenium/sulfur batteries has sprung up. Moreover, the working voltage of the SeS cathode can arrive at a high voltage of 4.5 V, which is beneficial for the achievement of high energy density of the battery. However, the shuttle effect problem in Li-S and Li-Se batteries also existed in Li-SeS batteries. The method of suppressing the shuttle effect for Li-Se battery is also applied to Li-SeS battery.

2.3.1 Selenium-sulfur solid solutions (Se_xS_y)

Selenium-sulfur solid solution (Se_xS_y) is the most commonly used active material form for SeS cathodes. The application of Se_xS_y solid solution as a cathode material for batteries could date back to 2012. Amine's group revealed the potential of SeS_2 as a cathode material for Li and Na rechargeable batteries for the first time[134]. Se_xS_y materials perform higher theoretical capacities than pure Se and have improved conductivity compared to pure S. Since then, there has appeared a boom in the study of sulfur-selenium solid solutions for lithium batteries. For example, Zhang *et al.* fabricated selenium-sulfide solid solutions and embedded it in a mesoporous carbon aerogel (MCA) to obtain a SeS_2@MCA composite[135]. As shown in **Fig. 13a** and **b**, the discharge process of SeS_2@MCA included four steps. The first and third steps were attributed to the conversion of

high-order polysulfides to low-order polysulfides and then to Li_2S_2 and Li_2S. The second and fourth steps were assigned to the transformation of Se to Li_2Se with the intermediate PSe. Benefiting from the high electron conductivity of Se and high capacity of S, the 3D interconnected porous carbon aerogels with SeS exhibited an initial discharge capacity of 1150 mA h g^{-1} at the current density of 50 mA g^{-1}. Wei *et al.* infiltrated S and Se powder with various mass ratios into the main body of mesoporous carbon microsphere (MCMs) by melt-diffusion method and successfully prepared a series of Se_xS_y/MCM composites[136]. As shown in **Fig. 13c**, the obtained Se_2S_5/MCM composites showed unique electrochemical behavior, with five reduction peaks observed. The additional reduction peak at 2.24 V indicates the formation of new intermediate phases. The new intermediates could probably be polysulfoselenide species ($Li_2Se_xS_y$, $4 \leqslant x+y \leqslant 8$). The result indicated that the Li-Se_xS_y battery is more than a simple hybrid of Li-S and Li-Se batteries in ether-based electrolytes.

SeS cathode could achieve a high initial capacity, however, the problem of capacity fading existed. Xu *et al.* found that their synthesized Se_2S_5/MPC cathode exhibited a high initial charge capacity of 1661.2 mA h g^{-1} at 0.1 C[137]. However, the capacity undergoes a rapid fading and then maintained at 345.5 mA h g^{-1} after 50 cycles. The same phenomenon was observed by Cui *et al.*[138]. The Li/SeS_2 cell had a high discharge capacity of more than 1300 mA h g^{-1}, and it soon dropped to 571 mA h g^{-1} in 50 cycles. Xu *et al.* attributed the capacity fading to the aggregation of long-strand PSe in the battery[137]. As shown in **Fig. 13d** and **e**, the inflection point observed in the contour plot of the XANES data in **Fig 13d** coincides well with the critical point in the fully discharged state. While the 2D contour plot for the second cycle in **Fig. 13e** is significantly different from that of the first cycle, reflecting the reduction of Se component and formation of Li_2Se are not completed. Even at the end of the second discharge, the Se K-edge for Se and Li_2Se can be both observed. Moreover, the Se K-edge has little shift in the second cycle, further confirming that the lithiation/delithiation reversibility of Se component was decreased. That is because the weaker binding energy of short-chain PSe with carbon surface than that of long-chain PSe suppressed the transformation of long-chain PSe to short-chain PSe. In this case, long-chain PSe will aggregate, which will lead to PSe shuttle and corrosion of lithium anode as well as increase the internal resistance, and further to the poor Coulombic efficiency and gradual capacity fading.

In order to better understand the physical properties of Se-S compounds and provide a theoretical basis for the development of a minimal shuttle effect in Se-S cathodes, a series of Se-S compounds with different designed mass ratios were synthesized and confined in N-doped mesoporous carbons host by Sun *et al.*[139]. Compared with homoatomic sulfur or selenium molecules, the heteroatomic selenium sulfide molecules exhibit higher polarizability due to the heteropolar Se–S bond, which is expected to have a stronger interaction with the carbon substrates. The binding energy of the carbons with Se–S-containing species was obtained by first-principle calculations based on density functional theory (DFT). As shown in **Fig. 13f**, the interaction of heteroatomic Se–S species with the N-doped sites was stronger than that of homoatomic S–S species. Among the best series of carbon-based sulfur/selenium cathode materials, the Se_2S_6/NMC sample exhibited the best electrochemical performance with the highest reversible capacity of 883 mA h g^{-1} after 100 cycles and the highest Coulombic efficiency of 96%. The electrolyte has great influence on the reaction process. In the hydrofluoroether (HFE)-based electrolyte, the formed robust SEI layer can desolvate Li^+ and prevent the attack of solvent molecules toward Se-S, and thus lead to the solid–solid lithiation process[140]. The dissolution of polysulfides/polyselenides can be inhibited by tailoring the (de)lithiation chemistry of space-confined Se-S cathodes. By rational design for the atomic ratio of S and Se, $S_{22.2}Se$/Ketjenblack cathodes achieved the highest reversible capacity with minimal shuttle effects during long-term and high rate cycling in HFE-based electrolyte.

By adjusting the ratio of the Se and S, the SeS could achieve good performance by suppressing the shuttle effect. However, the shuttle effect still exists in the Li-SeS batteries. The shuttle effect reduction method in the Li-Se battery is applied in Li-SeS battery. As mentioned above, the heteroatom-doped carbon material can reduce the dissolution of the PSe by chemical adsorption of heteroatoms. Therefore, encapsulating the selenium-sulfur solid solution into the heteroatom-doped carbon skeleton can further improve the performance of the lithium battery and researchers have made many efforts in this domain. For example, Hu *et al.* confined SeS_2 to 3D sulfur-doped mesoporous carbon (ISMC) and prepared a SeS_2@ISMC composite[141]. Benefiting from the synergy between sulfur doping and 3D network architecture, the SeS_2@ISMC cathode exhibited an initial discharge capacity of 858 mA h g^{-1} while quickly decayed to 486 mA h g^{-1} after200 cycles. In addition, a series of heteroatoms doped carbon materials were synthesized as SeS host materials, such as boron- and nitrogen-codoped vertically aligned hollow carbon nanotubes (VACNTs)[142],

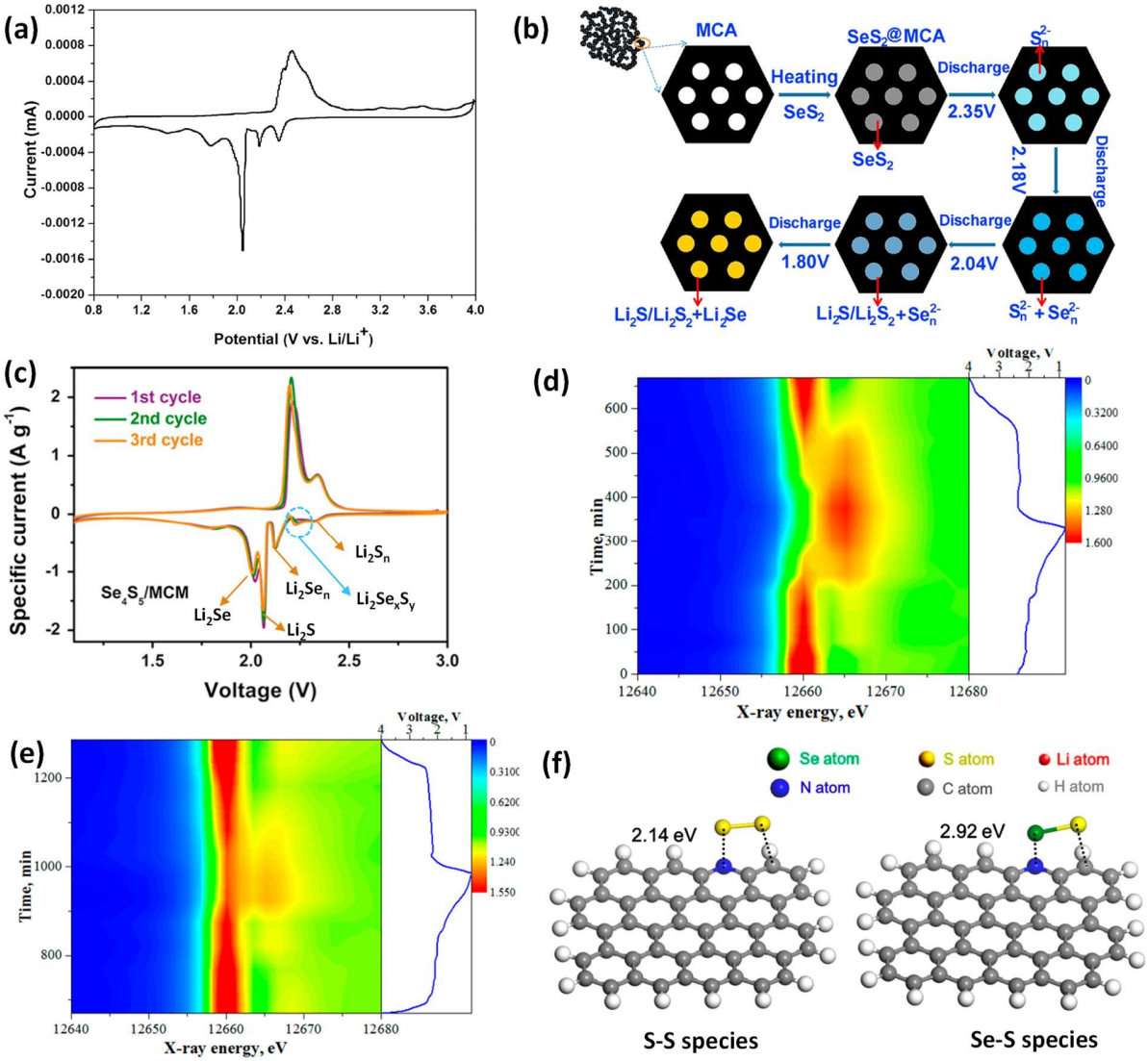

Fig 13 (a) CV curve of the SeS_2@MCA (mesoporous carbon aerogel) composite cathode at 0.2 mV s^{-1}.(b) Scheme of the heating-melt process and the possibility of discharge reaction model of the SeS_2@MCA composite cathode[135], (c) CV curves of Se_4S_5/MCM at 0.1 mV s^{-1}[136], 2D contour plot of in situ XANES data of Se_2S_5/MPC cathode at 0.2 C for the first cycle (d) and second cycle (e), respectively[137], (f) Results of first-principle calculations showing the most stable configurations and calculated binding energies of S–S and Se–S species with the carbon layer doped with pyridinic N[139].

cobalt- and nitrogen-doped porous carbon (Co-N-C) polyhedrons derived from MOF-67[143], and carbonized polyacrylonitrile (CPAN)[144]. These composites have been successfully employed as cathode materials in lithium metal batteries, exhibiting long cycling lifetime, good rate capability and high energy density. Besides heteroatoms doping, introduction of polar particles into the

cathode host is also an effective method. For example, Zhang *et al.* decorate multi-channel carbon fibers with CoS_2 to enhance the adsorption capacity of SeS_2[145]. The carbon fibers network decorated with CoS_2 nanoparticles provided efficient sulfiphilic sites for restricting the dissolution of polysulfides and PSe during the cycle processes, thereby successfully suppressing the shuttle effect and maintaining excellent cycling stability after 400 cycles at 0.5 A g^{-1}. Guo *et al.* synthesized double-walled N-doped carbon@$NiCo_2S_4$ hollow capsules for SeS_2 host[146]. The presence of Ni, Co and N suppressed the shuttle effect of polyselenium/sulfide by the combined chemical and physical adsorption, and the hollow structure buffered the volume expansion caused by Se_2Li and S_2Li products. Furthermore, by adding polydopamine (PDA) coating layer protection, a highly ordered mesoporous carbon (CMK-3) framework confined SeS_2 CMK-3/SeS_2@PDA composite was synthesized[147]. Compared with CMK-3/SeS_2, CMK-3/SeS_2@PDA exhibited a high capacity of more than 1200 mA h g^{-1} and prolonged life over 500 cycles at 0.2 A g^{-1}.

The SeS cathode could improve the specific capacity of the battery by combing the advantages of high conductivity of Se and high theoretical capacity of S. However, the problem of shuttle effect and volume expansion still exists. The rapid capacity fading of the SeS battery hinders its future development. The heteroatoms doping, polar particles introduction and protection layer coating could suppress the shuttle effect to some degree. There is still great space to maintain a higher capacity. Thus, further efforts are required in this system.

2.3.2 Hybrid sulfur-selenium co-polymers

Sulfur-rich polymers have been explored as cathode materials in lithium batteries and have shown unique properties such as ease of synthesis, structural tunability, and precise active sites. In a pioneering work, Pyun *et al.* utilized elemental sulfur and 1, 3-diisopropenylbenzene (DIB) as co-monomers to synthesize sulfur-rich polymers by the inverse vulcanization method, as shown in **Fig. 14a**[148]. A central motivation of the inverse vulcanization chemistry was to enable modification of elemental sulfur into a processable polymeric form that still retained the electrochemical activity of elemental sulfur. The cyclic voltammetry (CV) result in **Fig. 14b** confirmed that poly(S-r-DIB) copolymers exhibited very similar electrochemical behavior to that of S_8. Different from the S cathode, the S in sulfur-polymers is tightly bonded with polymers, the shuttle effect thus will disappear. The prepared copolymers showed higher initial specific capacity

than elemental sulfur, indicating a promising prospect for the chemical confinement of polysulfides within polymer matrix.

In order to improve the solubility of organo-diselenide in electrolyte and obtain a high capacity of the battery, Fu's group *via* the addition of phenyl diselenide (PDSe) synthesized PDSe-S and PDSe-S_2[149]. The function process of PDSe-S_2 in lithium battery is shown in **Fig. 14c**. Compared with the low initial capacity of PDSe (118 mA h g^{-1}), PDSe-S and PDSe-S_2 exhibited higher initial capacity of 252 and 330 mA h g^{-1}, respectively. Later, phenyl selenosulfide (PhS-SePh) was synthesized by an exchange reaction between phenyl disulfide and diselenide[150]. PhS-SePh shows

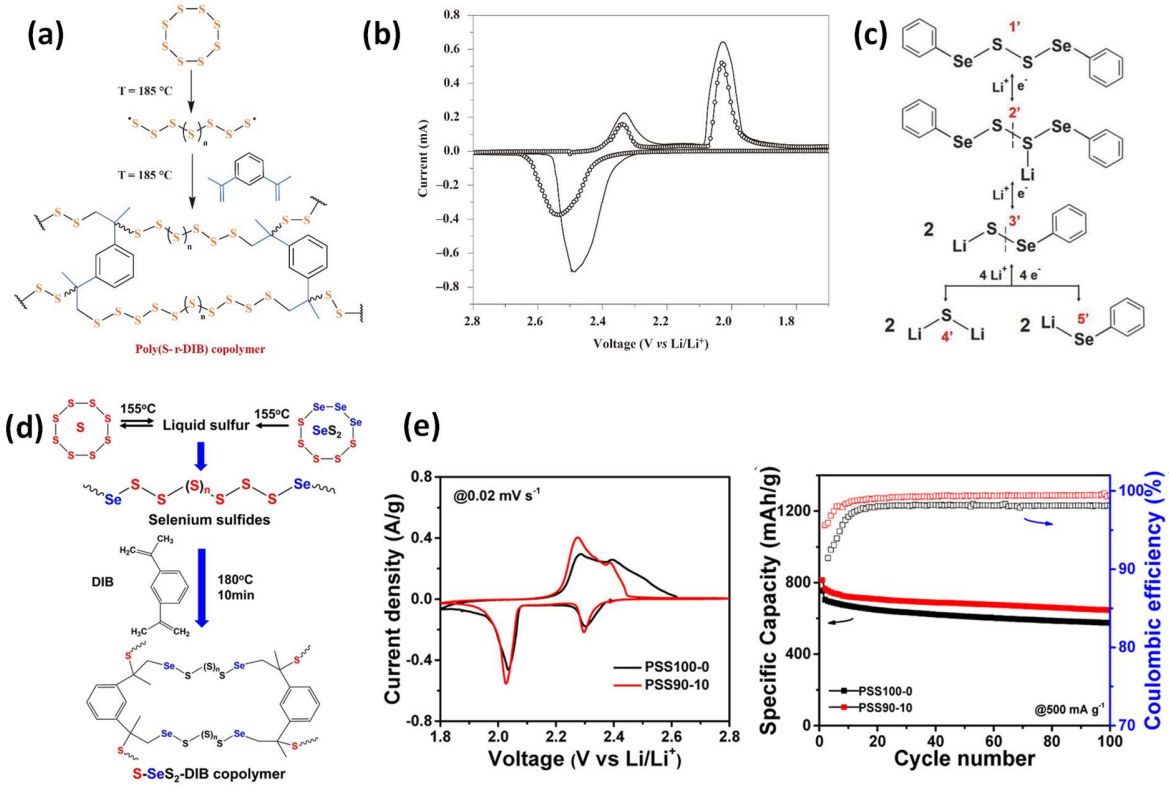

Fig. 14 (a) Synthetic scheme for the copolymerization of S_8 with DIB to form chemically stable sulfur copolymers. (b) CV of pure sulfur (solid black line) and poly(S-r-DIB) (10 wt.% DIB, open circles) at a scan rate of 20μV s^{-1}[148]. (c) Redox reactions of PDSe-S2 in rechargeable lithium batteries[149]. (d) Synthesis route of polymeric selenium sulfides via inverse vulcanization method. (e) The first cycle CV curves at 0.02 mV s^{-1} and constant-current cycling performances of pure PSS100-0 and PSS90-10 co-polymers (PSS(100 – x)–x: The S–SeS2–DIB co-polymers with desired S/SeS2 mass ratios, where x is the weight percentage of SeS2 in S/SeS2.)[152].

better kinetics and much better cycling stability than PhS-SPh and PhSe-SePh for its higher entropy of the mixture and thus lower Gibbs free energy. Zhou *et al.* synthesized a selenium-doped organic polymer material (PDATtSSe) and obtained an improved volumetric capacity and Coulombic efficiency[151]. Compared to pure sulfur electrodes, the doping of Se significantly enhances the electronic conductivity of battery electrodes and the formation of long-chain lithium polysulfides was completely restricted.

Introducing Se into the sulfur-rich polymer could enhance electronic conductivity, improve Li-ion transport, and suppress the shuttle effect. Thus, the inverse vulcanization method has been extended to the synthesis of hybrid organic-inorganic sulfur-selenium co-polymers. Dong *et al.* introduced SeS_2 into the polymeric sulfur and obtained sulfur-rich polymeric selenium sulfides (S-SeS_2-DIB, DIB: 1,3-diisopropenylbenzene)[152]. In the structure, divinyl functional groups of DIB were chemically cross-linked with S/SeS_2 chain radicals through a ring-opening polymerization, as is shown in **Fig. 14d**. The newly formed bonds of C-S, C-Se, and S-Se in S-SeS_2-DIB copolymers effectively alleviated the shuttle effects of polysulfides/polyselenides, achieving a higher stability than pure S–DIB, as shown in **Fig. 14e**. Moreover, Gomez *et al.* prepared poly(Se_xS_{1-x}-DIB) composite and the sulfur-selenium co-polymer cathode exhibit enhanced C-rate capability and high cycling stability[153].

In sulfur-selenium co-polymers, the short sulfur and selenium chains in hybrid sulfur-selenium co-polymers are chemically capped by organic groups, which makes long polysulfides and PSe difficult to form in the following cycling process. In this case, the shuttle effect could be greatly decreased. Another obvious benefit of the co-polymers is their low quantity requirement for the liquid electrolyte. However, due to the limitation of the linked active materials, the energy density of the batteries cannot reach high value, although they indeed achieve a high specific capacity, enhanced cycling stability and Coulombic efficiency.

2.4 Li_2Se cathode

Se cathode has the problems of shuttle effect and huge volume expansion. Some researchers look for its substitution such as Li_2Se used as active material in Li-Se battery. Li_2Se undergoes 40% volume shrinkage rather than 80% volume expansion of Se. This makes the cathode keep more stable. The most attractive is that using prelithiated Li_2Se as active material, the lithium anode can

be replaced with a non-lithium anode. Thus, the active Li_2Se worked as active material was carried out although the related works are limited. To deal with the problems of low conductivity of Li_2Se and shuttle effect, the Li_2Se active material is confined inside the porous carbon host. For example, Wu *et al.* synthetized Li_2Se nanoparticles by a simple and fast route, as shown in **Fig. 15a**[154]. The capacity of pure Li_2Se nanoparticles exhibited a rapid drop, arriving at less than 100 mA h g^{-1} in 100 cycles (**Fig. 15b**). This is due to the fact that they attributed the capacity fading to the production of dendrites, as shown in **Fig. 15cII**. By coating with a carbon shell protection layer, the obtained nanostructured carbon (C)-Li_2Se with additional carbon shell (C-Li_2Se@C) composite achieved stable cycle capacity and less lithium dendrites grown (**Fig. 15cIV**). Lu *et al.* synthesized Li_2Se cathode composed of alternating active layers and barrier layers (**Fig. 15d**), the Li_2Se cathode

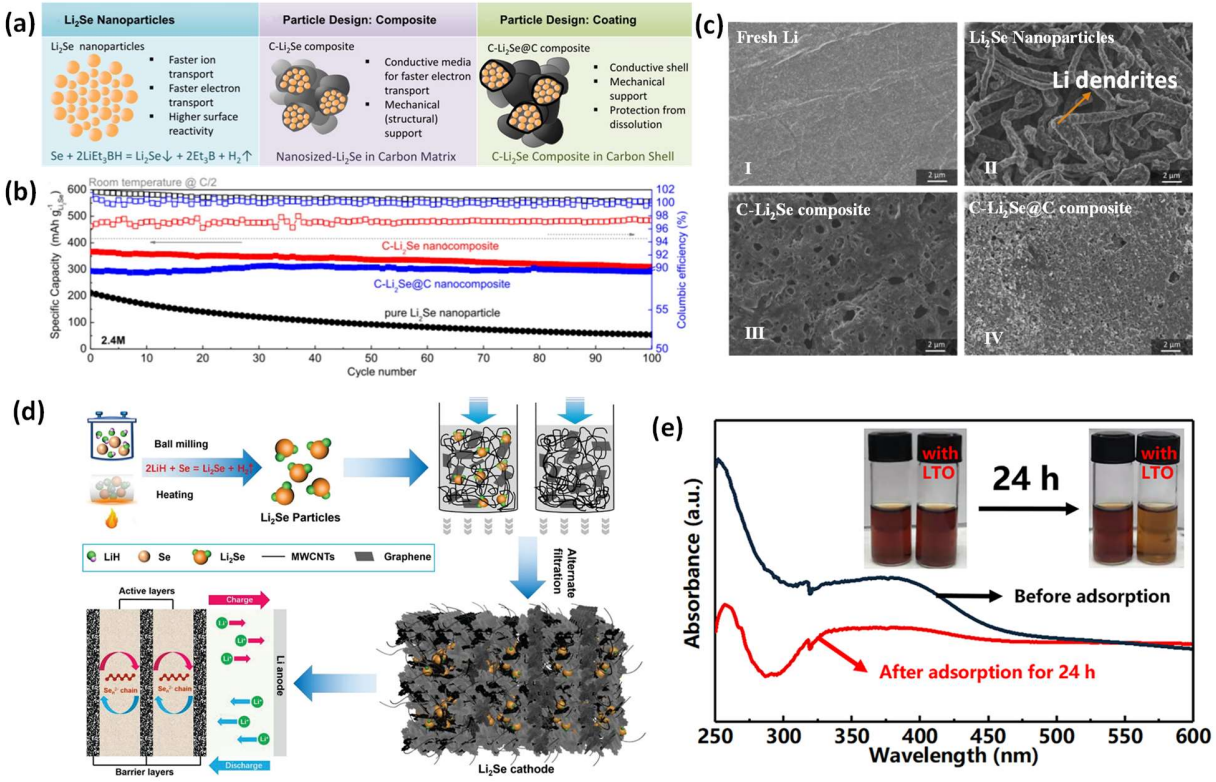

Fig. 15 (a) Schematic diagram and properties of pure Li_2Se nanoparticles, C-Li_2Se composite and C-Li_2Se@C nanocomposites, (b) Retention of specific capacity and coulombic efficiency during 100 galvanostatic cycles at 0.5 C, (c) SEM micrographs of fresh Li anode, pure Li_2Se nanoparticle cathode, C-Li_2Se composite particle cathode and C-Li_2S@C shell-protected cathode after 140 cycles[154], (d) Schematic diagram of the synthesis process of Li_2Se particles and Li_2Se cathodes[155], (e) UV-vis spectra of Li_2Se_6 solution with $LiTiO_2$ before/after adsorption test[156].

exhibited a high capacity of 698 mA h g^{-1} at 50 mA g^{-1} by the barrier layers adsorption for the PSe[155]. As Se cathode, introducing polar particles to enhance the adsorption for the PSe is also an effective method to decrease the shuttle effect. Xia *et al.* fabricated pre-lithiated Li_2Se-$LiTiO_2$ composite cathode materials by a facile solid-phase synthesis method in Li-Se battery[156]. As is shown in **Fig. 15e**, the color of Li_2Se_6 solution changed from dark brown to light brown with added $LiTiO_2$, reflecting its superior PSe trapping ability, which is favorable to achieve stable electrochemical performance of Li-Se batteries.

However, the problems of the shuttle effect still exist in Li_2Se cathode battery. The capacity fading happened in the charge/discharge process due to the production of the Li dendrites. Moreover, Li_2Se has the new problems of difficult production and high price. There is a long way to go to solve these problems.

2.5 Freestanding electrodes

Most common cathodes currently used in Li-Se battery consist of active material, binder, super carbon and metal current collector. In particular, the metal current collector accounts for 75 wt.%, it does not make any other contribution to improving the capacity of the battery apart from working as a carrier. Freestanding electrode could easily form a cathode membrane without assistant of additional conductive additives, polymer binders and metal current collectors, which greatly increases the amount of the active Se and thereby achieves high energy density. Therefore, using freestanding carbon host cathode becomes a good choice in Li-Se battery. Furthermore, the battery with a free-standing electrode demonstrates a relatively small interface impedance, which is beneficial for the rapid transportation of lithium ions. Above all, batteries with excellent cycle stability and ultra-high rate performance can be produced by introducing freestanding electrodes.

Flexibility provides mechanical stability of the film, which is the characteristic of the free-standing cathode materials. Moreover, in order to suppress the shuttle effect of PSe, porosities of the host material should be preserved. One-dimensional porous carbon nanofiber/nanobelts combining the flexibility and porous structure characteristics are good approach. For example, Zeng *et al.* prepared a kind of porous carbon nanofibers (PCNFs) as the skeleton for the self-supporting electrode by electrospinning the precursor solution of polyacrylonitrile (PAN) and triblock copolymer Pluronic F127, as shown in **Fig. 16a**[157]. The flexible porous carbon nanofibers freestanding Se@PCNFs cathode exhibited excellent cycle stability, retained a reversible capacity

of 516 mA h g^{-1} in the 900th cycle at the current of 0.5 A g^{-1}, even at 4 A g^{-1} a high capacity of 306 mA h g^{-1} was achieved. Cai *et al.* confined Se in hollow-core nitrogen-doped carbon (CNx) nanobelts as a freestanding cathode material in Li-Se battery[158]. This novel freestanding electrode could accommodate large volume expansion of Li_2Se and promote electron and ion transfer, while providing physical adsorption for PSe, thereby generating high specific capacity, good rate capability and cyclic stability.

Besides the flexibility, graphene has rapid electrons and ions transportability, thus it is commonly used in the freestanding cathode. For example, Han *et al.* by embedding selenium impregnated mesoporous carbon nanoparticles (Se/MCN) in reduced graphene oxide (GRO) sheets synthesized Se/MCN-RGO binder-free cathode material [159]. The layer structure free-standing Se/MCN-RGO is shown in **Fig. 16b**. The Se/MCN-RGO freestanding cathode with 62 wt.% selenium loading exhibited a high initial discharge capacity close to the theoretical value (655 mA h g^{-1}) at 0.1 C and an ultra-long cycling stability, which accounted for 61% of the initial value after 1300 cycles at 1 C. Moreover, He *et al.* combined the advantages of CNT and graphene together and synthesized three-dimensional graphene-CNT@Se (3DG-CNT@Se) aerogel[160]. The 3D mesoporous conductive network provides channels for highly efficient electron transfer and ionic diffusion, the hierarchical structure prevents fast dissolution of PSe and suppresses volume expansion of Se in charge/discharge process. In **Fig. 16c**, compared with regular Li_2Se–graphene interaction, the Li_2Se molecule that placed between two graphene sheets has a shorter distance with graphene as well as a larger interaction electron density, indicating the strong adsorption to PSe in shuttle effect suppression. Han *et al.* synthesized a flexible self-standing graphene-Se@CNT composite film[162]. It exhibited much higher reversible capacity and cycling stability (315 mA h g^{-1} after 100 cycles at 0.1 C) than graphene–Se composite film. The good performance was mainly attributed to the synergistic effects of graphene and CNT. Furthermore, a ultrahigh Se loading (13.5 mg cm^{-2}) freestanding layer-structure (composed of alternant barrier layers and active layers) cathodes was synthesized by Xia *et al*[161]. The Se loading can be reached at 4.5 mg cm^{-2}. The barrier layers play roles in confining polyselenide and reducing cell polarization. The suppression function can be proven by the slight color of the cycled freestanding layer-structure Se cathode (FLSC) cathode, as shown in **Fig. 16d**.

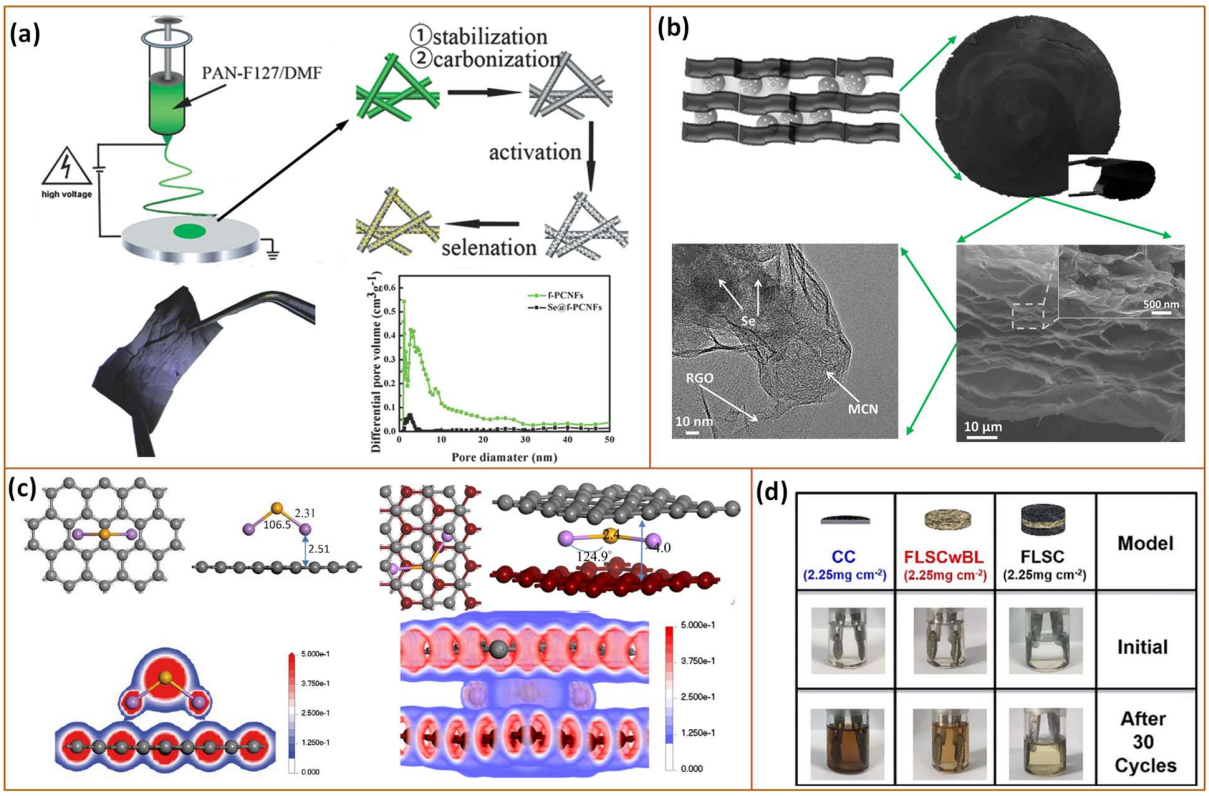

Fig.16 (a) Schematic illustration of the synthesis process of the Se@PCNFs electrode and Photograph of free-standing and flexible Se@PCNFs electrode[157], (b) Scheme of the synthesis route of Se/MCN-RGO paper, photo of the free-standing Se/MCN-RGO paper electrode and Cross-sectional FESEM and TEM images of Se/MCN-RGO[159], (c) Predicted optimized configuration of Li_2Se intercalated into normal Se–graphene interaction (left) and two graphene interlayers (right) and corresponding electron density map[160], (d) Digital images of different Se cathodes before/after 30 cycles[161].

Above all, 3D freestanding structures exhibit many advantages in enhancing the performance of Li-Se battery. The 3D interconnected structure facilitates the transmission of electrons, meanwhile, makes a great contribution to reducing the mass of the battery. Moreover, the highly efficient preparation method greatly simplifies the synthesis of the electrode. Therefore, freestanding cathodes have great potential application in Li-Se battery. However, due to the flexible property requirement of the freestanding cathode materials (one-dimensional or graphene), the application of the freestanding cathode is limited. More material exploration should be done in the future.

For Se cathode, lots of efforts have been made to improve the properties of the Li-Se battery. As a result, numerous C/Se composite cathodes exhibiting significant electrochemical

performances were fabricated. All the efforts focus on the following areas: 1) suitable pore sizes (hierarchical porous carbon) and particular structure (3 D interconnected structure) to encapsulate a large amount of Se, suppress the dissolution of PSe and generate high energy density; 2) introducing polar sites to increase the adsorption capacity of Se to further improve the electrochemical performance of Li-Se batteries. It is worth mentioning that biological carbon used as a precursor, not only showed remarkable electrochemical performance but also greatly reduced the price of the whole battery. Moreover, the SeS cathode, Li_2Se cathode and freestanding cathode are efficient directions to solve the shuttle effect of the Li-Se battery.

3 Electrolyte

Electrolyte, an extremely important part of the battery, has a great influence on the utilization of selenium, the dissolution of PSe and the growth of dendrites. The function of the electrolyte is to facilitate the transfer of ions between anode and cathode. Thus, the characteristics of higher ionic conductivity, lower electronic conductivity, wider electrochemical window and high stability are desired. The organic liquid electrolytes that meet all requirements are commonly used in lithium batteries. However, the intermediate PSe produced by the electrochemical reaction have high solubility in the liquid organic electrolyte, leading to the loss of Se and finally reducing the cycle stability of the battery. Thus, the solubility of PSe has a major effect to the reaction process and performance of the Li-Se battery. In order to solve the problem efficiently, studying the compatibility between electrolytes and electrodes, and their effects on electrochemical performance are extremely important. Research has proven that electrolytes have important effects on improving the performance of Li-O_2 and Li-S batteries[163, 164]. Since selenium is an element of the same main group with O and S, modifying the electrolyte in Li-Se battery should significantly improve electrochemical performance. Researchers made a lot of efforts on electrolytes to solve the above problems both decreasing the dissolution of PSe and forming a solid SEI layer on the surface of cathode are effective methods to suppress the shuttle effect and improve selenium utilization. At the same time, the flammable organic solvent in the liquid electrolyte poses safety hazards. In order to solve this problem, researchers proposed the concept of solid electrolytes and solid-liquid hybrid electrolytes.

3.1 Liquid electrolyte

The theoretical voltage window between selenium and lithium is about 3 V (*vs.* Li/Li^+). All protic solvents release hydrogen gas at 2.2 V, which makes them unsuitable as electrolyte solvents for the Li/Se system. Thus, the liquid electrolytes used in lithium batteries are organic-based. The liquid organic electrolyte commonly consists of a lithium salt and an organic solvent, which works as a carrier for ion transport in the lithium battery. The liquid organic solvents should have the characteristics of effective electrolyte solvents, notably, high ionic conductivity, low electrical conductivity, high transference number, high and low temperature stability, high dielectric permittivity, low viscosity, inertness to all other cell components (e.g., the separator, electrode, spacer, etc.), low flammability, low toxicity, and low cost. Organic carbonates and ethers, which meet almost all the criteria, are widely used in lithium batteries. Electrolyte solvation chemistry of Li–Se batteries dictates the solubility and speciation of LiPSes, and determines electrochemical properties of the cell, such as voltage profile, Li_2Se precipitation and redox kinetics. The LiPSe stability is critically linked with applied solvents, which consequently influences of chemical equilibrium among diverse chain-length polysulfide dianions and radicals. Therefore, the main two kinds of electrolytes, carbonate-based and ether-based, undergo different lithiation/delithiation mechanisms[17].

Carbonate-based electrolyte

Mixtures of cyclic carbonates (ethylene carbonate (EC) and propylene carbonate) with high viscosity and linear carbonates (dimethyl carbonate (DMC) and diethyl carbonate (DEC)) with low viscosity, feature the optimum properties of an effective electrolyte solvent and have been used in Li-ion batteries for two decades. It was expected that these electrolytes could also be used in the Li/Se system. Carbonate solvents cannot dissolve PSe due to their large dielectric constant. In carbonate-based electrolyte, Se undergoes a one-step electrochemical reaction and is directly converted to Li_2Se without an intermediate phase due to the insolubility of PSe in the carbonated solvent[165]. The PSe in carbonate-based electrolytes undergo a solid-solid phase transformation, which could avoid the problem shuttle effect caused by the dissolution of the PSe. However, as shown in **Fig. 17a**, due to the large dipole moment of carbonate electrolyte, the nucleophilic polysulfides intermediates in the multiple reduction steps attack the single-bonded carbon atoms attached to the oxygen atoms of the linear DEC and cyclic EC molecules and have a irreversibly react with carbonates-based electrolyte to form a sulfide carbonate complex. In addition, since the selenium anion is more nucleophilic than the sulfur anion, the uniformly dispersed selenium

exhibits higher reactivity with the carbonyl group in the carbonate-based electrolyte[134]. Thus, the reaction between carbonate-based electrolyte and PSe in Li-Se battery resulted in loss of capacity and low Coulomb efficiency in the first cycle[166].

To avoid the inverse reaction between polysulfides and carbonate-based electrolyte, metastable small molecule sulfur ($S_{2\sim4}$, an allotrope of sulfur) was used by Xin *et al.*to composite with conductive microporous carbon[167]. Since small molecule sulfur is used as electrode active material, it can prevent the transformation of S_8 to long-chain polymorphism in lithium-sulfur batteries. In this case, the problem of lithium polysulfide dissolution and its reaction with carbonate solvents is completely solved. However, in the process of lithium sulfide conversion, only a discharge platform of about 1.9 V appears, the capacity of the high-voltage platform is lost. This finding also applies to lithium-selenium batteries[168]. Thus, in order to inverse reaction between PSe and carbonate-based electrolyte, the active Se should be uniformly dispersed and confined in the micro/meso pores of host materials to ensure that it is in the state of a small molecule.

Appropriate isolation of electrolyte and PSe is an effective way to avoid continuous consumption of PSe during the discharge/charge process. The SEI layer can be used as a positive factor to protect the cathode. Forming a thin uniform solid electrolyte layer (SEI) on the surface of the cathode is an effective method to protect Se from reduction. The protective layer keeps lithium ions permeable while preventing the transport of polyselenide, thereby significantly enhancing the cycle stability of the Li-Se battery. Zhou *et al.* added 10% battery-grade fluoroethylene carbonate (FEC) into carbonate-based electrolyte (ethylene carbonate (EC) and dimethyl carbonate (DMC)) containing difluoro(oxalato)borate (LiDFOB), the obtained LiDFOB/EC-DMC-FEC electrolyte performed excellent compatibility in Li-Se battery[168]. By addition of FEC, a highly stable and Li^+ permeable SEI layers formed on both Li anode and Se/ microporous carbon cathode. The SEI layer avoids the continuous inverse reaction of PSe with carbonate-based electrolytes and reduces the generation of lithium-branched crystals, resulting in compact and smooth lithium electrodes.

Ether-based electrolyte

1.0 M lithium bis(trifluoromethane)sulfonimide (LiTFSI) in 1,3-dioxolane (DOL) and 1,2-dimethoxyethane (DME) mixture solvents (v/v = 1/1) with 1 wt.%~5 wt.% lithium nitrate ($LiNO_3$) became the most widely used commercial ether-electrolyte[169]. The choice of LiTFSI with large

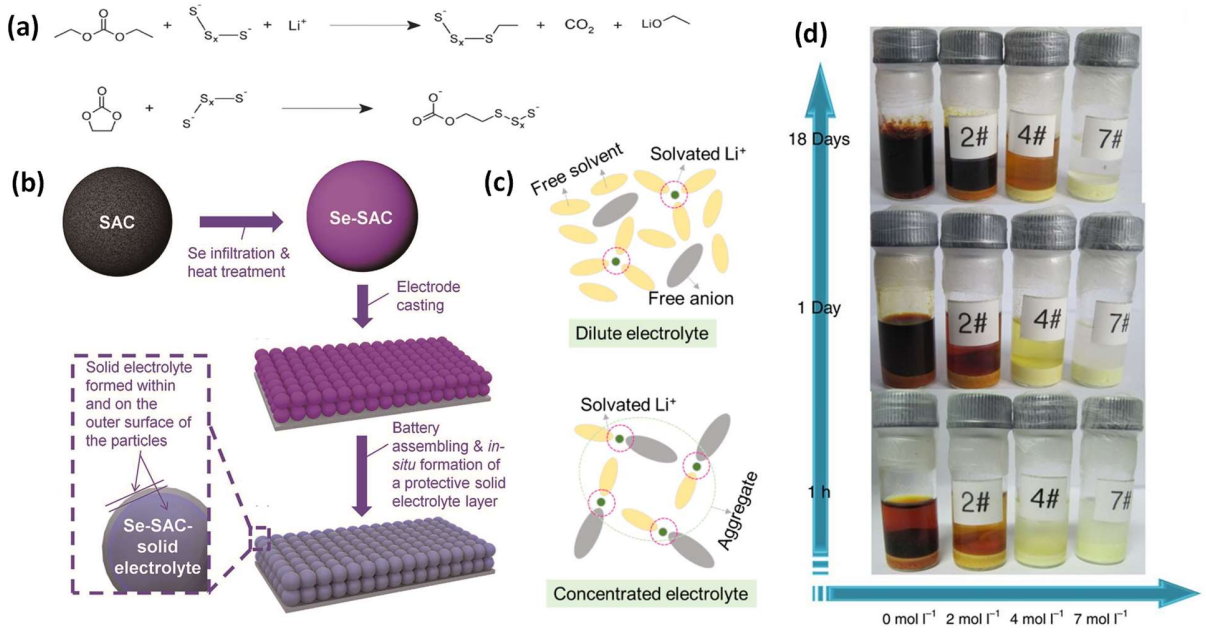

Fig. 17 (a) Proposed reaction mechanism of polysulfides in carbonate electrolyte[166], (b) Schematic illustration of the *in situ* formation of protective solid electrolyte layer with FECs[171], (c) Schematics of coordination structures of (up) dilute and (down) concentrated solutions[170], (d)The color changes of four samples with different salt concentrations containing the same amount of Li_2S_8 along with time[172].

complex anions allows sufficient solubility in ether solvents due to its high disassociation ability. The LiTFSI is dissociated into Li^+ and $TFSI^-$. The Li^+ is coordinated by stoichiometric solvents, forming the Li solvated complex, which is surrounded by uncoordinated solvents[170]. The linear DME solvent with high dielectric constant can dissolve high concentration of long-/medium-chain LiPSes, which greatly facilitates reduction of insulating selenium and acts as solution-mediated pathway to drive solid product precipitation. Most importantly, due to the low dipole moment, ethers do not react with PSe or selenium radicals during charging and discharging processes, which makes them suitable electrolytes for the Li-Se system. The cyclic DOL solvent exhibits low viscosity and tends to cleavage and polymerization, forming a robust solid electrolyte interphase (SEI) with assistance of $LiNO_3$ decomposition.

In the ether-based electrolyte, the high dissolution PSe is good for the reaction kinetics by multi-step liquid-solid-liquid transformation. The active Se is firstly reduced to lithium polyselenide Li_2Se_n at the upper plateau (~2.04 V) and then reduced to Li_2Se_2 and Li_2Se at the lower plateau (~1.95 V). Conversely, during the charging process, Li_2Se is oxidized to selenium

via a Li_2Se_n intermediate[168]. However, the dissolution of PSe in electrolytes is a double-edged sword, which could promote the electrochemical reaction of the Li-Se battery, but at the same time, causes a loss of Se due to shuttle effect, which eventually deteriorates the cycle stability of the battery. There are two methods to solve this problem, one is to adjust the solvent to reduce the solubility of polyselenide or to form an SEI layer, another one is to increase the concentration of the electrolyte and reduce the amount of free solvent.

Chen *et al.* added 50% (in volume) of diisopropyl ether (DIPE) into DOL/DME electrolyte solvent obtained a mixed diisopropyl ether (DIPE)-based electrolyte[173]. DIPE possesses suitable solubility of Li salts to afford necessary ionic conductivity, while LiPSs are difficult to be dissolved in DIPE, thus shuttle effect was suppressed and Li metal anode was effectively protected. SEI layer on the surface of the cathode could prevent the transport of the polyselenide while keeping the Li ion permeable, which significantly enhances the cycle stability of the battery. Lee *et al.* added an additive battery grade FEC to the ether-based electrolyte to form an SEI layer on the cathode during the first cycle, as shown in **Fig. 17b**[171]. The additives greatly reduced the reactivity of PSe with FEC. Thus, they have successfully demonstrated a significant improvement in the stability and rate performance of the Se cathode with the protective SEI layer. Xu *et al.* changed the electrolyte solvent from DME to HFE and kept the other components in 1 M LiTFSI/DOL+DME (1/1, v/v)) unchanged[140]. The SEI layer was formed on the surface of the cathode due to the high nucleophilicity of HFE reaction with electrolyte, which increased the stability of the battery. Unlike the traditional encapsulation strategies that inhibit the shuttle effect, the SEI layer method directly circumscribes the formation of PSe. As a result of the presence of the SEI layer, the reaction pathway was converted from solid-liquid-solid to solid-solid phase.

A considerable amount of free solvent molecules in dilute electrolytes (1 M) readily solvate LiPSs (**Fig. 17c**), allowing super high LiPSs solubility, which leads to the battery decay. Increasing Li salt concentration renders the less number of free solvent molecules and boosts electrolyte viscosity, which thus results in a decreased solubility of LiPSs. At extremely high LiTFSI concentration, all solvents coordinate to Li^+ and form unique contact ion pairs or aggregates, exhibiting an extremely low solubility for LiPSs. **Fig. 17d** reflects the trend of the solubility with the increase of the concentration of the lithium salt of the electrolyte. This bifunctional "solvent-in-salt" electrolyte benefits the high Columbic efficiency and long-term cyclability. This high concentration electrolyte method may be extended to lithium selenium batteries.

Modifying the solvent or adding addictive material of the electrolyte to adjust the solubility of the PSe or form a thin uniform SEI layer is a good method to solve the problem of shuttle effect. Moreover, the high concentration lithium salt electrolyte may work well due to leak of solvent to dissolve PSe. It should be noted that excess electrolytes are ubiquitously employed in cells to ensure sufficient redox kinetics and preclude the interference of the electrolyte depletion due to side reactions with the lithium metal anode. However, this is not the case in a real cell scenario, where electrolyte-to-selenium ratio (E/S) < 4.5 is highly advocated to achieve the high-energy–density goal. Thus, developing lean electrolytes in particular battery still a great challenge.

3.2 All solid electrolyte

Ionic conductance in solids originates from the movement of point defects, such as vacancies or interstitial ions in the crystal[174]. Transition metal oxides, sulfides and halides can form non-stoichiometric chemicals with higher intrinsic defect concentrations due to the higher valence states of transition metals, which makes it possible to work as ionic solid electrolyte in the battery. Compared with flammable liquid electrolytes, all solid-state lithium batteries (ASSBs) using solid electrolyte not only solve the safety problem of electrolyte leakage but also effectively block the shuttle effect of polysulfides and inhibit the growth of lithium dendrites[175]. Moreover, the potential compatibility of solid electrolytes with Li metal anodes permits the battery to achieve high specific energy densities, making it possible to utilize it in mobile electronics, electric vehicles and large-scale energy storage systems[176]. Some types of ISEs, such as oxides, sulfides and halides, have received much attention and have been considered as promising candidate materials in ASSBs.

The oxides solid electrolytes have good electrochemical and chemical stabilities even at high temperature, but their large interfacial resistance restricts the battery assembly. Jin *et al.* synthesized a kind of solid garnet-type $Li_{6.4}La_3Zr_{1.4}Ta_{0.6}O_{12}$ (LLZTO) tube electrolyte[177]. The LLATO battery operated at high temperature of 240-300 °C. In this case, Li and Se in the anode and cathode materials were liquid, which facilitated rapid ion transport and low electrode-electrolyte interfacial impedance, as liquid-solid interfaces were formed rather than solid-solid interfaces. At the same time, the produced polyselenide shuttle effects were prevented by the compact ceramic LLZTO tube. Thus, the ASSBs battery system with LLZTO solid electrolyte achieved high energy density and superior electrochemical performance at 240–300 °C.

Sulfides become a member of the solid electrolyte due to their higher ionic conductivity and better deformability. Li *et al.* fabricated a novel all-solid Li-Se battery by pressing the commercial Li_3PS_4 powder[163]. The Li^+ transport over the Se–Li_3PS_4 interface is as high as 1.4×10^{-5} S cm^{-1}, the Li^+ diffusion during the electrochemical cycle was greatly reduced by the interface between the solid electrolyte and the active material. However, Li_3PS_4 is not electrochemically stable when it is in direct contact with bare Li during cycling, which leads to the formation of a large interfacial resistance and overshadows the advantages of sulfide. A protective layer on the surface of lithium anode maybe could solve this problem.

Rare earth-based halide solid electrolytes are recently considered as research hotspots in the field of ASSBs. The halide solid electrolytes possess high ionic conductivity, credible deformability, and good stability, bringing excellent electrochemical performances for ASSBs. For example, Li *et al.* synthesized Li_3HoCl_6 as solid electrolyte; the battery achieved a reversible capacity of 402 mA h g^{-1} after 750 cycles[178]. Shi *et al.* used the more simpler vacuum evaporation-assisted method and fabricated Li_3HoBr_6 electrolyte[179]. The ionic conductivity of the large-scale prepared LHB achieved a high value of $1.25 \pm 0.08 \times 10^{-3}$ S cm^{-1}. The LHB based Li-In/LHB/Se ASSBs exhibited stable discharge–charge curves and more than 500 mA h g^{-1} specific capacity after 150 cycles with high Coulombic efficiency close to 100% and excellent rate performances.

All solid state electrolytes could suppress the shuttle effect and achieve high ionic conductivity. However, the transport of Li^+ is greatly limited by the high interface impedance between electrode and electrolyte, which restricts the development of all-solid Li battery. Therefore, the application and commercialization of solid electrolyte battery still face major challenges in terms of rechargeability, cycle stability and rate performance.

3.3 Solid-liquid hybrid electrolyte

Batteries with liquid electrolytes have the defects of shuttle effect produced by the dissolution of PSe and a potential safety hazard posed by leakage. All solid state electrolyte batteries could overcome the problems of leakage and shuttle effect, but due to poor interface contact and large volume change between the electrolyte and electrode, modification of interface property has become the biggest challenge. Therefore, in order to combine the advantages of both liquid electrolyte batteries and solid electrolyte batteries, solid-liquid hybrid electrolytes were developed as an effective solution for building safe and stable lithium battery.

Zhou *et al.* reported a novel Li-Se battery employing a hybrid electrolyte, which utilizes both the shuttle-free property of a solid electrolyte and a rapid liquid phase Se redox reaction based on an ether electrolyte[180]. The hybrid electrolyte consisted of a solid ion-conductor ($Li_{1.5}Al_{0.5}Ge_{1.5}(PO_4)_3$ (LAGP)) sandwiched between liquid electrolyte on both sides (1.0 M LiTFSI tetraethylene glycol dimethyl ether (TEGDME) in the cathode side and 1.0 M LiTFSI with 2 wt.% $LiNO_3$ in TEGDME in the anode side). In this structure, the solid electrolyte acted as a barrier to prevent the diffusion of the PSe intermediate to the anode, while the liquid electrolyte helped in promoting the transport of Li-ion, and eventually accelerating the (de) lithiation process of the cathode.

In conclusion, by adjusting the organic solvent or introducing additives into liquid electrolyte, the low solubility of polyselenids or the formed SEI layer can effectively prevent the dissolution of the PSe and relieve the problem of low selenium utilization. Solid state electrolyte is obviously safer and more stable than the liquid electrolyte, but the new problem of slow diffusion of lithium ions occurs. Therefore, a research breakthrough in solid-liquid hybrid electrolytes may be of great significance to developing an efficient Li-Se battery.

4 Isolation layer processing

Inserting an isolation layer between the separator and the cathode can block the diffusion of PSe and greatly improve the performance of the Li-Se battery. The main function of the separator is to separate the positive and negative electrodes of the battery so as to avoid short-circuit produced by contact between the two poles, and simultaneously allow the lithium ions in the electrolyte to pass through. However, some PSe produced can pass through the separator to reach the anode, where they directly react with lithium, thereby reducing the utilization of selenium. Therefore, preventing the soluble PSe of the C/Se composite from passing through the separator becomes an effective remedial measure. To achieve this goal, researchers have tried many methods and achieved some excellent results. In summary, the modification methods can be summarized into three parts: 1) directly adding a third layer between cathode and separator, 2) coating barrier material on the surface of the separator, 3) constructing a coating on the surface of the Se/C composites.

4.1 Inserting interlayer between Se electrode and separator

Adding an interlayer between Se electrode and the separator is a direct and efficient way to introduce the isolation layer. Although there are different kinds of interlayer materials, all need to possess some common properties, such as high electrical conductivity, preventing the passage of PSe and, at the same time, promoting the transport of lithium ions.

CNTs and graphene meet all the requisites mentioned above and are good choices as the interlayer materials for Li-Se batteries. For example, Peng *et al.* placed a CNT membrane between the reduced graphene oxide encapsulated Se (Se@RGO) cathode (**Fig. 18a**) and separator to serve as the barrier layer to further defer the shuttle effect of PSe[181]. The superior electrochemical performance as shown in **Fig. 18b** suggests that the Se@RGO composite and the CNT barrier layer played a great role in preventing shuttle effect of PSe. Zhang *et al.* placed a carbonized filter paper between the selenium electrode and the separator as a separate carbon intermediate layer to improve the electrochemical performance of the Li-Se battery[182]. The high conductive porous carbon intermediate layer serves as an excellent substrate for holding and containing the dissolved intermediate PSe. The introduction of the simple, low-cost intermediate layer enhanced the specific capacity and cycle performance of the battery. Xia *et al.* prepared a Se cathode having an alternating barrier layer and active layer structure by a simple syringe filtration method, where the barrier layers functioned as the interlayers[161]. The barrier layer consisted of intertwined multi-walled carbon nanotubes (MWCNTs) and graphene, which served both as PSe intercepting barrier and highly conductive current collector. The interlayer had a strong PSe trapping ability to confine selenium in the active layer, and also rapid redox conversion ability and high PSe recyclability.

4.2 Coating interlayer on the surface of the separator

Coating the protection layer on the surface of the separator is another way to achieve the interlayer between the Se electrode and the separator by simple filtration or drop-casting method. CNT and graphene have good conductivity and porous structure are good choices for interlayer. For example, *Li et al.* introduced CNTs interlayer on the cathode side of a Celgard 2400 separator to form a CNTs interlayer-coated separator by filtering[72]. The thin CNTs layer functions as a barrier layer to restrict the diffusion of PSe through the separator, thereby enhancing the cycling performance. Besides, Fang *et al.* coated graphene on the surface of a polymer separator, which acts as an interlayer between the cathode and the separator[183], as shown in **Fig. 18c**. It has been proved that the added interlayer could effectively adsorb PSe produced between cathode and

separator, thereby greatly improving the performance of the Li-Se battery. In addition, Gu *et al.* prepared an ultra-light, conductive, and free-standing nitrogen and sulfur co-doped graphene N, S-G film that acted as a current collector and simultaneously as a barrier to increasing the loading of active material[184]. The conductive N, S-G film (electric conductivity 148 S m^{-1}) (**Fig. 18d**) was found to improve the electrical conductivity of electrons and lithium ions, and achieved high selenium utilization even with high selenium content in the battery. On the other hand, it can effectively limit the shuttle effect by physical/chemical inhibition and provide stable cycle life to the battery due to its enhanced adsorption to polyselenides.

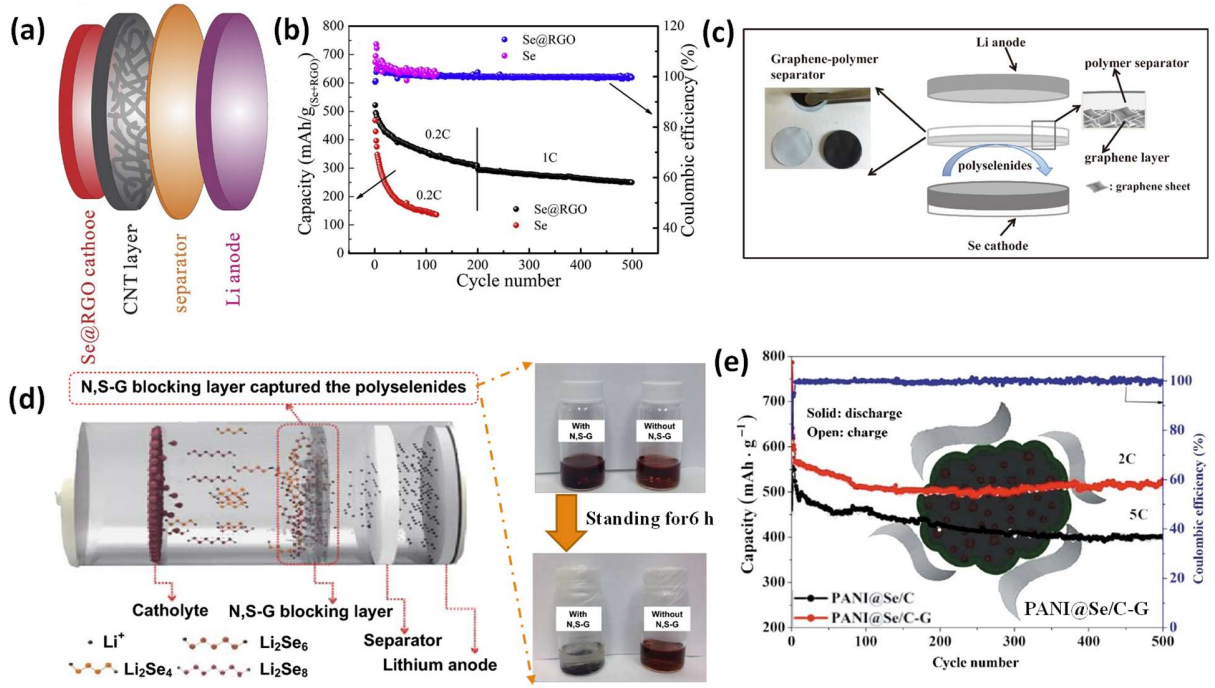

Fig.18 (a) Schematic diagram of Se NPs encapsulated with RGO. (b) Capacity retention and Coulombic efficiency for 200 cycles at 0.2 C and another 300 cycles at 1 C obtained from the Se@RGO composite cathode and 120 cycles at 0.2 C from the pure Se cathode.[181] (c) Schematic configuration of a Li-Se cell with a graphene-polymer separator. The left figure shows a photograph of a graphene-polymer separator with the black side of graphene and the white side of polymer.[183] (d) N,S-G membrane as an interlayer for trapping polyselenides and digital photographs of polyselenide adsorption by N,S-G interlayers.[185] (e) Schematic illustration of PANI@Se/C-G composite and cycle performance at a current density of 0.2 C between 1.0 and 3.0 V.[186]

In addition, some oxides have strong adsorption to PSe, which can function as interlayer materials. For example, Mukkabla *et al.* loaded tungsten oxide in the separator by drop-casting method to obtain a tungsten oxide interlayer to further avoid the problems of dissolution and shuttling effect of PSe[187]. The WO_3 interlayer applied to the separator was able to conduct Li-ions and at the same time prevent the PSe from being dissolved and shuttled. Therefore, introduction of WO_3 on the surface of separator could enhance the cycle stability of the battery and maintain high specific capacity. With the introduction of the WO_3 intermediate layer, the Li-WO_3@Separator/Se-AAC battery showed an initial charge capacity of 808 mA h g^{-1} and 510 mA h g^{-1} after 100 cycles, which clearly demonstrated the role of WO_3 in limiting the capacity decay in Li-Se-AAC cells.

Porous material working as ionic sieve could effectively suppress the shuttle effect of the battery. For example, Bai *et al.* present a metal-organic framework (MOF)-based battery separator to mitigate the shuttling problem[188]. The small pore size distribution of MOF-based separator (approximately 9 Å) plays the role of an efficient ionic sieve towards polysulfides migrating to the anode while having negligible influence on the transfer of Li^+ ions across the separator. Si *et al.* introduced a covalent organic framework prepared by the polymerization of 2,5-Dimethoxy-1,4 Dicarboxaldehyde and Tetrakis(4-aminophenyl)ethane (DMTA-COF) on the surface of separator[186]. The strong sieving effect from the nanopores of DMTA-COF can significantly inhibit the shuttle effect during the cycling process and greatly improve the cycling performance of the battery.

4.3 Coating interlayer on the surface of the Se/C composite

Besides the two methods mentioned above, coating a protection layer on the surface of the Se/C composite is another method to prevent the dissolution of the PSe. In addition, due to the high electron conductivity of the coating, the transmission of electrons could increase. Several related works have been carried out in recent years. Zhang *et al.* introduced graphene to encapsulate selenium/polyaniline core-shell nanowires and formed G@Se/PANI nanocomposite to enhance the electrochemical performance of Li-Se batteries[190], as shown in **Fig. 18e**. The G@Se/PANI nanocomposite exhibited excellent cycling performance showing a reversible discharge capacity of 567.1 mA h g^{-1} at 0.2 C in 200th cycle, and a good rate capacity of 510.9 mA h g^{-1} at 2 C due to the introduction of the protection layer. Ge *et al.* used graphene to encapsulate selenium/carboxylated carbon nanotubes. The obtained Se/CCNTs-RGO composites also exhibited

excellent electrochemical performances[191]. Wang *et al.* developed PANI@Se/C-G composite by encapsulating polyaniline (PANI)-coated Se/C nanocomposite into graphene sheets with the help of electrostatic interactions[186]. Besides, Ye *et al.* employing PANI layer coating UIO-67 (Zr-metal organic frameworks)@Se composite obtained UIO-67@Se@PANI[192]. Luo *et al.* encapsulated Se/C composites in ultra-thin $Ni(OH)_2$ nanosheets to form Se/C-$Ni(OH)_2$ cathode[193]. Due to the ultra-thin $Ni(OH)_2$ nanosheets forming a strong protective layer outside of the Se/C composites, the dissolution and shuttle effect of PSe were reduced greatly. Moreover, the ultra-thin $Ni(OH)_2$ nanosheets improved the diffusion of Li^+ in Li-Se batteries, enabling the batteries to have excellent discharge capacity, cycle stability and almost 100% Coulomb efficiency.

Interlayers play an important role in suppressing the shuttling effect in Li-Se battery. In general, Se confinement materials in cathodes can be candidates for the application of barrier layers. The interlayers prevent the PSe dissolved from the selenium cathode from reaching the Li anode through the separator. However, the suppression basically depends on the pores remaining in the interlayer material, which can slow down the rate of the migration process of PSe to the negative electrode, but cannot let the shuttle effect disappear. Thus, introducing interlayer cannot completely suppress the shuttle effect. In addition, the addition of intercalation materials indeed suppresses the shuttle effect, however the improved quality of the battery reduces its energy density. Research on the preparation of new, high-efficiency, and lightweight separators has a long way to go.

5 Li metal anode

Lithium metal with ultra-high theoretical capacity (3860 mA h g^{-1}) and low reduction potential (-3.04 V *vs.* standard hydrogen electrode, SHE) is considered one of the most attractive anode materials for electrochemical energy storage. The metallic lithium is a kind of source of Li^+ during the lithiation process. In addition, lithium, an active metal material, has a reaction with electrolyte at the low voltage to form SEI layer, which can protect the electrolyte avoiding further reaction with Li. However, due to the uneven current density on the surface of Li foil, the ordinarily formed SEI layer is not stable, which will peel off and regenerate with the expansion of the lithium anode, thereby worsening the local current unevenness. Due to the different lithium deposition rate at the different local places of current densities, the lithium dendrites appear which accelerate the fragmentation of the SEI. As shown in **Fig. 19**, lithium as the anode of Li-Se battery has some challenges to overcome: 1) Uneven current density leads to the formation of lithium dendrites,

which will pierce the separator leading to the short circuit. 2) The pieced Li dendrites lose contact with the electrode and become inactive "dead" lithium. 3) The large volume expansion of the Li metal anode during the plating/striping cycles. 4) The PSe shuttle to Li, where they have a direct reaction to form Li_2Se, resulting in loss of active Se. The uncontrolled lithium dendrites and infinite volume expansion, "dead" lithium and loss of active Se during repeated plating/peeling cycles result in poor cycle stability, lower Coulombic efficiency and posing safety hazards, greatly hindering the practical application of lithium metal anode[194]. For decades of research, the lithium dendrites can be avoided by the strategies: 1) averaging of the current density distribution on the surface of the current collector and 2) forming a stable and uniform SEI layer on the surface of lithium anode.

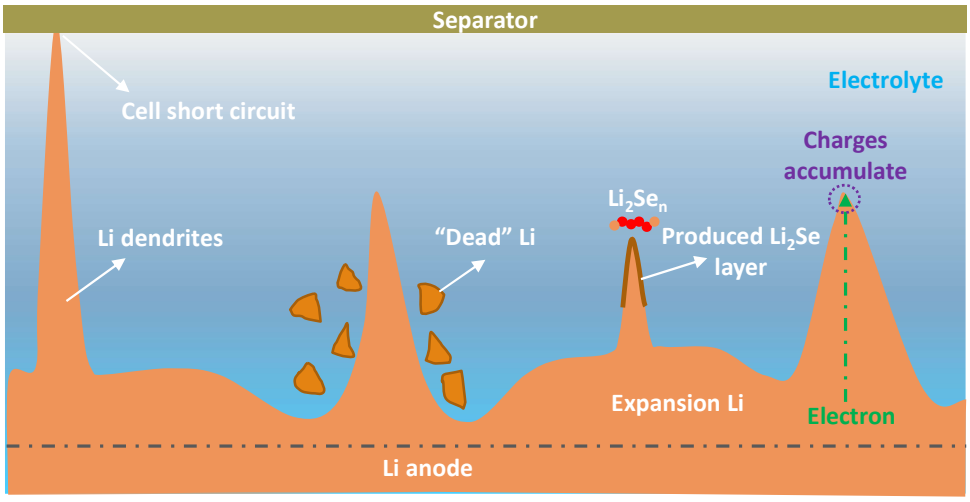

Fig. 19 The problems that possibly exist in the Li anode.

5.1 Homogeneous lithium ion flow on the surface of Li anode

The ununiform current density on the substrate is the most root reason for the Li dendrites formation. The uneven spatial distribution and excessive local current of lithium ions on the surface of the anode result in the generation of lithium dendrites. According to Chazalviel's model, the onset time of uneven deposition is inversely proportional to the square of current density ($\tau \approx J^{-2}$) [195]. Porous conductive skeleton with large surface area was structured to decrease and uniformize the current density on the anode surface as well as reduce the volume expansion. The substrates can be 3D metal (Cu, Ni, etc.) current collectors, porous carbon framework, inorganic and conductive polymers.

5.1.1 3D metal current collectors

Cu with good conductivity, soft changeable, and high stability in air is commonly used as the anode current collector. The current collectors have a major impact on the initial nucleation stage of lithium plating, which is critical for subsequent lithium plating. The initial plating of Li on a planar current collector usually tends to produce uneven deposition of Li particles. 3D copper network current collector with a large specific surface area and macroscopic pore structure can make the lithium ion flow uniform and reduce the local current density. In addition, the 3D porous copper mesh also provides a certain deposition surface for lithium ion deposition, reducing the volume expansion of lithium and smoothing the deposition of lithium.

As is shown in **Fig. 20a**, small Li dendrites (0.1–0.5 μm in diameter) are easy to form on the smooth surface of the planar copper current collector. As the charges accumulate at sharp ends of the previously formed small Li dendrites, they will work as charge centers and amplify the growth of the Li dendrites. While on the submicron skeleton of the 3D Cu foil as shown in **Fig. 20b**, numerous protuberant tips exist on the surface, which can uniformize the electric field and function as nucleation sites. Which resulted in uniformly dispersed Li growing along the Cu skeleton and eventually forming a relatively even Li[196]. Li anode in the 3D current collector can run for 600 h without a short circuit and exhibits low voltage hysteresis. Different from the surface modification grafting method[194], the interconnected porous structure of the copper matrix has the same effect in suppressing the growth of lithium dendrites[198-200].

When the electroplating Li exceeded 5 mA h cm^{-2}, lithium dendrites will grow rapidly and gradually cover the Cu frameworks electrode surface densely. That is due to the equilibrium-immiscible nature of Cu with Li, the nucleation barrier of Li on its surface is high, Li deposition on Cu is sluggish, resulting in the formation of dendritic Li. Thus, introducing some lithiophilic sites on surface of the Cu current collector is an efficient way to decrease the Li dendrites. Introduction of an artificial-protective film on the copper framework surface is commonly used. The effective protective layer shall be homogeneous and usually possesses weak electronic conductivity but excellent ionic conductivity to promote uniform and rapid Li^+ transportation and homogeneous deposition of Li on the current collector, suppressing the formation of the Li dendrite. The lithiophilic particles that meet the above characteristics can be some inorganics (oxides, sulfides, etc.), polymers or metals.

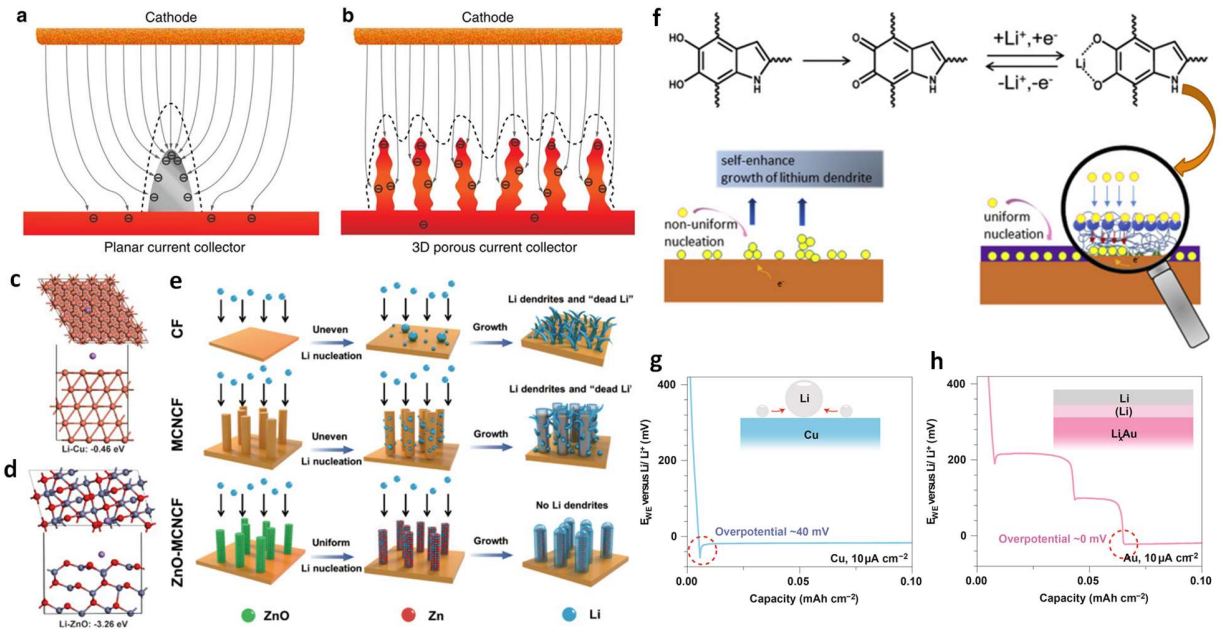

Fig. 20 Illustration of the proposed electrochemical deposition processes of Li metal on (a) planar current collector and (b) 3D current collector[196]. The most stable adsorption configurations of Li on the structure of (c) Cu and (d) ZnO. (e) Schematic representation of different Li metal deposition behavior on CF (Cu foam), MCNCF (multi-level Cu nanofibers on a Cu foam) and ZnO-MCNCF[201]. (f) Diagram of the mechanism of PDA-induced Li deposition and the possible reaction between Li and PDA during the plating process[202]. Overpotential during Li deposition on (g) Cu substrates, (h) Au coated Cu substrate.

The first-principles calculations show that ZnO exhibits a much larger Li absorption energy of -3.26 eV (**Fig. 20d**) than the Cu (111) surface of -0.46 eV (**Fig. 20c**), revealing that the electrodeposited ZnO layer is much more lithiophilic than the pure Cu framework substrate[201]. Lithium can selectively nucleate with ZnO on the electrode surface through two consecutive reactions: $Li^{+}+ZnO \rightarrow Li_2O+Zn$, $Li^{+}+Zn \rightarrow LiZn$. In this way, Li tends to form grains rather than branches. The Li on the surface was very smooth, and no dendrites were observed even with the continuous Li deposition over 5 mA h cm^{-2} (**Fig. 20e**). Because of their high chemical reactivity with Li, Cu_2O[203], Cu_2S[204] were applied as lithophilic sites also.

Polymer such as polydopamine[202], tamarind seed polysaccharide[205] and polyaniline[206] can be used as lithophilic coating on the surface of Cu substrate to suppress the formation of Li dendrites. Because of their rich of hydroxyl groups or amino-nitrogen functional groups inside, the lithium ions will firstly react with functional groups and form a uniformly distributed lithium complexing functional groups during lithium depositing (**Fig. 20f**). These groups, worked as

nucleation sites, are favorable for the uniform and stable deposition of lithium metal on the current collector, thereby effectively suppressing the formation and growth of dendrite.

It is found that the Li nuclei size and nuclei number density on Cu depend on the overpotential **(Fig. 20g)**, which can be tuned to depress dendrite growth[207]. Substrates with certain solubility in Li metal, such as Au, Ag, Zn or Mg, generate a solid solution buffer layer before Li metal formation, resulting in no overpotential for Li nucleation, as is shown in **Fig. 20h**. Al and Pt have relatively small solubility in Li metal and show small but observable overpotential for Li nucleation (5 mV for Al, 8 mV for Pt). While Cu and Ni, because of no solubility in lithium, show a clear overpotential (~30 mV) for Li metal nucleation. These Li soluble materials can be utilized as heterogeneous seeds for Li growth. Controlling heterogeneous seeds uniformity and coverage is a prerequisite. Hou *et al.*[208] and Zhang *et al.*[209] design a uniform nanostructured Ag and Zn lithiophilic layer *via* an electroless plating process, respectively. Liu *et al*.[210] used the method of magnetically sputtered formed uniform lithiophilic Zn coated within inner pores and reduced Li nucleation overpotential. Both of them obtained a stable dendrite-free lithium metal anode.

The 3D porous Ni current collector and Ni foam are used as current collectors due to their lightweight and large specific surface by Wen *et al.*[211] and Yu *et al.*[212], respectively. Which provided a highly conductive network for Li, effectively reduced Li plating/stripping current densities, suppressed the formation of "dead" Li, and increased Li^+ transport to the electrode surface. Especially, Wen *et al. in-situ* coated a polymerizing polypyrrole (PPy) layer on Ni foam to decrease the contact between Li metal and electrolyte, and even Li deposition underneath the layer, leading to a dendrite-free Li anode.

The porous Cu frameworks indeed reduce and lever the current density on the surface of substrate, and the decorated lithiophilic sites further accelerate uniform deposition of lithium and suppress the growth of Li dendrites. Especially, combined with the protection coating layer, the Li dendrites could decrease greatly or even disappear. However, the complex process for the porous Cu synthesis and additional coating process greatly increases the cost and is time consuming. Besides, the extra Cu or Ni foil as the current collector will greatly increase the weight of the electrode and is against the realization of high specific energy of the battery. Some other lighter 3D current collector and *in-situ* polar sites introduction are likely directions for future efforts.

5.1.2 3D porous carbon as Li host materials

Carbon materials with the properties of light, high conductivity, stability, abundant reserves and diverse porous structure become a good choice for the anode current collector. Moreover, similar to the porous copper framework, the 3D porous carbon with increased surface area greatly reduces the effective current density, so that the electric field on the anode surface is evenly distributed to further inhibit dendrites. Dispersed lithium deposition can reduce volume changes, and electrodes with a stable volume can avoid stress fluctuations in the battery and improve its safety. The porous carbon can be used in the same way as the porous copper without pre-stored Li; in this case, lithium is introduced by the deposition process. Also, the carbon porous can be used with the pre-stored Li method (i.e. plating). In detail, the carbon host and Li are fully mixed at high temperature and cooled to solid at room temperature.

Carbon fiber with large specific surface area is a promising material for Li deposition. As shown in **Fig. 21a**, the utilized light-weight, flexible, and free-standing 3D hollow carbon fiber (3D-HCF) as a current collector[213], significantly reduced local current density and improved Li deposition behavior. Lithium was confined within the interspace among the fibers and inside the hollow tubular fibers without uncontrollable Li dendrites. Liu *et al.* structured interconnected lithiophilic carbon nanotube (CNT) on the porous carbon cloth, as is shown in **Fig. 21b**[214]. The 3D interconnected CNTs successfully changed the lithiophobic carbon cloth into lithiophilic nature and Li successfully infiltrated into the host material, reducing the polarization of the electrode, ensuring homogenous Li nucleation and continuous smooth Li plating. Moreover, it reported that the surface graphitized carbon nanofibers exhibited good wettability with molten Li[217]. Zuo *et al.* synthesized graphitized carbon fibers as anode host, which could realize the reversible Li^+ insertion/extraction and metallic Li plating/stripping reactions at the same time[218].

The main challenge of developing a hosted Li anode with a carbon host is mainly from the poor Li wettability due to the mismatch of polarity between the carbon host and Li metal. Besides the above complicated process to increase the Li wettability with the host, indispensable additional lithiophilic sites are usually required. As with the porous Cu framework substrate, the introduction of lithiophilic sites can be realized by heteroatom doping or additional polar material. For example, Liu *et al.* synthesized oxygen-rich carbon nanotube (O-CNT) network on Ni foam[215]. The DFT calculation results in **Fig. 21c, d** indicate that introducing C=O group on CNT, the adsorption energies for Li atom (−2.79 eV) was more negative than the pure CNT (−0.76 eV) and Ni substrate

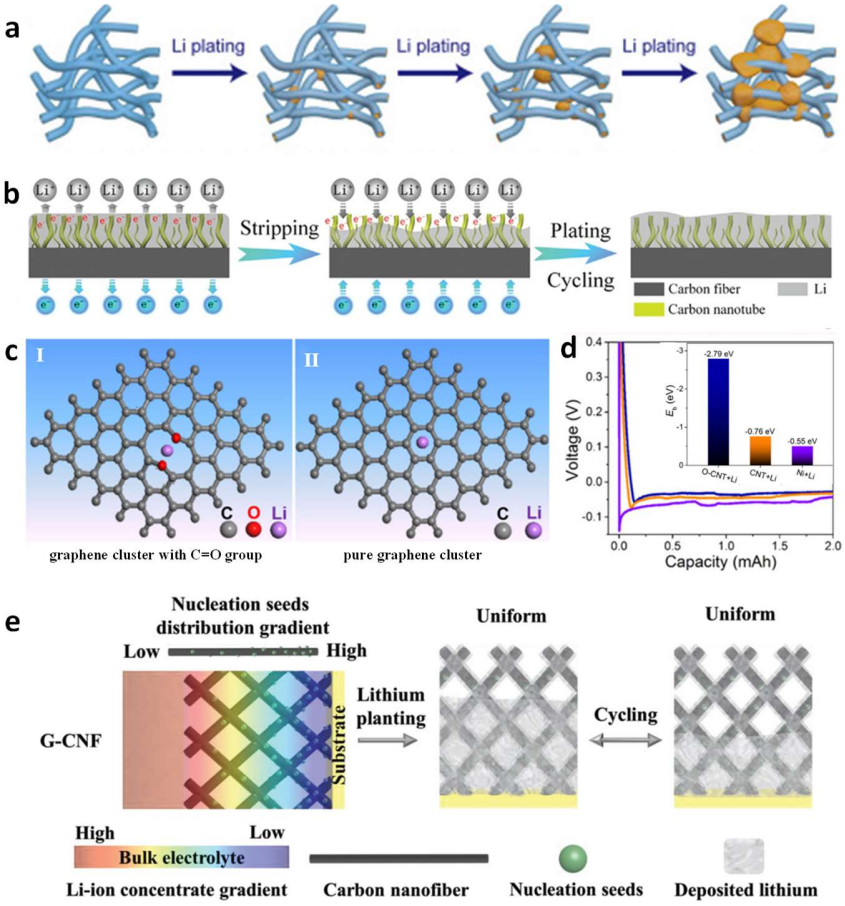

Fig. 21 Schematic diagrams of Li deposition behavior of (a) 3D-HCFs, Blue, 3D-HCFs; orange, Li[213]. (b) schematic illustration of morphology evaluations of 3D interconnected lithiophilic carbon nanotube (CNT) on a porous carbon cloth (CC)[214]. (c) The optimized models of the Li atom adsorption on (I) graphene cluster with C=O group and (II) pure graphene cluster (d) The voltage–time curves during Li nucleation at 0.5 mA cm^{-2} on O-CNT, R-CNT, and Ni foam[215]. The inset image is the calculated adsorption energies of O-CNT + Li, CNT + Li and Ni + Li. (e) The schematic diagram of the working principle of G-CNF in regulating lithium deposition[216].

(−0.55 eV). The C=O groups on the CNT surface act as efficient lithiophilic sites, achieving much lower overpotential (-31.3 mV) high than pure CNT (-41.3 mV), which was favorable for guiding the nucleation and growth of Li-metal. The advantages of oxygen-containing groups of carbon substrate were also proved by Wang *et al.*[219]. Manipulating the ratio of oxygen containing groups on reduced graphene oxide papers can be used to control the Li plating/striping behavior. When the C=O group content reached 8.4%, a stable dendrite-free Li metal anode was achieved on the reduced graphene oxide paper[220]. For the nitrogen-enriched carbon sponge[221], the high N-doping

level up to 9.87 at% enables dense and uniform distribution of lithiophilic N-containing functional groups, availing spatially homogeneous Li nucleation and achieving a uniform dendrite-free morphology. Other muti-heteroatom doped porous carbon with a high specific surface area were fabricated from polyacrylonitrile (PAN)[222] or MOF precursors [223-227].

Metal nanoparticles such as Ag[228, 229], Au[230], Sn[231, 232], Co[233], Zn[234] and Cu[235, 236] can be worked as heterogeneous seeded for Li deposition owing to its zero or low overpotential of Li nucleation. Moreover, for the pre-filling of Li host, molten Li easily infuses into the carbon fiber framework due to the addition of those lithiophilic nature sites[237]. Another kind of lithiophilic nano seeds like ZnO[216, 238-240], Al_2O_3[241], CuO[242], MgO[243] and SnS_2[244] are employed to optimize Li metal anode mainly *via* forming conductive alloys, therefore attracting and controlling Li deposition. Framework porphyrin (POF) has covalently linked porphyrin units, which proved to be highly lithiophilic and the molten Li successfully infiltrated into the composite of CNT and POF to fabricate the hybrid Li metal anode[245].

Coating lithophilic sites on the surface of carbon host substrates is a good way to control Li uniform deposition. But due to the uneven electrochemical polarization within the matrix and shorter Li-ion diffusion pathway on the surface layer, the Li ions always prefer to deposit on the surface of the host and suppress the Li dispersion in voids, thus leading a low energy density. Liao *et al.* coated the Au on the opposite side (the side distant from the separator) of multichannel carbon fibers (MCNF)[230]. The multichannel structure provides abundant space for Li depositing and Li quick transfer. Au modified on the back side of the matrix enables Li to fill the deep voids between the fibers *via* heterogeneous nucleation. Moreover, Nan *et al.* constructed gradient-distributed nucleation seeds on the conductive host, as shown in **Fig. 21e**[216]. The ZnO particles distribution gradient is opposite to the lithium-ion concentration gradient, which could reverse the lithium nucleation tendency in the 3D hosts and lead to stable deposition of lithium.

Combining the porous carbon host, lithophilic site modification and gradient-distributed nucleation seeds, the composites have achieved great success in suppressing Li dendrites. However, how to construct this kind of host material in a simple and accessible method is still a big challenge to overcome.

5.1.3 Inorganic lithiophilic frameworks as Li host

Li metal was found to prefer to deposit on the top of the 3D current collector due to the faster electron transport than Li^+ diffusion[246], which gradually leads to a loose structure occurring in the underlayer of deposited lithium. With repeated cycling, the surface of the conductive matrix can be covered by a layer of newly deposited lithium, losing its function of stabilizing lithium metal anode. The porous carbon with lithiophilic seeds reduces nucleation/deposition polarization and guides uniform lithium deposition. However, the preferential selectivity of lithium nucleation and growth will reduce the use of effective voids to accommodate lithium metal, and improve cycle stability at the expense of reduced specific capacity. Thus, the research focus of Li metal host materials moves from using conductive matrix to dielectric matrix, forming dense and uniform Li electrodeposits with acceptable sacrifice on local surface area for charge transfer. Lithophilic skeletons are selected through first-principles calculations. It is determined by calculating the strength of the binding energy of these materials with lithium.

CeO_2 has been extensively studied as alternative anode material by Sun *et al.*[247] As shown in **Fig. 22a**, Li metal was uniformly deposited into the voids of the 3D CeO_2 ceramic framework due to the lithiophilic nature of CeO_2. Furthermore, due to the high rigidity of the porous ceramic host, the host structure has imperceptible volumetric and morphological changes during intense lithiation/delithiation cycles. Metallic lithium diffuses into the 3D Al_2O_3 skeleton with the help of the surface fabrication process formed thin layer of lithium aluminum oxide (Li-Al-O)[249]. The Li-Al-O interphase provides ultrahigh affinity to Li^+, which can effectively redistribute lithium ions and regulate their deposition behavior, thus suppressing the initiation of dendrite growth. The nonconductive 3D Al_2O_3-based skeleton serves as a Li host to guide Li^+ to deposit regularly from the bottom to the top rather than directly depositing on the surface of the host. At higher current densities, the electrode architecture plays a big role in the morphological evolution of Li deposition. It found that an excessive buildup of Li plating occurs on a sharp curvature area, introducing “hot spots” for Li dendrite formation, as shown in **Fig. 22bI and II**. Therefore, there is a strong need to develop a 3D scaffold that features uniform surface curvature along with a vertically aligned structure. Tantratian *et al.* fabricated well-spaced TiO_2 nanotubes arrays anode host material with ultrauniform surface curvature[248]. As is shown in **Fig. 22bIV**, the ultrauniform nanotubular surface generates uniform local electric fields that evenly attract Li-ions to the surface, thereby inducing even current density distribution. The well-defined nanotube spacing offers Li diffusion pathways to the electroactive areas as well as the confined spaces to host deposited Li.

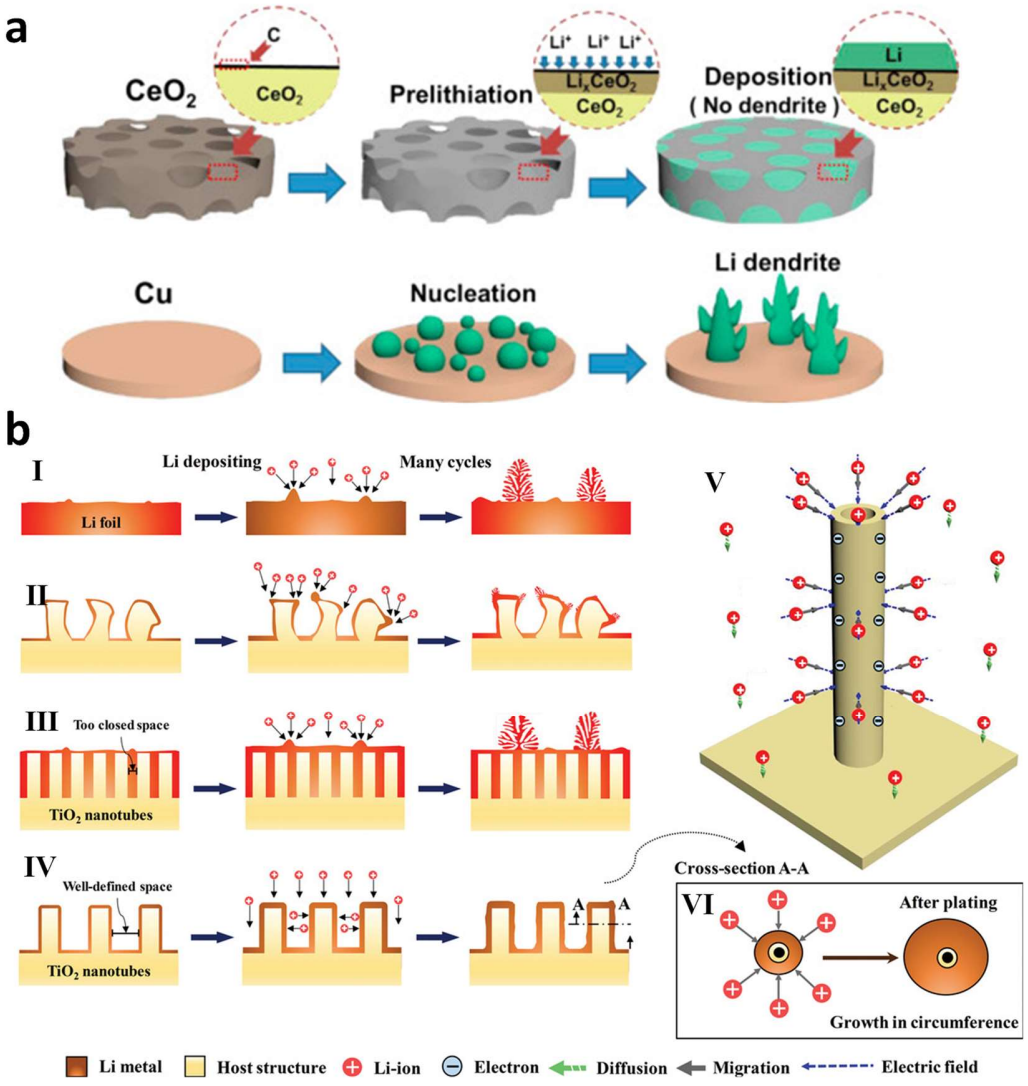

Fig. 22 (a) Schematic illustration of the plating-stripping process of in CeO_2 host and commercial Cu foil[247], (b) Schematic of Li deposition on four different anode structures: I) Li foil, II) vertically aligned structure with nonuniform surface curvature, III) closed Li nanotubes, and IV) spaced Li nanotubes. V) 3D schematic illustration of Li-ion transport under the influence of diffusion and the uniform electrostatic forces that guide Li-ions to distribute over the nanotube surface uniformly. VI) 2D cross-section of a Li nanotube illustrating the unique electrodeposition manner, i.e., the circumferential growth of the spaced Li nanotubes[248].

5.1.4 Dielectric/insulative organic framework as Li host

The dielectric/insulative polymers can be functionalized with well-designed chemical groups to regulate ion distribution near the anode surface. A the same time, the light and porous structure

could mitigate the volume change during Li stripping and plating process. Polyacrylonitrile (PAN)-based insulative microfiber (IMF) matrix was used as substrate material for the Li metal anode[247]. The insulative properties ensure the prevention of undesired side reactions with the electrolyte and the prevention of undesired Li metal formation on the top part of the 3D matrix, which is expected to decrease the possibility of Li metal dendrite growth. Fan *et al.* synthesized 3D porous poly-melamine-formaldehyde (PMF)/Li composite anode[251]. PMF with a large number of polar groups (amine and triazine) can effectively homogenize Li-ion concentration when these ions approach the anode surface and thus achieve uniform Li deposition. As for the dielectric 3D frameworks, the surfaces are usually decorated with polar functional groups, which can homogenize Li^+ ions flux in the pores so as to inhibit the formation of Li dendrite during charging. However, because dielectric material cannot support electron transport, the electrochemical process hardly take place in most of the areas, therefore the Se in the pores of framework cannot be fully utilized. In order to exploit the lightness and flexibility advantages of polymers, and at the same time, to fully utilize the pore rooms inside the framework, conductive-dielectric frameworks were designed. For example, Shi *et al.* and Wang *et al.* fabricated Ti_3C_2TX MXene-melamine foam (MXene-MF)[252] and melamine sponge@silver nanowires (MS@AgNWs)[253], respectively. Li *et al.* designed a kind of conductive-dielectric gradient framework (i.e., melamine sponge) structure by introducing a thickness-dependent gradient structure of conductive Nickel (Ni) nanolayer on a porous dielectric scaffold[254]. The conductive-dielectric gradient framework can guide a “bottom-up” Li deposition and “top-down” Li dissolution within this structure, rendering controllable and stable Li metal deposition/dissolution process.

In copper and carbon current collectors, especially with the lithophilic sites or coating on their surface, the lithium dendrites during the plating/striping are suppressed in some degree. However, at the high current density working of battery, the transfer of Li^+ cannot follow the fast electrons transfer, thus the lithium will be deposition on the surface of the anode, and the structured 3D current collectors will lose their function. On one hand, dielectric/insulative inorganic or organic framework could solve the problem of up-surface lithium deposition by decreasing the rapid electrons transfer. On the other hand, this method occurs a reduction in the activation kinetics. The conductive-dielectric gradient framework can combine the advantages of high conductivity and bottom-up lithium deposition. However, the design is not easy to realize and its application is

limited. Thus, the low price, easy obtained and light current collectors need further exploration to avoid the production of lithium dendrites.

5.2 The SEI film formation to protect Li anode

Li metal can spontaneously react with almost any available liquid electrolyte to form a SEI on its surface due to the highly negative electrochemical potential of Li^+/Li. Many research indicated that the main contents of the SEI layer are composed of Li_2O, Li_2CO_3 and $ROCO_2Li$. Depending on the species of electrolyte or Li salts, LiF, Li_3N, and Li_3P could also be present. Theoretically, the electrically insulating but ionically conductive SEI layer is capable of avoiding the excessive depletion of Li and electrolyte. However, the naturally formed fragile and unstable SEI layer with these components is easily ruptured by stresses originated from the huge volume change during Li plating/stripping processes, facilitating Li dendrite formation through the cracks. Therefore, the uniformity and stability of SEI layer have critical effects on the Li nucleation behavior and thus plays a vital role in suppressing the formation of Li dendrite. A homogeneous SEI layer not only guarantees the uniformity of ion conduction on the deposition area, but also avoids the formation of spinous protrusion.

Multiple technological approaches have been developed to form SEI protective films with various thickness, different chemical compositions and structural features on the Li metal, which in generally classified into two categories[205]. The first one is direct *in-situ* deposition of a protective SEI layer on a pre-existing surface of Li metal by electrolyte modification. The other category, instead, assumes a reverse sequence, in which a protective *ex-situ* SEI layer is firstly deposited on the surface of the current collector or Li metal.

5.2.1 In-situ formation of SEI

The electrolyte configuration is an available and economical route to construct stable and uniform Li/electrolyte interface, which can *in-situ* form a protective layer to strengthen the stability and uniformity of originated SEI layer. Additives decompose, polymerize or adsorb on the surface of the lithium anode, participate in the formation of the SEI film as a reactant to change the composition and structure of the SEI film. Additives can modify the physical and chemical properties of the SEI, and can also be used as a surfactant to change the reactivity of the lithium negative electrode surface, adjusting the uniform current distribution during lithium deposition.

The additive material can be from different kinds of SEI layers, such as lithium-halide, nitride, polymer-based, oxide, alloy, etc.

5.2.1.1 Inorganic *in-situ* SEI

$LiNO_3$ additive formed SEI

The *in-situ* electrochemical decomposition reaction between the additive and electrolyte to form a stable SEI is an efficient method to avoid the lithium dendrites. $LiNO_3$ is a commonly used additive for SEI film formation (LiN_xO_y, ROLi and $ROCO_2Li$) on lithium surface in ether based electrolyte in order to prevent the formation of lithium dendrites. Zhao *et al.* constructed a ternary-salt (LiTFSI–$LiNO_3$–Li_2S_5) electrolyte to build a stable and dense protective SEI layer by the Li_2SO_3 formation through the reactions between $LiNO_3$ and Li_2S_5[255]. However, $LiNO_3$ does not work well in carbonic ester electrolytes due to its extremely low solubility inside. CuF_2 as a dissolving promoter was added into the carbonate electrolyte by Yan et al. to increase the solubility of $LiNO_3$ by forming Cu_2^+-NO_3^- complex[256]. Liu *et al.* demonstrated nanocapsules made from metal-organic frameworks for sustained release of $LiNO_3$ as surface passivation additive in commercial carbonate-based electrolyte[257]. More than ten times of the solubility limit of $LiNO_3$ can be introduced into electrolyte. As shown in **Fig. 23a**, $LiNO_3$ was continuously consumed to remedy the SEI layer and replenished by the nanocapsules during battery operation. Moreover, Guo *et al.* combing vinylene carbonate and $LiNO_3$ as a hybrid electrolyte additive introduced into electrolyte to form a stable rich-Li_3N SEI layer in carbonic ester electrolytes[258]. Fu *et al.* constructed a Li/$LiNO_3$ (LLNO) composite foil by a facile mechanical kneading approach, as shown in **Fig. 23b**[259]. The uniform dispersion of $LiNO_3$ and its derivatives in the bulk of the LLNO composite avoids the exhaustion of $LiNO_3$ in the electrolyte during cycling and helps to make a stable Li^+ conductive species (e.g., Li_3N and LiN_xO_y) SEI and enable long cycle life of batteries.

Construction of the effective component of SEI

Adjusting the additives of the electrolytes to form the SEI rich in effective components (e.g., LiF) is more targeted strategy. Compared with Li_2CO_3, the main ingredient in native SEI film, Li halides are beneficial to make for a dendrite-free surface due to their high mechanical strength, lower surface diffusion barriers and accumulative space charge effect. Lithium fluoride (LiF) is regarded as one of the most important components in these *in situ* SEI as it promises great potential to manage Li deposition behaviors. Shen *et al.* added copper fluoride (CuF_2) into the electrolyte, a

solid electrolyte layer (SEI) was obtained by a facile chemical reaction between CuF_2 and Li metal (CuF_2+2Li→2LiF+Cu)[260]. Lithium oxalyldifluoroborate (LiODFB) additive was applied by Wu *et al.* to promote the formation of a LiF-rich passivation layer on the lithium metal surface, which not only blocks the polysulfide shuttle, but also stabilizes the lithium surface[261]. Liu *et al.* constructed a homogeneous, dense SEI layer using a new dual-salt electrolyte containing 0.5 M lithium difluorobis(oxalato) phosphate (LiDFBOP) and 0.5 M lithium bis(fluorosulfonyl) imide

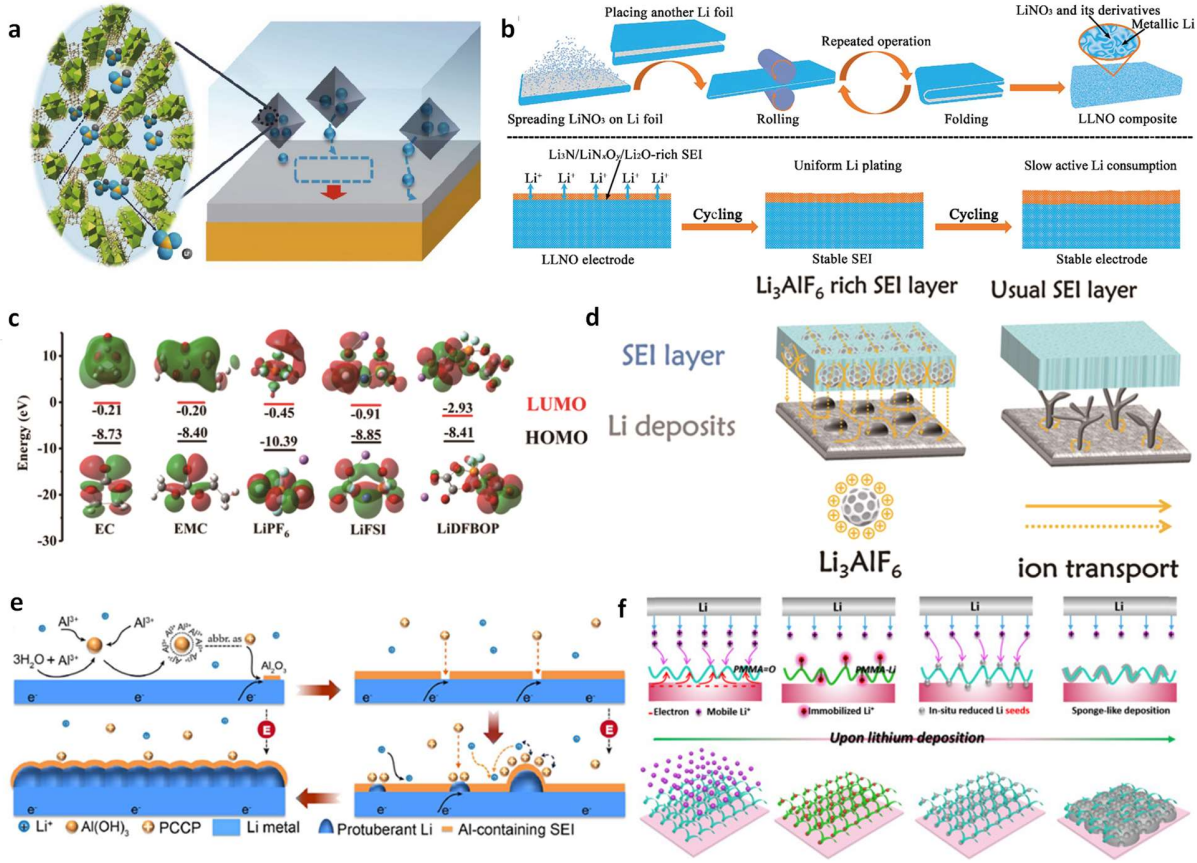

Fig. 23 (a) Schematic illustration of $LiNO_3$ encapsulated into MOF-808 and its sustained release in electrolyte[257]. (b) The fabrication of LLNO composite and added $LiNO_3$ function during electrochemical cycling[259]. (c) Highest occupied molecular orbital (HOMO) and lowest unoccupied molecular orbital (LUMO) energies of the lithium salts ($LiPF_6$, LiFSI, and LiDFBOP) and solvents (EC, EMC)[262]. (d) Scheme of Li electroplating and morphology evolution depending on Li_3AlF_6-rich SEI and usual SEI layers. The high bulk Li-ion conductivity and positively charged surface of Li_3AlF_6 solid electrolyte additive are crucial to suppress Li dendrite growth at anode side[263]. (e). Schematic diagrams showing the Li plating process in the electrolyte with $AlCl_3$ additive[264] (f) Proposed mechanism for sponge-like lithium deposition[266].

(LiFSI) in organic solvents[262]. Due to the lowest unoccupied molecular orbital (LUMO) energy (**Fig. 23c**), the preferential reduction of LiDFBOP occurred prior to LiFSI and carbonate solvents and its reduction products ($Li_2C_2O_4$ and P−O species) bind to LiF prevented the formation of Li dendrites. In order to further increase the Li^+ diffusion, Li_3AlF_6 (**Fig. 23d**) was synthesized and worked as additive in electrolyte[263]. It possesses a much higher ion conductivity ($\sim 10^{-5}$ S cm^{-1}) than LiF and textured nanoporous morphology, which would accelerate the Li-ion transport and homogenize the current distribution across SEI layer.

Further studies have also shown that nanoscale Al_2O_3 layer can effectively stabilize the Li/electrolyte interface and protect Li metal against corrosion in electrolytes. Ye *et al.* added controllable $AlCl_3$ as an additive to the electrolyte to form a dendrite-free Li deposition[264]. The additive reacted with traces of water in the electrolyte to form a stable Al_2O_3-rich solid electrolyte mesophase (SEI) layer on the surface of the Li and Al-based positively charged colloidal particles (PCCP) in the electrolyte (**Fig. 23e**). PCCPs could form a positively charged electrostatic shield around the protruding lithium during the deposition process and induce the subsequent Li deposition to the adjacent regions of the protruded Li, enabling a uniform and dendrite-free Li morphology. Cheng *et al.* added nanodiamonds to the electrolyte and Li ions co-deposit with nanodiamond particles onto the substrate, producing uniform and dendrite-free Li deposits, therefore, resulting in stable electrochemical cycling[265].

5.2.1.2 *In-situ Polymer SEI*

With the deep research, the SEI protection layer has been extended. For example, Guo *et al.* intruded Polymethyl methacrylate (PMMA) into electrolyte to assist Li deposition[266]. As is shown in **Fig. 23f**, lithium ions react with PMMA and become immobilized during discharge process. These pre-trapped lithium ions are then *in-situ* reduced into initial lithium seeds to guide sequential lithium deposition at the vicinity, ending up with a morphology modeled following the 3D PMMA molecular chains. Such morphology provides 3D continuous pathways for fast electron transport to eliminate dead Li formation without the help of foreign host. 3,5-bis(trifluoromethyl)thiophenol (BTB) worked as eletrolyte additive by Wei *et al.*, its active sulfhydryl group reacts with Li metal generated Ph–S− component as organic ingredients in SEI[267]. The Ph–S− component can repel LiPSs by electrostatic repulsion. Therefore, the organosulfur-containing SEI is able to mitigate the

side reactions between Li metal and LiPSs. The surface of Li anode maintains smooth and uniform, decreasing the depletion of fresh Li and electrolyte.

5.2.1.3 *In-situ alloy SEI*

Another type of degradable additive containing alloyable cation can be converted into dense Li-M (M = In, Sn, and Al) alloy protection layer or porous metal network layer with sufficient Li diffusion coefficient on Li anode. For example, Ishikawa *et al.* added magnesium iodide (MgI_2) into electrolyte of lithium hexafluorophosphate ($LiPF_6$) in propylene carbonate (PC) and dimethyl carbonate (DMC)[268]. The MgI_2 have a reaction with Li to form Li-Mg alloy, which provides a compact and morphologically uniform conductive low-resistance interface on the surface of Li anode. Then, they pretreated Li electrode with AlI_3 additive, showing that the modified interface is durable, which given a fine cycling efficiency even after transferring the "treated" Li electrode into an electrolyte without any additives[269].

5.2.1.4 Long term additive strategy

However, the self-sacrificial nature of SEI forming additives limits their capability to stabilize Li anode for long-term cycling. To solve this problem, Wang *et al.* incorporate LiI into the electrolyte. LiI does not react with the Li but only induces the organic solvent polymerization to *in-situ* form an ion-conductive SEI layer containing flexible oligomer on Li surface[270]. Also, it promotes the migration of Li ion, thus rendering uniform Li deposition and decreasing the side reaction between the Li/electrolyte interface. He *et al.* proved that $LiClO_4$ behaves like a catalyst, it optimizes the chemical composition of SEI by promoting the decomposition of the main salt of LiTFSI *via* ionic association effect, while $LiClO_4$ itself will not be consumed during cycles[271].

In-situ formation of an SEI protection layer with different species and components can be achieved by easy and efficient electrolyte modification method. However, the introduced additives are continuously consumed during the cycle and eventually lose their effectiveness. The long-term working additive is not easy to choose and the species is limited. More importantly, the additives in electrolyte may affect the stability of the battery system.

5.2.2 Constructing ex situ SEI

Adding additives to the electrolyte to form SEI layer (activation process) on the surface of lithium is a simple and effective method. However, the additives added to the electrolyte can hinder

the long-term cycle stability of the battery. Thus, dividing the activation and cycling process by introducing an artificial SEI is a promising method to get a high lifespan battery. The introduced SEI layer should have the properties of high stress, uniform surface, high Li^+ diffusion. Therefore, it is critical to create a conformal SEI layer that can regulate the lithium ion flux on the lithium metal anode surface while being mechanically robust and ionically conductive. A smooth distribution of Li ions is achieved by applying a membrane with rich polar functional groups on top of the Li anode, which inhibits the movement of Li ions toward protrusions induced by the tip effect[272]. The artificial SEI for lithium metal has been extensively explored – polymer, inorganic coatings, alloy and organic-inorganic composite[273].

5.2.2.1 Ex-situ polymer SEI layer

Polymers having good ionic conductivity, superior processability and high flexibility, they are commonly used as SEI layer. Especially, the abundant lithophilic polar groups of polymers can induce uniform lithium deposition. For example, polyvinylidene fluoride (PVDF) with large number of CH_2 and CF_2 groups along the polymer chains displayed spatial arrangement, which contributes to the high mechanical strength, good thermal stability, high chemical stability and high hydrophobic feature. The coated PVDF protection layer enabled uniform deposition of Li and increased the cycle lifespan of rechargeable batteries[274]. Li *et al.* inserted high selectivity and high permeability porous PVDF membrane as a protection layer to avoid the formation of dendrites[275]. Moreover, 3D oxidized polyacrylonitrile (PAN) nanofiber layer has been reported to immobilize Li ions onto polar functional groups (e.g., -OH, C-N, C-O, and C-N), thereby preventing Li ions from gathering around protrusions, resulting in a smooth Li deposit[272]. As shown in **Fig. 24a**, pendant poly(ethylene oxide)–ureido-pyrimidinone (PEO–UPy) polymer as a robust artificial protective layer firmly adhered on the Li surface to achieve long-term Li plating/stripping cycling at high current densities and high areal capacity[276]. The obtained LiPEO-UPy@Li layer is much more stable in air than bare Li (**Fig. 24b**). UPy groups had a spontaneous reaction with Li metal and formed the LiPEO–UPy SEI layer on its surface (**Fig. 24c**). Moreover, the PEO in the LiPEO–UPy layer can provide Li-ion diffusion pathway, as well as slow down and homogenize the fast Li^+ flux to the surface of the Li metal owing to the electrostatic interactions between the PEO polar segments and Li^+ in the electrolyte. Kang *et al.* formed a Li-alkoxide protective layer on Li metal *via* a facile reaction between the surface Li and n-terminal alcohols, which effectively decreased the interfacial resistance and Li deposition overpotential[277].

The silk fibroin (SF) provides abundant polar group sites including -CO-NH-, N-H and C=O groups, which *in situ* react with Li to form a high Li-ion conductivity and high Young's modulus Li_3N-rich SEI. Li *et al.* synthesized the silk fibroin-polyvinyl alcohol (SF-PVA) layer to uniformize the Li ion flux at the electrolyte/lithium interface and realize a significantly improved lithium-ion transference number[278]. The PVA enabled the silk fibroin to undergo a secondary structure transformation from random coil to β-sheets, which can further facilitate the Li ion transport. The cellulose fibers, provided by Kimwipe (KWs) paper with abundant polar functional groups (e.g., -OH, C-N, C=O, and C=N) to adhere to Li ions, provide excellent wettability and impede the aggregation of Li ions around protrusions[279]. The poly(3,4-ethylenedioxythiophene)-co-poly(ethylene glycol) (PEDOT-co-PEG) copolymer has strong adhesion to lithium surface and high ionic conductivity, stabilizes the interface of the lithium anode during prolonged contact with the ether-based electrolyte. The formed stable and low-resistance SEI effectively inhibited lithium dendrite growth[280]. Chen *et al. in situ* fabricate a thin (10 nm) but rigid (6.8 GPa) covalent organic frameworks (COF)-based artificial SEI layer to reconstruct the Li plating/stripping for Li dendrite inhibition[281].

5.2.2.2 Inorganic ex-situ layer

Based on first-principles calculations, it was found that most oxides, sulfides and halides can inhibit the growth of lithium dendrites. The robust LiF-enriched SEI with high interfacial energy to Li metal effectively promotes planar growth of Li metal on the Li surface and meanwhile prevents its vertical penetration into the LiF-enriched SEI from forming Li dendrites. Combing with its high chemical stability, low solubility in carbonate based electrolytes and high shear modulus, LiF becomes an ideal SEI film component. The LiF layer is usually obtained by the electrochemical reaction between Li and additional additive materials. For example, Yuan *et al.* fabricated the LiF-rich SEI by chemical reaction between Li and NH_4HF_2-dimethyl sulfoxide (DMSO) solution[282] and Cui *et al.* formed the LiF-enriched interphase through the lithiation of surface-fluorinated mesocarbon microbeads (MCMB-F) anodes by CoF_3[283]. Other additives, such as polyvinylidene fluoride (PVDF)-dimethyl formamide (DMF)[284], CuF[285], graphite fluoride (GF)[286] were applied also. Moreover, Liu *et al.* fabricated a homogeneous LiF protective layer by a facile vacuum evaporation method[287].

Polycrystalline Li_3N with an exceptionally high Li-ion conductivity (approximately 10^{-3} S cm^{-1}), low electronic conductivity ($<10^{-12}$ S cm^{-1}) combined with the unique stability of nitride anions to lithium metal[288], became a good SEI candidate. Ma *et al.*[289] and Li *et al.*[290] fabricated Li_3N protection layer on the surface of lithium anode by direct reaction between the Li and N_2 gas at room temperature. Ye *et al.* designed an artificial SEI layer (N-organic/Li_3N), consisting of Li_2CN_2 and Li_3N phases by the reaction with C_3N_4 and Li[291]. The N-organic/Li_3N layer with a high Li ionic conductivity can effectively facilitate the transport of Li ions across the electrode surface and lead to uniform Li ionic flux on Li electrodes via strong interactions between Li ions and N-organic groups, resulting in dendrite-free Li stripping/plating.

The metal oxide, most representative Al_2O_3 layer, is an efficient protection layer for lithium foil. Kozen *et al.*[292] and Zhao *et al.*[293] deposited Al_2O_3 coatings by atomic layer deposition and molecular-layer-deposition (MLD), respectively. ZnO has the lithiophilic property which induced lithium deposition. As shown in **Fig. 24d**, a various ZnO-coated CNT lithiophilic–lithiophobic gradient interfacial layer strategy was designed by Zhang *et al.*[294] The bottom lithiophilic zinc oxide/carbon nanotube sublayer facilitates the formation of a stable solid electrolyte interphase. Together with the top lithiophobic carbon nanotube sublayer, the gradient interfacial layer effectively suppresses dendrite growth and ensure ultralong-term stable lithium stripping/plating. Lai *et al.* developed an ionic gradient and lithiophilic inter-phase film, which promises to produce a durable and high-rate Li-metal anode[295]. The film, containing an ionic-conductive $Li_{0.33}La_{0.56}TiO_3$ (LLTO) nanofiber (NF) layer on the top and a thin lithiophilic Al_2O_3 NF layer on the bottom. During cycling, the top layer forms a spatially homogenous ionic field distribution over the anode, while the bottom layer reduces the driving force of Li-dendrite formation by decreasing the nucleation barrier, enabling dendrite-free plating-stripping behavior. Silicon, as the same main group of oxygen, has the same property. Li *et al.* introduced Poly (dimethylsiloxane) which directly reacted with Li to form a rich Li-O-Si protective layer, benefiting the conduction of lithium-ion[296]. Pathak *et al.* proposed an ultrathin film of graphite–SiO_2 bilayer on Li metal[297]. The graphite acts as an electrical bridge between the plated Li and the Li electrode, which lowers the impedance and buffers the volume expansion during Li plating/stripping. The ultrathin SiO_2 layer facilitates Li-ion diffusion and lithiation/delithiation, provides higher electrolyte affinity, higher chemical stability, and higher Young's modulus to suppress the Li dendrite growth.

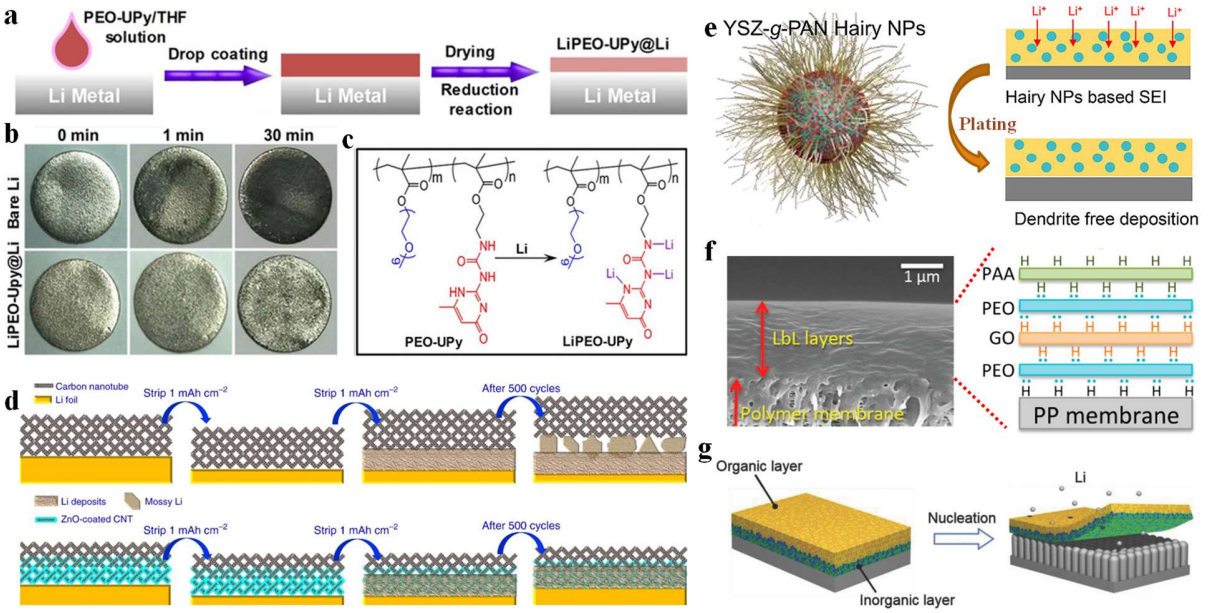

Fig. 24 (a) Schematic diagram of PEO–UPy coating on Li metal surface. (b) Photographs of bare Li and LiPEO–UPy@Li anodes exposed to ambient air for different durations. (c) Chemical structures of the PEO-UPy and LiPEO-UPy polymers[276]. (d) Li stripping/plating mechanism of Li foils coated with a CNT and ZnO-coated CNT interfacial layer[294]. (e) The structure of YSZ-g-PAN hairy nanoparticles and lithium deposition behavior of YSZ-g-PAN hairy NPs[302]. (f) SEM cross-sectional image of LbL assembly on a porous support and according schematic illustration of the protection LbL layer[303]. (g) Schematic diagram of the dual-layered film formation on Li metal anode through FEC treatments[304].

Sulfide, selenide or phosphide is also an effective SEI layer to suppress the production of lithium dendrites. SeS_2 reacts with top layer fresh Li metal to form homogeneous mixed lithium-ion conductive Li_2S/Li_2Se (LSSe) protection layer ($6Li+SeS_2 \rightarrow 2Li_2S+Li_2Se$)[298]. The Li_2S and Li_2Se with high lithium-ion migration ability, conductivity can offer high mechanical resistance and enable rapid and homogenous transfer of Li ions to the whole-electrode surface, preventing the Li dendrite growth. Li *et al.* demonstrated that the Li_3PO_4 SEI layer by *in situ* reaction of polyphosphoric acid with Li metal could suppress dendrite growth and restrain side reactions between Li metal anodes and liquid electrolytes[299]. The phosphating−nitriding method is developed through the reaction between lithium metal and a PCl_5−$LiNO_3$ complex by Li *et al.*[300]. An as-formed hybrid interface, consisting of Li_3N, Li_3PO_4, and nanocrystalline LiCl, offers high ionic conductivity and strong mechanical stability for uniform lithium electrodeposition. A Li_3PS_4

based protective layer was successfully constructed by Lu *et al.* on the surface of lithium metal by a spontaneous and rapid reaction between Li metal and THF solution of P_2S_5/S[301].

5.2.2.3 Alloy SEI protective layer

Li-based surface composite alloy films ($Li_{13}In_3$, LiZn, Li_3Bi, or Li_3As), generated by direct *in situ* reduction of the metal chlorides by Li at room temperature (xLi+MClx→M+xLiCl (M=In, Zn, Bi, As), provide a stable interface for lithium electrodeposition[305]. These alloys have much higher lithium diffusion coefficients than lithium metal. In addition, the resistive nature of the film provided by the insulating LiCl component in the alloy layer inhibits reduction of lithium ions on the surface, and generates a driving force for deposition of lithium under the protective alloy surface layer. The alloy protection layer also can be achieved by adding metal nanoparticles. For examples, Liu *et al.* dropped gallium (Ga) nanoparticle dispersion onto the surface of Li foil, *in-situ* formed a self-repairing alloy layer (Li_xGa) with the self-repairing ability[306]. During lithiation, the formed chemical stability (LixGa) decreases the Li ion diffusion barrier, resulting in homogeneous deposition of Li metal. During delithiation, the liquid Ga partially recovered from dealloying process, which fills the small SEI cracks due to the favourable flowability timely, avoiding the microcracks emersion. Luo *et al.* reduced the garnet/Li-metal interfacial resistance by depositing a thin germanium (Ge) (20 nm) layer on garnet[307]. The garnet/Li-metal interfacial resistance greatly decreased due to an alloying reaction between the Li metal and the Ge. Kim *et al.* formed very thin Li–Al layer on the surface of Li by curing the two laminated foils at elevated temperatures[308]. Xia *et al.* introduced a conformal thin Sn coating on lithium anode[309]. The coating layer could effectively inhibit the side reactions of Li metal with both electrolyte and polysulfide as well as accommodate the huge volume changes of Li metal anode during cycling. Tan *et al.* introduced Sn/SnO_2 and carbon paper composite framework to improve the wettability to molten Li[310]. The formed Li-Sn alloy has good Li ion transportability and excellent lithiophilicity. Moreover, a Li_xSi alloy film was fabricated by Xu *et al*., which allowed fast Li^+ diffusion to underlying Li and suppressed direct Li plating on surface. Gu *et al.* dropped the solution of $AgNO_3$ on the Li anode to *in-site* form difunctional protecting layer, which is consisted of the LiAg alloy and the modified SEI film by $LiNO_3$[311].

To generate a LiF and Li-Al alloy anode protection layer on Li metal surface, Wang *et al.* coated a Poly(vinylidene-co-hexafluoropropylene) PVDF-HFP/AlF_3 composite layer on one side

of Celgard separator[312]. AlF_3 particles can react with Li metal and the synergy of robust LiF-rich SEI layer coupled with a Li-Al alloy with fast Li^+ migration can regulate homogeneous Li deposition and enhance cycling stability of Li metal. Wang *et al.* formed hybrid compositions SEI (Ag_xLi_y, Ag_2S, LiF, and Li_2O) by simply dropping a LiTFSI and $AgNO_3$-containing solution on Li metal[313]. These hybrid compositions provide the Li anode with a lithiophilic surface, low Li depositing/stripping overpotential and protective interface film, yielding a "self-spreading" deposition behavior of Li and excellent cycling stability of Li-metal batteries.

5.2.2.3 Organic-inorganic composite protective layer

Polymer coatings could be easily formed by solution casting or *in situ* formation, exhibiting a certain extent of flexibility/flowability. However, typical polymer coatings have low ionic conductivity ($<10^{-5}$ S cm^{-1} at room temperature) and poor mechanical strength, especially when swollen by organic electrolyte. Moreover, due to the low transference number of most polymer materials, they are inefficient at regulating the flux of lithium ions at the anode/electrolyte interface. Conversely, inorganic coatings, such as SiO_2, Al_2O_3, ZnO, etc., have been proposed as an alternative, because of their high shear modulus, functionality, and lithiophilicity. Nevertheless, typical brittle inorganic layers cannot withstand the anode volume fluctuation during lithium plating/stripping. Therefore, it is compelling to fabricate an inorganic/polymer hybrid SEI that combines advantages of both types of artificial SEI (i.e. facile preparation, high flexibility, ductility, transference number, and ionic conductivity) and overcomes their respective weaknesses.

Li *et al.* fabricated an effective artificial SEI of inorganic/polymer as shown in **Fig. 24e**. The YSZ-g-PAN hybrid hairy nanoparticles were covalently grafted polyacrylonitrile (PAN) from oxygen vacancy (Vo)-rich yttria-stabilized zirconia nanoparticles (YSZ NPs) *via* surface-initiated atom transfer radical polymerization[302]. The YSZ NPs accelerate and uniformly distribute the Li^+ flux, and the grafted PAN polymer chains maintained good structural integrity. Their combined action enables SEI layer to achieve uniform Li deposition while suppressing dendrite growth. Xu *et al.* rationally hybridized poly(vinylidene-co-hexafluoropropylene) (PVDF-HFP) and LiF into a composite film and serves as an artificial protective layer on Li metal anode[314]. A multifunctional sulfur-containing hybrid Li polysulfidophosphate and poly(2-chloroethyl acrylate) cross-linking film was demonstrated to show superior protection for a Li metal anode[315]. This protective layer

on the Li metal anode can facilitate forming a stable organic/inorganic hybrid SEI layer containing multiple components to stabilize lithium metal anode.

Lee *et al.* applied ultrathin films on top of a commercially available porous polypropylene (PP) membrane using an ion-conductive polymer and graphene oxide (GO)[303]. The protected film was layer structured by poly(ethylene oxide)–GO–poly(ethylene oxide)–Poly(acrylic acid) (PEO–GO–PEO–PPA). As is shown in **Fig. 24f**, the layer-by-layer (LbL) assembly was accomplished using hydrogen bonding between PEO, an ionically conductive polymer that promotes Li transport, and GO, which served as a nanoscale selective barrier layer. PAA plays the role of an intermediary layer that also hydrogen bonds with PEO. This approach greatly suppressed Li dendritic growth and improved Li-anode lifetime while maintaining low thickness and mass. Yan *et al.* constructed a dual-layered film on Li metal anode by spontaneous reaction between Li metal and fluoroethylene carbonate (FEC) solvent[304]. As is shown in **Fig. 24g**, the ionic conductive film exhibits a compact dual-layered feature with organic components ($ROCO_2Li$ and ROLi) on the top and abundant inorganic components (Li_2CO_3 and LiF) in the bottom. The organic layer contributes good flexibility to avoid damages, and inorganic Li_2CO_3–LiF layer guides ordered nucleation sites and suppresses the formation of lithium dendrites. Zhao *et al.* synthesized natural solid electrolyte interphase-inspired dual protective layers[316]. On one hand, the dense ALD films as inner layers can be used to transport Li^+ while blocking the pathway of electrons and the reactions between electrolyte and Li metals. On the other hand, the highly flexible and porous MLD films are used as an outer shell to provide the channel for electrolyte diffusion and relieve the volume change of Li metals during cycling.

Organic/polymer compounds with the properties of facile preparation, high flexibility, ductility, transference number, and ionic conductivity is an ideal SEI to suppress the growing of lithium dendrites. However, the organic/polymer compounds are difficult to simultaneously achieve both good mechanical strength and ionic conductivity, because the mechanically strong polymer film requires high crystallinity while ion conductive polymer film need low crystallinity that allow the polymer chain swing. On this regard, a brilliant surface layer with both high strength and good ionic conductivity is highly desired to achieve dendrite-free lithium metal deposition.

In conclusion, *ex situ* coatings, composed of polymer, inorganic ceramics, and their hybrids, are able to offer controllable mechanical strength, thus overcoming the fragility issue that in situ

SEI essentially meets. Nevertheless, low ionic conductivity, insufficient mechanical robustness of polymer, and poor interfacial contact of ceramics remain formidable challenges to render efficient and dendrite-free Li metal anodes for practical applications. Therefore, it is of vital importance to develop an effective protective layer on Li metal anode, which is requested to provide rapid Li ion diffusion, high mechanical modulus, and good shape conformability simultaneously.

Optimization of SEI, achieved by electrolytes improvement or artificial interphase engineering, is a good way to balance the contradiction between Li dendrite inhibition and Li ion conductivity. However, the composition of SEI largely affects the battery performance. There also have a long way to go.

5.3 Li alloy-based materials as Li host

Alloy-based materials are promising anodes for rechargeable batteries because of their higher theoretical capacities in comparison to graphite. The alloy framework is functionalized as a lithiophilic current collector in the lithiation process, featuring enhanced structural stability and suppressed Li dendrite growth. Unfortunately, the huge volume changes during cycling cause serious structural degradation and undesired parasitic reactions with electrolytes, resulting in fragile solid-electrolyte interphase formation and serious capacity decay. In addition, the alloy electrodes have a high reduction potential, leading to low energy density. In order to maximize the utilization of Li metal anode capacity and solve the problem of Li dendrite growth, strategies were carried out by the researchers.

Constructing a Li-rich alloy framework is a direction where to put efforts. For example, Kong *et al.* used Li-rich Li-Mg alloy as anode of Li-S battery[317]. As shown in **Fig. 25a**, the volume change of pure Li anode during repeated Li stripping/plating has no limit in a plate electrode, the floating interface and the resulted internal stress will destroy Li anode. While for the Li-rich Li-Mg anode (**Fig. 25b**), due to the very broad range of Li-Mg alloy phases, the Li–Mg alloy framework can kept stable. After stripping process, the matrix of Li-poor Li–Mg alloy with high electric and ionic conductivity as a porous skeleton structure can be formed, which can guarantee the structural integrity of the anode in the bulk during Li stripping/plating process. Jia *et al.* designed a 3D dual-phase Li-Ca alloy framework (Li metal phase and alloy phase) with microsized patterns which significantly improved with a Li metal phase as the reservoir providing reversible capacity[318]. In principle, the Li metal phase is responsible for reversible capacity, and the alloy

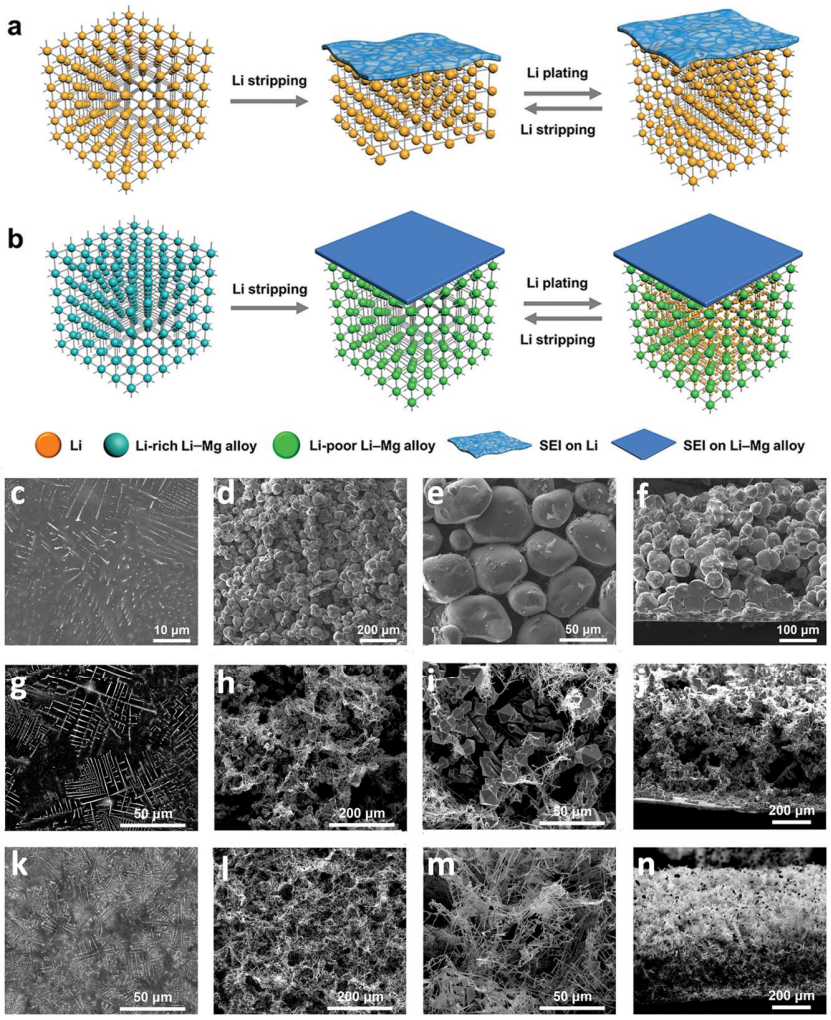

Fig. 25 Schematic structure illustration in the bulk and at the surface for a) Li and b) Li–Mg alloy anodes during Li stripping/plating process[317]. Morphologies of the $LiCu_x$ solid solution skeleton after removing metallic Li from the Li-Cu alloy: (c-f) Cu_2Li_3, (g-j) $CuLi_{10}$, (k-n) $CuLi_{60}$[319].

phase is designed as a 3D lithiophilic framework for regulating the uniform deposition of Li^+ ions, as well as a host to regulate volume variation upon cycling. Later, they fabricated Li-Cu alloy anode, where the metallic Li phase distributed in the network of $LiCu_x$ solid solution phase[319]. The $LiCu_x$ nanowires (Li-CuNW) framework after Li removal is shown in **Fig. 25c**, which reflects that the morphology of Li-Cu alloy phase can be variable by adjusting the ratio of Li and Cu. Among all the different Li-rich Li-Cu alloy, $CuLi_{60}$ achieved best performance. The obtained lithiophilic $LiCu_x$ nanowires guide conformal plating of Li and the porous framework provides superior dimensional stability for the anode. Duan *et al.* and Zhang *et al.* synthesized Li-B alloy

fibrillar network framework filling of metallic lithium as anode, respectively[320, 321]. The Li-B alloy restrains the formation of lithium dendrites and cracks in the anode.

The formation of Li-Sn alloy undergoes huge volume expansion, so Sn-based anodes usually buffer their volume changes by adding inert phases to improve their cycling stability. For example, Qiu *et al.* dispersed CMK-3/Sn powder inside Li metal by multiple folding and rolling, and reacted with Li to form Li_xC and Li_ySn alloys[322], which reduce the overpotential of Li deposition, promote uniform Li deposition and inhibit Li dendrite growth. To stabilize the lithium alloy surfaces, Zhong *et al. in situ* coated Li-Al alloy layer on the Li-B electrode surface by a pressing treatment process[323]. Because of the electronic conductivity of Li-Al alloy layer is much lower than that of Li-B alloy, the Li deposition occurs beneath the Li-Al layer, keeping the stable of the Li-Al alloy layer.

Lithium alloy anode materials have the advantages of high specific capacity and low cost, and the volume effect and lithium dendrite growth of alloy electrode materials can be alleviated through nanostructure design and preparation of materials with uniform composition. However, the problems of high first cycle irreversible capacity, suboptimal cycle performance, volume expansion etc. still exist. The optimized design of multi-component lithium alloys, the stabilization treatment of lithium alloy surfaces, and the construction of composite materials maybe able to solve the above problems.

Although the performance of Li anodes has been greatly improved by various strategies, there are still many problems before it is put into commercial production, such as the safety problem caused by the high activity of lithium, the leakage of organic electrolyte, the volume expansion problem and the inevitable lithium dendrites production under high current and long cycle charge/discharge process. Moreover, the mechanism of modification of lithium anode needs to be further explored.

Conclusion and outlook

In recent decade years, research on the high energy density Li-Se batteries has made great progress. This chapter addresses the issues of low utilization rate of selenium, shuttle effect of PSe and lithium dendrites by summarizing the optimization scheme of various aspects of Li-Se battery. The modification of Li-Se battery was carried out from selenium cathode, including physical adsorption by designed pores and chemisorption by introduced polar sites. Inserting a SEI barrier

layer between cathode and separator is beneficial to prevent the diffusion of polyselenides and generation of lithium dendrites. In addition, the modification of the electrolyte and the separator also reduces the speed of the PSe passing through the separator to some extent. At the end, methods to suppress lithium dendrites, one of the most vexing problems in lithium-selenium batteries, are discussed. Among above modifications, the high surface area Se particles and 3D carbon frameworks are designed, and an SEI protection layer is introduced. To induce the uniform lithium deposition, lithium alloy anode materials are applied. All these efforts by scientists have made a positive contribution to improve the performance of Li-Se battery. However, they still leave us with many key scientific issues to be deeply studied. For example, the reaction mechanism of the C/Se interface and electrolyte/SeC composite interface during charge and discharge progress, the mechanism of polyselesides movement in electrolyte and the interaction mechanism with negative electrode. Solid electrolytes and high-concentration liquid electrolyte adjustment strategies can solve these problems to a certain extent. However, at the same time, new problems such as high interfacial resistance problems and ion transport problems caused by the increased electrolyte viscosity will appear. Besides, there are also some technical issues that deserve a further research. For instance, how to obtain a selenium electrode with a high thickness that is not easily disintegrated by volume expansion, how to solve the contradiction between high content of selenium and its low utilization rate and how to solve the contradiction between battery safety and transmission rate of electron and lithium-ion. How to obtain an ultra-thin protective lithium sheet is also a problem that needs to be considered in the practical process of metal lithium batteries. In addition, establishing a practical and objective evaluation standard of the battery has important industrial significance for the development of Li-Se battery. In order to solve these problems, on the one hand, we can promote the practical application of Li-Se battery by industry-university-research cooperation; on the other hand, deeply exploring the reaction mechanism of the battery is urgently needed. Moreover, continuous technological innovation, and breakthrough in the development of Li-Se battery by exploring new materials and new theories may be a new direction to achieve bright prospects.

Table 1 Chemical performance of various Li-Se batteries with different cathodes.

Electrode materials	Capacity (mA h g^{-1}) at different rate (mA g^{-1})									Cycling performance (mA h g^{-1}) (cycles, Rae)	Se loading	Ref.
	100	200	400	500	1000	2000	3000	4000	5000			
Se_8/mesoporous carbon	500(0.1C)							229(5C)		480(1000,0.25 C)	30 wt.%	[15]
3DGCNT@ Se	608.5(0.2C)	585.5(0.5C)	558.3(1C)	523.6(2C)	486.5(3C)	436.4(4C)	370.7(6C)	295.8(8C)	192.9(10C)	504.3(150,0.2C)	51 wt.%	[156]
Se@CNx	679(80 mA g^{-1})	656(160mA g^{-1})	612(320)	539(800)	474(1600)					608.8(100,1C) 453.2(400,800mAg^{-1})	62.5 wt.%	[154]
hollow nanosphereSe@RGO	500（0.1C）	454(0.2C)	423(0.5C)	394(1C）						343(50,0.2C)	70 wt.%	[26]
CB free Se NPs@CTAB-MWCNTs	790.8(0.1C)	649.3(0.2C)	501.7(0.3C)	403.8(0.5C)	223.5(1C)	73.1(2C)				157（500,0.5C）	72 wt.%	[30]
Se@Al2O3 core-shell nanowires										258(50,150 mA g^{-1})		[28]
NP-Se										206(20,100 mA g^{-1})		[27]
Se/CMK-3				486(1C)	471(2C)			361(5C)		353(500,1C)	49.0 wt.%	[31]
Se/EDTA			473.6(0.6C)		353.1(2.4C)			291(4.8C)		538.4(100,0.24C)	~50 wt.%	[32]
HCPS/Se			393.2(0.5C)		246.8(2C)					298.7(100,0.5C)	41.2 wt.%	[46]
Tube-in-Tube carbon (TTC)		518(0.2C)	497(0.5C)	351(1C)	364(2C)					403(800,0.2C)	70 wt.%	[50]
Se/MCNF	560(0.1C)	546(0.2C)	522(0.5C)	495(1C)	463(2C)			420(5C)		400(2000,1C)	50 wt.%	[55]
Se/HPCF-rGO		584(0.2C)	532(0.5C)	492(1C)	455(2C)			408(5C)		485(500,1C),418(1000,2C),287(3000,5C),208(5000,10C)	57 wt.%	[71]
RFCS/Se-50		592.1(0.2C)	~550(0.5C)	~480(1C)	420(2C)			358.2(5C)		643.9(100,0.2C),411.4(1000,0.2C)	38.78wt.%	[40]
Se/PCNs	650(0.2C)	605(0.5C)	580(1C)	555(2C)	525(4C)	508(6C)	492(8C)	479(10C)	440/386(15/20C)	~2000 mAh cm^{-3}(1200,1C)	70.5 wt.%	[41]
GC-TiO/Se			630(0.5)						435(10C)	584(850,0.5C)	70 wt%,	[42]
A4-carbon/Se microspheres		~680		~620	~540	~470		~360	265(6 A g^{-1})	582(500,0.5 A g^{-1}),343(2000,2.0 A g^{-1})	59 wt.%	[43]
Se/PHCSs										338(50,0.1C)	60.0 wt.%	[47]
Se@PPy HS	~420(0.1C)	~400(0.2C)	~350(0.5C)	~300(1C)				238(2C)		400(80,0.2C)	52.4 wt.%	[321]
Sn-Se@C core shell	681					496				525(1000,0.5 A g^{-1})	59.5 wt.%	[44]
MWCNT/Se			~620(0.5C)	~560(1C)	~490(2C)		~360(4C)			355.5(100,0.5C)	56.17 wt.%	[49]
CPAN/Se	~600(0.1C)		~500(0.5C)	~430(1C)	~380(2C)	290(3C)				600(500,0.3C)		[52]
Se@CNFs-CNT	618(0.05 mA g^{-1})				485					517(500, 0.5 A g^{-1})	35 wt.%	[53]
PCNFW/Se		485.1(0.2C)		345.6(1C)						414.5(100,0.2C),323.7(300,1C)	33.2 wt.%	[54]
Se@CCNFs-20-PCZ	1071(0.1)	482(0.2C)	427.7(0.3C）	338.6(0.5C)	205.6（1C)	110.8(2C)				640.3(100,0.1C)	60 wt.%	[56]
G-SeHMs		610(0.2C)	505(0.5C)	400(1C)	355(2C)			301(5C)		544(100,0.1C)	80 wt.%	[57]
Se/CNSs-850	700(0.1C)								390(10C)	600(100,0.1C),376(1000,0.5C)	60 wt.%	[58]
potassium citrate derived carbon/Se-700							415.2(4C)			498.9(60,0.2C),362.8(500,2C)	55wt.%	[59]
HPCA/Se				400(1C)				301(5C)		309(100,0.5C)	45 wt.%	[60]
CNTs@Se/graphene-CNTs		665				479				538(80,0.5 A g^{-1})	70 wt.%–75 wt.%	[143]
Se/SPC	438(0.2C)	426(0.33C)	417(0.5C)	405(1C)	375(2C)			321(5C)		417(100,0.2C)	57.5 wt.%	[72]
Se/ABPC	610(0.1C)	562(0.2C)	510(0.5C)	469(1C)	429(2C)					591(98,0.1C)	66.67 wt.%	[78]
HPTCs/Se		500(0.2C)	458(0.3C)	435(0.5C)	380(1C)	325(2C)				317(900,2C)	53 wt%.	[80]

Se/MMPBc-3			507.2(0.5C)	460.9(1C)	421(2C)					466.8(300,0.2C)）	56.1 wt.%	[81]
Se/PPDC	650(150 mA g^{-1})		600(300 mA g^{-1})	530(600 mA g^{-1})	410(900 mA g^{-1})					490(100,150 mA g^{-1})	47 wt.%	[82]
SPC/Se		~520(0.2C)	~440(0.3C)	~380(0.5C)	~290(1C)	~170(2C)				290(840,1C)	63 wt.%	[83]
N-LSCM-900		655.4(0.2C)	613.4(0.5C)	572.8(1C)	504.5(2C)			358.4(5C)		350(1000, 1356 mA g−1),		[84]
PCM/Se										230(510,2C)	~52 wt.%	[86]
PCc-2/Se		530.8(0.2C) 388.2 or	438.1(0.5C)	388.2(1C)	339.5(2C)	295.8(4C)				431.9(60, 0.2C)	57 wt.%	[87]
Se-50.2/CPC		670(0.2C)					477(4C)			633.9(100,0.1C)	50.2 wt.%	[89]
N,O Co-doped carbon/Se	549.6(0.48C)	506(0.96)	450.4(1.92C)					342.8(4.8C)		446.9(100,0.24C)	50 wt.%	[322]
Se–CP			~620(0.5C)	~550(1C)	~500(2C)		~400(5C)	~360(10C)	303(20C)	506(150,1C)	60 wt.%	[91]
Se/N-MPCS	635(0.09C)	590(0.19C)	560(0.47C)	520(0.93C)	485(1.87C)			440(4.7C)		570(350,0.5C)	~50 wt.%	[92]
Se@N-CT	1261(0.1C)	630(0.2C)		404(1C)	350(2C)	271(3C)				403(100,0.2C),365(100,1C)	48 wt.%	[93]
Se_{50}/HDHPC			681(0.5C)	~680(1C)	~650(2C)		~580(5C)	~520(10C)	416(20C)	545(1500,0.5C),320(5000,2C)	48 wt.%(5:5)	[90]
Se–NCHPC					348(0.5C)			261(5C)		305(60,2C)	56.2 wt.%	[94]
Se-NCSs		475(0.2C)	~430(0.5C)	~339(1C)	275(2C)					480(100,0.1C),301(500,1C)	56 wt.%	[95]
MCMs/Se			455(0.5C)	~499(1C)	~380(2C)			320(5C)		300(100,0.5C)	50 wt.%	[96]
Ag2Se@Se/NMC		~630(0.2C)	~550(0.5C)	~400(1C)		~350(3C)		294(5C)		382(100,0.2C),206(400,0.5C),193(400,1C)	67 wt.%	[97]
NHCS/Se-52		545(0.2C)	493(0.5C)	443(1C)	410(2C)				265(10C)	541(500,0.2C)	52 wt.%	[98]
NCS-0.5/Se-50		553(0.2C)	512(0.5C)	478(1C)	416(2C)	293(5C)	231(7C)	155(10C)		483/480/429/387/344/324/344(2/10/100/500/1000/2000/3000,1C)	50 wt.%	[99]
Se@KF65	1166.4	1041.4		935.5	842.8	750.1			614.3	917.8(600,1 A g^{-1})	60 wt.%	[100]
meso-C@Se			448.9(0.5C)		385.9(2C)			323.8(5C)		306.9(100,0.5C),279.5(100,2C)	48 wt.%	[102]
SeS_2/HMCNCs	930.3	815.5		767.4	699.3	588.6			455.1	812.6(100,0.2 A g^{-1})	78.1 wt.%	[103]
NPC/CGB-Se			564(0.5C)	552(1C)	527(2C)	487(5C)	467(7C)	442(10C)	409(15C)	462(1000,0.5C)	59.8 wt.%	[106]
BP-CNF/Se			696(0.5C)	670(1C)	645(2C)			607(5C)	568(10C)	588(300,0.5C)	60 wt.%	[117]
Se-NCSs	605(0.1C)	575.9(0.2C)	513.4(0.5C)	456.9(1C)	392.6(2C)			286.6(5C)		443.2(200th，0.5C）	50 wt.%	[113]
Se@CoSe2-PC		631(0.2C)	509(0.5C)	428(1C)	356(2C)			275(5C)	210(10C)	408(100,1C)	43 wt.%	[243]
$MoS_{1.5}Se_{0.5}$-3D rGO	775(0.1C)	700(0.2C)	690(0.5C)	600(1C)	550(2C)			500(5C)	400(10C,1 C=680mA g^{-1})	1225(200,100mA g^{-1})		[323]
ZIF-67@Se@MnO2				746(1C)	397(2C)	347(5C)	305(10C)	256(20C)	147(50C)	329(100,1C),273/232 (100,2 C/5 C)	38 wt.%	123
Se/CMCs		420.4(0.2C)						218.1(5C)		425.2(100,0.2C)	49.7 wt.%	[116]
C-Co-N/Se	668.7(0.1C)	630.2(0.2C)	601.7(0.5C)	543.7(1C)	478.2(2C)	422(4C)	350.2(6C)	273.5(8C)	196.9(10C)	574.2(200,0.1C)	76.5 wt.%	[105]
Co-N-C/SeS_2	1193.5(0.1C)	1080.7(0.2C)	928.2(0.5C)	760(1C)	604.1(2C)		439.7(4C)	300.3(6C)	138.1(8C)	970.2(200,0.2C)	66.5 wt.% of SeS_2	[139]
$S_{0.94}Se_{0.06}$/C	1123	1105		1034	961	926	802(10A g^{-1})	617(20 A g^{-1})	863	910(100,1 A g^{-1}),1105(100,0.2 A g^{-1})	50 wt.%	[324]
SeS2@MCA	1074(250 mA g^{-1})			731		371				601(10, 500 mA g^{-1})	49.3 wt.%SeS_2	[131]
Se_xS_y/MCM				965.3(1C)	829.8(2C)			688.8(5C)		796.4(100,0.5C)		[132]
SeS2@ISMC		882(250)		751	649	544		465		486(200,0.5A g^{-1})	49.7 wt.% SeS	[137]
$S_{0.87}Se_{0.13}$/CPAN	1371(60)	1218(120)	964(300)	557(600)	284					1210(100,120mA g^{-1}),989(200,300mA g^{-1})	$S_{0.87}Se_{0.13}$-40 wt.%	[140]

S/Se@CB⊂NNH					~766	~662	~572		~488	804.3(300th),~753(500,0.2Ah g-1)	Se/S 64.8 wt.%	[325]
Se_2S_6/NMC				~900	~790		~620		~480	883/780(100/200,250 mA g^{-1})	60 wt.%	[135]
Se_xS_{8-x}-M_{32}/VACNTs		1068(0.2C)	927(0.5C)	853(1C)	739(2C)			632(5C)		818(500,500 mA g^{-1})	72.4 wt.%	[138]
PDSe-S/PDSe-S_2	214/318(0.1C)	169/232(0.2C)	150/205(0.5C)	136/193(1C)	113/174(2C)						64 wt.%/67 wt.%	[145]
PDATtSSe	740(50 mA g−1)	632(100)	570(200)	490(500)	422(800)	373(1000)	333(1200)			500(400,0.6 A g^{-1})	71.6 wt.%	[147]
Se@PCNFs	637	604		566	545	460		306		643(100,0.05 A g^{-1}),516(900,0.5A g^{-1})	52.3 wt.%	[153]
freestanding Se@MCNFs	642	616		578	526	379				596(100,0.1 A g^{-1}),430(300,0.5 A g^{-1})	48 wt.%	[326]
self-standing grapheneeSe@CNT	~330(0.1C)	~230(0.2C)	~140（0.5C)	80(1C）						315(100,0.1C)	30 wt.%	[158]
Se/MCN-RGO	650(0.1C)	593(0.2)	525(0.5C)	462(1C)	377(2C)	274(3C)				400(1300,1C)	62 wt.%	[155]
CNF/Se as barrier layers and active layers were prepared	580(50),~480(100)	~460	~430	~420(400)	389(800)					508(300,50 mA g^{-1})	63.5 wt.%	[157]
GO@Se@Ni	~550(0.1C)	~430(0.2C)	~280(0.5C)	~200(1C)	~160(2C)	100(3C)				266(100,0.1C)		[327]
Se-Li_3PS_4-C	652,649(150)	642,611(300)	574		462(800)					585(100,50 mA g^{-1})		[159]
Se/MC			603(0.5C)	591(1C)	588(2C)		584(5C)	575(10C)	569(20C)	511(1000,5C)	51.4 wt.%	[165]
Li-WO3@separator/Se-AAC	799(0.1)	510(0.2C)	451(0.3C)	375(0.5C)	238(1C)	126(2C)				494 (100,0.1C)	70 wt.%	[184]
G@Se/PANI		633.1(0.2C)	563.7(0.5 C)	530.6(1C)	510.9(2C)					567.1(200,0.2C)	66.18 wt.%	[328]
PANI@Se/C-G					529.2(2C)	514.2(3C)	499.8(4C)	475.6(5C)		588.7(200,0.2C),528.6(500,2C)	51.9 wt.%	[183]
Se/C-$Ni(OH)_2$		606(0.25C)	555(0.5C)	474(1C)	395(2C)					323(300,1A g^{-1})	71.8 wt.%	[190]

References

[1] J. Gao, Y. Li, L. Shi, J. Li, G. Zhang, Rational design of hierarchical nanotubes through encapsulating CoSe2 nanoparticles into MoSe2/C composite shells with enhanced lithium and sodium storage performance, ACS applied materials & interfaces, 10 (2018) 20635-20642.

[2] J. Chen, Recent progress in advanced materials for lithium ion batteries, Materials, 6 (2013) 156-183.

[3] K. Chen, X. Wang, G. Wang, B. Wang, X. Liu, J. Bai, H. Wang, A new generation of high performance anode materials with semiconductor heterojunction structure of SnSe/SnO2@ Gr in lithium-ion batteries, Chemical Engineering Journal, 347 (2018) 552-562.

[4] Y. Cui, X. Zhou, W. Guo, Y. Liu, T. Li, Y. Fu, L. Zhu, Selenium Nanocomposite Cathode with Long Cycle Life for Rechargeable Lithium-Selenium Batteries, Batteries & Supercaps, 2 (2019) 784-791.

[5] A. Manthiram, X. Yu, S. Wang, Lithium battery chemistries enabled by solid-state electrolytes, Nature Reviews Materials, 2 (2017) 1-16.

[6] E.P. Roth, C.J. Orendorff, How electrolytes influence battery safety, The Electrochemical Society Interface, 21 (2012) 45-49.

[7] Z. Zheng, Q. Su, H. Xu, Q. Zhang, H. Ye, Z. Wang, A pomegranate-like porous carbon nanomaterial as selenium host for stable lithium-selenium batteries, Materials Letters, 244 (2019) 134-137.

[8] L. Hu, C. Dai, J.-M. Lim, Y. Chen, X. Lian, M. Wang, Y. Li, P. Xiao, G. Henkelman, M. Xu, A highly efficient double-hierarchical sulfur host for advanced lithium–sulfur batteries, Chemical science, 9 (2018) 666-675.

[9] D. Su, M. Cortie, G. Wang, Fabrication of N-doped graphene–carbon nanotube hybrids from Prussian blue for lithium–sulfur batteries, Adv. Energy Mater., 7 (2017) 1602014.

[10] N. Feng, K. Xiang, L. Xiao, W. Chen, Y. Zhu, H. Liao, H. Chen, Se/CNTs microspheres as improved performance for cathodes in Li-Se batteries, Journal of Alloys and Compounds, 786 (2019) 537-543.

[11] L.-C. Zeng, W.-H. Li, Y. Jiang, Y. Yu, Recent progress in Li–S and Li–Se batteries, Rare metals, 36 (2017) 339-364.

[12] C. Chen, C. Zhao, Z. Hu, K. Liu, Synthesis of Se/chitosan-derived hierarchical porous carbon composite as Li–Se battery cathode, Functional Materials Letters, 10 (2017) 1650074.

[13] M.H.A. Shiraz, H. Zhu, Y. Liu, X. Sun, J. Liu, Activation-free synthesis of microporous carbon from polyvinylidene fluoride as host materials for lithium-selenium batteries, J. Power Sources, 438 (2019) 227059.

[14] S.-K. Park, J.-S. Park, Y.C. Kang, Trimodally porous N-doped carbon frameworks with an interconnected pore structure as selenium immobilizers for high-performance Li-Se batteries, Materials Characterization, 151 (2019) 590-601.

[15] C. Luo, Y. Xu, Y. Zhu, Y. Liu, S. Zheng, Y. Liu, A. Langrock, C. Wang, Selenium@ mesoporous carbon composite with superior lithium and sodium storage capacity, ACS nano, 7 (2013) 8003-8010.

[16] J. Jin, X. Tian, N. Srikanth, L.B. Kong, K. Zhou, Advances and challenges of nanostructured electrodes for Li–Se batteries, J. Mater. Chem. A, 5 (2017) 10110-10126.

[17] A. Eftekhari, The rise of lithium–selenium batteries, Sustain. Energy Fuels, 1 (2017) 14-29.

[18] R. Mukkabla, S. Deshagani, P. Meduri, M. Deepa, P. Ghosal, Selenium/graphite platelet nanofiber composite for durable Li–Se batteries, ACS Energy Lett., 2 (2017) 1288-1295.

[19] C.-P. Yang, Y.-X. Yin, Y.-G. Guo, Elemental selenium for electrochemical energy storage, J. Phys. Chem. Lett., 6 (2015) 256-266.

[20] X. Zhou, P. Gao, S. Sun, D. Bao, Y. Wang, X. Li, T. Wu, Y. Chen, P. Yang, Amorphous, crystalline and crystalline/amorphous selenium nanowires and their different (De) lithiation mechanisms, Chem. Mater., 27 (2015) 6730-6736.

[21] C.-X. Zu, H. Li, Thermodynamic analysis on energy densities of batteries, Energy Environ. Sci., 4 (2011) 2614-2624.

[22] W. Cao, J. Zhang, H. Li, Batteries with high theoretical energy densities, Energy Stor. Mater., 26 (2020) 46-55.

[23] Q. He, B. Yu, Z. Li, Y. Zhao, Density functional theory for battery materials, Energy & Environmental Materials, 2 (2019) 264-279.

[24] C. Li, H. Zhang, L. Otaegui, G. Singh, M. Armand, L.M. Rodriguez-Martinez, Estimation of energy density of Li-S batteries with liquid and solid electrolytes, J. Power Sources, 326 (2016) 1-5.

[25] Q. Wang, J. Jin, X. Wu, G. Ma, J. Yang, Z. Wen, A shuttle effect free lithium sulfur battery based on a hybrid electrolyte, Physical Chemistry Chemical Physics, 16 (2014) 21225-21229.

[26] M.R. Busche, P. Adelhelm, H. Sommer, H. Schneider, K. Leitner, J. Janek, Systematical electrochemical study on the parasitic shuttle-effect in lithium-sulfur-cells at different temperatures and different rates, Journal of Power Sources, 259 (2014) 289-299.

[27] L. Qi, X. Tang, Z. Wang, X.J.I.J.o.M.S. Peng, Technology, Pore characterization of different types of coal from coal and gas outburst disaster sites using low temperature nitrogen adsorption approach, 27 (2017) 371-377.

[28] S. Fan, Y. Zhang, S.-H. Li, T.-Y. Lan, J.-L. Xu, Hollow selenium encapsulated into 3D graphene hydrogels for lithium–selenium batteries with high rate performance and cycling stability, RSC Adv., 7 (2017) 21281-21286.

[29] L. Liu, Y. Hou, X. Wu, S. Xiao, Z. Chang, Y. Yang, Y. Wu, Nanoporous selenium as a cathode material for rechargeable lithium–selenium batteries, Chem. Commun., 49 (2013) 11515-11517.

[30] C. Wang, Q. Hu, Y. Wei, D. Fang, W. Xu, Z. Luo, Facile fabrication of selenium (Se) nanowires for enhanced lithium storage in Li-Se battery, Ionics, 23 (2017) 3571-3579.

[31] D. Kundu, F. Krumeich, R. Nesper, Investigation of nano-fibrous selenium and its polypyrrole and graphene composite as cathode material for rechargeable Li-batteries, J. Power Sources, 236 (2013) 112-117.

[32] R. Mukkabla, S. Deshagani, M. Deepa, S. Shivaprasad, P. Ghosal, Carbon black free Selenium/CTAB decorated carbon nanotubes composite with high selenium content for Li-Se batteries, Electrochim. Acta, 283 (2018) 63-74.

[33] C.P. Yang, S. Xin, Y.X. Yin, H. Ye, J. Zhang, Y.G. Guo, An advanced selenium–carbon cathode for rechargeable lithium–selenium batteries, Angew. Chem. Int. Ed., 52 (2013) 8363-8367.

[34] C. Zhao, S. Fang, Z. Hu, K. Liu, Synthesis of selenium/EDTA-derived porous carbon composite as a Li–Se battery cathode, Journal of Nanoparticle Research, 18 (2016) 201.

[35] H. Zhang, D. Jia, Z. Yang, F. Yu, Y. Su, D. Wang, Q. Shen, Alkaline lignin derived porous carbon as an efficient scaffold for lithium-selenium battery cathode, Carbon, 122 (2017) 547-555.

[36] Z. Zhang, X. Yang, X. Wang, Q. Li, Z. Zhang, TiO2–Se composites as cathode material for rechargeable lithium–selenium batteries, Solid State Ionics, 260 (2014) 101-106.

[37] W. Li, R. Fang, Y. Xia, W. Zhang, X. Wang, X. Xia, J. Tu, Multiscale porous carbon nanomaterials for applications in advanced rechargeable batteries, Batteries & Supercaps, 2 (2019) 9-36.

[38] H. Ye, Y.-X. Yin, S.-F. Zhang, Y.-G. Guo, Advanced Se–C nanocomposites: a bifunctional electrode material for both Li–Se and Li-ion batteries, Journal of Materials Chemistry A, 2 (2014) 13293-13298.

[39] Z. Zhang, X. Yang, Z. Guo, Y. Qu, J. Li, Y. Lai, Selenium/carbon-rich core–shell composites as cathode materials for rechargeable lithium–selenium batteries, Journal of Power Sources, 279 (2015) 88-93.

[40] C. Zhao, L. Xu, Z. Hu, K. Liu, Facile synthesis of selenium/potassium tartrate derived porous carbon composite as an advanced Li–Se battery cathode, RSC Adv., 6 (2016) 47486-47490.

[41] H. Tian, T. Wang, F. Zhang, S. Zhao, S. Wan, F. He, G. Wang, Tunable porous carbon spheres for high-performance rechargeable batteries, Journal of Materials Chemistry A, 6 (2018) 12816-12841.

[42] Y. Jun, W.-f. Liu, C. Cheng, C.-h. Zhao, K.-y. Liu, Synthesis and characterization of porous monodisperse carbon spheres/selenium composite for high-performance rechargeable Li-Se batteries, Transactions of Nonferrous Metals Society of China, 28 (2018) 1819-1827.

[43] Z. Li, L. Yuan, Z. Yi, Y. Liu, Y. Huang, Confined selenium within porous carbon nanospheres as cathode for advanced Li–Se batteries, Nano Energy, 9 (2014) 229-236.

[44] Y.J. Hong, K.C. Roh, Y.C. Kang, Mesoporous graphitic carbon microspheres with a controlled amount of amorphous carbon as an efficient Se host material for Li–Se batteries, Journal of Materials Chemistry A, 6 (2018) 4152-4160.

[45] G.D. Park, J.H. Kim, J.-K. Lee, Y.C. Kang, Carbon microspheres with well-developed micro- and mesopores as excellent selenium host materials for lithium–selenium batteries with superior performances, J. Mater. Chem. A, 6 (2018) 21410-21418.

[46] Y.J. Hong, Y.C. Kang, Selenium-impregnated hollow carbon microspheres as efficient cathode materials for lithium-selenium batteries, Carbon, 111 (2017) 198-206.

[47] J. Zhang, L. Fan, Y. Zhu, Y. Xu, J. Liang, D. Wei, Y. Qian, Selenium/interconnected porous hollow carbon bubbles composites as the cathodes of Li–Se batteries with high performance, Nanoscale, 6 (2014) 12952-12957.

[48] J. Li, X. Zhao, Z. Zhang, Y. Lai, Facile synthesis of hollow carbonized polyaniline spheres to encapsulate selenium for advanced rechargeable lithium–selenium batteries, Journal of Alloys and Compounds, 619 (2015) 794-799.

[49] Y. Lai, F. Yang, Z. Zhang, S. Jiang, J. Li, Encapsulation of selenium in porous hollow carbon spheres for advanced lithium–selenium batteries, RSC Advances, 4 (2014) 39312-39315.

[50] R. Pongilat, K. Nallathamby, Size-Dependent Charge Storage Behavior of Mesoporous Hollow Carbon Spheres for High-Performance Li–Se Batteries, J. Phys. Chem. C, 123 (2019) 5881-5889.

[51] X. Wang, Z. Zhang, Y. Qu, G. Wang, Y. Lai, J. Li, Solution-based synthesis of multi-walled carbon nanotube/selenium composites for high performance lithium–selenium battery, Journal of Power Sources, 287 (2015) 247-252.

[52] K. Balakumar, N. Kalaiselvi, Selenium containing Tube-in-Tube carbon: A one dimensional carbon frame work for selenium cathode in Li-Se battery, Carbon, 112 (2017) 79-90.

[53] D. Dutta, S. Gope, D.S. Negi, R. Datta, A. Sood, A.J. Bhattacharyya, Pressure-induced capillary encapsulation protocol for ultrahigh loading of sulfur and selenium inside carbon nanotubes: application as high performance cathode in Li–S/se rechargeable batteries, The Journal of Physical Chemistry C, 120 (2016) 29011-29022.

[54] H. Wang, S. Li, Z. Chen, H.K. Liu, Z. Guo, A novel type of one-dimensional organic selenium-containing fiber with superior performance for lithium–selenium and sodium–selenium batteries, RSC Adv., 4 (2014) 61673-61678.

[55] L. Zeng, X. Wei, J. Wang, Y. Jiang, W. Li, Y. Yu, Flexible one-dimensional carbon–selenium composite nanofibers with superior electrochemical performance for Li–Se/Na–Se batteries, J. Power Sources, 281 (2015) 461-469.

[56] J. Zhang, Z. Zhang, Q. Li, Y. Qu, S. Jiang, Selenium encapsulated into interconnected polymer-derived porous carbon nanofiber webs as cathode materials for lithium-selenium batteries, J. Electrochem. Soc., 161 (2014) A2093.

[57] Y. Liu, L. Si, Y. Du, X. Zhou, Z. Dai, J. Bao, Strongly bonded selenium/microporous carbon nanofibers composite as a high-performance cathode for lithium–selenium batteries, J. Phys. Chem. C, 119 (2015) 27316-27321.

[58] R. Mukkabla, Kuldeep, M. Deepa, Poly (carbazole)-Coated Selenium@ Conical Carbon Nanofibers Hybrid for Lithium–Selenium Batteries with Enhanced Lifespan, ACS Applied Energy Materials, 1 (2018) 6964-6976.

[59] H.-C. Youn, J.H. Jeong, K.C. Roh, K.-B. Kim, Graphene–selenium hybrid microballs as cathode materials for high-performance lithium–selenium secondary battery applications, Sci. Rep., 6 (2016) 1-8.

[60] S.-F. Zhang, W.-P. Wang, S. Xin, H. Ye, Y.-X. Yin, Y.-G. Guo, Graphitic nanocarbon–selenium cathode with favorable rate capability for Li–Se batteries, ACS Appl. Mater. Interfaces, 9 (2017) 8759-8765.

[61] C. Zhao, Z. Hu, J. Luo, Porous carbon nanoplate/Se composite derived from potassium citrate as high-performance Li-Se battery cathode: A study on structure-function relation, Colloids and Surfaces A: Physicochemical and Engineering Aspects, 560 (2019) 69-77.

[62] S. Jiang, Z. Zhang, Y. Lai, Y. Qu, X. Wang, J. Li, Selenium encapsulated into 3D interconnected hierarchical porous carbon aerogels for lithium–selenium batteries with high rate performance and cycling stability, Journal of Power Sources, 267 (2014) 394-404.

[63] X. Lu, H. Dou, B. Gao, C. Yuan, S. Yang, L. Hao, L. Shen, X. Zhang, A flexible graphene/multiwalled carbon nanotube film as a high performance electrode material for supercapacitors, Electrochimica Acta, 56 (2011) 5115-5121.

[64] Z. Fan, J. Yan, L. Zhi, Q. Zhang, T. Wei, J. Feng, M. Zhang, W. Qian, F. Wei, A three-dimensional carbon nanotube/graphene sandwich and its application as electrode in supercapacitors, Advanced materials, 22 (2010) 3723-3728.

[65] H. Choi, H. Kim, S. Hwang, M. Kang, D.-W. Jung, M. Jeon, Electrochemical electrodes of graphene-based carbon nanotubes grown by chemical vapor deposition, Scripta Materialia, 64 (2011) 601-604.

[66] V.C. Tung, J. Kim, J. Huang, Graphene oxide: single-walled carbon nanotube-based interfacial layer for all-solution-processed multijunction solar cells in both regular and inverted geometries, Advanced Energy Materials, 2 (2012) 299-303.

[67] S. Chen, P. Chen, Y. Wang, Carbon nanotubes grown in situ on graphene nanosheets as superior anodes for Li-ion batteries, Nanoscale, 3 (2011) 4323-4329.

[68] X. Chen, J. Zhu, Q. Xi, W. Yang, A high performance electrochemical sensor for acetaminophen based on single-walled carbon nanotube–graphene nanosheet hybrid films, Sensors and Actuators B: Chemical, 161 (2012) 648-654.

[69] J. Lu, S. Liu, S. Ge, M. Yan, J. Yu, X. Hu, Ultrasensitive electrochemical immunosensor based on Au nanoparticles dotted carbon nanotube–graphene composite and functionalized mesoporous materials, Biosensors and Bioelectronics, 33 (2012) 29-35.

[70] Z. Sui, Q. Meng, X. Zhang, R. Ma, B. Cao, Green synthesis of carbon nanotube–graphene hybrid aerogels and their use as versatile agents for water purification, Journal of Materials Chemistry, 22 (2012) 8767-8771.

[71] L.F. Chen, Y. Feng, H.W. Liang, Z.Y. Wu, S.H. Yu, Macroscopic-scale three-dimensional carbon nanofiber architectures for electrochemical energy storage devices, Adv. Energy Mater., 7 (2017) 1700826.

[72] J. Li, C. Zhang, C.-J. Wu, Y. Tao, L. Zhang, Q.-H. Yang, Improved performance of Li–Se battery based on a novel dual functional CNTs@ graphene/CNTs cathode construction, Rare Metals, 36 (2017) 425-433.

[73] L. Zeng, X. Chen, R. Liu, L. Lin, C. Zheng, L. Xu, F. Luo, Q. Qian, Q. Chen, M. Wei, Green synthesis of a Se/HPCF–rGO composite for Li–Se batteries with excellent long-term cycling performance, J. Mater. Chem. A, 5 (2017) 22997-23005.

[74] F. Dai, J. Shen, A. Dailly, M.P. Balogh, P. Lu, L. Yang, J. Xiao, J. Liu, M. Cai, Hierarchical electrode architectures for high energy lithium-chalcogen rechargeable batteries, Nano Energy, 51 (2018) 668-679.

[75] H. Li, W. Dong, C. Li, T. Barakat, M. Sun, Y. Wang, L. Wu, L. Wang, L. Xia, Z.-Y. Hu, Three-dimensional ordered hierarchically porous carbon materials for high performance Li-Se battery, J. Energy Chem., 68 (2022) 624-636.

[76] L. Yangdan, G. Yichuan, T. Yang, T. Haichao, Y. Zhizhen, L. Jianguo, Porous carbon derived from corncob as cathode host for Li–Se battery, Ionics, (2022) 1-9.

[77] Y. Lei, X. Liang, L. Yang, J. Chen, L. Qu, K. Xu, J. Feng, Li–Se batteries: Insights to the confined structure of selenium in hierarchical porous carbon and discharge mechanism in the carbonate electrolyte, Carbon, 191 (2022) 122-131.

[78] F. Li, F. Qin, K. Zhang, J. Fang, Y. Lai, J. Li, Hierarchically porous carbon derived from banana peel for lithium sulfur battery with high areal and gravimetric sulfur loading, Journal of Power Sources, 362 (2017) 160-167.

[79] M. Xue, C. Chen, Z. Ren, Y. Tan, B. Li, C. Zhang, A novel mangosteen peels derived hierarchical porous carbon for lithium sulfur battery, Materials Letters, 209 (2017) 594-597.

[80] M.K. Rybarczyk, H.-J. Peng, C. Tang, M. Lieder, Q. Zhang, M.-M. Titirici, Porous carbon derived from rice husks as sustainable bioresources: insights into the role of micro-/mesoporous hierarchy in hosting active species for lithium–sulphur batteries, Green Chemistry, 18 (2016) 5169-5179.

[81] G. Yuan, F. Yin, Y. Zhao, Z. Bakenov, G. Wang, Y. Zhang, Corn stalk-derived activated carbon with a stacking sheet-like structure as sulfur cathode supporter for lithium/sulfur batteries, Ionics, 22 (2016) 63-69.

[82] L.-S. Xie, S.-X. Yu, H.-J. Yang, J. Yang, J.-L. Ni, J.-L. Wang, Hierarchical porous carbon derived from animal bone as matric to encapsulated selenium for high performance Li–Se battery, Rare Metals, 36 (2017) 434-441.

[83] M. Xiang, Y. Wang, J. Wu, Y. Guo, H. Wu, Y. Zhang, H. Liu, Natural silk cocoon derived nitrogen-doped porous carbon nanosheets for high performance lithium-sulfur batteries, Electrochimica Acta, 227 (2017) 7-16.

[84] M. Jia, S. Lu, Y. Chen, T. Liu, J. Han, B. Shen, X. Wu, S.-J. Bao, J. Jiang, M. Xu, Three-dimensional hierarchical porous tubular carbon as a host matrix for long-term lithium-selenium batteries, Journal of Power Sources, 367 (2017) 17-23.

[85] H. Zhang, F. Yu, W. Kang, Q. Shen, Encapsulating selenium into macro-/micro-porous biochar-based framework for high-performance lithium-selenium batteries, Carbon, 95 (2015) 354-363.

[86] K. Sun, H. Zhao, S. Zhang, J. Yao, J. Xu, Selenium/pomelo peel-derived carbon nanocomposite as advanced cathode for lithium-selenium batteries, Ionics, 21 (2015) 2477-2484.

[87] M. Jia, Y. Niu, C. Mao, S. Liu, Y. Zhang, S.-j. Bao, M. Xu, Porous carbon derived from sunflower as a host matrix for ultra-stable lithium–selenium battery, J. Colloid Interface Sci., 490 (2017) 747-753.

[88] X. Gu, C.-J. Tong, S. Rehman, L.-M. Liu, Y. Hou, S. Zhang, Multifunctional nitrogen-doped loofah sponge carbon blocking layer for high-performance rechargeable lithium batteries, ACS Appl. Mater. Interfaces, 8 (2016) 15991-16001.

[89] R. Fang, Y. Xia, C. Liang, X. He, H. Huang, Y. Gan, J. Zhang, X. Tao, W. Zhang, Supercritical CO 2-assisted synthesis of 3D porous SiOC/Se cathode for ultrahigh areal capacity and long cycle life Li–Se batteries, Journal of Materials Chemistry A, 6 (2018) 24773-24782.

[90] M. Jia, C. Mao, Y. Niu, J. Hou, S. Liu, S. Bao, J. Jiang, M. Xu, Z. Lu, A selenium-confined porous carbon cathode from silk cocoons for Li–Se battery applications, RSC Advances, 5 (2015) 96146-96150.

[91] S. Liu, Q. Lu, C. Zhao, Hierarchical porous carbon/selenium composites derived from abandoned paper cup as Li-Se battery cathodes, Solid State Sciences, 84 (2018) 15-22.

[92] C. Luo, J. Wang, L. Suo, J. Mao, X. Fan, C. Wang, In situ formed carbon bonded and encapsulated selenium composites for Li–Se and Na–Se batteries, J. Mater. Chem. A, 3 (2015) 555-561.

[93] D. Jia, Z. Yang, H. Zhang, F. Liu, Q. Shen, High performance of selenium cathode by encapsulating selenium into the micropores of chitosan-derived porous carbon framework, J. Alloys Compd., 746 (2018) 27-35.

[94] X. Zhao, L. Yin, T. Zhang, M. Zhang, Z. Fang, C. Wang, Y. Wei, G. Chen, D. Zhang, Z. Sun, Heteroatoms dual-doped hierarchical porous carbon-selenium composite for durable Li–Se and Na–Se batteries, Nano Energy, 49 (2018) 137-146.

[95] Z. Yi, L. Yuan, D. Sun, Z. Li, C. Wu, W. Yang, Y. Wen, B. Shan, Y. Huang, High-performance lithium–selenium batteries promoted by heteroatom-doped microporous carbon, Journal of Materials Chemistry A, 3 (2015) 3059-3065.

[96] Y. Jiang, X. Ma, J. Feng, S. Xiong, Selenium in nitrogen-doped microporous carbon spheres for high-performance lithium–selenium batteries, J. Mater. Chem. A, 3 (2015) 4539-4546.

[97] D.B. Babu, K. Ramesha, Constraining polyselenide formation in ether based electrolytes through confinement of Se in microporous carbon matrix for Li-Se batteries, Electrochim. Acta, 219 (2016) 295-304.

[98] Y. Qu, Z. Zhang, S. Jiang, X. Wang, Y. Lai, Y. Liu, J. Li, Confining selenium in nitrogen-containing hierarchical porous carbon for high-rate rechargeable lithium–selenium batteries, Journal of Materials Chemistry A, 2 (2014) 12255-12261.

[99] H. Lv, R. Chen, X. Wang, Y. Hu, Y. Wang, T. Chen, L. Ma, G. Zhu, J. Liang, Z. Tie, High-performance Li–Se batteries enabled by selenium storage in bottom-up synthesized nitrogen-doped carbon scaffolds, ACS applied materials & interfaces, 9 (2017) 25232-25238.

[100] L. Liu, Y. Wei, C. Zhang, C. Zhang, X. Li, J. Wang, L. Ling, W. Qiao, D. Long, Enhanced electrochemical performances of mesoporous carbon microsphere/selenium composites by controlling the pore structure and nitrogen doping, Electrochim. Acta, 153 (2015) 140-148.

[101] F. Sun, Y. Li, Z. Wu, Y. Liu, H. Tang, X. Li, Z. Yue, L. Zhou, In situ reactive coating of metallic and selenophilic Ag 2 Se on Se/C cathode materials for high performance Li–Se batteries, RSC advances, 8 (2018) 32808-32813.

[102] B. Kalimuthu, K. Nallathamby, Designed Formulation of Se-Impregnated N-Containing Hollow Core Mesoporous Shell Carbon Spheres: Multifunctional Potential Cathode for Li–Se and Na–Se Batteries, ACS applied materials & interfaces, 9 (2017) 26756-26770.

[103] B. Kalimuthu, K. Nallathamby, Optimization of Structure and Porosity of Nitrogen Containing Mesoporous Carbon Spheres for Effective Selenium Confinement in Futuristic Lithium–Selenium Batteries, ACS Sustainable Chemistry & Engineering, 6 (2018) 7064-7077.

[104] J. Huang, Y. Lin, J. Yu, D. Li, J. Du, B. Yang, C. Li, C. Zhu, J. Xu, N-doped foam flame retardant polystyrene derived porous carbon as an efficient scaffold for lithium-selenium battery with long-term cycling performance, Chem. Eng. J., 350 (2018) 411-418.

[105] J. Guo, Z. Wen, Q. Wang, J. Jin, G. Ma, A conductive selenized polyacrylonitrile cathode material for re-chargeable lithium batteries with long cycle life, Journal of Materials Chemistry A, 3 (2015) 19815-19821.

[106] Y. Lai, Y. Gan, Z. Zhang, W. Chen, J. Li, Metal-organic frameworks-derived mesoporous carbon for high performance lithium–selenium battery, Electrochim. Acta, 146 (2014) 134-141.

[107] C. Liu, X. Huang, J. Wang, H. Song, Y. Yang, Y. Liu, J. Li, L. Wang, C. Yu, Hollow Mesoporous Carbon Nanocubes: Rigid-Interface-Induced Outward Contraction of Metal-Organic Frameworks, Advanced Functional Materials, 28 (2018) 1705253.

[108] Y.-X. Zhou, Y.-Z. Chen, L. Cao, J. Lu, H.-L. Jiang, Conversion of a metal–organic framework to N-doped porous carbon incorporating Co and CoO nanoparticles: direct oxidation of alcohols to esters, Chemical Communications, 51 (2015) 8292-8295.

[109] J. He, W. Lv, Y. Chen, J. Xiong, K. Wen, C. Xu, W. Zhang, Y. Li, W. Qin, W. He, Three-dimensional hierarchical C-Co-N/Se derived from metal-organic framework as superior cathode for Li-Se batteries, Journal of Power Sources, 363 (2017) 103-109.

[110] S.-K. Park, J.-S. Park, Y.C. Kang, Metal-organic-framework-derived N-doped hierarchically porous carbon polyhedrons anchored on crumpled graphene balls as efficient selenium hosts for high-performance lithium–selenium batteries, ACS Appl. Mater. Interfaces, 10 (2018) 16531-16540.

[111] G. Xu, P. Nie, H. Dou, B. Ding, L. Li, X. Zhang, Exploring metal organic frameworks for energy storage in batteries and supercapacitors, Mater. Today, 20 (2017) 191-209.

[112] S. Lim, K. Suh, Y. Kim, M. Yoon, H. Park, D.N. Dybtsev, K. Kim, Porous carbon materials with a controllable surface area synthesized from metal–organic frameworks, Chem. Commun., 48 (2012) 7447-7449.

[113] B. Liu, H. Shioyama, T. Akita, Q. Xu, Metal-organic framework as a template for porous carbon synthesis, J. Am. Chem. Soc., 130 (2008) 5390-5391.

[114] H. Furukawa, K.E. Cordova, M. O'Keeffe, O.M. Yaghi, The chemistry and applications of metal-organic frameworks, Science, 341 (2013) 1230444.

[115] X. Cao, C. Tan, M. Sindoro, H. Zhang, Hybrid micro-/nano-structures derived from metal–organic frameworks: preparation and applications in energy storage and conversion, Chemical Society Reviews, 46 (2017) 2660-2677.

[116] J. He, W. Lv, Y. Chen, J. Xiong, K. Wen, C. Xu, W. Zhang, Y. Li, W. Qin, W. He, Direct impregnation of SeS 2 into a MOF-derived 3D nanoporous Co–N–C architecture towards superior rechargeable lithium batteries, J. Mater. Chem. A, 6 (2018) 10466-10473.

[117] Z. Li, L. Yin, MOF-derived, N-doped, hierarchically porous carbon sponges as immobilizers to confine selenium as cathodes for Li–Se batteries with superior storage capacity and perfect cycling stability, Nanoscale, 7 (2015) 9597-9606.

[118] T. Liu, Y. Zhang, J. Hou, S. Lu, J. Jiang, M. Xu, High performance mesoporous C@ Se composite cathodes derived from Ni-based MOFs for Li–Se batteries, RSC Adv., 5 (2015) 84038-84043.

[119] J.-P. Song, L. Wu, W.-D. Dong, C.-F. Li, L.-H. Chen, X. Dai, C. Li, H. Chen, W. Zou, W.-B. Yu, MOF-derived nitrogen-doped core–shell hierarchical porous carbon confining selenium for advanced lithium–selenium batteries, Nanoscale, 11 (2019) 6970-6981.

[120] T. Liu, M. Jia, Y. Zhang, J. Han, Y. Li, S. Bao, D. Liu, J. Jiang, M. Xu, Confined selenium within metal-organic frameworks derived porous carbon microcubes as cathode for rechargeable lithium–selenium batteries, J. Power Sources, 341 (2017) 53-59.

[121] S.-K. Park, J.-S. Park, Y.C. Kang, Selenium-infiltrated metal–organic framework-derived porous carbon nanofibers comprising interconnected bimodal pores for Li–Se batteries with high capacity and rate performance, Journal of Materials Chemistry A, 6 (2018) 1028-1036.

[122] Y. Li, J. Fan, J. Zhang, J. Yang, R. Yuan, J. Chang, M. Zheng, Q. Dong, A honeycomb-like Co@ N–C composite for ultrahigh sulfur loading Li–S batteries, ACS nano, 11 (2017) 11417-11424.

[123] X. Tan, X. Wang, X. Wang, Y. Wang, C. Li, D. Xia, NiCo 2 S 4 yolk-shell hollow spheres with physical and chemical interaction toward polysulfides for advanced lithium-sulfur batteries, Ionics, 25 (2019) 4047-4056.

[124] Z. Li, J. Zhang, B.Y. Guan, X.W. Lou, Mesoporous carbon@ titanium nitride hollow spheres as an efficient SeS2 host for advanced Li–SeS2 batteries, Angew. Chem. Int. Ed., 56 (2017) 16003-16007.

[125] K. Wu, J. Wang, C. Xu, X. Jiao, X. Hu, W. Guan, Hollow Spherical α-MoO3: An Effective Electrocatalyst of Polyselenides for Lithium–Selenium Batteries, ACS Applied Energy Materials, 4 (2021) 10203-10212.

[126] W. Ye, W. Li, K. Wang, W. Yin, W. Chai, Y. Qu, Y. Rui, B. Tang, ZIF-67@ Se@ MnO2: a novel Co-MOF-based composite cathode for lithium–selenium batteries, J. Phys. Chem. C, 123 (2018) 2048-2055.

[127] R. Jayan, M.M. Islam, Functionalized MXenes as effective polyselenide immobilizers for lithium–selenium batteries: a density functional theory (DFT) study, Nanoscale, 12 (2020) 14087-14095.

[128] M. Wang, L. Fan, X. Sun, B. Guan, B. Jiang, X. Wu, D. Tian, K. Sun, Y. Qiu, X. Yin, Nitrogen-doped CoSe2 as a bifunctional catalyst for high areal capacity and lean electrolyte of Li–S battery, ACS Energy Lett., 5 (2020) 3041-3050.

[129] J. Yang, H. Gao, D. Ma, J. Zou, Z. Lin, X. Kang, S. Chen, High-performance Li-Se battery cathode based on CoSe2-porous carbon composites, Electrochim. Acta, 264 (2018) 341-349.

[130] W. Xiao, Q. He, Y. Zhao, Virtual screening of two-dimensional selenides and transition metal doped SnSe for lithium-sulfur batteries: A first-principles study, Appl. Surf. Sci., 570 (2021) 151213.

[131] M. Cui, X. Zhao, T. Wang, W. Qiu, E. Song, Predicting Transition-Metal/Benzenehexathiol Systems as Effective Cathodes of Li-S batteries with Conjugate Conductivity and Synergetic Discharge, ChemistrySelect, 5 (2020) 7783-7788.

[132] X. Tao, J. Wang, C. Liu, H. Wang, H. Yao, G. Zheng, Z.W. Seh, Q. Cai, W. Li, G. Zhou, Balancing surface adsorption and diffusion of lithium-polysulfides on nonconductive oxides for lithium–sulfur battery design, Nat. Commun., 7 (2016) 1-9.

[133] Z. Li, J. Zhang, Y. Lu, X.W.D. Lou, A pyrolyzed polyacrylonitrile/selenium disulfide composite cathode with remarkable lithium and sodium storage performances, Science advances, 4 (2018) eaat1687.

[134] A. Abouimrane, D. Dambournet, K.W. Chapman, P.J. Chupas, W. Weng, K. Amine, A new class of lithium and sodium rechargeable batteries based on selenium and selenium–sulfur as a positive electrode, J. Am. Chem. Soc., 134 (2012) 4505-4508.

[135] Z. Zhang, S. Jiang, Y. Lai, J. Li, J. Song, J. Li, Selenium sulfide@ mesoporous carbon aerogel composite for rechargeable lithium batteries with good electrochemical performance, J. Power Sources, 284 (2015) 95-102.

[136] Y. Wei, Y. Tao, Z. Kong, L. Liu, J. Wang, W. Qiao, L. Ling, D. Long, Unique electrochemical behavior of heterocyclic selenium–sulfur cathode materials in ether-based electrolytes for rechargeable lithium batteries, Energy Stor. Mater., 5 (2016) 171-179.

[137] G.-L. Xu, T. Ma, C.-J. Sun, C. Luo, L. Cheng, Y. Ren, S.M. Heald, C. Wang, L. Curtiss, J. Wen, Insight into the capacity fading mechanism of amorphous Se2S5 confined in micro/mesoporous carbon matrix in ether-based electrolytes, Nano Lett., 16 (2016) 2663-2673.

[138] Y. Cui, A. Abouimrane, J. Lu, T. Bolin, Y. Ren, W. Weng, C. Sun, V.A. Maroni, S.M. Heald, K. Amine, (De) Lithiation mechanism of Li/SeS x (x= 0–7) batteries determined by in situ synchrotron X-ray diffraction and X-ray absorption spectroscopy, J. Am. Chem. Soc., 135 (2013) 8047-8056.

[139] F. Sun, H. Cheng, J. Chen, N. Zheng, Y. Li, J. Shi, Heteroatomic Se n S8–n Molecules Confined in Nitrogen-Doped Mesoporous Carbons as Reversible Cathode Materials for High-Performance Lithium Batteries, ACS nano, 10 (2016) 8289-8298.

[140] G.L. Xu, H. Sun, C. Luo, L. Estevez, M. Zhuang, H. Gao, R. Amine, H. Wang, X. Zhang, C.J. Sun, Solid-State Lithium/Selenium–Sulfur Chemistry Enabled via a Robust Solid-Electrolyte Interphase, Adv. Energy Mater., 9 (2019) 1802235.

[141] J. Hu, H. Zhong, X. Yan, L. Zhang, Confining selenium disulfide in 3D sulfur-doped mesoporous carbon for rechargeable lithium batteries, Appl. Surf. Sci., 457 (2018) 705-711.

[142] H.N. Fan, S.L. Chen, X.H. Chen, Q.L. Tang, A.P. Hu, W.B. Luo, H.K. Liu, S.X. Dou, 3D Selenium Sulfide@ Carbon Nanotube Array as Long-Life and High-Rate Cathode Material for Lithium Storage, Advanced Functional Materials, 28 (2018) 1805018.

[143] J. He, W. Lv, Y. Chen, J. Xiong, K. Wen, C. Xu, W. Zhang, Y. Li, W. Qin, W. He, Direct impregnation of SeS2 into a MOF-derived 3D nanoporous Co–N–C architecture towards superior rechargeable lithium batteries, Journal of Materials Chemistry A, 6 (2018) 10466-10473.

[144] T. Zhu, Y. Pang, Y. Wang, C. Wang, Y. Xia, S0. 87Se0. 13/CPAN composites as high capacity and stable cycling performance cathode for lithium sulfur battery, Electrochimica Acta, 281 (2018) 789-795.

[145] J. Zhang, Design and synthesis of hollow nanostructures as highly efficient hosts for advanced lithium-sulfur/selenium sulfide batteries, in, 2019.

[146] B. Guo, T. Yang, W. Du, Q. Ma, L.-z. Zhang, S.-J. Bao, X. Li, Y. Chen, M. Xu, Double-walled N-doped carbon@ NiCo 2 S 4 hollow capsules as SeS 2 hosts for advanced Li–SeS 2 batteries, Journal of Materials Chemistry A, 7 (2019) 12276-12282.

[147] Z. Li, J. Zhang, H.B. Wu, X.W. Lou, An improved Li–SeS2 battery with high energy density and long cycle life, Advanced Energy Materials, 7 (2017) 1700281.

[148] W.J. Chung, J.J. Griebel, E.T. Kim, H. Yoon, A.G. Simmonds, H.J. Ji, P.T. Dirlam, R.S. Glass, J.J. Wie, N.A. Nguyen, The use of elemental sulfur as an alternative feedstock for polymeric materials, Nat. Chem., 5 (2013) 518-524.

[149] Y. Cui, J.D. Ackerson, Y. Ma, A. Bhargav, J.A. Karty, W. Guo, L. Zhu, Y. Fu, Phenyl selenosulfides as cathode materials for rechargeable lithium batteries, Adv. Funct. Mater., 28 (2018) 1801791.

[150] W. Guo, A. Bhargav, J.D. Ackerson, Y. Cui, Y. Ma, Y. Fu, Mixture is better: enhanced electrochemical performance of phenyl selenosulfide in rechargeable lithium batteries, Chemical communications, 54 (2018) 8873-8876.

[151] J. Zhou, T. Qian, N. Xu, M. Wang, X. Ni, X. Liu, X. Shen, C. Yan, Selenium-Doped Cathodes for Lithium–Organosulfur Batteries with Greatly Improved Volumetric Capacity and Coulombic Efficiency, Advanced Materials, 29 (2017) 1701294.

[152] P. Dong, K.S. Han, J.-I. Lee, X. Zhang, Y. Cha, M.-K. Song, Controlled synthesis of sulfur-rich polymeric selenium sulfides as promising electrode materials for long-life, high-rate lithium metal batteries, ACS Appl. Mater. Interfaces, 10 (2018) 29565-29573.

[153] I. Gomez, D. Mantione, O. Leonet, J.A. Blazquez, D. Mecerreyes, Hybrid Sulfur− Selenium Co-polymers as Cathodic Materials for Lithium Batteries, ChemElectroChem, 5 (2018) 260-265.

[154] F. Wu, J.T. Lee, Y. Xiao, G. Yushin, Nanostructured Li_2Se cathodes for high performance lithium-selenium batteries, Nano Energy, 27 (2016) 238-246.

[155] C. Lu, W. Zhang, R. Fang, Z. Xiao, H. Huang, Y. Gan, J. Zhang, X. He, C. Liang, D. Zhu, Facile and efficient synthesis of Li2Se particles towards high-areal capacity Li2Se cathode for advanced Li–Se battery, Sustainable Materials and Technologies, 29 (2021) e00288.

[156] Y. Xia, Z. Fang, C. Lu, Z. Xiao, X. He, Y. Gan, H. Huang, G. Wang, W. Zhang, A Facile Pre-Lithiated Strategy towards High-Performance Li2Se-LiTiO2 Composite Cathode for Li-Se Batteries, Nanomaterials, 12 (2022) 815.

[157] L. Zeng, W. Zeng, Y. Jiang, X. Wei, W. Li, C. Yang, Y. Zhu, Y. Yu, A Flexible Porous Carbon Nanofibers-Selenium Cathode with Superior Electrochemical Performance for Both Li-Se and Na-Se Batteries, Advanced Energy Materials, 5 (2015) 1401377.

[158] Q. Cai, Y. Li, Q. Li, J. Xu, B. Gao, X. Zhang, K. Huo, P.K. Chu, Freestanding hollow double-shell Se@ CNx nanobelts as large-capacity and high-rate cathodes for Li-Se batteries, Nano Energy, 32 (2017) 1-9.

[159] K. Han, Z. Liu, J. Shen, Y. Lin, F. Dai, H. Ye, A free-standing and ultralong-life lithium-selenium battery cathode enabled by 3D mesoporous carbon/graphene hierarchical architecture, Adv. Funct. Mater., 25 (2015) 455-463.

[160] J. He, Y. Chen, W. Lv, K. Wen, P. Li, Z. Wang, W. Zhang, W. Qin, W. He, Three-dimensional hierarchical graphene-CNT@ Se: a highly efficient freestanding cathode for Li–Se batteries, ACS Energy Lett., 1 (2016) 16-20.

[161] Y. Xia, C. Lu, R. Fang, H. Huang, Y. Gan, C. Liang, J. Zhang, X. He, W. Zhang, Freestanding layer-structure selenium cathodes with ultrahigh Se loading for high areal capacity Li-Se batteries, Electrochem. Commun., 99 (2019) 16-21.

[162] K. Han, Z. Liu, H. Ye, F. Dai, Flexible self-standing graphene–Se@ CNT composite film as a binder-free cathode for rechargeable Li–Se batteries, J. Power Sources, 263 (2014) 85-89.

[163] X. Li, J. Liang, X. Li, C. Wang, J. Luo, R. Li, X. Sun, High-performance all-solid-state Li–Se batteries induced by sulfide electrolytes, Energy & Environmental Science, 11 (2018) 2828-2832.

[164] M. Liu, D. Zhou, Y.-B. He, Y. Fu, X. Qin, C. Miao, H. Du, B. Li, Q.-H. Yang, Z. Lin, Novel gel polymer electrolyte for high-performance lithium–sulfur batteries, Nano Energy, 22 (2016) 278-289.

[165] Y. Cui, A. Abouimrane, C.-J. Sun, Y. Ren, K. Amine, Li–Se battery: absence of lithium polyselenides in carbonate based electrolyte, Chem. Commun., 50 (2014) 5576-5579.

[166] M.R. Kaiser, S. Chou, H.K. Liu, S.X. Dou, C. Wang, J. Wang, Structure–property relationships of organic electrolytes and their effects on Li/S battery performance, Adv. Mater., 29 (2017) 1700449.

[167] S. Xin, L. Gu, N.-H. Zhao, Y.-X. Yin, L.-J. Zhou, Y.-G. Guo, L.-J. Wan, Smaller sulfur molecules promise better lithium–sulfur batteries, J. Am. Chem. Soc., 134 (2012) 18510-18513.

[168] J. Zhou, J. Yang, Z. Xu, T. Zhang, Z. Chen, J. Wang, A high performance lithium–selenium battery using a microporous carbon confined selenium cathode and a compatible electrolyte, J. Mater. Chem. A, 5 (2017) 9350-9357.

[169] G. Di Donato, T. Ates, H. Adenusi, A. Varzi, M.A. Navarra, S. Passerini, Electrolyte measures to prevent polysulfide shuttle in Li-S batteries, Batteries & Supercaps.

[170] L. Kong, L. Yin, F. Xu, J. Bian, H. Yuan, Z. Lu, Y. Zhao, Electrolyte solvation chemistry for lithium–sulfur batteries with electrolyte-lean conditions, J. Energy Chem., 55 (2021) 80-91.

[171] J.T. Lee, H. Kim, N. Nitta, K.-s. Eom, D.-C. Lee, F. Wu, H.-T. Lin, B. Zdyrko, W.I. Cho, G. Yushin, Stabilization of selenium cathodes via in situ formation of protective solid electrolyte layer, J. Mater. Chem. A, 2 (2014) 18898-18905.

[172] L. Suo, Y.-S. Hu, H. Li, M. Armand, L. Chen, A new class of solvent-in-salt electrolyte for high-energy rechargeable metallic lithium batteries, Nat. Commun., 4 (2013) 1-9.

[173] W.-J. Chen, C.-X. Zhao, B.-Q. Li, Q. Jin, X.-Q. Zhang, T.-Q. Yuan, X. Zhang, Z. Jin, S. Kaskel, Q. Zhang, A mixed ether electrolyte for lithium metal anode protection in working lithium–sulfur batteries, Energy & Environmental Materials, 3 (2020) 160-165.

[174] C. Sun, J. Liu, Y. Gong, D.P. Wilkinson, J. Zhang, Recent advances in all-solid-state rechargeable lithium batteries, Nano Energy, 33 (2017) 363-386.

[175] S. Li, W. Zhang, J. Zheng, M. Lv, H. Song, L. Du, Inhibition of polysulfide shuttles in Li–S batteries: modified separators and solid-state electrolytes, Adv. Energy Mater., 11 (2021) 2000779.

[176] B.V. Lotsch, J. Maier, Relevance of solid electrolytes for lithium-based batteries: A realistic view, Journal of Electroceramics, 38 (2017) 128-141.

[177] Y. Jin, K. Liu, J. Lang, X. Jiang, Z. Zheng, Q. Su, Z. Huang, Y. Long, C.-a. Wang, H. Wu, High-energy-density solid-electrolyte-based liquid Li-S and Li-Se batteries, Joule, 4 (2020) 262-274.

[178] X. Li, J. Liang, J.T. Kim, J. Fu, H. Duan, N. Chen, R. Li, S. Zhao, J. Wang, H. Huang, Highly Stable Halide-Electrolyte-Based All-Solid-State Li–Se Batteries, Adv. Mater., (2022) 2200856.

[179] X. Shi, Z. Zeng, H. Zhang, B. Huang, M. Sun, H.H. Wong, Q. Lu, W. Luo, Y. Huang, Y. Du, Gram-Scale Synthesis of Nanosized Li3HoBr6 Solid Electrolyte for All-Solid-State Li-Se Battery, Small Methods, 5 (2021) 2101002.

[180] Y. Zhou, Z. Li, Y.-C. Lu, A stable lithium–selenium interface via solid/liquid hybrid electrolytes: Blocking polyselenides and suppressing lithium dendrite, Nano Energy, 39 (2017) 554-561.

[181] X. Peng, L. Wang, X. Zhang, B. Gao, J. Fu, S. Xiao, K. Huo, P.K. Chu, Reduced graphene oxide encapsulated selenium nanoparticles for high-power lithium–selenium battery cathode, J. Power Sources, 288 (2015) 214-220.

[182] Z. Zhang, Z. Zhang, K. Zhang, X. Yang, Q. Li, Improvement of electrochemical performance of rechargeable lithium–selenium batteries by inserting a free-standing carbon interlayer, RSC Advances, 4 (2014) 15489-15492.

[183] R. Fang, G. Zhou, S. Pei, F. Li, H.-M. Cheng, Localized polyselenides in a graphene-coated polymer separator for high rate and ultralong life lithium–selenium batteries, Chem. Commun., 51 (2015) 3667-3670.

[184] X. Gu, L. Xin, Y. Li, F. Dong, M. Fu, Y. Hou, Highly reversible Li–Se batteries with ultra-lightweight N, S-codoped graphene blocking layer, Nano-micro letters, 10 (2018) 59.

[185] X. Gu, L. Xin, Y. Li, F. Dong, M. Fu, Y. Hou, Highly reversible Li–Se batteries with ultra-lightweight N, S-codoped graphene blocking layer, Nano-micro Lett., 10 (2018) 1-10.

[186] B. Wang, J. Zhang, Z. Xia, M. Fan, C. Lv, G. Tian, X. Li, Polyaniline-coated selenium/carbon composites encapsulated in graphene as efficient cathodes for Li-Se batteries, Nano Res., 11 (2018) 2460-2469.

[187] R. Mukkabla, K. Killi, S.M. Shivaprasad, M. Deepa, Metal Oxide Interlayer for Long-Lived Lithium–Selenium Batteries, Chemistry–A European Journal, 24 (2018) 17327-17338.

[188] S. Bai, X. Liu, K. Zhu, S. Wu, H. Zhou, Metal–organic framework-based separator for lithium–sulfur batteries, Nature Energy, 1 (2016) 1-6.

[189] L. Si, J. Wang, G. Li, X. Hong, Q. Wei, Y. Yang, M. Zhang, Y. Cai, High energy density lithium-selenium batteries enabled by a covalent organic framework-coated separator, Materials Letters, 246 (2019) 144-148.

[190] G. Huang, F. Zhang, X. Du, Y. Qin, D. Yin, L. Wang, Metal organic frameworks route to in situ insertion of multiwalled carbon nanotubes in Co3O4 polyhedra as anode materials for lithium-ion batteries, ACS nano, 9 (2015) 1592-1599.

[191] J. Ge, Q. Zhang, Z. Liu, H. Yang, B. Lu, Solvothermal synthesis of graphene encapsulated selenium/carboxylated carbon nanotubes electrode for lithium–selenium battery, J. Alloys Compd., 810 (2019) 151894.

[192] W. Ye, K. Wang, W. Yin, W. Chai, Y. Rui, B. Tang, A novel Zr-MOF-based and polyaniline-coated UIO-67@ Se@ PANI composite cathode for lithium–selenium batteries, Dalton Transactions, 48 (2019) 10191-10198.

[193] R. Luo, Y. Lu, X. Hou, Q. Yu, T. Peng, H. Yan, X. Liu, J.-K. Kim, Y. Luo, Encapsulation of Se/C into ultra-thin Ni (OH) 2 nanosheets as cathode materials for lithium-selenium batteries, Journal of Solid State Electrochemistry, 21 (2017) 3611-3618.

[194] T. Li, H. Liu, P. Shi, Q. Zhang, Recent progress in carbon/lithium metal composite anode for safe lithium metal batteries, Rare Metals, 37 (2018) 449-458.

[195] S. Li, J. Yang, Y. Lu, Lithium metal anode, Inorganic Battery Materials, (2019) 75.

[196] C.-P. Yang, Y.-X. Yin, S.-F. Zhang, N.-W. Li, Y.-G. Guo, Accommodating lithium into 3D current collectors with a submicron skeleton towards long-life lithium metal anodes, Nat. Commun., 6 (2015) 1-9.

[197] Y. Zhao, S. Hao, L. Su, Z. Ma, G. Shao, Hierarchical Cu fibers induced Li uniform nucleation for dendrite-free lithium metal anode, Chem. Eng. J., 392 (2020) 123691.

[198] Y. Wang, Z. Wang, D. Lei, W. Lv, Q. Zhao, B. Ni, Y. Liu, B. Li, F. Kang, Y.-B. He, Spherical Li deposited inside 3D Cu skeleton as anode with ultrastable performance, ACS Appl. Mater. Interfaces, 10 (2018) 20244-20249.

[199] H. Qiu, T. Tang, M. Asif, X. Huang, Y. Hou, 3D porous Cu current collectors derived by hydrogen bubble dynamic template for enhanced Li metal anode performance, Adv. Funct. Mater., 29 (2019) 1808468.

[200] H. Zhao, D. Lei, Y.B. He, Y. Yuan, Q. Yun, B. Ni, W. Lv, B. Li, Q.H. Yang, F. Kang, Compact 3D copper with uniform porous structure derived by electrochemical dealloying as dendrite-free lithium metal anode current collector, Adv. Energy Mater., 8 (2018) 1800266.

[201] R. Zhang, Y. Li, L. Qiao, D. Li, J. Deng, J. Zhou, L. Xie, Y. Hou, T. Wang, W. Tian, Atomic layer deposition assisted superassembly of ultrathin ZnO layer decorated hierarchical Cu foam for stable lithium metal anode, Energy Stor. Mater., 37 (2021) 123-134.

[202] Y. He, H. Xu, J. Shi, P. Liu, Z. Tian, N. Dong, K. Luo, X. Zhou, Z. Liu, Polydopamine coating layer modified current collector for dendrite-free Li metal anode, Energy Stor. Mater., 23 (2019) 418-426.

[203] M. Chen, L. Cheng, J. Chen, Y. Zhou, J. Liang, S. Dong, M. Chen, X. Wang, H. Wang, Facile and scalable modification of a Cu current collector toward uniform Li deposition of the Li metal anode, ACS Appl. Mater. Interfaces, 12 (2019) 3681-3687.

[204] D. He, Y. Liao, Z. Cheng, X. Sang, L. Yuan, Z. Li, Y. Huang, Facile one-step vulcanization of copper foil towards stable Li metal anode, Science China Materials, 63 (2020) 1663-1671.

[205] J.-H. You, S.-J. Zhang, L. Deng, M.-Z. Li, X.-M. Zheng, J.-T. Li, Y. Zhou, L. Huang, S.-G. Sun, Suppressing Li dendrite by a protective biopolymeric film from tamarind seed polysaccharide for high-performance Li metal anode, Electrochim. Acta, 299 (2019) 636-644.

[206] X.-Y. Hu, P. Xu, S. Deng, J. Lei, X. Lin, Q.-H. Wu, M. Zheng, Q. Dong, Inducing ordered li deposition on a pani-decorated cu mesh for an advanced li anode, J. Mater. Chem. A, 8 (2020) 17056-17064.

[207] K. Yan, Z. Lu, H.-W. Lee, F. Xiong, P.-C. Hsu, Y. Li, J. Zhao, S. Chu, Y. Cui, Selective deposition and stable encapsulation of lithium through heterogeneous seeded growth, Nature Energy, 1 (2016) 1-8.

[208] Z. Hou, Y. Yu, W. Wang, X. Zhao, Q. Di, Q. Chen, W. Chen, Y. Liu, Z. Quan, Lithiophilic Ag nanoparticle layer on Cu current collector toward stable Li metal anode, ACS Appl. Mater. Interfaces, 11 (2019) 8148-8154.

[209] D. Zhang, A. Dai, B. Fan, Y. Li, K. Shen, T. Xiao, G. Hou, H. Cao, X. Tao, Y. Tang, Three-dimensional ordered macro/mesoporous Cu/Zn as a lithiophilic current collector for dendrite-free lithium metal anode, ACS Appl. Mater. Interfaces, 12 (2020) 31542-31551.

[210] S. Liu, X. Zhang, R. Li, L. Gao, J. Luo, Dendrite-free Li metal anode by lowering deposition interface energy with Cu99Zn alloy coating, Energy Stor. Mater., 14 (2018) 143-148.

[211] Z. Wen, Y. Peng, J. Cong, H. Hua, Y. Lin, J. Xiong, J. Zeng, J. Zhao, A stable artificial protective layer for high capacity dendrite-free lithium metal anode, Nano Res., 12 (2019) 2535-2542.

[212] L. Yu, N.L. Canfield, S. Chen, H. Lee, X. Ren, M.H. Engelhard, Q. Li, J. Liu, W. Xu, J.G. Zhang, Enhanced stability of lithium metal anode by using a 3D porous nickel substrate, ChemElectroChem, 5 (2018) 761-769.

[213] L. Liu, Y.-X. Yin, J.-Y. Li, N.-W. Li, X.-X. Zeng, H. Ye, Y.-G. Guo, L.-J. Wan, Free-standing hollow carbon fibers as high-capacity containers for stable lithium metal anodes, Joule, 1 (2017) 563-575.

[214] F. Liu, R. Xu, Z. Hu, S. Ye, S. Zeng, Y. Yao, S. Li, Y. Yu, Regulating lithium nucleation via CNTs modifying carbon cloth film for stable Li metal anode, Small, 15 (2019) 1803734.

[215] K. Liu, Z. Li, W. Xie, J. Li, D. Rao, M. Shao, B. Zhang, M. Wei, Oxygen-rich carbon nanotube networks for enhanced lithium metal anode, Energy Stor. Mater., 15 (2018) 308-314.

[216] Y. Nan, S. Li, Y. Shi, S. Yang, B. Li, Gradient-Distributed Nucleation Seeds on Conductive Host for a Dendrite-Free and High-Rate Lithium Metal Anode, Small, 15 (2019) 1903520.

[217] J. Lang, Y. Jin, X. Luo, Z. Liu, J. Song, Y. Long, L. Qi, M. Fang, Z. Li, H. Wu, Surface graphited carbon scaffold enables simple and scalable fabrication of 3D composite lithium metal anode, J. Mater. Chem. A, 5 (2017) 19168-19174.

[218] T.T. Zuo, X.W. Wu, C.P. Yang, Y.X. Yin, H. Ye, N.W. Li, Y.G. Guo, Graphitized carbon fibers as multifunctional 3D current collectors for high areal capacity Li anodes, Adv. Mater., 29 (2017) 1700389.

[219] Q. Wang, C. Yang, J. Yang, K. Wu, L. Qi, H. Tang, Z. Zhang, W. Liu, H. Zhou, Stable Li metal anode with protected interface for high-performance Li metal batteries, Energy Stor. Mater., 15 (2018) 249-256.

[220] Y. Yu, W. Huang, X. Song, W. Wang, Z. Hou, X. Zhao, K. Deng, H. Ju, Y. Sun, Y. Zhao, Thermally reduced graphene paper with fast Li ion diffusion for stable Li metal anode, Electrochim. Acta, 294 (2019) 413-422.

[221] G. Hou, X. Ren, X. Ma, L. Zhang, W. Zhai, Q. Ai, X. Xu, L. Zhang, P. Si, J. Feng, Dendrite-free Li metal anode enabled by a 3D free-standing lithiophilic nitrogen-enriched carbon sponge, J. Power Sources, 386 (2018) 77-84.

[222] Y. Liu, X. Qin, S. Zhang, Y. Huang, F. Kang, G. Chen, B. Li, Oxygen and nitrogen co-doped porous carbon granules enabling dendrite-free lithium metal anode, Energy Stor. Mater., 18 (2019) 320-327.

[223] J. Lee, S.H. Choi, H. Qutaish, Y. Hyeon, S.A. Han, Y.-U. Heo, D. Whang, J.-W. Lee, J. Moon, M.-S. Park, Structurally stabilized lithium-metal anode via surface chemistry engineering, Energy Stor. Mater., 37 (2021) 315-324.

[224] M. Wang, Y. Guo, B. Wang, H. Luo, X. Zhang, Q. Wang, Y. Zhang, H. Wu, H. Liu, S. Dou, An engineered self-supported electrocatalytic cathode and dendrite-free composite anode based on 3D double-carbon hosts for advanced Li–SeS 2 batteries, J. Mater. Chem. A, 8 (2020) 2969-2983.

[225] C. Zhao, S. Xiong, H. Li, Z. Li, C. Qi, H. Yang, L. Wang, Y. Zhao, T. Liu, A dendrite-free composite Li metal anode enabled by lithiophilic Co, N codoped porous carbon nanofibers, J. Power Sources, 483 (2021) 229188.

[226] T.S. Wang, X. Liu, Y. Wang, L.Z. Fan, High Areal Capacity Dendrite-Free Li Anode Enabled by Metal–Organic Framework-Derived Nanorod Array Modified Carbon Cloth for Solid State Li Metal Batteries, Adv. Funct. Mater., 31 (2021) 2001973.

[227] K. Xu, M. Zhu, X. Wu, J. Liang, Y. Liu, T. Zhang, Y. Zhu, Y. Qian, Dendrite-tamed deposition kinetics using single-atom Zn sites for Li metal anode, Energy Stor. Mater., 23 (2019) 587-593.

[228] C. Yang, Y. Yao, S. He, H. Xie, E. Hitz, L. Hu, Ultrafine silver nanoparticles for seeded lithium deposition toward stable lithium metal anode, Adv. Mater., 29 (2017) 1702714.

[229] H. Song, X. Chen, G. Zheng, X. Yu, S. Jiang, Z. Cui, L. Du, S. Liao, Dendrite-free composite Li anode assisted by Ag nanoparticles in a wood-derived carbon frame, ACS Appl. Mater. Interfaces, 11 (2019) 18361-18367.

[230] Y. Liao, L. Yuan, J. Xiang, W. Zhang, Z. Cheng, B. He, Z. Li, Y. Huang, Realizing both high gravimetric and volumetric capacities in Li/3D carbon composite anode, Nano Energy, 69 (2020) 104471.

[231] T. Liu, J. Hu, C. Li, Y. Wang, Unusual conformal Li plating on alloyable nanofiber frameworks to enable dendrite suppression of Li metal anode, ACS Applied Energy Materials, 2 (2019) 4379-4388.

[232] Y. Yu, L. Gu, C. Zhu, P.A. Van Aken, J. Maier, Tin nanoparticles encapsulated in porous multichannel carbon microtubes: preparation by single-nozzle electrospinning and application as anode material for high-performance Li-based batteries, J. Am. Chem. Soc., 131 (2009) 15984-15985.

[233] T. Zhou, J. Shen, Z. Wang, J. Liu, R. Hu, L. Ouyang, Y. Feng, H. Liu, Y. Yu, M. Zhu, Regulating Lithium Nucleation and Deposition via MOF-Derived Co@ C-Modified Carbon Cloth for Stable Li Metal Anode, Adv. Funct. Mater., 30 (2020) 1909159.

[234] S. Xia, X. Zhang, H. Zhao, J. Xie, L.Y. Chou, Y. Yu, W. Liu, High-Performance Three-Dimensional Li Anode Scaffold Enabled by Homogeneous Zn Nanoclusters, Small, 16 (2020) 2001257.

[235] J. Qian, S. Wang, Y. Li, M. Zhang, F. Wang, Y. Zhao, Q. Sun, L. Li, F. Wu, R. Chen, Lithium Induced Nano-Sized Copper with Exposed Lithiophilic Surfaces to Achieve Dense Lithium Deposition for Lithium Metal Anode, Adv. Funct. Mater., 31 (2021) 2006950.

[236] Y. Liu, X. Qin, S. Zhang, L. Zhang, F. Kang, G. Chen, X. Duan, B. Li, A scalable slurry process to fabricate a 3D lithiophilic and conductive framework for a high performance lithium metal anode, J. Mater. Chem. A, 7 (2019) 13225-13233.

[237] R. Zhang, X. Chen, X. Shen, X.-Q. Zhang, X.-R. Chen, X.-B. Cheng, C. Yan, C.-Z. Zhao, Q. Zhang, Coralloid carbon fiber-based composite lithium anode for robust lithium metal batteries, Joule, 2 (2018) 764-777.

[238] Y. Zhang, W. Luo, C. Wang, Y. Li, C. Chen, J. Song, J. Dai, E.M. Hitz, S. Xu, C. Yang, High-capacity, low-tortuosity, and channel-guided lithium metal anode, Proceedings of the National Academy of Sciences, 114 (2017) 3584-3589.

[239] X.-Y. Yue, J. Bao, S.-Y. Yang, R.-J. Luo, Q.-C. Wang, X.-J. Wu, Z. Shadike, X.-Q. Yang, Y.-N. Zhou, Petaloid-shaped ZnO coated carbon felt as a controllable host to construct hierarchical Li composite anode, Nano Energy, 71 (2020) 104614.

[240] X. Wang, Z. Pan, Y. Wu, X. Ding, X. Hong, G. Xu, M. Liu, Y. Zhang, W. Li, Infiltrating lithium into carbon cloth decorated with zinc oxide arrays for dendrite-free lithium metal anode, Nano Res., 12 (2019) 525-529.

[241] Y. Zhang, B. Liu, E. Hitz, W. Luo, Y. Yao, Y. Li, J. Dai, C. Chen, Y. Wang, C. Yang, A carbon-based 3D current collector with surface protection for Li metal anode, Nano Res., 10 (2017) 1356-1365.

[242] X.-Y. Yue, X.-L. Li, W.-W. Wang, D. Chen, Q.-Q. Qiu, Q.-C. Wang, X.-J. Wu, Z.-W. Fu, Z. Shadike, X.-Q. Yang, Wettable carbon felt framework for high loading Li-metal composite anode, Nano Energy, 60 (2019) 257-266.

[243] C. Jin, O. Sheng, Y. Lu, J. Luo, H. Yuan, W. Zhang, H. Huang, Y. Gan, Y. Xia, C. Liang, Metal oxide nanoparticles induced step-edge nucleation of stable Li metal anode working under an ultrahigh current density of 15 mA cm− 2, Nano Energy, 45 (2018) 203-209.

[244] D. Xie, H.-H. Li, W.-Y. Diao, R. Jiang, F.-Y. Tao, H.-Z. Sun, X.-L. Wu, J.-P. Zhang, Spatial confinement of vertical arrays of lithiophilic SnS2 nanosheets enables conformal Li nucleation/growth towards dendrite-free Li metal anode, Energy Stor. Mater., 36 (2021) 504-513.

[245] X.R. Chen, B.Q. Li, C. Zhu, R. Zhang, X.B. Cheng, J.Q. Huang, Q. Zhang, A Coaxial-Interweaved Hybrid Lithium Metal Anode for Long-Lifespan Lithium Metal Batteries, Adv. Energy Mater., 9 (2019) 1901932.

[246] C. Sun, T. Wu, J. Wang, W. Li, J. Jin, J. Yang, Z. Wen, Favorable lithium deposition behaviors on flexible carbon microtube skeleton enable a high-performance lithium metal anode, J. Mater. Chem. A, 6 (2018) 19159-19166.

[247] J. Sun, B. Li, C. Jin, L. Peng, D. Dai, J. Hu, C. Yang, C. Lu, R. Yang, Construction of 3D porous CeO2 ceramic hosts with enhanced lithiophilicity for dendrite-free lithium metal anode, J. Power Sources, 484 (2021) 229253.

[248] K. Tantratian, D. Cao, A. Abdelaziz, X. Sun, J. Sheng, A. Natan, L. Chen, H. Zhu, Stable Li metal anode enabled by space confinement and uniform curvature through lithiophilic nanotube arrays, Adv. Energy Mater., 10 (2020) 1902819.

[249] L. Fan, S. Li, L. Liu, W. Zhang, L. Gao, Y. Fu, F. Chen, J. Li, H.L. Zhuang, Y. Lu, Enabling stable lithium metal anode via 3D inorganic skeleton with superlithiophilic interphase, Adv. Energy Mater., 8 (2018) 1802350.

[250] S. Matsuda, Y. Kubo, K. Uosaki, S. Nakanishi, Insulative microfiber 3D matrix as a host material minimizing volume change of the anode of Li metal batteries, ACS Energy Lett., 2 (2017) 924-929.

[251] L. Fan, H.L. Zhuang, W. Zhang, Y. Fu, Z. Liao, Y. Lu, Stable Lithium Electrodeposition at Ultra-High Current Densities Enabled by 3D PMF/Li Composite Anode, Adv. Energy Mater., 8 (2018) 1703360.

[252] H. Shi, M. Yue, C.J. Zhang, Y. Dong, P. Lu, S. Zheng, H. Huang, J. Chen, P. Wen, Z. Xu, 3D Flexible, Conductive, and Recyclable Ti3C2T x MXene-Melamine Foam for High-Areal-Capacity and Long-Lifetime Alkali-Metal Anode, ACS nano, 14 (2020) 8678-8688.

[253] H. Wang, J. Wu, L. Yuan, Z. Li, Y. Huang, Stable Lithium Metal Anode Enabled by 3D Soft Host, ACS Appl. Mater. Interfaces, 12 (2020) 28337-28344.

[254] J. Li, P. Zou, S.W. Chiang, W. Yao, Y. Wang, P. Liu, C. Liang, F. Kang, C. Yang, A conductive-dielectric gradient framework for stable lithium metal anode, Energy Stor. Mater., 24 (2020) 700-706.

[255] C.-Z. Zhao, X.-B. Cheng, R. Zhang, H.-J. Peng, J.-Q. Huang, R. Ran, Z.-H. Huang, F. Wei, Q. Zhang, Li2S5-based ternary-salt electrolyte for robust lithium metal anode, Energy Stor. Mater., 3 (2016) 77-84.

[256] C. Yan, Y. Yao, X. Chen, X. Cheng, X. Zhang, J. Huang, Q. Zhang, Solvation chemistry of lithium nitrate in carbonate electrolyte for high-voltage lithium metal battery, Angew. Chem. Int. Ed., 57 (2018) 14055-14059.

[257] Q. Liu, Y. Xu, J. Wang, B. Zhao, Z. Li, H.B. Wu, Sustained-Release Nanocapsules Enable Long-Lasting Stabilization of Li Anode for Practical Li-Metal Batteries, Nano-micro Lett., 12 (2020) 1-12.

[258] J. Guo, Z. Wen, M. Wu, J. Jin, Y. Liu, Vinylene carbonate–LiNO3: a hybrid additive in carbonic ester electrolytes for SEI modification on Li metal anode, Electrochem. Commun., 51 (2015) 59-63.

[259] L. Fu, X. Wang, L. Wang, M. Wan, Y. Li, Z. Cai, Y. Tan, G. Li, R. Zhan, Z.W. Seh, A salt-in-metal anode: stabilizing the solid electrolyte interphase to enable prolonged battery cycling, Adv. Funct. Mater., 31 (2021) 2010602.

[260] X. Shen, X. Cheng, P. Shi, J. Huang, X. Zhang, C. Yan, T. Li, Q. Zhang, Lithium–matrix composite anode protected by a solid electrolyte layer for stable lithium metal batteries, J. Energy Chem., 37 (2019) 29-34.

[261] F. Wu, J. Qian, R. Chen, J. Lu, L. Li, H. Wu, J. Chen, T. Zhao, Y. Ye, K. Amine, An effective approach to protect lithium anode and improve cycle performance for Li–S batteries, ACS Appl. Mater. Interfaces, 6 (2014) 15542-15549.

[262] S. Liu, Q. Zhang, X. Wang, M. Xu, W. Li, B.L. Lucht, LiFSI and LiDFBOP dual-salt electrolyte reinforces the solid electrolyte interphase on a lithium metal anode, ACS Appl. Mater. Interfaces, 12 (2020) 33719-33728.

[263] J. Hu, K. Chen, C. Li, Nanostructured Li-rich fluoride coated by ionic liquid as high ion-conductivity solid electrolyte additive to suppress dendrite growth at Li metal anode, ACS Appl. Mater. Interfaces, 10 (2018) 34322-34331.

[264] H. Ye, Y.-X. Yin, S.-F. Zhang, Y. Shi, L. Liu, X.-X. Zeng, R. Wen, Y.-G. Guo, L.-J. Wan, Synergism of Al-containing solid electrolyte interphase layer and Al-based colloidal particles for stable lithium anode, Nano Energy, 36 (2017) 411-417.

[265] X.-B. Cheng, M.-Q. Zhao, C. Chen, A. Pentecost, K. Maleski, T. Mathis, X.-Q. Zhang, Q. Zhang, J. Jiang, Y. Gogotsi, Nanodiamonds suppress the growth of lithium dendrites, Nat. Commun., 8 (2017) 1-9.

[266] Y. Guo, Y. Ouyang, D. Li, Y. Wei, T. Zhai, H. Li, PMMA-assisted Li deposition towards 3D continuous dendrite-free lithium anode, Energy Stor. Mater., 16 (2019) 203-211.

[267] J.Y. Wei, X.Q. Zhang, L.P. Hou, P. Shi, B.Q. Li, Y. Xiao, C. Yan, H. Yuan, J.Q. Huang, Shielding Polysulfide Intermediates by an Organosulfur-Containing Solid Electrolyte Interphase on the Lithium Anode in Lithium–Sulfur Batteries, Adv. Mater., 32 (2020) 2003012.

[268] M. Ishikawa, S.-i. Machino, M. Morita, Electrochemical control of a Li metal anode interface: improvement of Li cyclability by inorganic additives compatible with electrolytes, J. Electroanal. Chem., 473 (1999) 279-284.

[269] M. Ishikawa, H. Kawasaki, N. Yoshimoto, M. Morita, Pretreatment of Li metal anode with electrolyte additive for enhancing Li cycleability, J. Power Sources, 146 (2005) 199-203.

[270] G. Wang, X. Xiong, D. Xie, X. Fu, X. Ma, Y. Li, Y. Liu, Z. Lin, C. Yang, M. Liu, Suppressing dendrite growth by a functional electrolyte additive for robust Li metal anodes, Energy Stor. Mater., 23 (2019) 701-706.

[271] Y. He, Y. Zhang, P. Yu, F. Ding, X. Li, Z. Wang, Z. Lv, X. Wang, Z. Liu, X. Huang, Ion association tailoring SEI composition for Li metal anode protection, J. Energy Chem., 45 (2020) 1-6.

[272] Z. Liang, G. Zheng, C. Liu, N. Liu, W. Li, K. Yan, H. Yao, P.-C. Hsu, S. Chu, Y. Cui, Polymer nanofiber-guided uniform lithium deposition for battery electrodes, Nano Lett., 15 (2015) 2910-2916.

[273] M.D. Tikekar, S. Choudhury, Z. Tu, L.A. Archer, Design principles for electrolytes and interfaces for stable lithium-metal batteries, Nature Energy, 1 (2016) 1-7.

[274] Z. Gao, S. Zhang, Z. Huang, Y. Lu, W. Wang, K. Wang, J. Li, Y. Zhou, L. Huang, S. Sun, Protection of Li metal anode by surface-coating of PVDF thin film to enhance the cycling performance of Li batteries, Chin. Chem. Lett., 30 (2019) 525-528.

[275] M. Li, X. Li, V. Tung, Y. Li, Z. Lai, Protection of Lithium Anode by a Highly Porous PVDF Membrane for High-Performance Li–S Battery, ACS Applied Energy Materials, 3 (2020) 2510-2515.

[276] G. Wang, C. Chen, Y. Chen, X. Kang, C. Yang, F. Wang, Y. Liu, X. Xiong, Self-Stabilized and Strongly Adhesive Supramolecular Polymer Protective Layer Enables Ultrahigh-Rate and Large-Capacity Lithium-Metal Anode, Angew. Chem., 132 (2020) 2071-2076.

[277] D. Kang, N. Hart, J. Koh, L. Ma, W. Liang, J. Xu, S. Sardar, J.P. Lemmon, Rearrange SEI with artificial organic layer for stable lithium metal anode, Energy Stor. Mater., 24 (2020) 618-625.

[278] X. Li, L. Yuan, D. Liu, M. Liao, J. Chen, K. Yuan, J. Xiang, Z. Li, Y. Huang, Elevated Lithium Ion Regulation by a "Natural Silk" Modified Separator for High-Performance Lithium Metal Anode, Adv. Funct. Mater., 31 (2021) 2100537.

[279] C.H. Chang, S.H. Chung, A. Manthiram, Dendrite-Free Lithium Anode via a Homogenous Li-Ion Distribution Enabled by a Kimwipe Paper, Advanced Sustainable Systems, 1 (2017) 1600034.

[280] G. Ma, Z. Wen, Q. Wang, C. Shen, J. Jin, X. Wu, Enhanced cycle performance of a Li–S battery based on a protected lithium anode, J. Mater. Chem. A, 2 (2014) 19355-19359.

[281] D. Chen, S. Huang, L. Zhong, S. Wang, M. Xiao, D. Han, Y. Meng, In situ preparation of thin and rigid COF film on Li anode as artificial solid electrolyte interphase layer resisting Li dendrite puncture, Adv. Funct. Mater., 30 (2020) 1907717.

[282] Y. Yuan, F. Wu, Y. Bai, Y. Li, G. Chen, Z. Wang, C. Wu, Regulating Li deposition by constructing LiF-rich host for dendrite-free lithium metal anode, Energy Stor. Mater., 16 (2019) 411-418.

[283] C. Cui, C. Yang, N. Eidson, J. Chen, F. Han, L. Chen, C. Luo, P.F. Wang, X. Fan, C. Wang, A highly reversible, dendrite-free lithium metal anode enabled by a lithium-fluoride-enriched interphase, Adv. Mater., 32 (2020) 1906427.

[284] J. Lang, Y. Long, J. Qu, X. Luo, H. Wei, K. Huang, H. Zhang, L. Qi, Q. Zhang, Z. Li, One-pot solution coating of high quality LiF layer to stabilize Li metal anode, Energy Stor. Mater., 16 (2019) 85-90.

[285] C. Yan, X.B. Cheng, Y.X. Yao, X. Shen, B.Q. Li, W.J. Li, R. Zhang, J.Q. Huang, H. Li, Q. Zhang, An armored mixed conductor interphase on a dendrite-free lithium-metal anode, Adv. Mater., 30 (2018) 1804461.

[286] X. Shen, Y. Li, T. Qian, J. Liu, J. Zhou, C. Yan, J.B. Goodenough, Lithium anode stable in air for low-cost fabrication of a dendrite-free lithium battery, Nat. Commun., 10 (2019) 1-9.

[287] S. Liu, Y. Ma, J. Wang, P. Zuo, C. Du, G. Yin, Y. Gao, Regulating Li deposition by constructing homogeneous LiF protective layer for high-performance Li metal anode, Chem. Eng. J., 427 (2022) 131625.

[288] Y. Zhu, X. He, Y. Mo, Strategies based on nitride materials chemistry to stabilize Li metal anode, Advanced Science, 4 (2017) 1600517.

[289] G. Ma, Z. Wen, M. Wu, C. Shen, Q. Wang, J. Jin, X. Wu, A lithium anode protection guided highly-stable lithium–sulfur battery, Chem. Commun., 50 (2014) 14209-14212.

[290] Y. Li, Y. Sun, A. Pei, K. Chen, A. Vailionis, Y. Li, G. Zheng, J. Sun, Y. Cui, Robust pinhole-free Li3N solid electrolyte grown from molten lithium, ACS central science, 4 (2018) 97-104.

[291] S. Ye, L. Wang, F. Liu, P. Shi, H. Wang, X. Wu, Y. Yu, g-C3N4 Derivative Artificial Organic/Inorganic Composite Solid Electrolyte Interphase Layer for Stable Lithium Metal Anode, Adv. Energy Mater., 10 (2020) 2002647.

[292] A.C. Kozen, C.-F. Lin, A.J. Pearse, M.A. Schroeder, X. Han, L. Hu, S.-B. Lee, G.W. Rubloff, M. Noked, Next-generation lithium metal anode engineering via atomic layer deposition, ACS nano, 9 (2015) 5884-5892.

[293] Y. Zhao, L.V. Goncharova, Q. Sun, X. Li, A. Lushington, B. Wang, R. Li, F. Dai, M. Cai, X. Sun, Robust metallic lithium anode protection by the molecular-layer-deposition technique, Small Methods, 2 (2018) 1700417.

[294] H. Zhang, X. Liao, Y. Guan, Y. Xiang, M. Li, W. Zhang, X. Zhu, H. Ming, L. Lu, J. Qiu, Lithiophilic-lithiophobic gradient interfacial layer for a highly stable lithium metal anode, Nat. Commun., 9 (2018) 1-11.

[295] Y. Lai, Y. Zhao, W. Cai, J. Song, Y. Jia, B. Ding, J. Yan, Constructing Ionic Gradient and Lithiophilic Interphase for High-Rate Li-Metal Anode, Small, 15 (2019) 1905171.

[296] Q. Li, F.-L. Zeng, Y.-P. Guan, Z.-Q. Jin, Y.-Q. Huang, M. Yao, W.-K. Wang, A.-B. Wang, Poly (dimethylsiloxane) modified lithium anode for enhanced performance of lithium-sulfur batteries, Energy Stor. Mater., 13 (2018) 151-159.

[297] R. Pathak, K. Chen, A. Gurung, K.M. Reza, B. Bahrami, F. Wu, A. Chaudhary, N. Ghimire, B. Zhou, W.H. Zhang, Ultrathin bilayer of graphite/SiO2 as solid interface for reviving Li metal anode, Adv. Energy Mater., 9 (2019) 1901486.

[298] F. Liu, L. Wang, Z. Zhang, P. Shi, Y. Feng, Y. Yao, S. Ye, H. Wang, X. Wu, Y. Yu, A mixed lithium-ion conductive Li2S/Li2Se protection layer for stable lithium metal anode, Adv. Funct. Mater., 30 (2020) 2001607.

[299] N.W. Li, Y.X. Yin, C.P. Yang, Y.G. Guo, An artificial solid electrolyte interphase layer for stable lithium metal anodes, Adv. Mater., 28 (2016) 1853-1858.

[300] S. Li, Q. Liu, X. Wang, Q. Wu, L. Fan, W. Zhang, Z. Shen, L. Wang, M. Ling, Y. Lu, Constructing a Phosphating–Nitriding Interface for Practically Used Lithium Metal Anode, ACS Materials Letters, 2 (2019) 1-8.

[301] Y. Lu, S. Gu, X. Hong, K. Rui, X. Huang, J. Jin, C. Chen, J. Yang, Z. Wen, Pre-modified Li3PS4 based interphase for lithium anode towards high-performance Li-S battery, Energy Stor. Mater., 11 (2018) 16-23.

[302] S. Li, T. Liu, J. Yan, J. Flum, H. Wang, F. Lorandi, Z. Wang, L. Fu, L. Hu, Y. Zhao, Grafting polymer from oxygen-vacancy-rich nanoparticles to enable protective layers for stable lithium metal anode, Nano Energy, 76 (2020) 105046.

[303] S.H. Lee, J.R. Harding, D.S. Liu, J.M. D'Arcy, Y. Shao-Horn, P.T. Hammond, Li-anode protective layers for Li rechargeable batteries via layer-by-layer approaches, Chem. Mater., 26 (2014) 2579-2585.

[304] C. Yan, X.B. Cheng, Y. Tian, X. Chen, X.Q. Zhang, W.J. Li, J.Q. Huang, Q. Zhang, Dual-layered film protected lithium metal anode to enable dendrite-free lithium deposition, Adv. Mater., 30 (2018) 1707629.

[305] X. Liang, Q. Pang, I.R. Kochetkov, M.S. Sempere, H. Huang, X. Sun, L.F. Nazar, A facile surface chemistry route to a stabilized lithium metal anode, Nature Energy, 2 (2017) 1-7.

[306] S. Liu, Q. Zhao, X. Zhang, J. Liu, L. Dai, L. Wang, J. Luo, A high rate and long cycling life lithium metal anode with a self-repairing alloy coating, J. Mater. Chem. A, 8 (2020) 17415-17419.

[307] W. Luo, Y. Gong, Y. Zhu, Y. Li, Y. Yao, Y. Zhang, K. Fu, G. Pastel, C.F. Lin, Y. Mo, Reducing interfacial resistance between garnet-structured solid-state electrolyte and Li-metal anode by a germanium layer, Adv. Mater., 29 (2017) 1606042.

[308] H. Kim, J.T. Lee, D.-C. Lee, M. Oschatz, W.I. Cho, S. Kaskel, G. Yushin, Enhancing performance of Li–S cells using a Li–Al alloy anode coating, Electrochem. Commun., 36 (2013) 38-41.

[309] S. Xia, X. Zhang, C. Liang, Y. Yu, W. Liu, Stabilized lithium metal anode by an efficient coating for high-performance Li–S batteries, Energy Stor. Mater., 24 (2020) 329-335.

[310] L. Tan, S. Feng, X. Li, Z. Wang, W. Peng, T. Liu, G. Yan, L. Li, F. Wu, J. Wang, Oxygen-induced lithiophilicity of tin-based framework toward highly stable lithium metal anode, Chem. Eng. J., 394 (2020) 124848.

[311] J. Gu, C. Shen, Z. Fang, J. Yu, Y. Zheng, Z. Tian, L. Shao, X. Li, K. Xie, Toward High-Performance Li Metal Anode via Difunctional Protecting Layer, Frontiers in chemistry, 7 (2019) 572.

[312] L. Wang, S. Fu, T. Zhao, J. Qian, N. Chen, L. Li, F. Wu, R. Chen, In situ formation of a LiF and Li–Al alloy anode protected layer on a Li metal anode with enhanced cycle life, J. Mater. Chem. A, 8 (2020) 1247-1253.

[313] H. Wang, M. Liu, X. Wang, W. Zhang, Y. Che, L. Chen, Y. Wu, W. Li, A self-smoothing Li-metal anode enabled via a hybrid interface film, J. Mater. Chem. A, 8 (2020) 12045-12054.

[314] R. Xu, X.Q. Zhang, X.B. Cheng, H.J. Peng, C.Z. Zhao, C. Yan, J.Q. Huang, Artificial soft–rigid protective layer for dendrite-free lithium metal anode, Adv. Funct. Mater., 28 (2018) 1705838.

[315] Y. Zhao, G. Li, Y. Gao, D. Wang, Q. Huang, D. Wang, Stable Li metal anode by a hybrid lithium polysulfidophosphate/polymer cross-linking film, ACS Energy Lett., 4 (2019) 1271-1278.

[316] Y. Zhao, M. Amirmaleki, Q. Sun, C. Zhao, A. Codirenzi, L.V. Goncharova, C. Wang, K. Adair, X. Li, X. Yang, Natural SEI-inspired dual-protective layers via atomic/molecular layer deposition for long-life metallic lithium anode, Matter, 1 (2019) 1215-1231.

[317] L.L. Kong, L. Wang, Z.C. Ni, S. Liu, G.R. Li, X.P. Gao, Lithium–magnesium alloy as a stable anode for lithium–sulfur battery, Adv. Funct. Mater., 29 (2019) 1808756.

[318] W. Jia, Z. Wang, J. Li, X. Yu, Y. Wei, Z. Yao, Y. Liu, Y. Wang, A. Zhou, W. Zou, A dual-phase Li–Ca alloy with a patternable and lithiophilic 3D framework for improving lithium anode performance, J. Mater. Chem. A, 7 (2019) 22377-22384.

[319] W. Jia, Y. Liu, Z. Wang, F. Qing, J. Li, Y. Wang, R. Xiao, A. Zhou, G. Li, X. Yu, Low-temperature fusion fabrication of Li-Cu alloy anode with in situ formed 3D framework of inert LiCux nanowires for excellent Li storage performance, Science Bulletin, 65 (2020) 1907-1915.

[320] B. Duan, W. Wang, H. Zhao, A. Wang, M. Wang, K. Yuan, Z. Yu, Y. Yang, Li-B alloy as anode material for lithium/sulfur battery, ECS Electrochemistry Letters, 2 (2013) A47.

[321] X. Zhang, W. Wang, A. Wang, Y. Huang, K. Yuan, Z. Yu, J. Qiu, Y. Yang, Improved cycle stability and high security of Li-B alloy anode for lithium–sulfur battery, J. Mater. Chem. A, 2 (2014) 11660-11665.

[322] H. Qiu, T. Tang, M. Asif, W. Li, T. Zhang, Y. Hou, Stable lithium metal anode enabled by lithium metal partial alloying, Nano Energy, 65 (2019) 103989.

[323] H. Zhong, Y. Wu, F. Ding, L. Sang, Y. Mai, An artificial Li-Al interphase layer on Li-B alloy for stable lithium-metal anode, Electrochim. Acta, 304 (2019) 255-262.

[324] J. Guo, Z. Wen, G. Ma, J. Jin, W. Wang, Y. Liu, A selenium@ polypyrrole hollow sphere cathode for rechargeable lithium batteries, RSC Advances, 5 (2015) 20346-20350.

[325] C. Zhao, J. Luo, Z. Hu, Hierarchical porous N, O Co-doped carbon/Se composite derived from hydrothermal treated chitosan as Li–Se battery cathode, Micro & Nano Letters, 13 (2018) 1386-1389.

[326] L. Ma, X. Wang, B. Zhao, J. Yang, X. Zhang, Y. Zhou, J. Chen, Novel metal chalcogenide supported on three-dimensional graphene foam for enhanced lithium storage, Journal of Alloys and Compounds, 762 (2018) 149-156.

[327] X. Li, J. Liang, K. Zhang, Z. Hou, W. Zhang, Y. Zhu, Y. Qian, Amorphous S-rich S 1− x Se x/C (x≤ 0.1) composites promise better lithium–sulfur batteries in a carbonate-based electrolyte, Energy & Environmental Science, 8 (2015) 3181-3186.

[328] T. Meng, Y. Liu, L. Li, J. Zhu, J. Gao, H. Zhang, L. Ma, C.M. Li, J. Jiang, Smart Merit Combination of Sulfur, Selenium and Electrode Engineering To Build Better Sustainable Li-Storage Batteries, ACS Sustainable Chemistry & Engineering, 7 (2018) 802-809.

[329] B. Yuan, X. Sun, L. Zeng, Y. Yu, Q. Wang, A Freestanding and Long-Life Sodium–Selenium Cathode by Encapsulation of Selenium into Microporous Multichannel Carbon Nanofibers, Small, 14 (2018) 1703252.

[330] D. Huang, S. Li, Y. Luo, X. Xiao, L. Gao, M. Wang, Y. Shen, Graphene oxide-protected three dimensional Se as a binder-free cathode for Li-Se battery, Electrochim. Acta, 190 (2016) 258-263.

[331] J. Zhang, Y. Xu, L. Fan, Y. Zhu, J. Liang, Y. Qian, Graphene–encapsulated selenium/polyaniline core–shell nanowires with enhanced electrochemical performance for Li–Se batteries, Nano Energy, 13 (2015) 592-600.

Chapter II

The objectives and scientific strategy

1. Objective

Batteries, worked as a kind of green renewable energy, have been popularly used in many fields, such as vehicles, electronic equipment, etc. Li-Se batteries, with the advantages of high specific capacity, small volume and much higher conductivity of Se than S, are possible to be introduced to the market in the future. Unlike Li-ion batteries, Li-Se batteries give electrical power by the reaction of Se and Li. Due to the low density of the product of Li_2Se, the Se cathode experiences the volume expansion, which leads to the splitting off of the cathode. During the discharge/charge process, the intermediates of polyselenides are produced. The soluble polyselenides dissolution and shuttle between cathode and anode lead to the fast capacity decay of the Li-Se batteries. Thus, before introducing Li-Se batteries into the market, these intractable problems of shuttle effect, volume expansion, and fast capacity decay should be solved first. This is exactly the main objective of the present research work.

2. The scientific strategy

Many researches on Se cathodes have been carried out focusing on the above problems, such as enlarging surface area of the active Se by special morphological design, fabricating kinds of carbon host materials of different dimensions, selenium-sulfur solid solutions (Se_xS_y), hybrid sulfur-selenium co-polymers and binding free cathode. In addition, adjusting the composition of electrolyte and introducing the interlayer between cathode and separator can suppress the shuttle effect. Based on the previous works, we find that confining active Se inside the cathode to avoid the diffusion of the polyselenies is an efficient method to deal with these problems. In this respect, porous conductive carbon frameworks are promising Se host materials. Carbon materials possess high conductivity, which is beneficial for the transfer of electrons. In addition, various pores size and distribution can be easily designed and introduced. Most importantly, the carbon source is easily obtained at low price.

In our work, inspired by the natural organism whose pore sizes decrease across multiple scales and finally terminate in size-invariant units, the hierarchically micro-meso-macroporous carbon host materials were designed. The micropores provide abundant reaction sites and interconnected meso-macroporous pathways accelerate the mass transfer of the system, which will work well in the field of Li-Se battery. The difficulty is how to choose the size of these three scale pores and how to combine them efficiently. With the help of the templating method, SiO_2 and PS (Polystyrene

Spheres) worked as mesopores and macroporous templated to enlarge the range of the pores. Guided by the generalized Murray's law, the best pore size distribution will be explored by tuning macropore size of synthesized hierarchically porous carbon.

The unpolar pure carbon host materials have weak interaction with polar polyselenides. In order to further increase the strength of the adsorption of polyselenides, heteroatom doping is a good choice. Achieving heteroatom doping starts with the selection of precursors. MOF is a kind of framework rich in micropores and N atoms. MOF can be easily transformed to N-dopped carbon material by the pyrolysis process. Combing the advantages of the optimized micro-meso-macroporous structure and MOF precursor is expected to further increase the electrochemical performance of the battery.

However, considering the limitation of polar sites by the method of heteroatom doping, direct introduction of polar particles into the carbon host system may become a new option. A lot of previous work proved that oxides, nitrides, and sulfides not only have strong adsorption to polyselenides but also catalyze the reaction of discharge/charge. By achieving more polar sites to enhance the adsorption to PSe, amorphous polar particles will be used. Moreover, looking for a suitable polar particle with proper strength ensures the adsorption to polyselenides, while not being too strong to avoid causing decomposition of polyselenides is a challenge.

Guided by these strategies, the host materials will be synthesized. The properties of the host materials and corresponding Se@C composite cathode will be analyzed by characterization methods. Afterwards, the Se@C composite cathodes are fabricated. Se cathodes will be used to assemble Li-Se batteries. The electrochemical performance will be evaluated. At last, we hope our work could give some guidance for other's future work.

Chapter III

Experimental part: Chemicals and Characterization

1. Chemicals

All chemical reagents were of analytical grade and used without further purification.

1,2-dimethoxyethane (DME, Sigma-Aldrich)

1,3-dioxolane (DOL, Sigma-Aldrich)

2-methylimidazole ($C_4H_6N_2$, Acros Organics)

Ammonia solution ($NH_3.H_2O$, Fisher scientific)

Ammonium persulfate ($(NH_4)_2S_2O_8$, Sinopharm Chemical Reagent Co., Ltd.)

Cobalt (II) chloride ($CoCl_2$, Alfa Aesar)

Carbon nanotubes (CNTs, Nanografi Nano Technoligy)

Ethanol (absolute, Fisher Chemical)

Lithium selenide (Li_2Se, Xian function material group Co. Ltd.)

Methanol (CH_3OH, Carl Roth)

Hydrofluoric acid (HF, Sigma-Aldrich)

Polyvinyl pyrrolidone (PVP K30, Tokyo Chemical Industry Co. Ltd.)

Potassium persulfate ($K_2S_2O_8$, Acros Organics)

Selenium (Se-100 mesh, Sigma-Aldrich)

Silica sol (Ludox HS-30 colloidal silica, 12 nm, Sigma-Aldrich)

Silica sol (Ludox AS-40 colloidal silica, 22 nm, Alfa Aesar)

Sodium hydroxide (NaOH, Carl Roth)

Sodium laurylsulfonate ($C_{12}H_{25}NaO_3S$, Sigma-Aldrich)

Styrene (C_8H_8, Aladdin Industrial Corporation)

Sucrose ($C_6H_{12}O_6$, Sigma-Aldrich)

Sulfuric acid (H_2SO_4, Sigma-Aldrich)

Tin (IV) chloride ($SnCl_4$, Sigma-Aldrich)

Trisodium citrate dihydrate ($C_6H_5Na_3O_7 \cdot 2H_2O$, Roth)

Zinc nitrate hexahydrate ($Zn(NO_3)_2 \cdot 6H_2O$, Sigma-Aldrich)

2. Characterization

The main experimental equipment and instruments that were used in the thesis are listed below:

Instruments	Model
X-ray diffraction (XRD)	PANalytical X'pert Pro
In-situ XRD	STOE STADI MP
Raman	DXR, Thermo Fisher Scientific Inc.
X-ray photoelectron spectroscopy (XPS)	Thermo Scientific K-Alpha XPS
Scanning electron microscopy (SEM)	JSM-7500F
Transmission electron microscopy (TEM)	Tecnai 10
Energy-dispersive X-ray spectroscopy (EDX/EDS)	JSM-7500F
High-angle annular dark-field scanning transmission electron microscopy (HAADF-STEM), high-resolution transmission electron microscopy (HRTEM), and selected-area diffraction (SAED)	Talos F200s
Brunauer-Emmett-Teller (BET) surface area analysis	ASAP 2420 apparatus
Thermogravimetric analysis (TGA)	Mettler Toledo TGA/DSC3+
UV–visible Spectrophotometry (UV-Vis)	Perkin Elmer 750s UV/Vis/NIR spectrophotometer
Cell assembly, Ar-filled glove box	Vigor-SG1200/750TS
Cyclic voltammetry (CV)	LK 2005A electrochemical workstation

electrochemical impedance spectroscopy (EIS)	LK 2005A electrochemical workstation
Galvanostatic intermittent titration technique (GITT)	Land CT2001A multi-channel battery testing system
Galvanostatic charge and discharge experiments	Land CT2001A multi-channel battery testing system

2.1 Materials characterization

2.1.1 Power X-ray diffraction (PXRD) and *in-situ* XRD

XRD is a rapid analytical technique primarily used for phase identification of a crystalline material. The technique used to reveal structural information, such as chemical composition, crystal structure, crystallite size, strain, preferred orientation and layer thickness. The Li-Se battery assemble for *in-situ* XRD is shown in Fig.1[1], and the beryllium (Be) window is used due to its good X-ray penetration.

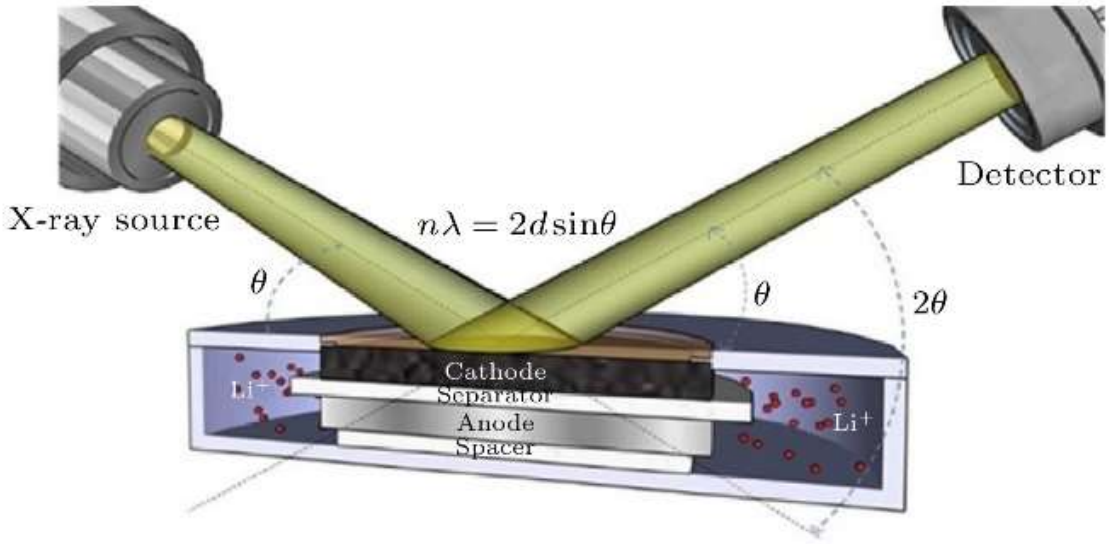

Fig.1 Schematic diagram of typical setup for *in-situ* XRD of batteries in reflection mode.

2.1.2 Scanning electron microscope (SEM)

SEM is a type of electron microscope that produces images of a sample by scanning the surface with a focused beam of electrons. In the most common SEM mode, secondary electrons emitted by atoms excited by the electron beam are detected using a secondary electron detector (Everhart–Thornley detector). The specimen topography can be reflected by the number of secondary electrons that can be detected and the signal intensity.

2.1.3 Energy-dispersive X-ray spectroscopy (EDX/EDS)

EDX/EDS is an analytical technique used for the elemental analysis or chemical characterization of a sample. It relies on an interaction of some source of X-ray and a sample. Its characterization capabilities are due in large part to the fundamental principle that each element has a unique atomic structure allowing a unique set of peaks on its electromagnetic emission spectrum.

2.1.4 Transmission electron microscopy (TEM)

TEM is a microscopy technique in which a beam of electrons is transmitted through a specimen to form an image. The specimen is most often an ultrathin section less than 100 nm thick or a suspension on a grid. An image is formed from the interaction of the electrons with the sample as the beam is transmitted through the specimen. The image is then magnified and focused onto an imaging device.

2.1.5 High-resolution transmission electron microscopy (HRTEM)

HRTEM is an imaging mode of specialized transmission electron microscopes that allows for direct imaging of the atomic structure of samples. It is a powerful tool to study properties of materials on the atomic scale.

2.1.6 Thermogravimetric analysis (TGA)

TGA is a method of thermal analysis in which the mass of a sample is measured over time as the temperature changes. This measurement provides information about physical phenomena, such as phase transitions, absorption, adsorption and desorption; as well as chemical phenomena including chemisorptions, thermal decomposition, and solid-gas reactions.

2.1.7 Brunauer-Emmett-Teller (BET) surface area analysis

BET theory aims to explain the physical adsorption of gas molecules on a solid surface and serves as the basis for an important analysis technique for the measurement of the specific surface area of solid or porous materials.

2.1.8 X-ray photoelectron spectroscopy (XPS)

XPS is a surface-sensitive quantitative spectroscopic technique based on the photoelectric effect that can identify the elements within a material (elemental composition) or on its surface, as well as their chemical state, and the overall electronic structure and density of the electronic states in the material.

2.1.9 Raman spectroscopy

Raman spectroscopy is a spectroscopic technique typically used to determine vibrational modes of molecules. Rotational and other low-frequency modes of systems may also be observed. Raman spectroscopy is commonly used in chemistry to provide a structural fingerprint by which molecules can be identified.

2.1.10 UV–visible Spectrophotometry (UV-Vis)

The UV–Vis refers to absorption spectroscopy or reflectance spectroscopy in part of the ultraviolet and the full, adjacent visible regions of the electromagnetic spectrum. UV/Vis spectroscopy is routinely used in analytical chemistry for the quantitative determination of diverse analytes or sample, such as transition metal ions, highly conjugated organic compounds, and biological macromolecules.

2.2 Electrochemical measurements

All the electrochemical measurements were carried out at room temperature.

2.2.1 Battery assembly

Because of the high sensitivity of the lithium, electrolyte and intermediate of polyselenides to O_2 and H_2O in atmosphere, Li-Se battery should be assembled in the glove box full of argon with less than 1 ppm of H_2O and O_2 inside.

2.2.2 Cyclic voltammetry (CV)

CV is an electrochemical technique which measures the current that develops in an electrochemical cell under conditions where voltage is in excess of that predicted by the Nernst equation. CV is

performed by cycling the potential of a working electrode (Fig. 2)[2], and measuring the resulting current. CV is generally used to study the electrochemical properties of an analyte in solution or of a molecule that is adsorbed onto the electrode.

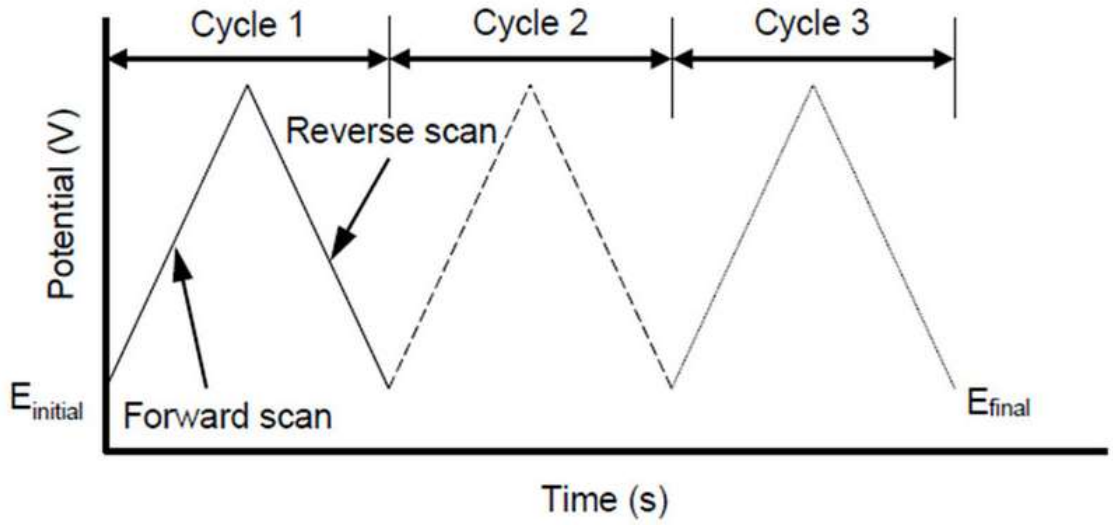

Fig. 2 Typical excitation signal for cyclic voltammetry with a triangular potential waveform.

2.2.3 Electrochemical impedance spectroscopy (EIS)

EIS is a highly sensitive characterization technique used to establish the electrical response of chemical systems in a nondestructive manner. EIS systems characterize the time response of chemical systems using low amplitude alternating current (AC) voltages over a range of frequencies. Quantitative measurements are produced by the EIS and enable the evaluation of small scale chemical mechanisms at the electrode interface and within the electrolytic solution. EIS is useful in determining a wide range of dielectric and electrical properties of components in research fields studying batteries, corrosion, etc.

2.2.4 Galvanostatic intermittent titration technique (GITT)

GITT, a variant of the Electrochemical Energy experiment, is used to determine the chemical diffusion coefficient, as well as thermodynamic information for the active material in the positive electrode.

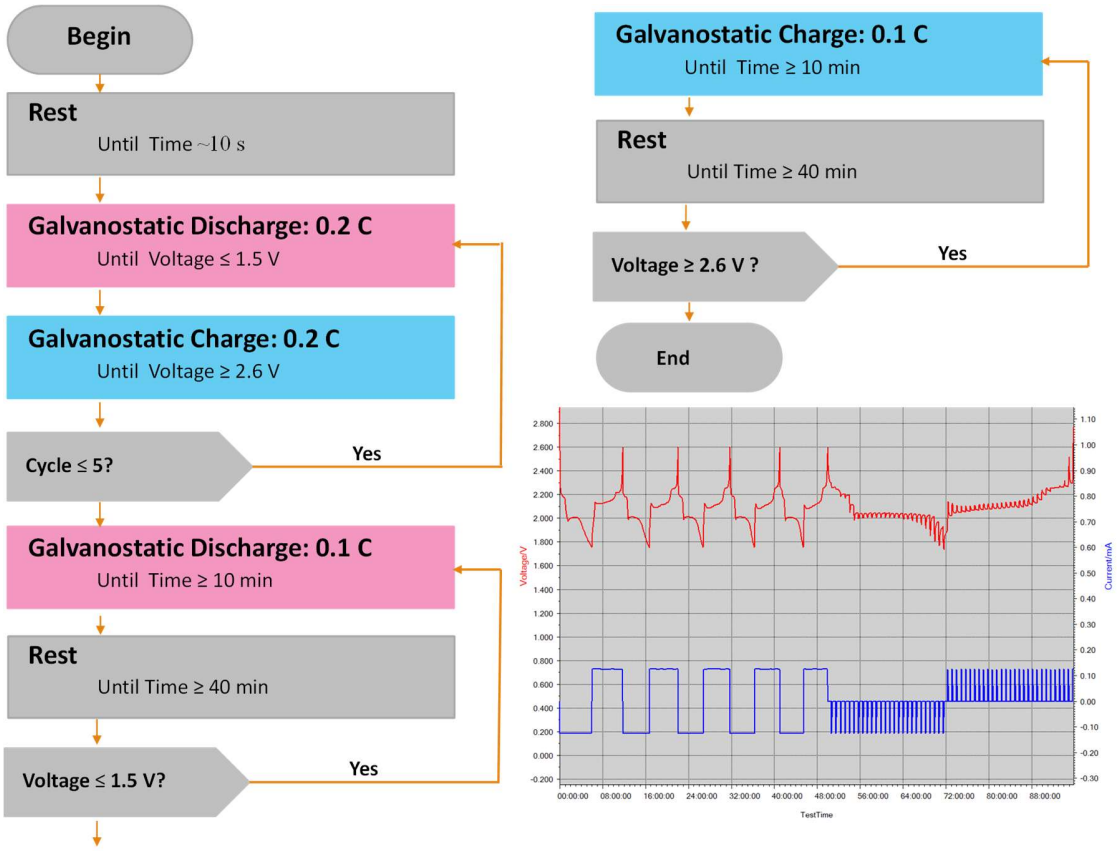

Fig. 3 The program and tested curves of Galvanostatic intermittent titration technique (GITT).

2.2.5 Galvanostatic discharge/charge performance.

In this thesis, the galvanostatic discharge/charge performance includes cycle performance and high rate performance of Li-Se battery. It is used to evaluate the property of the battery. For my Li-Se battery, the voltage range is 1.75-2.6 V and the current value setting is 0.2 C (e.g. 0.2×678 mA/g×weight of active Se). The program is shown below:

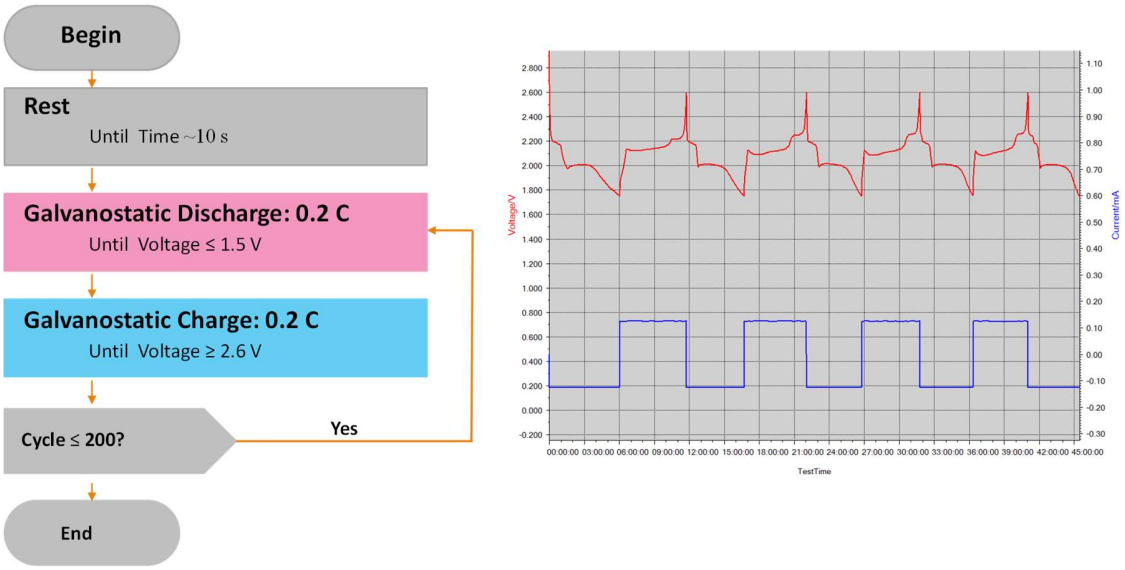

Fig. 4 The program and tested curves of Galvanostatic discharge/charge measurement.

References

[1] Alice V. Llewellyn ,Alessia Matruglio, Dan J. L. Brett, Rhodri Jervis and Paul R. Shearing, Condens. Matter 2020, 5(4), 75, https://doi.org/10.3390/condmat5040075

[2] Chi-yuen Hui, Chi-wai Kan, Chee-leung Mak and Kam-hong Chau, Processes, 2019, 7(12), 922, https://doi.org/10.3390/pr7120922

Chapter IV

Three-dimensional ordered hierarchically porous carbon materials for high performance Li-Se battery

The work described in this chapter has been published in:

H.Y. Li, W.D. Dong, C. Li, J. Energy Chem., 2022, 68, 624-636.

Abstract

Developing host materials with high specific surface area, good electron conductivity, and fast ion transportation channel is critical for high performance lithium-selenium (Li-Se) batteries. Herein, a series of three dimensional ordered hierarchically porous carbon (3D OHPC) materials with micro/meso/macropores are designed and synthesized for Li-Se battery. The porous structure is tuned by following the concept of the generalized Murray's law to facilitate the mass diffusion and reduce ion transport resistance. The optimized 3D Se/OHPC cathode exhibits a very high 2nd discharge capacity of 651 mA h g^{-1} and retains 361 mA h g^{-1} after 200 cycles at 0.2 C. Even at a high current rate of 5 C, the battery still shows a discharge capacity as high as 155 mA h g^{-1}. The improved electrochemical performance is attributed to the synergy effect of the interconnected and well-designed micro, meso and macroporosity while shortened ions diffusion pathways of such Murray materials accelerate its ionic and electronic conductivities leading to the enhanced electrochemical reaction. The diffusivity coefficient in Se/OHPC can reach a very high value of 1.3×10^{-11} cm^2 s^{-1}, much higher than those in single pore size carbon hosts. Their effective volume expansion accommodation capability and reduced dissolution of polyselenides ensure the high stability of the battery. This work, for the first time, established the clear relationship between textural properties of cathode materials and their performance and demonstrates that the concept of the generalized Murray's law can be used as efficient guidance for the rational design and synthesis of advanced hierarchically porous materials and the great potential of 3D OHPC materials as a practical high performance cathode material for Li-Se batteries.

Keywords

3D ordered hierarchically porous carbon (OHPC), Shuttle effect, Cyclability, High rate capability, The generalized Murray's law, Li-Se batteries

1. Introduction

In the past decades, batteries with high capacity and safety have gained considerable attention for their use in portable electronic devices and emerging electric vehicles[1, 2]. The Li-S battery with high theoretical gravimetric capacity (1675 mA h g^{-1}) and volumetric capacity (3467 mA h cm^{-3}) has been widely recognized as one of the ideal candidates for the next generation of Li batteries[3-5]. However, its electrochemical performance is limited by the low conductivity of sulfur and the shuttle phenomenon of polysulfides, as well as the volume expansion caused by the low density of the Li_2S products[6-8].

Selenium (Se), as analogs of sulfur (S), shows a comparable volumetric capacity of 3253 mA h cm^{-3} and a theoretical gravimetric capacity of 675 mA h g^{-1}[9]. Most importantly, Se (1×10^{-3} S m^{-1}) has a much higher electrical conductivity than S (5×10^{-28} S m^{-1}), which is quite beneficial for the transportation of electrons and accelerates the discharge/charge reaction. This makes it a strong alternative to S in Li battery[10-12]. However, similar to S, Se cathodes face the problems of shuttle effect and volume expansion, resulting in fast capacity fading, low coulombic efficiency and the unsatisfactory cycling stability[13-16].

Considerable efforts have been carried out to solve the problems of shuttle effect and the disintegration of Se cathode, mainly focusing on Se dispersion and suppression of shuttle phenomenon of polyselenides. For instance, Fan *et al.*[17] and Kundu *et al.*[18] synthesized Se nanofibers and hollow Se nanospheres, respectively, to relieve volume expansion and increase the Se reaction sites. Li *et al.*[19] used ordered mesoporous carbon (CMK-3) framework and Zhao *et al.*[20] synthesized N, O-doped hierarchically porous carbon as the host material to improve the Se loading and enhance the adsorption of the polyselenides. Li *et al.*[21] decorated CNT-layer on the surface of separator and Gu *et al.*[22] inserted ultra-lightweight N, S-codoped graphene blocking layer to prevent the transportation of polyselenides between Se cathode and separator. All the studies show that the most simple and efficient way is confining Se in a conductive porous framework[23-26]. Pores with different size ranges at different length scale levels possess different functions. Micropores provide active Se loading sites, active reaction centers and confined space to inhibit the dissolution of polyselenides[27, 28]. In addition to loading selenium, mesopores also offer fast ion channels between host and guest that facilitate ion diffusion into micropores[29]. Macropores can considerably improve the diffusion and accessibility of guest ions to the active

sites and offer the volume expansion accommodation capability[30]. Hierarchically micro/meso/macroporous materials spanning three scale levels can overlap the advantages provided by all three levels of pores, making them well suited for Li-Se battery[31-34]. It is well known that for hierarchically porous materials, the pore size distribution and their matching is a very important parameter to achieve high electrochemical performance[35]. It affects the specific surface area as well as the efficiency of ion and electron transport and therefore ultimately determines the electrochemical performance of the material[36]. However, how to combine these advantages in one material and what is the best combination of pore sizes at different length scales to maximize the benefits of the hierarchical structure still remain great challenging.

Most recently, it was found that the ZnO Murray material designed by following the generalized Murray's law facilitates mass exchange and transfer in liquid–solid, gas–solid and electrochemical reactions and performs enhanced properties in photocatalysis, gas sensing, and Li-ion battery electrodes[33-35]. In fact, to achieve transfer and exchange of substance with extremely high efficiency and minimum energy consumption and transport resistance, evolution has endowed many classes of organisms with hierarchically porous networks established following the generalized Murray's law in which the pore sizes regularly decrease across multiple length scales and finally terminate in size-invariant units. Such hierarchically porous systems can offer organisms self-healing and many other complex functions to adapt external environments. This suggests that the generalized Murray's law can be used as guiding principle to rationally design hierarchically porous carbon host for fast transportation of electrolyte and ions. Such system can be expected to avoid the shuttle effect and volume expansion to realize high-performance Li-Se battery.

Here, we optimize the macropore diameter of the hierarchically porous carbon structure following the concept of the generalized Murray's law for high performance Li-Se battery. A series of three dimensional ordered hierarchically porous carbon (3D OHPC) framework materials with tunable size of macropores which are interconnected with meso and micropores are synthesized by dual-templating method by adjusting the 3D ordered macropores inside the OHPC. The diffusion of Se into the micropores can be facilitated and the infiltration of the liquid electrolyte can be accelerated to enhance the ionic conductivity and the contact of electrolyte with the surface of host materials. Meanwhile, the interconnected walls of the whole 3D OHPC framework provide pathways for quick electron transportation. In particular, a large number of micropores provide

sufficient space for Se loading and a large number of reaction sites for the active Se species as well as the physical confinement for polyselenides. This work suggests that rational design by following the concept of the generalized Murray's law can lead to the synthesis of high performance hierarchically porous host for advanced Li-Se batteries.

2. Experimental

2.1. Preparation of 3D OHPC

All chemical reagents were of analytical grade and used without further purification. OHPC materials were prepared as follows: Firstly, uniform polystyrene (PS) spheres with a tunable diameter (50, 100, 150, 200, 400 and 600 nm) were synthesized as soft templates by emulsion polymerization method[36, 37]. The detailed preparation process of PS spheres is described in the supporting information and Fig. 1. Then silica sol (Ludox AS-40 colloidal silica, 22 nm, Alfa Aesar) was added to the synthesized polystyrene suspension as mesopores templates and the resulting solution was stirred for 1 h. Sucrose (Sigma-Aldrich) as a carbon source was then dissolved in the suspension (step 1). After stirring for 10 min, sulfuric acid (Sigma-Aldrich) was added dropwise under stirring. The as-prepared suspension was subsequently moved to oven and dried at 60 °C overnight, then kept at 110 °C for 6 h and 160 °C for another 6 h. The mixture was calcined at 700 °C for 4 h under argon atmosphere with a heating rate of 2 °C min^{-1} (step 2). After cooling down to room temperature, the obtained black powder was firstly etched with hydrofluoric acid (Sigma-Aldrich) to remove silica particles then washed using deionized water until a pH value of 7 was reached (step 3). Finally, the sample was dried at 60 °C overnight to obtain the powder with designed structure.

In order to improve the proportion of micropores, the obtained powder was uniformly mixed with KOH (Sigma-Aldrich) at a weight ratio of 1:2 in an appropriate amount of deionized water. The dried mixture was then activated in a corundum boat under argon atmosphere at 800 °C for 1 h with a heating rate of 2 °C min^{-1}. The mechanism of the KOH activation is shown in supporting information. After cooling down to room temperature, the product was washed with hydrochloric acid (Fisher Scientific) and deionized water to eliminate unreacted KOH until the filtered solution reaches neutrality. Then, the OHPC materials with interconnected micro-meso-macropores and variable macropore sizes were obtained after drying overnight at 60 °C (step 4). For the initial reaction mixture, the mass composition of PS, SiO_2, $C_{12}H_{22}O_{11}$ and H_2SO_4 was 100:15:15:1.5.

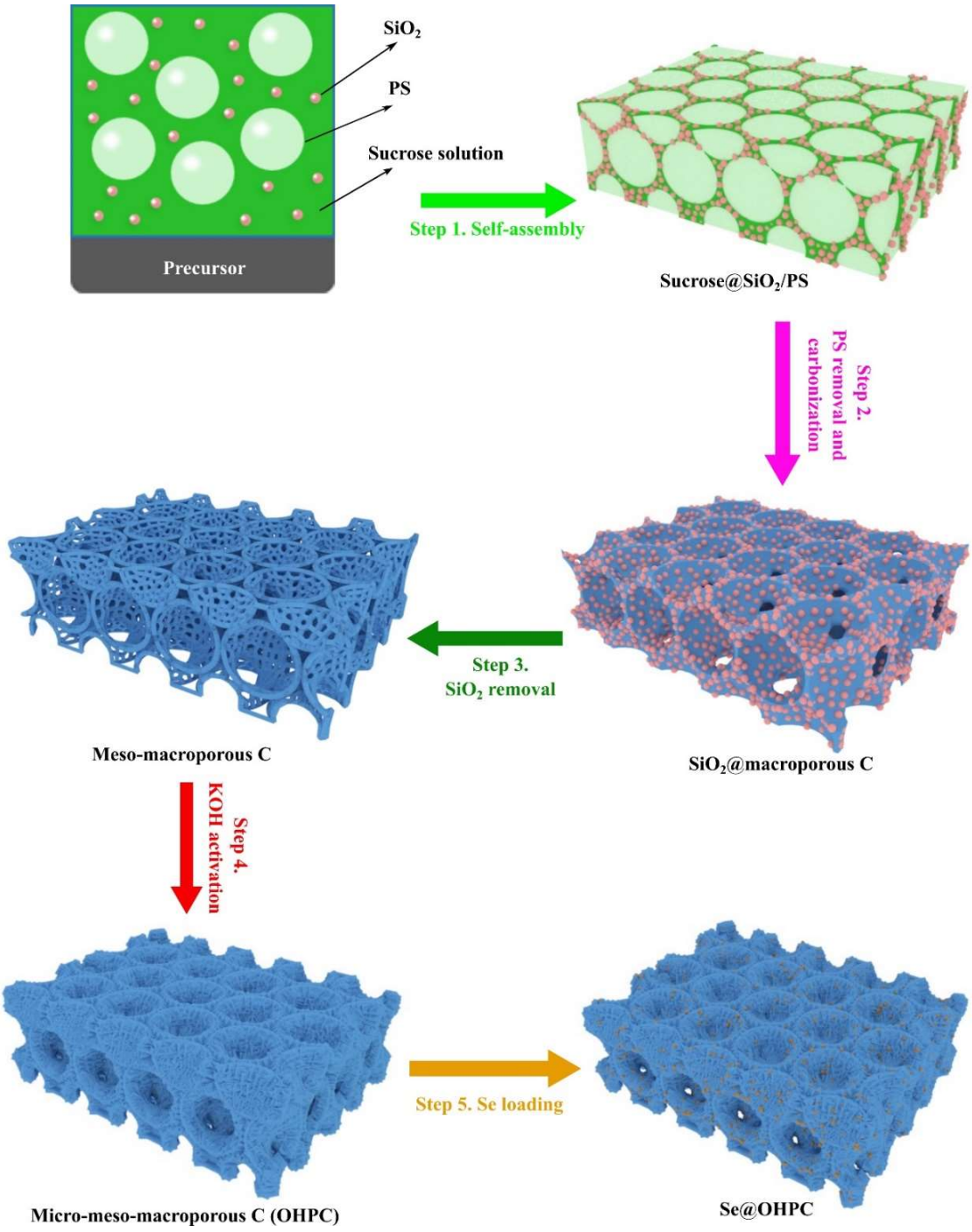

Fig. 1. Schematic illustration of the formation of 3D OHPC.

As reference, carbon materials containing solely microporosity (C-micro), mesoporosity (C-meso) and macroporosity (C-macro) were also prepared using the same process as OHPC, except for the C-micro whose synthesis did not use any template, while the C-meso used only SiO_2 template, and

the C-macro used only PS template size of 100 nm. C-meso and C-macro samples skip the activation process to avoid the generation of micropores and thereby obtained C-meso and C-macro contain either mesopores or macropores. The detailed chemical compositions and the template diameter of different carbon host materials are shown in Table S2.

2.2. Synthesis of Se/OHPC composites

The Se/OHPC composites were fabricated by the melting-diffusion method. The as-prepared OHPC was mixed with Se powder (Sigma-Aldrich) by mortar grinding in a weight ratio of 1:2. Subsequently, the mixture was moved to a tubular furnace and heated at 260 °C for 20 h with a heating rate of 2 °C min^{-1} under argon atmosphere. Then, the temperature was further increased to 300 °C and maintained for another 2 h in order to remove the residual Se on the surface of carbon host materials. After cooling to room temperature, the Se/OHPC composites were obtained (step 5). The reference composites were prepared with the same process and named Se/C-micro, Se/C-meso, and Se/C-macro, respectively.

2.3. Materials characterization

The morphology of carbon host materials and Se/C composites was studied using a field emission scanning electron microscopy (FESEM, JSM-7500F), and microstructure was analyzed by transmission electron microscopy (TEM, Tecnai 10) and high-resolution transmission electron microscopy (HRTEM, Talos F200s). Elemental analysis of the samples was made by energy-dispersive X-ray spectroscopy (EDX). The crystalline phase of the materials was investigated by X-ray diffraction (XRD, PANalytical X'pert Pro) with Cu K_α radiation (λ = 1.5418 Å, 45 kV, 30 mA) between 5° and 90°. The Raman spectra were collected using a Raman microscope (DXR, Thermo Fisher Scientific Inc., USA) with a laser wavelength of 532 nm at room temperature. The Se contents of the Se/C composites were detected by thermogravimetric analysis (TGA, SDT Q600) measurements, where the temperature rose from 25 to 800 °C at a heating rate of 2 °C min^{-1} under nitrogen atmosphere. The Brunauer-Emmett-Teller (BET) surface area and pore size and volume were analyzed by N_2 physisorption using ASAP 2420 apparatus (Micromeritics Instrument Corp., USA) at 77 K. Mesopores and micropores of carbon hosts and corresponding Se/C composites were estimated by the analysis methods of Barrett-Joyner-Halenda (BJH) and Horvath-Kawazoe (H-K), respectively. X-ray photoelectron spectroscopy (XPS) analysis was performed using an AXIS ULTRA DLD (Kratos Analytical Ltd., UK) with a monochromatic Al K_α X-ray source.

Typically, the hydrocarbon C 1*s* line at 284.6 eV from adventitious carbon is used for energy reference.

2.4. Electrochemical measurements

Electrochemical measurements were carried out using CR2032 coin-type cells at room temperature. The Se cathode was prepared by a slurry coating procedure. First, the Se/C composite, carbon black (Super P, Timcal) and water-soluble binder sodium alginate (SA, Sigma-Aldrich) were mixed at a respective weight ratio of 8:1:1. The resulting slurry was coated on current collector aluminum foil and dried in a vacuum oven at 60 °C overnight. Then the coated aluminum foil was cut into discs with a diameter of 14 mm. The mass loading of Se on the electrodes is in the range of 1.5–2 mg cm^{-2}. Coin cells were assembled in an argon-filled glove box (Vigor-SG1200/750TS, LTD, Suzhou), the oxygen and water contents were less than 1 ppm, in which lithium foil as the counter electrode, GF/D borosilicate glass fiber as separator, and commercial 1.0 M LiTFSI in DME/DOL (1:1, *v*/*v* by volume) with 1.0% $LiNO_3$ as electrolyte. Galvanostatic cycling tests were conducted on a Land CT2001A multi-channel battery testing system in the voltage range of 1.75–2.6 V (*vs.* Li^+/Li) at different current rates. Galvanostatic intermittent titration techniques (GITT) were carried out in the same equipment, first performing a discharge for 10 min, then maintaining the interruption for 40 min, continuing the process until the voltage dropped to 1.75 V. Afterwards, the battery was charged with the same process till the voltage reached 2.6 V. Cyclic voltammetry (CV) tests were performed on an LK 2005A electrochemical workstation at 0.1 mV s^{-1} in the voltage range of 1.75–2.6 V. The electrochemical impedance spectroscopy (EIS) was carried out in LK 2005A electrochemical workstation also, in the frequency range of 100 kHz to 0.01 Hz with an AC voltage amplitude of 5 mV. All the electrochemical measurements were carried out at room temperature. After 200 cycles of discharge/charge measurements, the selenium cathode electrodes were disassembled and washed by dimethyl carbonate in an argon-filled glove box, the obtained Se/C materials were analyzed by SEM and XPS.

3. Results and discussion

3.1.Structural analysis

The schematic synthesis procedure of the 3D OHPC materials is illustrated in Fig. 1. The precursor with sucrose and silica sol (hard templates, 22 nm) was introduced into the interstitial

space of opaline structure composed of PS spheres with different sizes ranging from 50 to 600 nm to get OHPC materials with different macropore size (step 1). The micropores are generated by a post treatment using KOH (step 4). SEM image of the opaline structure of highly ordered arrangement of PS spheres as templates with a diameter of 150 nm as representative sample is shown in Fig. S1. After calcination (step 2), etching (step 3) and activation treatment (step 4), the OHPC host materials were obtained and presented an inverse opal structure. The obtained 3D hierarchically porous structure contains interconnected micro-meso-macro porosity at different length scales. Following the concept of generalized Murray's law, the macropore size was adjusted by changing the size of PS spheres to find the best combination of micro-meso-macropore size to achieve the optimal diffusion of substances. The Se/OHPC composites were obtained after infusion of Se into the pores of OHPC via a typical melting-diffusion process (step 5).

The morphology and structure of the as-prepared materials were studied by SEM and TEM, respectively. Fig. 2(a) shows a large-scale SEM image of OHPC-150 as the representative sample, where the ordered "air spheres" and interconnected walls form the 3D inverse opal porous structure. Fig. 2(b) shows a typical inverse opal structure unit. The unit includes macropores with a diameter of 150 nm (created by the removal of PS template), arranged in a close-packed structure. Also, "windows" (green line) with a diameter of 60–80 nm are observed in OHPC. Abundant mesopores with the pore size of ~18 nm are observed in the interconnected walls as revealed in TEM image of OHPC-150 in Fig. 2(c), consistent with the size of SiO_2 colloidal spheres. Fig. 2(d) demonstrates the HRTEM image of OHPC-150, clearly showing the abundant micropores and some graphene-like few layers. The dispersed diffraction rings in the selected area electron diffraction (SAED) pattern reveal the amorphous nature of the carbon host material. Naturally, the interconnected 3D ordered porous structure with micro-, meso-, and macropores provides high specific area and abundant active sites. The SEM and TEM images of C-micro, C-meso, C-macro, and a series of OHPCs are also provided in Figs. S2 and S3, respectively. All OHPC materials (OHPC-50, -100, -150, -200, -400 and -600) exhibit the 3D highly ordered porous structure although the thickness of the interconnected wall, pore size of macroporous "air spheres" and "windows" increase when the diameter of PS spheres varies from 50 to 600 nm. The size of the mesopores remains constant as the size of colloidal SiO_2 used is the same for the synthesis of all these samples. C-micro in Figs. S2(a–c) and S3(a–c) shows a smooth surface, because without using any template all the pores

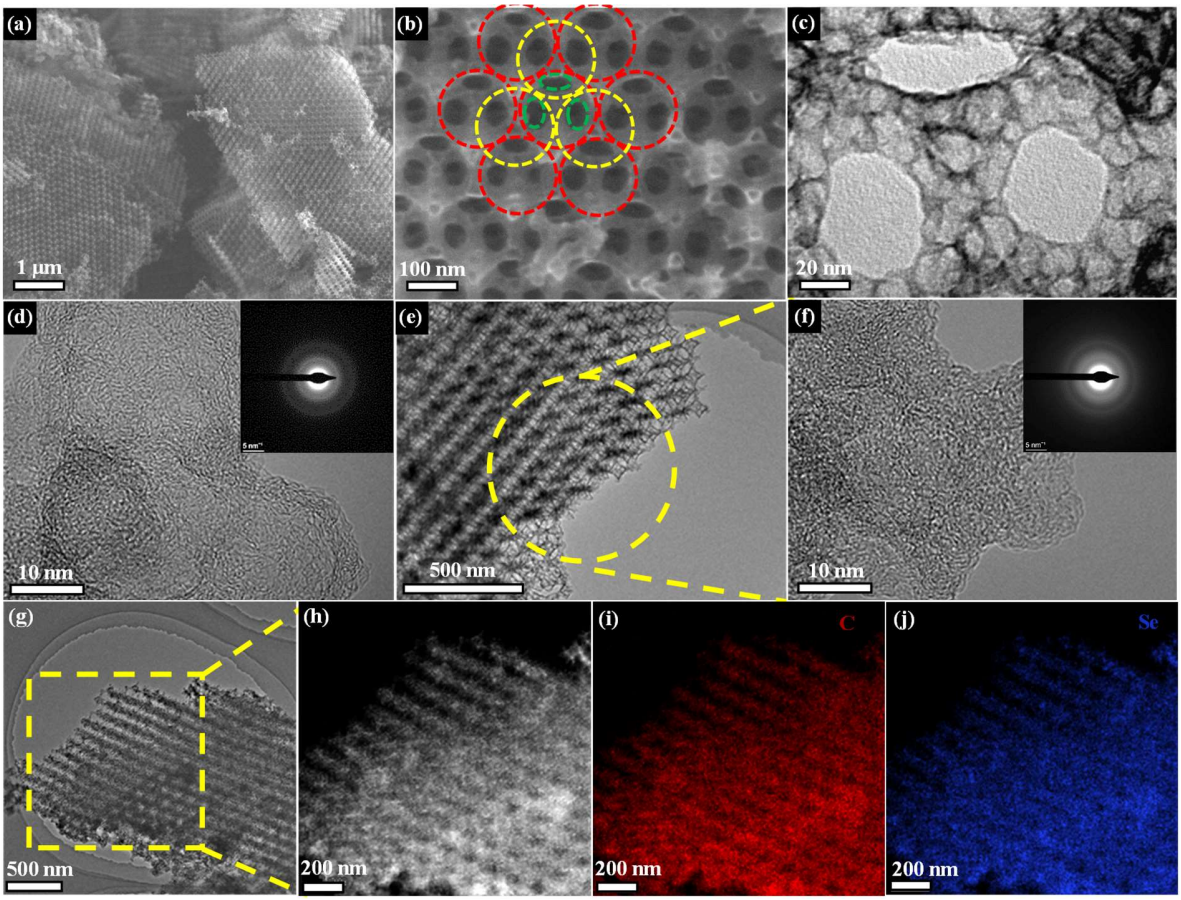

Fig. 2. (a and b) SEM and (c) TEM images of OHPC-150 at different magnifications, (d) HRTEM image and corresponding SAED pattern (inset) of OHPC-150, (e) TEM image of Se/OHPC-150, (f) HRTEM image and corresponding SAED pattern (inset) of Se/OHPC-150, (g) TEM image of Se/OHPC-150, (h) HAADF-STEM image of the area indicated by the yellow box and (i and j) corresponding STEM-EDX elemental maps: C (red), Se (blue).

inside the material are micropores. C-meso in Figs. S2(d–f) and S3(d–f) has a relatively rough surface because there are quantity of mesopores after etching SiO_2. In images of C-macro (Figs. S2g–i and S3g–i), the macropores have highly ordered arrangement, compared with OHPC-100, C-macro displays a thick and tightness interconnected wall due to the lack of micropores and mesopores. Thus, C-micro, C-meso and C-macro samples contain solely micropores, mesopores and macropores, respectively. Ordered OHPC-50, -100, -150, -200, -400, -600 possess micropores and mesopores in addition to macropores whose size increases as the size of PS spheres increases.

The Se/OHPC-150 composite as the representative sample in Fig. 2(e) shows an identical inverse opal structure to that of pure OHPC-150, indicating that the introduction of Se did not

induce structural damage. The HRTEM image of Se/OHPC-150 in Fig. 2(f) shows a more disordered carbon phase and a darker colour than pure OHPC-150 (Fig. 2d), reflecting the encapsulation of Se into the pores of OHPC-150. The inserted SAED pattern proves that the Se is in amorphous state. In contrast, a large number of Se particles with a diameter of 20–30 nm appear on the surface of the Se/C-micro (Fig. S4), indicating that Se remains in clusters and the microporous character of C-micro is unfavorable for a good diffusion and dispersion of Se. The Se state in Se/C-meso and Se/C-macro will be discussed later by the measurements of XRD and Raman. To analyze the amorphous Se distribution in OHPC host materials, Se/OHPC-150 as a representative sample is characterized by STEM-EDX elemental mapping. TEM (Fig. 2g) and HAADF-STEM (Fig. 2h) images confirm well organized OHPC structure after inclusion of Se and corresponding STEM-EDX elemental mapping results (Fig. 2i and j) of Se/OHPC-150 indicate the uniform distribution of Se in OHPC host[38, 39]. Thus, benefiting from the hierarchical pores designed by following the concept of the generalized Murray's law, Se obtains sufficient loading space and small diffusion barriers to be uniformly distributed in the OHPC host material in an amorphous state.

XRD patterns of as-synthesized samples were shown in Fig. 3(a) and Fig. S5(a). Two broad peaks at ~23 and ~43.5° are observed in the XRD pattern of carbon host materials (C-micro, C-meso, C-macro and OHPC), indicating their amorphous nature[40]. Pure Se powder gives strong diffraction peaks belonging to trigonal crystalline phase of selenium [PDF#06-0362]. For Se/C-micro, the peaks belonging to crystalline Se are present with high intensity, reflecting that Se is in trigonal crystalline phase. This result is in good agreement with the SEM observation of Se particles deposited on the surface and diffraction rings appearing in SAED pattern. The micropore size is too small to allow the diffusion of Se. The high intensity of Se peaks in Se/C-macro demonstrates that Se also at least partly presents in form of crystals due to the sole presence of macropores leading to a low surface area and the large pore size for the formation of large particles of Se. However, when Se is introduced to OHPC-100, those characteristic diffraction peaks of crystalline Se completely disappear. The absence of characteristic crystalline Se peaks confirms that benefited from the hierarchically porous structure, Se has already transformed from the crystalline to amorphous state and well infiltrated into the pores of OHPC-100 during the melting diffusion process[41]. The result is consistent well with SAED pattern. The presence of interconnected

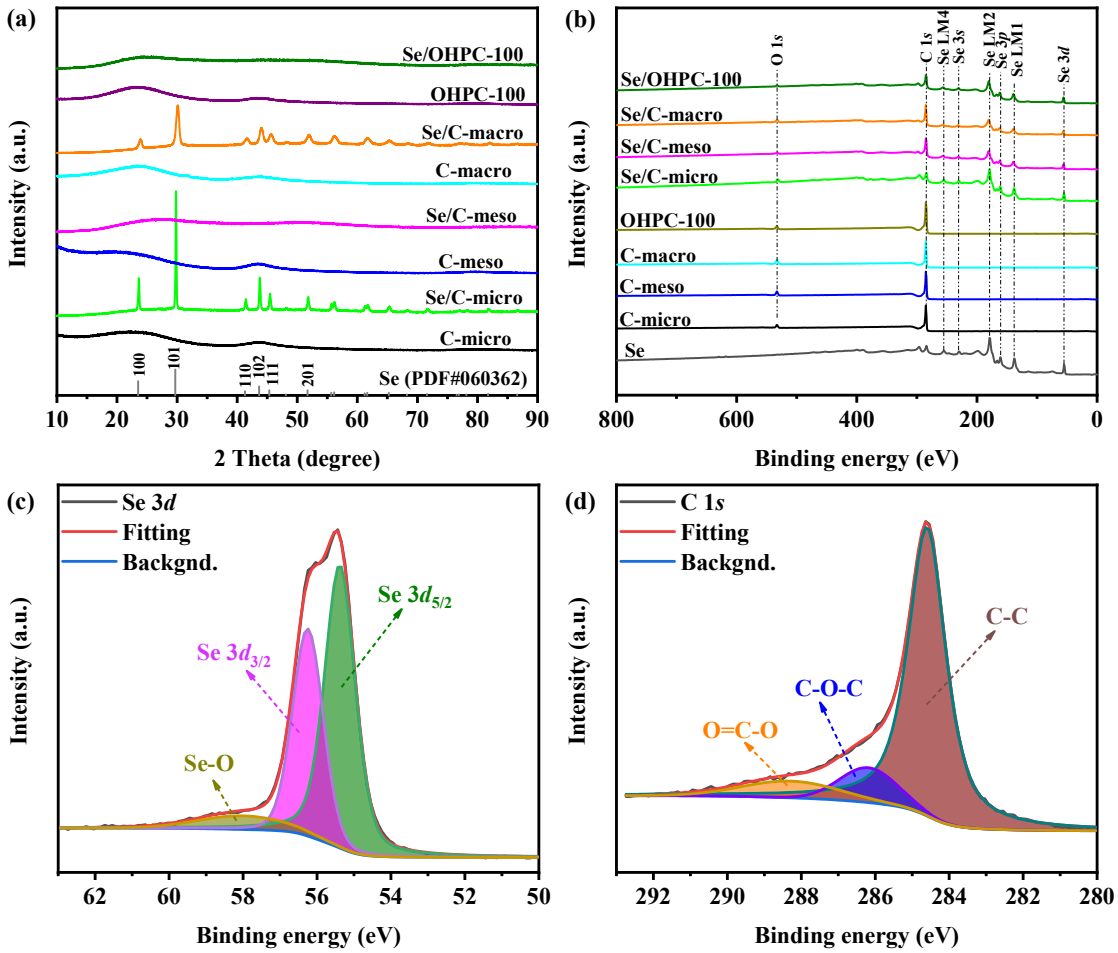

Fig. 3. (a) XRD patterns and (b) XPS spectra survey scan of pristine Se, C-micro, C-meso, C-macro, OHPC-100 and corresponding Se/C composites, (c) Se spectra and (d) C spectra of Se/OHPC-100 composite.

macropores, mesopores and micropores facilitates the dispersion of Se in mesopores and micropores. The XRD pattern of Se/C-meso shows the same observation as Se/OHPC-100, indicating good dispersion of Se in C-meso host material. This result suggests that C-meso has enough high surface area and pore size to allow the good dispersion Se in C-meso host material. XRD pattern of other Se/OHPC (-50, -150, -200, -400, -600) very similar to that of Se/OHPC-100 proves that Se also presents in amorphous nature.

Raman spectroscopy was used to further investigate the structure of Se phase. As shown in Fig. S5(b and c), pristine Se powder exhibits pronounced peaks at 143, 238, and 460 cm^{-1}, which correspond to E0, A1, and 2nd-order modes of trigonal Se composed of helical Se chains, respectively[42]. No characteristic peak of Se is observed in the Se/OHPC and Se/C-meso

composites, which further proves that Se exists in a highly dispersed amorphous state in the pores of OHPC and C-meso, being consistent with XRD results. In contrast, Se/C-micro and Se/C-macro show a strong peak of Se, suggesting that at least part of Se is in the crystal state. Besides, there are two apparent peaks at ~1330 and ~1590 cm^{-1} in the spectra, assigned to the D- and G-bands of carbon, respectively[43, 44]. The D-bands are related to the defected disordered carbon and the G-bands are originated from the typical graphitic sp^2 hybrid carbon atoms[45, 46]. The graphitization degree of the carbon material can be evaluated by the intensity ratio of I_D to I_G, the smaller of the value, the higher of the graphitization degree[47]. The intensity ratio I_D/I_G of all carbon host materials range of 0.97–1.2, indicate a considerable amount of local graphitization in carbon host materials, being beneficial for the conductivity of the materials.

Surface chemical composition and valence states of all the as-prepared carbon host materials and Se/C composites were investigated by XPS measurements. The survey spectra are shown in Fig. 3(b) and Fig. S5(d). The peaks corresponding to elemental selenium are observed in Se/C-micro, Se/C-meso, Se/C-macro and Se/OHPC composites. This again confirms the incorporation of Se in carbon host materials. Fig. 3(c) shows the high-resolution spectrum of Se 3*d* of Se/OHPC-100 composite as representative sample and its fitting results. The two peaks at around 56.24 and 55.37 eV are assigned to the $3d_{3/2}$ and $3d_{5/2}$ electrons of elemental Se. The broad peak at around 58 eV is attributed to Se–O bonds[48]. Simultaneously, C 1*s* spectrum of the Se/OHPC-100 in Fig. 3(d) displays the coexistence of C–O–C, O=C–O and C–C at 286.2, 288.3 and 284.6 eV, respectively[49]. These results indicate that the vast majority of elements of Se and C are in the ground state, and a very small part of these elements inevitably react with or adsorb oxygen during the synthesis process and form valence bonds with oxygen.

The isotherms and the pore size distributions of the C-micro, C-meso, C-macro and all the OHPC carbon host materials and corresponding Se/C composites are given in Fig. 4(a and b), respectively. For a better comparation, the isotherms and the pore size distributions of C-micro, C-meso, C-macro and OHPC-100 as the representative sample of OHPC, are depicted in Fig. 4(c and d), respectively. It is clearly seen that C-micro sample gives a type I isotherm (black curve of Fig. 4c), characteristic of microporous materials[50]. The pore size distribution gives a peak centered at 0.5 nm (black curve of Fig. 4d), indicating the microporous character of C-micro host. C-meso sample shows a type IV isotherm (blue curve of Fig. 4c), characteristics of mesoporous materials. The pore size distribution gives only one peak centered at 18 nm and evidences its mesoporous

character (blue curve of Fig. 4d). C-macro sample gives a type II isotherm (sky blue curve of Fig. 4c), characteristics of macroporous materials[51]. A relative broad pore size distribution over 50 nm (sky blue curve of Fig. 4d) is observed, indicating that C-macro sample contains only macropores. All the OHPC samples show type IV isotherm (violet curve of Fig. 4c) with two hysteresis in the range of $p/p_0 = 0.4–0.9$ and $p/p_0 > 0.9$, indicating clearly the presence of mesopores and macropores in the OHPC samples, respectively[52]. The analysis by H-K method also shows the existence of microporosity at 0.5 nm (Fig. S6). The mesopores and macropores of OHPC-100 situated at 15 and 85 nm (violet curve of Fig. 4d), respectively. These results clearly indicate that the hierarchically porous carbon OHPC host materials with micro, meso and macroporosity and tunable macropore size following the concept of generalized Murray's law are successfully synthesized. The information about pore size of all the carbon host materials is listed in Table S3. The surface area and porous volume of all the carbon host materials are also given in Table S3. It is clearly seen that C-macro material has the lowest surface area and C-micro possesses a good surface area but very low porous volume. Both C-macro and C-micro carbon host materials are not favorable for the

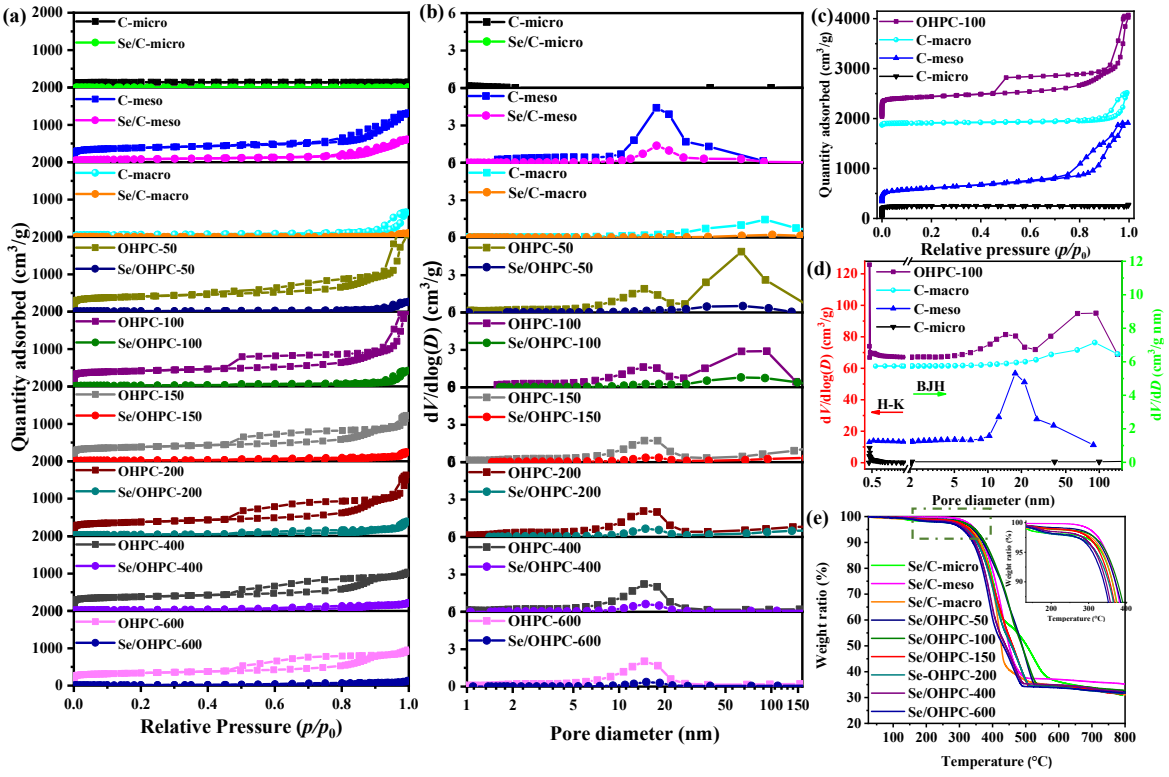

Fig. 4. (a and c) N_2 adsorption-desorption isotherms of all the carbon host and Se/C composites, (b and d) corresponding pore size distribution, (e) TGA curves of various Se/C composites.

inclusion of Se. All the OHPC materials and C-meso give a very high surface area and porous volume, favorable for high Se loading. It is worth noting that increasing PS spheres size, i.e., macropore size of the OHPC carbon host materials, the surface area increases from 1363 $m^2 g^{-1}$ for OHPC-50 to 1391 $m^2 g^{-1}$ for OHPC-100 and then gradually decreases to 1137 $m^2 g^{-1}$ for OHPC-600. After Se loading, all the isotherms except for C-micro sample became type II (Fig. 4a) and the surface area and porous volume sharply decrease (Table S4), showing the very successful dispersion of Se inside of pore structure of carbon host materials.

The weight percentage of Se in the Se/C composites was determined by TGA. The results are shown in Fig. 4(e). From the TGA curves, a very slight initial weight loss of around 1.5% below 150 °C is observed for all the samples, which can be attributed to the evaporation of adsorbed water and moisture[53]. The sharp weight loss observed in Se/C composites between 300 and 500 °C is attributed to the evaporation of loaded Se[54]. The evaporation temperature of Se/C composites is related to the force of physical adsorption of the Se in pores[55]. Thus, it is very interesting to observe that Se/C-micro gives two evident weight losses, one in the zone of 360–430 °C and another in the zone of 430–557 °C. These two weight losses correspond to Se located on the external surface (crystalline) and in the micropores of C-micro host (amorphous), respectively. The turning point (where the evaporation rate of selenium changes) of C-macro appears at the temperature of ~440 °C. Because of the amorphous Se and very good dispersion of Se in Se/C-meso and Se/OHPC, no turning points appear. With increasing macropore size from 50 to 600 nm, the start and end temperature of Se evaporation tend to decrease and achieve the highest start/end temperature with Se/OHPC-100 at 385 and 528 °C for its enhanced physical adsorption. Afterwards, the composite is stable at temperatures up to ~500 °C. The Se loading of the Se/OHPC and Se/C-meso composites quantitatively calculated at ~65 wt%. The high Se content is due to the large specific surface area and pore volume of OHPCs. The mass proportions of Se in Se/C-micro composite is also ~65 wt%. Because of blocking of Se diffusion, partial Se is located on the external surface of carbon materials in Se/C-micro and still remained in crystalline state. The Se loading in Se/C-macro is around 65% while a large part of Se is present in form of crystalline clusters in macropores. All the results obtained from SEM, TEM, XRD, XPS, Raman, TGA and N_2 adsorption-desorption are in excellent agreement. The same mass percentages of Se in all the Se/C composites provide a good reference for comparing the performances of batteries using these different cathode materials.

3.2. Electrochemical properties

The CV measurements were conducted to investigate the reaction process of the Se/C cathodes. Fig. 5(a) shows the CV curves of Se/OHPC-100 as representative samples of Se/OHPC composites for the initial ten cycles in ether-based electrolyte between 1.75 and 2.6 V *vs.* Li^+/Li at a scan rate of 0.1 mV s^{-1}. The curves clearly show two pairs of reversible redox peaks, indicating the occurrence of two-phase transformation reactions during the electrochemical process. The well-defined cathodic peaks in the initial cycle center at 2.13 and 1.94 V, indicating that the reduction of elemental Se to soluble long-chain polyselenides Li_2Se_n ($n \geq 4$), and then further reduction to Li_2Se in the following process[56]. In the delithiation process, two anodic peaks at 2.19 and 2.25 V correspond to the oxidation of Li_2Se to Se with the formation of the intermediate Li_2Se_n[57] In the following cycles of lithiation process, the peak at 2.13 V very slightly shifts to 2.14 V and finally stabilizes at 2.22 V. This shift is possibly due to the formation of SEI layer between cathode and electrolyte as well as the Se activation process in the first few cycles[14, 29]. In the subsequent scans, all the curves overlap well with each other, demonstrating very good reversibility. The galvanostatic discharge/charge voltage curves of Se/OHPC-100 cathode from the 1st to the 200th cycle in the potential range of 1.75–2.6 V at the current density of 0.2 C (1 C = 675 mA g^{-1}) are displayed in Fig. 5(b). All the curves show two discharge/charge platforms, and with the increase of the cycle number, the changing trend of platforms is consistent well with the peaks of CV results. The higher voltage platform in discharge curve corresponds to the reaction of Se to Li_2Se_n ($n \geq 4$). The specific capacity gains a rapid increase at the second platform attributed to the conversion of Li_2Se_n to Li_2Se. The two platforms of charge curves undergo an inverse reaction with discharge process, from Li_2Se to Li_2Se_n and finally back to Se.

The cycling performance of all the different Se/C composites was conducted at a current density of 0.2 C for 200 cycles, as shown in Fig. 5(c). The initial discharge and charge capacity of the Se/OHPC-100 composite is 763 and 711 mA h g^{-1}, respectively, which are higher than the theoretical capacity (675 mA h g^{-1}) for the reason of the occurrence of solid electrolyte interphase (SEI) formation and the irreversible side reaction[14, 58]. It is further proved by the cycle performance of pure OHPC-100 as shown in Fig. S7. With the discharge process progressing, the electrolyte undergoes a reduction on the surface of carbon host at low voltage to form SEI layer[14]. The discharge capacity of the pure OHPC-100 in the first cycle reaches 252 mA h g^{-1}, which

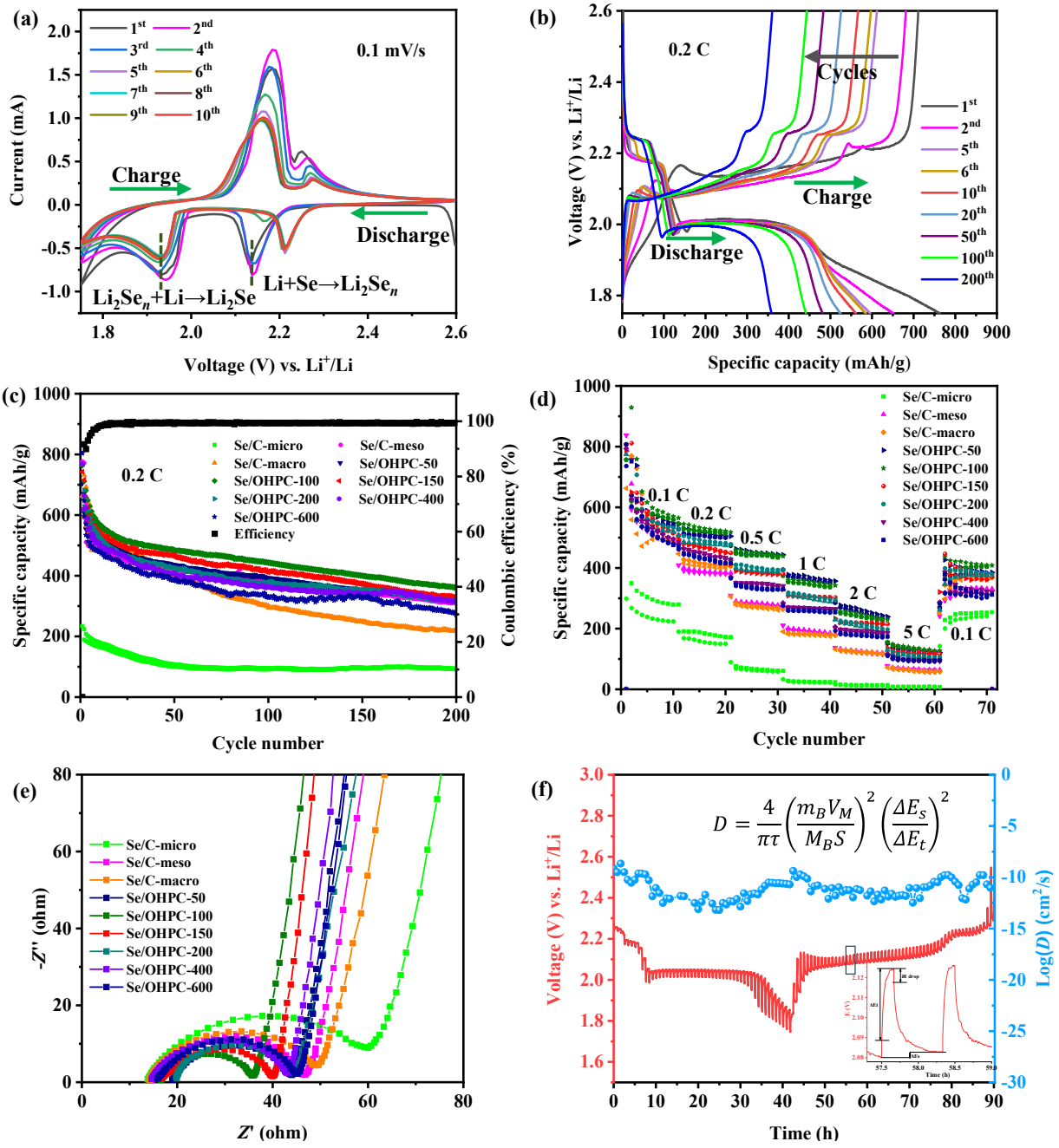

Fig. 5. (a) CV curves of Se/OHPC-100 cathode at a scanning rate of 0.1 mV/s in the voltage range of 1.75–2.6 V vs. Li^+/Li. (b) Galvanostatic discharge/charge profiles of the Se/OHPC-100 composite at 0.2 C. (c) Cycling performance of Se/C cathodes at 0.2 C with coulombic efficiency of Se/OHPC-100. (d) Rate performance of the Se/C cathodes, (e) Nyquist plots of the cells with different Se/C cathode materials, (f) GITT curves in the range of 1.75–2.6 V at 0.1 C and calculated *D* from the GITT data (the inset is the magnification of the framed part).

sharply decreases to 65 mA h g^{-1} due to the formed SEI layer separating electrolyte with cathode which can avoid further electrolyte reduction and the irreversible side reaction. Then, the reversible discharge/charge capacity of pure OHPC-100 stabilizes at ~35 mA h g^{-1} after 10 cycles. Afterwards, the Se is the main contribution to the battery capacity of Se/OHPC-100. The SEI formation can only contribute a little bit to the capacity. The 2^{nd} and 200^{th} cycle discharge capacity of the cathodes is shown in Table S4. Se/C-micro has the lowest capacity and stability because most of the crystalline Se are located at the external surface of C-micro. The formed polyselenides after lithiation can be easily dissolved, leading to the shuttle effect. Se/C-macro has a relatively low capacity accompanied by rapid decay, due to the bulk Se state in the low surface area host material. The 2^{nd} capacity and cycle stability of Se/C-meso achieve great improvement owing to good dispersion of the amorphous Se in mesopores. Compared with the above reference samples, Se/OHPC composites exhibit the enhanced cycle performance due to the contribution of different pores. With the increase of macropores from 50 to 600 nm, the specific capacity of OHPC tends to increase and then decrease, reaching maximum at the size of 100 nm, being in line with the variation in the surface area of the samples. Thus, the Se/OHPC-100 cathode with the highest surface area delivers the highest 2^{nd} discharge capacity of 651 mA h g^{-1}, with the coulombic efficiency of 93%. After 200 cycles, the reversible discharge and charge specific capacity still maintain high values of 360 and 361 mA h g^{-1}, respectively, showing the best cycle stability and a coulomb efficiency almost up to 100%. The result means that hierarchically ordered porous structures have great advantages in improving battery performance and Se/OHPC-100 achieves the highest Se utilization and the fastest charge transfer. To better demonstrate the superior ion diffusion and electron transport advantages of the OHPC host, the high Se loading cathode (~5 mg/cm^2) is assembled and the performance is tested at 0.2 C as shown in Fig. S8(a). It displays that after 50 cycles the capacity of Se/OHPC-100 maintains at 357 mA h g^{-1}, while the Se/C-meso only remains at 58 mA h g^{-1}. This result illustrates the advantages of the structure design that following the concept of the generalized Murray's law for mass transfer.

The rate capability study used to reflect the discharge/charge rate of the battery was carried out from the current of 0.1 to 5 C, and finally come back to the current of 0.1 C. The results are shown in Fig. 5(d) and Table S4. With the increase of the discharge/charge current, the capacity of battery gets lower for the reason of the limitation of charge transfer and polarization. The rate capability of Se/C-micro, Se/C-meso and Se/C-macro is poor due to the limitation of single pore

distribution. While Se/OHPC cathodes show improved rate performance benefiting from the three levels of interconnected pores and display a trend of "volcano" curve as the size of macropores increases. Se/OHPC achieves the best rate capacity at the macropore size of 100 nm. Fig. S8(b) presents the discharge/charge voltage profiles of Se/OHPC-100 at different current densities. Se/OHPC-100 exhibits 2nd cycle capacity of 620 mA h g^{-1} at 0.1 C, even at the high rate of 5 C, the discharge capacity remains at a very high value of 155 mA h g^{-1}. When the current density is tuned back to 0.1 C, the reversible capacity reverses to 404 mA h g^{-1} with a capacity retention of 65%, showing excellent capacity and reversibility. In addition, the battery performance of Se/OHPC-100 and Se/C-meso cathode as the representatives is also tested at higher current rate of 1 C for 200 cycles (Fig. S8c). Again, the capacity of Se/OHPC-100 remains at 200 mA h g^{-1} after 200 cycles, which is much higher than the capacity of Se/C-meso (135 mA h g^{-1}). This further confirms the talents of the OHPC cathode that following the concept of the generalized Murray's law for Li-Se batteries.

The battery performance is strongly related to the interfacial charge transfer and diffusion coefficient in the cathode materials. Thus, EIS measurements of Se/C cathode cells were performed to explore their electrochemical performance. The Nyquist plots of the cells with different Se/C cathodes are shown in Fig. 5(e). The plots consist of a semicircle in the high-frequency region representing the charge-transfer resistance (R_{ct}) at the electrode-electrolyte interface, and a sloping line in the low-frequency region is related to the Warburg diffusion process inside the solid[59]. The calculated R_{ct} values of all Se/C cathodes are given in Table S5. Battery with Se/C-micro and Se/C-macro cathode has large R_{ct} of 49.4 and 34.6 Ω for the bulky Se state and blocked charge transfer kinetics. Due to the existence of large quantity of mesopores, the R_{ct} of Se/C-meso is much smaller, about 31.1 Ω. Se/OHPC achieves further decreased R_{ct} value attributing to the rational hierarchical structure design, and the values of R_{ct} from OHPC-50 to OHPC-600 also perform a "volcano" shape. Se/OHPC-100 has the lowest impedance for the charge transfer (~18.4 Ω), reflecting its fast charge transfer ability, which is extremely important for the utilization of Se.

The galvanostatic intermittent titration technique (GITT) measurement has been widely used as a standard method to evaluate the chemical diffusion coefficients of Li^+ (D_{Li+}) in Li ion battery[60-63]. The surface diffusion of Li_2Se_n species on conductive solid substrates and their rapid electrochemical kinetics conversion can play an important role in Li-Se battery electrochemical performance[64]. Due to the presence of the mixing species (e.g., Li_2Se_n and Li^+)

in the battery, the diffusion coefficient of Li^+ is very hard to ascertain[65]. Although it is very different to get the diffusivity of Li_2Se_n on the surface from the electrochemical measurement, the lithium diffusivity in the whole Li-Se battery has been reported to estimate the important information about Li_2Se_n surface diffusion to some extent[64, 66]. In this work, we have thus used GITT measurement to check the ion diffusion in our materials. The values of D were calculated by the following equation[67]:

$$D = \frac{4}{\pi\tau}\left(\frac{m_B V_M}{M_B S}\right)^2 \left(\frac{\Delta E_s}{\Delta E_t}\right)^2,$$

where τ denotes the constant current interval time, V_M is the molar volume of the selenium material, m_B and M_B are the mass and the molecular weight of the selenium that is infiltrated in the electrode material, S is the contact area of the electrode-electrolyte interface, ΔE_s is the change of the steady-state voltage in a single-step GITT current pulse, ΔE_t is the voltage change during a constant current pulse, eliminating the iR drop (iR: the voltage drop when current flows through an impedance). Fig. S8(d) depicts the specific capacity-voltage GITT curves of representative Se/OHPC-100, which include 10 min of constant current discharge/charge and 40 min of relaxation. The long interruption time is to make sure the battery recovers back to steady state. Fig. 5(f) shows the time-voltage GITT curve of Se/OHPC-100, and the diffusion coefficient of the battery is calculated from this plot. The D value of other Se/C cathodes are calculated in the same way and displayed in Table S5. The Se/C-micro and Se/C-macro have very low value of lithium species diffusion coefficient (7.5×10^{-15} and 3.9×10^{-13} cm^2 s^{-1}) for the lack of diffusion pathway and bulk Se state. The rate of lithium species diffusion has a degree of increase in Se/C-meso due to amorphous Se and interconnected mesopores pathway, but also limited by the channel size. The diffusion coefficient in the Se/OHPC cathodes achieves an accelerated transport and performs an upward and then downward trend. The diffusivity of Se/OHPC-100 exhibits the maximum value of 1.3×10^{-11} cm^2 s^{-1}, showing the best Li^+ as well as the Li_2Se_n diffusion capacity. The enhanced flexibility of Li_2Se_n diffusion and further kinetically accelerates Li_2Se_n redox conversion leading to the low solubility and the low accumulation of intermediate lithium polyselenides, thereby leading to the inhibited shuttle-effect. Benefiting from the optimal cooperation of fast electron transport and excellent lithium species diffusion capability, the Se/OHPC-100 cathode achieves the best electrochemical performance.

To study the impact of long cycling on the structure and morphology of cathodes, SEM images and XPS spectra of the Se/C electrodes (Se/OHPC-100 cathode as representative sample of Se/OHPC) recovered after 200 discharge/charge cycles were recorded and the results are shown in Fig. 6. After 200 cycles, the surface of Se/OHPC-100 cathode (Fig. 6e) still maintains its perfect initial structural integrity and shows an indistinguishable difference in morphology compared with its fresh state (Fig. 6d), implying that OHPC carbon host materials have a very stable structure during cycling. This result also indicates that the active Se is effectively localized into the 3D hierarchically porous carbon network during the lithiation/delithiation process. While for Se/C-meso (Fig. 6b) cathode, a certain degree of structural damage exists and some extra Se particles appear on the electrode surface, reflecting their unstable state in the discharge/charge process. SAED pattern and HRTEM of Se/meso after 200 cycles in Fig. S9 prove that the appeared particles are selenium or polyselenides crystals. The corresponding STEM-EDX elemental mapping reflects large Se or polyselenides particles produced without uniform distribution. The disassembled Se/C-meso cathode after 200 cycles in Fig. 6(c) displays a red colour, indicating the presence of shuttle polyselesides. In contrast, Se/OHPC-100 in Fig. 6(f) shows a slight colour due to the strong adsorption to the polyselenides.

Fig. S10 shows the XPS testing result of the Se, OHPC-100, Se/OHPC-100 composite, and fresh and cycled Se/OHPC-100 cathode. After cycling, the appearance of F 1*s* spectra at 687.5 eV and the increase of O 1*s* intensity indicate the formation of the SEI layer on the surface of the cathode[68]. Fig. S11 presents the Se 3*d* and C 1*s* XPS spectra of fresh and cycled cathode materials, respectively. After 200 cycles, the Se peaks of Se/OHPC (-50, -100, -150, -200, -400, -600) composites in Fig. S11(a) shift to higher binding energy because Li and Se bind together to form Li_2Se[69]. Se/OHPC-100 is selected as the representative sample of Se/OHPC. Its Se 3*d* and C 1*s* spectra are respectively shown in Fig. 6(g and h). The energy of Se $3d_{5/2}$, Se $3d_{3/2}$ and Se-O are shifted 0.1 eV higher after running. Moreover, a new peak appears in the high binding energy regain (~59 eV) in Se 3*d* spectrum, assigned to the formation of Se–C bond from the reaction between Se and electrolyte. The Se–C peak at ~290 eV in C 1*s* spectrum further confirms this reaction[58]. However, the Se 3*d* peaks of C-meso in Fig. S11(a) shift towards lower binding energy, as a result of dissolution of Se and polyselenides[68]. The detail peaks location are displayed in Fig. 6(i), the peaks of Se $3d_{5/2}$, Se $3d_{3/2}$ achieve 0.6 eV lower than the fresh cathode. This reveals polyselenides or Se on the surface of the cathode, consistent with the SEM images in Fig. S9 and

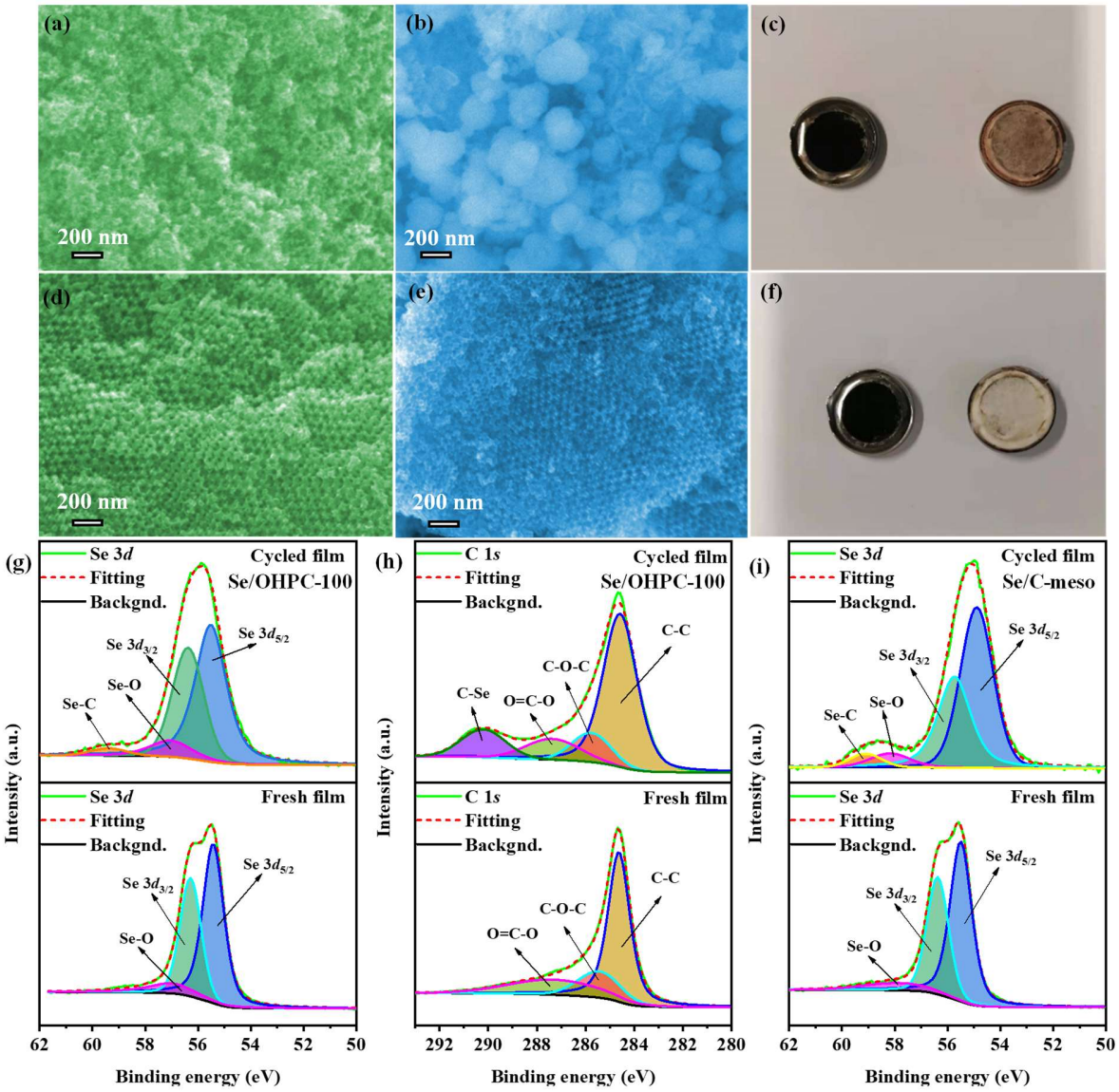

Fig. 6. SEM images of fresh (a and d) and cycled (b and e) cathodes extracted from the Li-Se cells after 200 discharge/charge cycles at 0.2 C. (a and b) Se/C-meso cathode, (d and e) Se/OHPC-100 cathode. Disassembled cells after 200 cycles running: (c) Se/C-meso, (f) Se/OHPC-100. XPS spectra of Se 3*d* (g) and C 1*s* (h) of the fresh (bottom) and cycled (top) Se/OHPC-100 cathode film, (i) Se 3*d* spectra of fresh (bottom) and cycled (top) Se/C-meso cathode film.

picture of Fig. 6(c). The polyselenides in Se/C-meso could explain its poor cycle performance and rate ability.

In order to better understand the relationship between carbon host materials and their performance in battery, all the data are summarized in Fig. 7. C-micro and C-macro possess low

specific surface area and C-meso has an increased surface area. The series of three-scale pores OHPCs with tunable macropore size designed by following the concept of the generalized Murray's law[33-37, 70] have the further improved surface area, and as the size of the macropores increases, the surface area has the trend to increase first and then decrease, achieving the highest surface area value at the size of 100 nm of 1391 m^2 g^{-1}. Moreover, the pore volume of the carbon

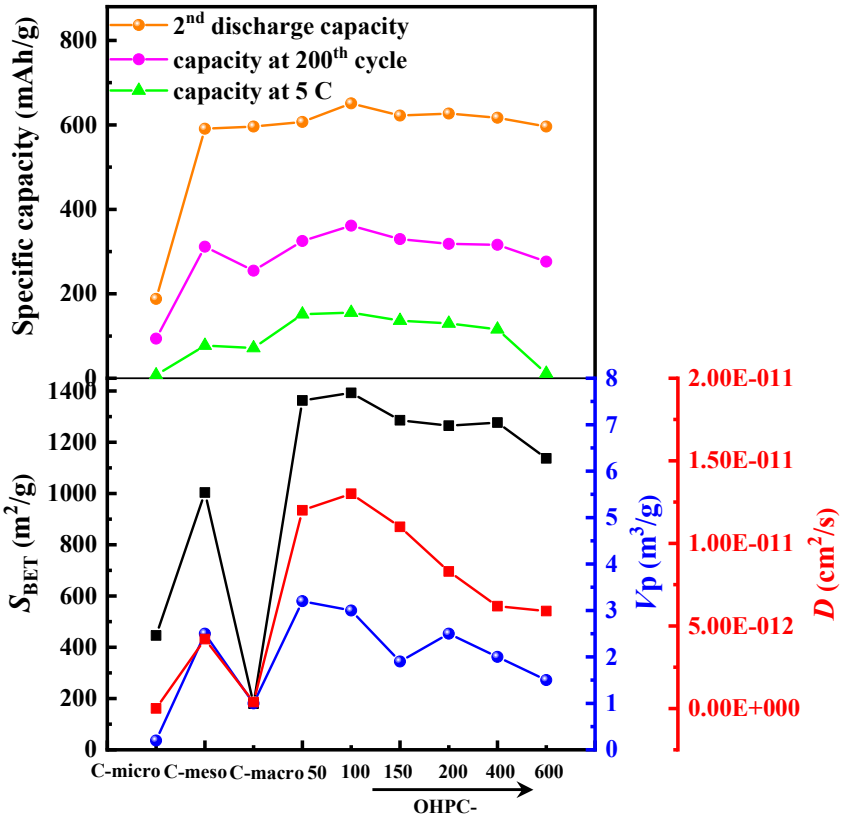

Fig. 7. The summary of the carbon host materials properties and the corresponding Se/C batteries performance (the upper part shows the capacity of the batteries and the bottom part shows the properties of carbon host materials).

host materials has the same tendency. The high surface area and pore volume in addition to the three-scale pores distribution lead to the Se/OHPC batteries achieving the improved performance. The Se/OHPC-100 exhibits the highest 2nd specific capacity, the best stability and rate capacity. OHPC-100 is the material that better follows the generalized Murray's law, which could facilitate the mass transfer of the system, minimum energy consumption and coordinate pores at three length scales to work at the high state of efficiency. The superiority of the OHPC-100 is proved by the diffusion coefficients. C-micro and C-macro have low lithium species diffusion coefficient of 7.5

$\times 10^{-15}$ and 3.9×10^{-13} cm^2 s^{-1}, respectively. The diffusion rate of C-meso has one to two orders of magnitude higher, being 4.2×10^{-12} cm^2 s^{-1}. The series of OHPCs perform a shape of "volcanic" as the size of the macropore increases from 50 to 600 nm and OHPC-100 achieves the rapid mass transfer rate. Although OHPC-600 has the lowest diffusion coefficient among all the OHPCs, it is still higher than C-meso. This proves that the OHPC host materials with micro/meso/macropores designed by following the concept of the generalized Murray's law exhibit better performance than carbon host materials with single size pores.

To better visualize the advantages of the OHPC host materials, the ionic and electronic transportation mechanisms are sketched in Fig. 8. As schematically illustrated, the macropores provide channels for the rapid transportation of Li^+. The micropores and mesopores of OHPC materials provide enough space for the loading of active selenium and their confinement. The continuous thin walls facilitate the rapid transportation of electrons. Given the above results and analysis, the OHPC host materials perform extraordinary high rate capability and improve cycling performance for the reasons: (1) The abundant micropores and mesopores provide confinement effect for Se, which is essential for the stability of the battery. (2) The ordered macropores present many channels in the cathode, acting as reservoirs/highways for Se diffusion, electrolyte impregnation and lithium species transport. (3) The interconnected thin walls enable the rapid

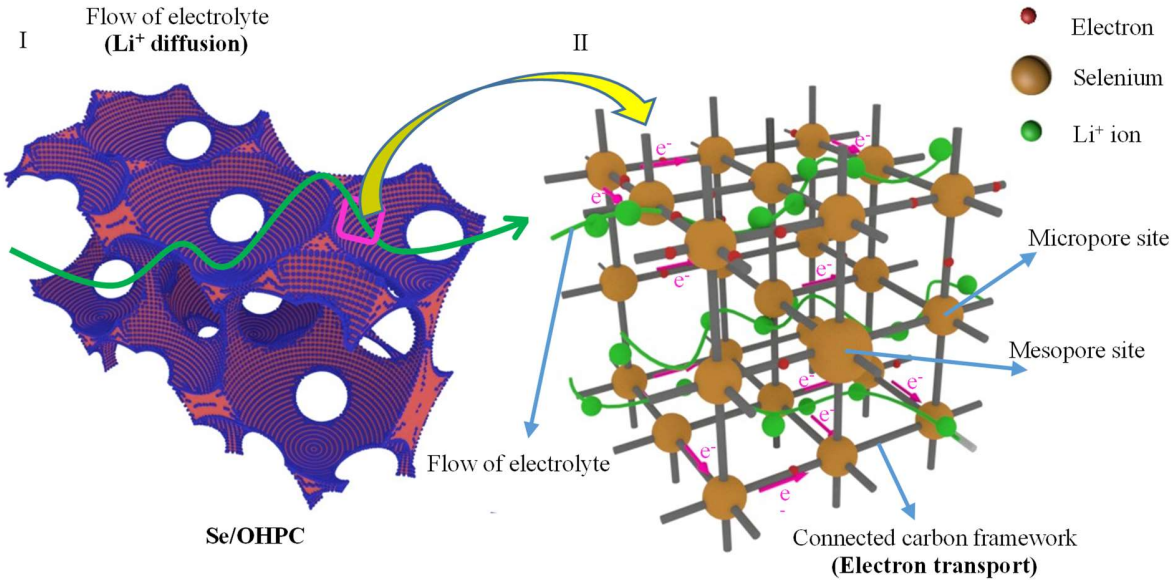

Fig. 8. Schematic illustration for the ion and electron transport in the Se/OHPC composites: (I) macropores and framework, (II) in interconnected walls (mostly mesopores and micropores).

transportation of electrons, beneficial to the full utilization of selenium. On the contrary, C-micro only with micropores is unfavorable for the diffusion pathway of Se and electrolyte, leading to a poor property. As for C-macro cathode, the lack of micropores, mesopores and low surface area leads to the formation of many Se crystallites on the surface of the large size macropores, resulting in the active Se species loss during the reaction process. As providing many mesopores channels, C-meso achieves better electrochemical performance compared with C-micro and C-macro, but is still limited by the diffusion. Therefore, beneficial of the hierarchically porous structure following the concept of the generalized Murray's law[33-37, 70], the stability and rate capacity of the Se/OHPC battery exhibit further improvement. With the macropore size increases from 50 to 600 nm, the property of Se/OHPC has an increase first and then decrease, and achieves the maximum at the size of 100 nm. This means that the structure of OHPC-100 has the most optimized hierarchical structure which follows the generalized Murray's law[33-37, 70], leading to the fastest electron transfer, favorable ion kinetics via the optimal pores size matching, displaying the outstanding performance of high initial specific capacity, long-term cycle life, and excellent rate capability. Thus, porous structures designed by following the concept of the generalized Murray's law have proven to be the most efficient and energy saving in terms of mass exchange and transfer.

4. Conclusion

3D OHPC materials with tunable macropore size designed by following the concept of the generalized Murray's law have been successfully synthesized using a dual-template method. After Se is infiltrated, the obtained Se/OHPC composites with hierarchically porous structure are served as cathode material in Li-Se battery and perform much higher rate performance and ultra-long cyclic stability compared to those based on sole micropores, mesopores or macropores. The Se/OHPC-100 cathode delivers the highest 2nd discharge capacity of 651 mA h g^{-1} at 0.2 C and a prolonged cycle life over 200 cycles, maintaining at 360 mA h g^{-1}. Even at the current of 5 C, it exhibits the discharge capacity of 154 mA h g^{-1}. The high specific capacity and good stability of the Li-Se battery are due to the fact that: (1) the high percentage of micropores and part of mesopores that serve confinement to Se and physical adsorption to polyselenides adsorption, (2) mesopores and macropores constructing diffusion highway channels accelerating ion kinetics and the interconnected walls facilitating the transportation of electrons. The high outstanding performance of Se/OHPC-100 proves that its pores distribution, best following the generalized Murray's law, could maximize the properties for advanced Li-Se battery. This suggests that the

Se/OHPC composites are promising electrode materials for practical application in Li-Se batteries. The strategy here provides the basis for the subsequent structure design and material pore size tailoring for other advanced energy storage systems.

Acknowledgments

H.Y. Li thanks the financial support from the China Scholarship Council (CSC) and a scholarship from the Laboratory of Inorganic Materials Chemistry, Université de Namur, Belgium. The authors thank Prof. Olivier. Deparis for his language assistance in preparing this manuscript. We thank the PC2 technological platform at the University of Namur for access to Power X-ray diffractometer and TGA/DSC. This research used resources of Electron Microscopy Service located at the University of Namur. This service is member of the ‘‘Plateforme Technologique Morphologie Imagerie”. This work was financially supported by the National Postdoctoral Program (Grant No. 2020M672782), the National Natural Science Foundation of China (Grant No. U1663225), the the Program of Introducing Talents of Discipline to Universities National 111 Project from the Ministry of Science and Technology and the Ministry of Education of China (Grant No. B20002), and the National Key R&D Program of China (Grant No. 2016YFA0202602).

References

[1] A. Manthiram, X. Yu, S. Wang, Nat. Rev. Mater 2 (2017) 1-16.

[2] X. Li, J. Liang, X. Li, C. Wang, J. Luo, R. Li, X. Sun, Energy Environ. Sci. 11 (2018) 2828-2832.

[3] M. Xiang, H. Wu, H. Liu, J. Huang, Y. Zheng, L. Yang, P. Jing, Y. Zhang, S. Dou, H. Liu, Adv. Funct. Mater. 27 (2017) 1702573.

[4] N. Zhou, W.D. Dong, Y.J. Zhang, D. Wang, L. Wu, L. Wang, Z.Y. Hu, J. Liu, H. S. H. Mohamed, Y.Li, L.H. Chen, B.L. Su, Sci. China Mater. (2021). doi: 10.1007/s40843-021-1669-9.

[5] W. Dong, D. Wang, X. Li, Y. Yao, X. Zhao, Z. Wang, H.-E. Wang, Y. Li, L. Chen, D. Qian, B.L. Su, J. Energy Chem. 48 (2020) 259-266.

[6] Y. Yu, M. Yan, W.D. Dong, L. Wu, Y.W. Tian, Z. Deng, L.H. Chen, T. Hasan, Y. Li, B.L. Su, Chem. Eng. J. 417 (2021) 129241.

[7] Y. Zhang, X. Liu, L. Wu, W. Dong, F. Xia, L. Chen, N. Zhou, L. Xia, Z.-Y. Hu, J. Liu, H.S.H. Mohamed, Y. Li, Y. Zhao, L. Chen, B.L. Su, J. Mater. Chem. A 8 (2020) 2741-2751.

[8] M. Yan, Y. Zhang, Y. Li, Y. Huo, Y. Yu, C. Wang, J. Jin, L. Chen, T. Hasan, B. Wang, B.L. Su, J. Mater. Chem. A 4 (2016) 9403-9412.

[9] J. He, Y. Chen, W. Lv, K. Wen, P. Li, Z. Wang, W. Zhang, W. Qin, W. He, ACS Energy Lett. 1 (2016) 16-20.

[10] Z.P. Zhuang, X. Dai, W.D. Dong, L.Q. Jiang, L. Wang, C.F. Li, J.X. Yang, L. Wu, Z.Y. Hu, J.Liu, L.H. Chen, Y. Li, B.L. Su, Electrochim. Acta 393 (2021) 139042.

[11] T.C. Mendes, C. Nguyen, A.J. Barlow, P.V. Cherepanov, M. Forsyth, P.C. Howlett, D.R. MacFarlane, Sustain. Energy Fuels 4 (2020) 2322-2332.

[12] W. Dong, H. Chen, F. Xia, W. Yu, J. Song, S. Wu, Z. Deng, Z.-Y. Hu, T. Hasan, Y. Li, H. Wang, L. Chen, B.L. Su, J. Mater. Chem. A 6 (2018) 22790-22797.

[13] X. Gao, X. Yang, S. Wang, Q. Sun, C. Zhao, X. Li, J. Liang, M. Zheng, Y. Zhao, J. Wang, J. Mater. Chem. A 8 (2020) 278-286.

[14] W.D. Dong, C.Y. Wang, C.F. Li, F.J. Xia, W.B. Yu, L. Wu, H.S.H. Mohamed, Z.Y. Hu, J. Liu, L.H. Chen, Y. Li, B.L. Su, Mater. Today Energy 21 (2021) 100808.

[15] Z. Lei, Y. Lei, X. Liang, L. Yang, J. Feng, J. Power Sources 473 (2020) 228611.

[16] X. Li, G. Guo, N. Qin, Z. Deng, Z. Lu, D. Shen, X. Zhao, Y. Li, B.L. Su, H.E. Wang, Nanoscale 10 (2018) 15505-15512.

[17] S. Fan, Y. Zhang, S.H. Li, T.Y. Lan, J.L. Xu, RSC Adv. 7 (2017) 21281-21286.

[18] D. Kundu, F. Krumeich, R. Nesper, J. Power Sources 236 (2013) 112-117.

[19] Z. Li, J. Zhang, H.B. Wu, X.W. Lou, Adv. Energy Mater. 7 (2017) 1700281.

[20] X. Zhao, L. Yin, T. Zhang, M. Zhang, Z. Fang, C. Wang, Y. Wei, G. Chen, D. Zhang, Z. Sun, Nano Energy 49 (2018) 137-146.

[21] J. Li, C. Zhang, C.-J. Wu, Y. Tao, L. Zhang, Q.-H. Yang, Rare Metals 36 (2017) 425-433.

[22] X. Gu, L. Xin, Y. Li, F. Dong, M. Fu, Y. Hou, Nano-micro Lett. 10 (2018) 1-10.

[23] L. Zeng, X. Chen, R. Liu, L. Lin, C. Zheng, L. Xu, F. Luo, Q. Qian, Q. Chen, M. Wei, J. Mater. Chem. A 5 (2017) 22997-23005.

[24] Y.J. Hong, K.C. Roh, Y.C. Kang, J. Mater. Chem. A 6 (2018) 4152-4160.

[25] Y.J. Hong, Y.C. Kang, Carbon 111 (2017) 198-206.

[26] C. Zhao, Z. Hu, J. Luo, Colloids Surf. Physicochem. Eng. Aspects 560 (2019) 69-77.

[27] Y. Liu, L. Si, Y. Du, X. Zhou, Z. Dai, J. Bao, J. Phys. Chem. C 119 (2015) 27316-27321.

[28] W.D. Dong, W.B. Yu, F.J. Xia, L.D. Chen, Y.J. Zhang, H.G. Tan, L. Wu, Z.Y. Hu, H.S. Mohamed, J. Liu, Z. Deng, Y. Li, L.H. Chen, B.L. Su, J. Colloid Interface Sci. 582 (2021) 60-69.

[29] R. Fang, Y. Xia, C. Liang, X. He, H. Huang, Y. Gan, J. Zhang, X. Tao, W. Zhang, J. Mater. Chem. A 6 (2018) 24773-24782.

[30] C. Li, Y. Wang, H. Li, J. Liu, J. Song, L. Fusaro, Z.Y. Hu, Y. Chen, Y. Li, B.L. Su, J. Energy Chem. 59 (2021) 396-404.

[31] M. Jia, S. Lu, Y. Chen, T. Liu, J. Han, B. Shen, X. Wu, S.J. Bao, J. Jiang, M. Xu, J. Power Sources 367 (2017) 17-23.

[32] F. Dai, J. Shen, A. Dailly, M.P. Balogh, P. Lu, L. Yang, J. Xiao, J. Liu, M. Cai, Nano Energy 51 (2018) 668-679.

[33] X. Zheng, G. Shen, C. Wang, Y. Li, D. Dunphy, T. Hasan, C.J. Brinker, B.L. Su, Nat. Commun. 8 (2017) 1-9.

[34] L.H. Chen, Y. Li, B.L. Su, Natl. Sci. Rev. 7 (2020) 1626-1630.

[35] L. Wu, Y. Li, Z. Fu, B.L. Su, Natl. Sci. Rev. 7 (2020) 1667-1701.

[36] M.H. Sun, J. Zhou, Z.Y. Hu, L.H. Chen, L.Y. Li, Y.D. Wang, Z.K. Xie, S. Turner, G. Van Tendeloo, T. Hasan, Matter 3 (2020) 1226-1245.

[37] M.H. Sun, L.H. Chen, S. Yu, Y. Li, X.G. Zhou, Z.Y. Hu, Y.H. Sun, Y. Xu, B.L. Su, Angew. Chem. Int. Ed. 59 (2020) 19582-19591.

[38] J.P. Song, L. Wu, W.D. Dong, C.F. Li, L.H. Chen, X. Dai, C. Li, H. Chen, W. Zou, W.B. Yu, Z.Y. Hu, J. Liu, H.E. Wang, Y. Li, B.L. Su, Nanoscale 11 (2019) 6970-6981.

[39] M. Yan, H. Chen, Y. Yu, H. Zhao, C.F. Li, Z.Y. Hu, P. Wu, L. Chen, H. Wang, D. Peng, H. Gao, T. Hasan, Y. Li, B.L. Su, Adv. Energy Mater. 8 (2018) 1801066.

[40] J. Hu, H. Zhong, X. Yan, L. Zhang, Appl. Surf. Sci. 457 (2018) 705-711.

[41] P. Wu, L.H. Chen, S.S. Xiao, S. Yu, Z. Wang, Y. Li, B.L. Su, Nanoscale 10 (2018) 11861-11868.

[42] J. Zhang, L. Fan, Y. Zhu, Y. Xu, J. Liang, D. Wei, Y. Qian, Nanoscale 6 (2014) 12952-12957.

[43] T. Liu, M. Jia, Y. Zhang, J. Han, Y. Li, S. Bao, D. Liu, J. Jiang, M. Xu, J. Power Sources 341 (2017) 53-59.

[44] J. Zhang, Y. Xu, L. Fan, Y. Zhu, J. Liang, Y. Qian, Nano Energy 13 (2015) 592-600.

[45] C. Zhao, L. Xu, Z. Hu, K. Liu, RSC Adv. 6 (2016) 47486-47490.

[46] H. Chen, W.D. Dong, F.J. Xia, Y.J. Zhang, M. Yan, J.P. Song, W. Zou, Y. Liu, Z.Y. Hu, J. Liu, Y. Li, H.E. Wang, L.H. Chen, B.L. Su, Chem. Eng. J. 381 (2020) 122746.

[47] I. Shlimak, A. Haran, E. Zion, T. Havdala, Y. Kaganovskii, A. Butenko, L. Wolfson, V. Richter, D. Naveh, A. Sharoni, Phys. Rev. B 91 (2015) 045414.

[48] B. Wang, J. Zhang, Z. Xia, M. Fan, C. Lv, G. Tian, X. Li, Nano Res. 11 (2018) 2460-2469.

[49] F.Y. Wei, Y. Liu, H. Zhao, X.N. Ren, J. Liu, T. Hasan, L.H Chen, Y. Li, B.L. Su, Nanoscale 10 (2018) 4515-4522.

[50] L. Qi, X. Tang, Z. Wang, X. Peng, Int. J. Min. Sci. Technol. 27 (2017) 371-377.

[51] F.J. Sotomayor, K.A. Cychosz, M. Thommes, ACC. Mater. Surf. Res 3 (2018) 34-50.

[52] Z. Lyu, D. Xu, L. Yang, R. Che, R. Feng, J. Zhao, Y. Li, Q. Wu, X. Wang, Z. Hu, Nano Energy 12 (2015) 657-665.

[53] J. Zhou, J. Yang, Z. Xu, T. Zhang, Z. Chen, J. Wang, J. Mater. Chem. A 5 (2017) 9350-9357.

[54] J. He, W. Lv, Y. Chen, J. Xiong, K. Wen, C. Xu, W. Zhang, Y. Li, W. Qin, W. He, J. Power Sources 363 (2017) 103-109.

[55] S. Lee, J. Lee, W. Kim, H.J. Kim, C. Pak, J.T. Lee, K. Eom, J. Power Sources 408 (2018) 111-119.

[56] J. Huang, Y. Lin, J. Yu, D. Li, J. Du, B. Yang, C. Li, C. Zhu, J. Xu, Chem. Eng. J. 350 (2018) 411-418.

[57] Y. Cui, A. Abouimrane, J. Lu, T. Bolin, Y. Ren, W. Weng, C. Sun, V.A. Maroni, S.M. Heald, K. Amine, J. Am. Chem. Soc. 135 (2013) 8047-8056.

[58] K. Balakumar, N. Kalaiselvi, Carbon 112 (2017) 79-90.

[59] Y.D. Xu, J. Zhang, Z.G. Wu, C.L. Xu, Y.C. Li, W. Xiang, Y. Wang, Y.J. Zhong, X.D. Guo, H. Chen, Energy Technol. 8 (2020) 1900498.

[60] C. Fu, B.M. Wong, K.N. Bozhilov, J. Guo, Chem. Sci. 7 (2016) 1224-1232.

[61] K.Wang, Y.P. Guan, Z.Q. Jin, W.K.Wang, A.B.Wang, J. Energy Chem. 39 (2019), 249-255.

[62] H. Tian, H.J Tian, S.J Wang, S.M. Chen, F. Zhang, L. Song, H. Liu, J. Liu, G.X Wang, Nat. Commun. 11 (2020) 5025.

[63] X.F. Zhou, L.F. Wang, Y. Yao, Y. Jiang, R. Xu, H.Y. Wang, X.J. Wu, Y. Yu, Adv. Funct. Mater. 30 (2020) 2003871.

[64] P. Wang, F.H. Sun, S.L. Xiong, Z.C.Y Zhang, B. Duan, C.H. Zhang, J.K. Feng, B.J. Xi, Angew. Chem. Int. Ed. (2021) doi: 10.1002/ange.202116048.

[65] X.Y. Tao, J.G.Wang, C. Liu, H.T.Wang, H.B. Yao, G.Y. Zheng, Z.W. Seh, Q.X. Cai, W.Y. Li, G.M. Zhou, C.X. Zu, Yi Cui, Nat. Commun. 7 (2016) 11203.

[66] J. Qian, Y. Xing, Y. Yang, Y. Li, K.X. Yu, W.L. Li, T. Zhao, Y.S. Ye, L. Li, F. Wu, R.J. Chen, Adv. Mater. 33 (2021) 2100810.

[67] K. Shaju, G.S. Rao, B. Chowdari, J. Mater. Chem. 13 (2003) 106-113.

[68] Z. Li, L. Yuan, Z. Yi, Y. Liu, Y. Huang, Nano Energy 9 (2014) 229-236.
[69] L. Sha, P. Gao, X. Ren, Q. Chi, Y. Chen, P. Yang, Chem. Eur. J. 24 (2018) 2151-2156.
[70] B.L. Su, D.Y. Zhao, Natl. Sci. Rev. 7 (2020) 1623-1623.

Supporting Information

Three-Dimensional Ordered Hierarchically Porous Carbon Materials for High Performance Li-Se Battery

Experiment

In a typical synthesis, the styrene without polymerization inhibitor was added into suitable deionized water containing an appropriate amount of sodium laurylsulfonate. After bubbling with the nitrogen gas for 15 min, the mixture was raised to the specified temperature under stirring and kept for half an hour. Subsequently, potassium persulfate was added to the mixture under stirring for a certain time. Reactions were performed under nitrogen atmosphere. A milk-like product containing monodispersed PS spheres was thus obtained. Reaction conditions and reagent quantities are all detailed in Table S1.

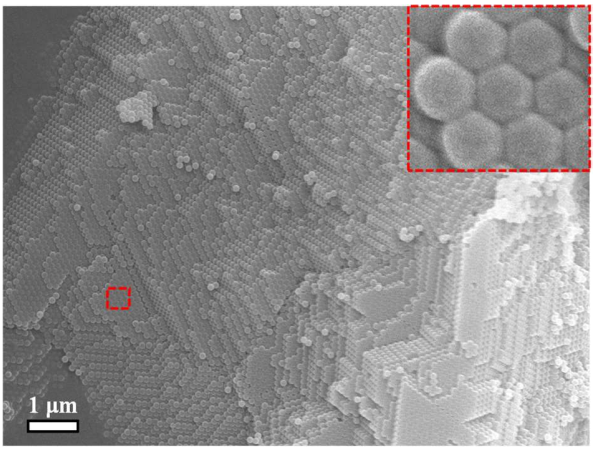

Fig. S1. SEM images of the self-assembly of PS spheres.

The mechanism of the KOH activation:

1) at the temperature (T) range of 400-600 ºC,

$$2C + 6KOH \rightarrow 2K_2CO_3 + 3H_2 \quad (1)$$

2) when the T rise to 600 ºC,

$$K_2CO_3 \rightarrow K_2O + CO_2 \quad (2)$$

$$CO_2 + C \rightarrow 2CO \quad (3)$$

3) when the T over than 700 ºC,

$$K_2CO_3 + 2C \rightarrow 2K + 3CO \quad (4)$$

$$C + K_2O \rightarrow 2K + CO \quad (5)$$

The reactions between C and different chemicals (KOH, CO_2, K_2CO_3, K_2O) form a porous network structure. The generated H_2O and CO_2 can gasify carbon at high temperature to further increase the porosity of the carbon framework. The metal K can interest layer of carbon, leading to irreversible expansion. All the reasons ablow lead to the activation of carbon material with the help of KOH.

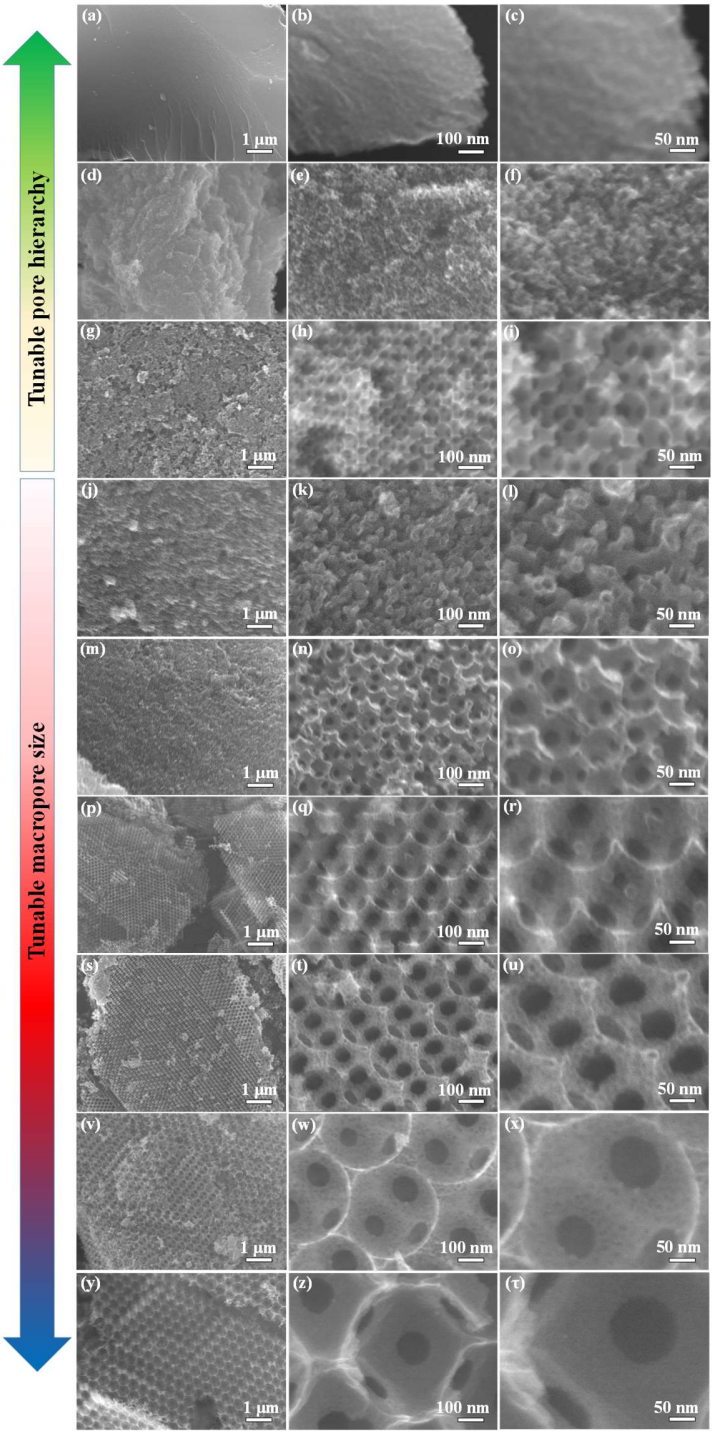

Fig. S2. SEM images of C-micro (a-c), C-meso (d-f), C-macro (g-i), OHPC-50 (j-l), OHPC-100 (m-o), OHPC-150 (p-r), OHPC-200 (s-u), OHPC-400 (v-x) and OHPC-600 (y-τ).

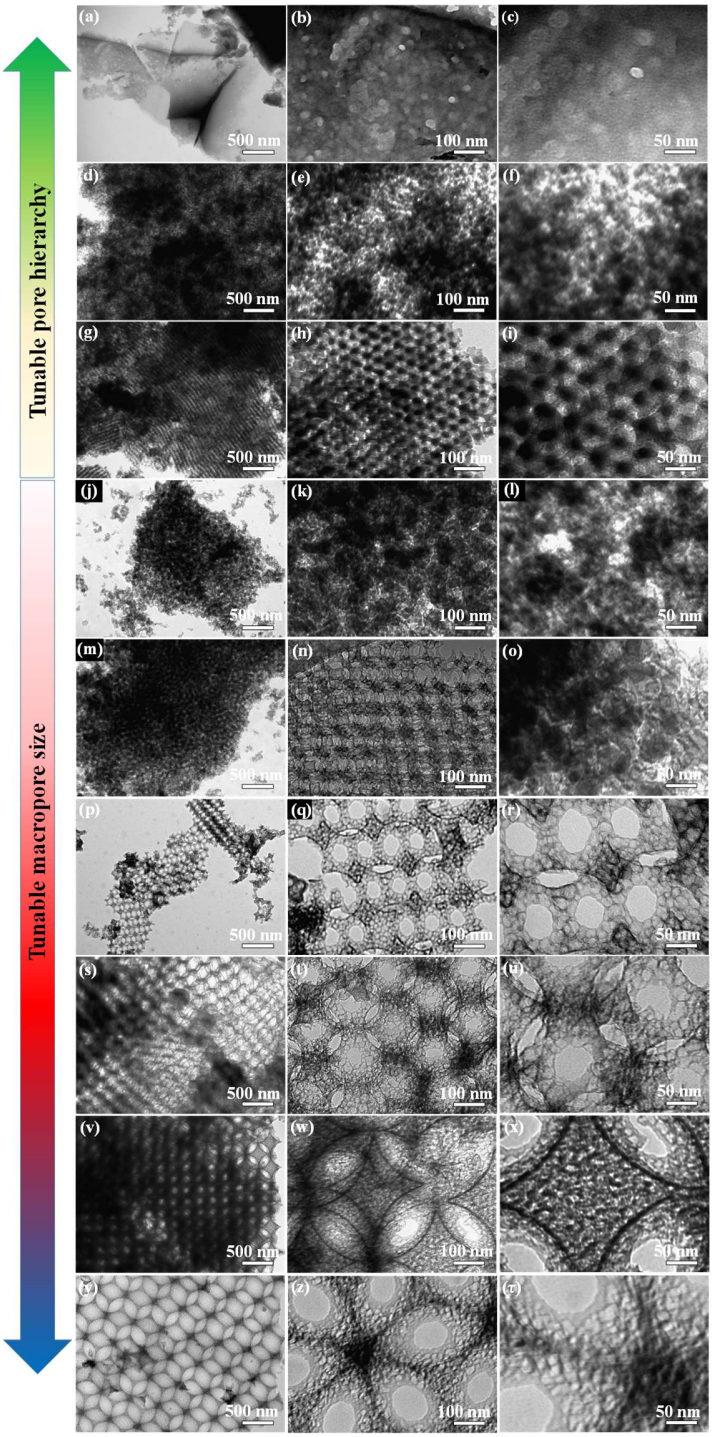

Fig. S3. TEM images of C-micro (a-c), C-meso (d-f), C-macro (g-i), OHPC-50 (j-l), OHPC-100 (m-o), OHPC-150 (p-r), OHPC-200 (s-u), OHPC-400 (v-w) and OHPC-600 (x-τ).

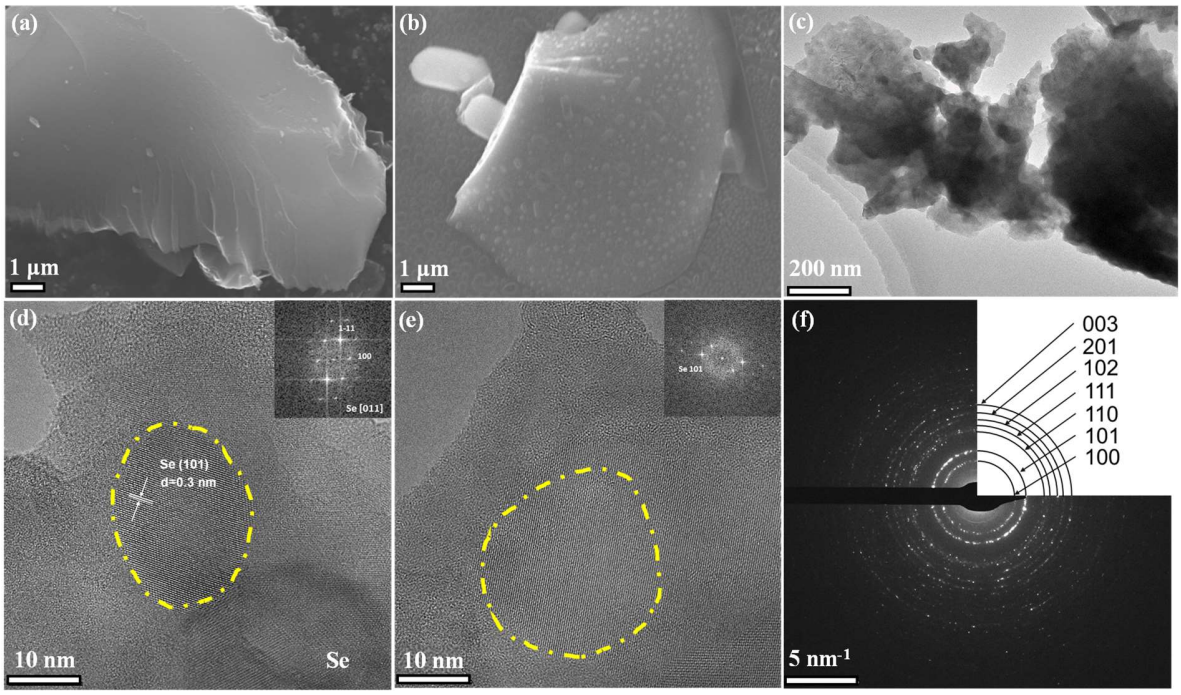

Fig. S4. SEM images of C-micro (a) and Se/C-micro composite (b), TEM (c) and HR-TEM (d and e) images of Se/C-micro (inset FFT pattern) and its corresponding SAED pattern (f).

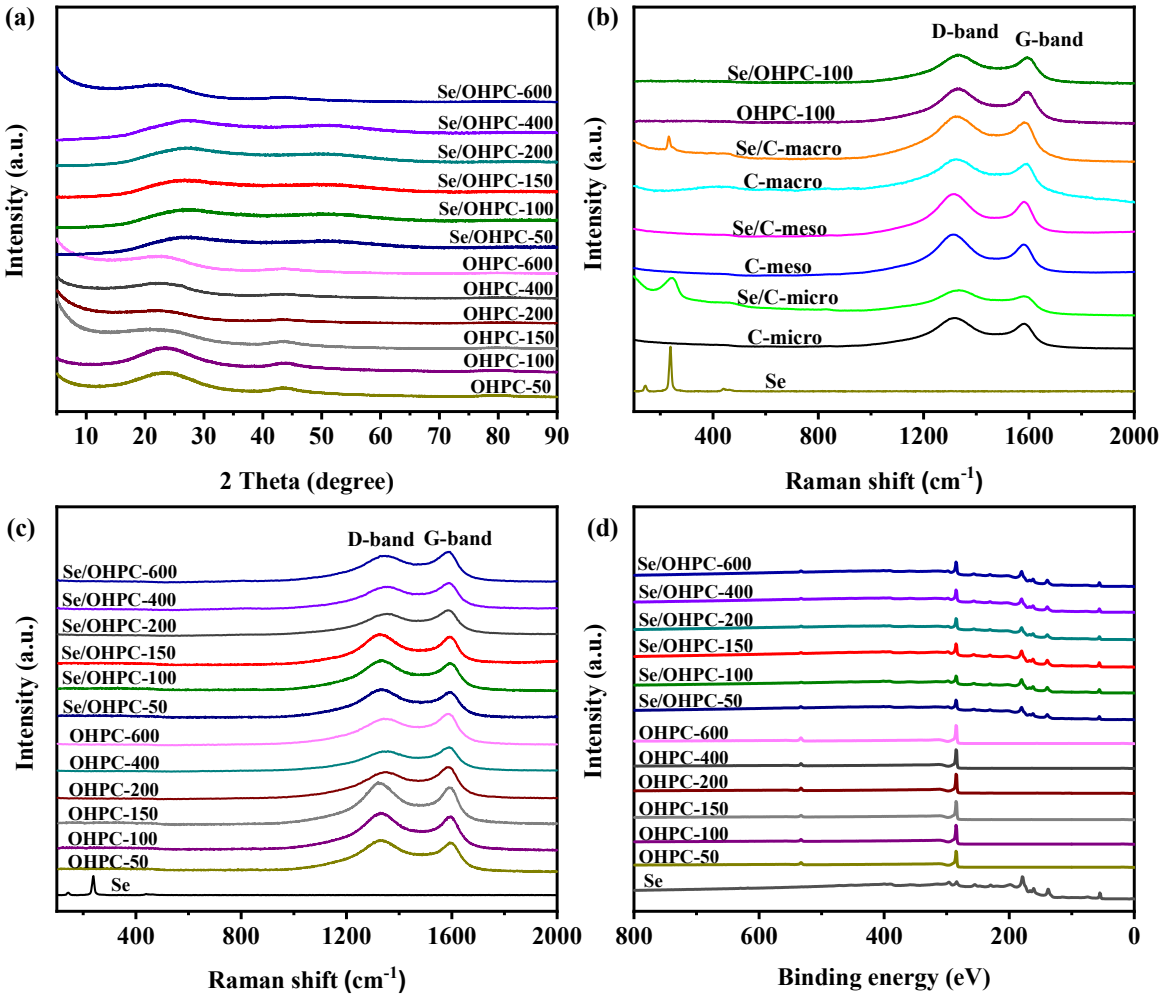

Fig. S5. (a) XRD patterns of OHPCs and Se/OHPC composites, (b) Raman spectra of pristine Se, C-micro, C-meso, C-macro, OHPC-100 and corresponding Se/C composites, (c) Raman spectra and (d) XPS spectrum of OHPCs and Se/OHPC composites.

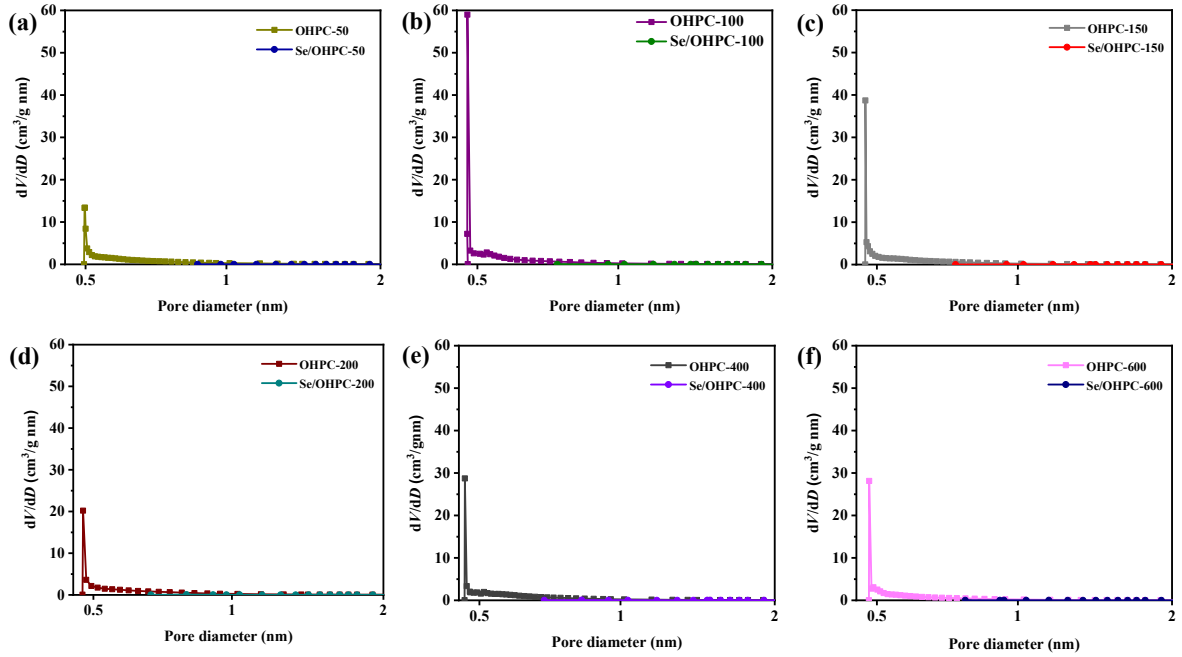

Fig. S6. Micropores size distribution of OHPC host materials and Se/OHPC composites.

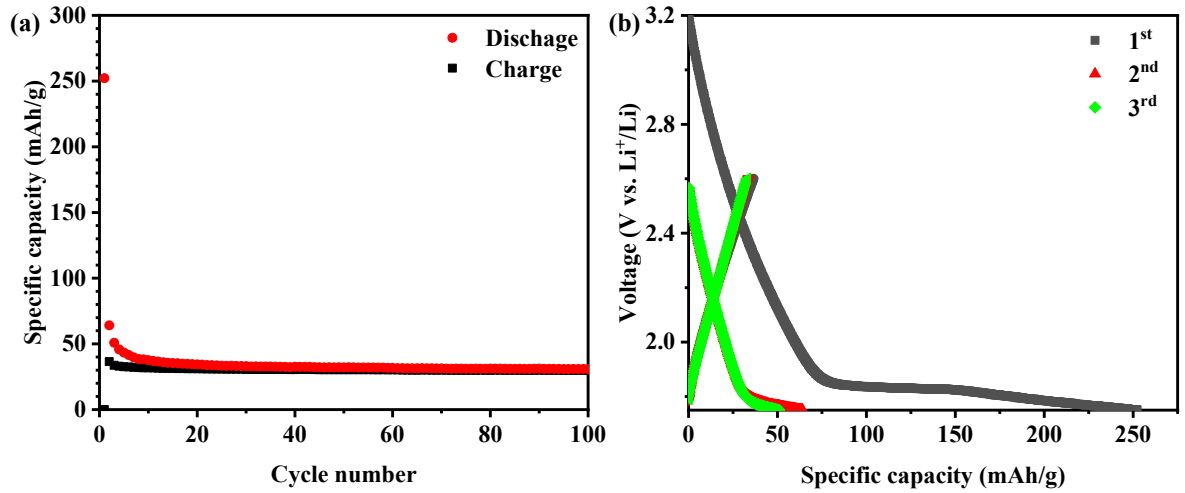

Fig. S7. The cycle performance (a) and Galvanostatic discharge/charge profiles (b) of pure OHPC-100 at the current of 0.2 C.

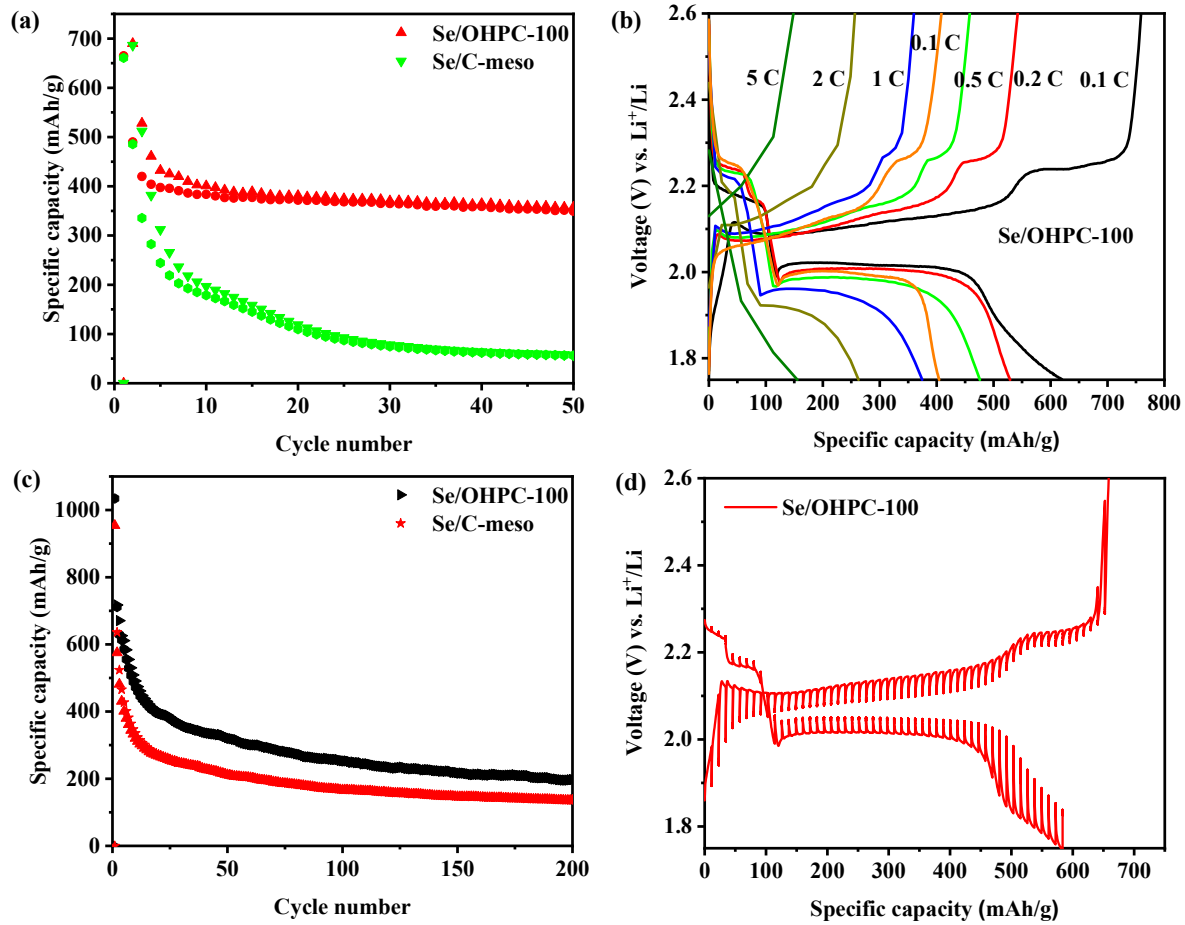

Fig. S8. (a) Cycling performance of Se/OHPC-100 and Se/C-meso cathodes with high Se loading of ~5 mg cm^{-2}, (b) Galvanostatic discharge/charge plots of Se/OHPC-100 at different currents, (c) Cycling performance of Se/OHPC-100 and Se/C-meso cathodes at the high current of 1 C and (d) Discharge/charge GITT curves of Se/OHPC-100 at 0.1 C.

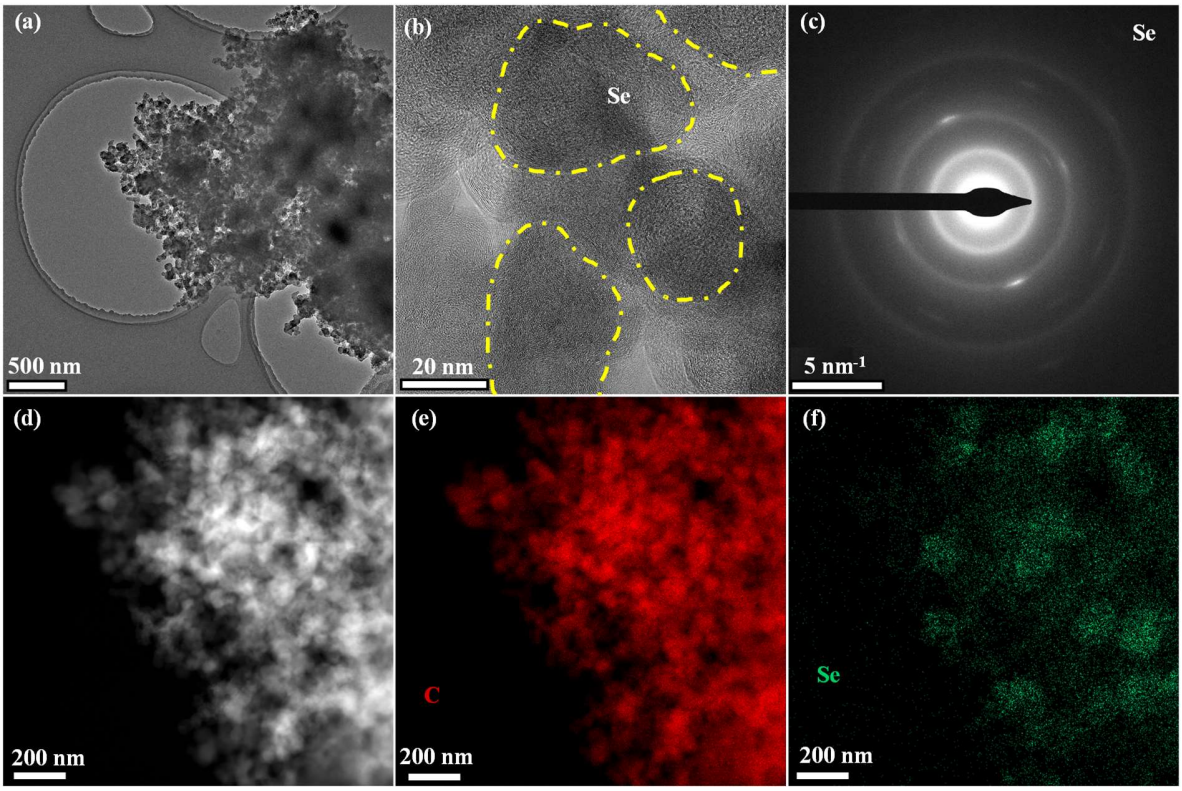

Fig. S9. (a) TEM image, (b) HR-TEM and (c) SAED pattern of Se/meso after 200 cycles, respectively. (d-f) corresponding STEM-EDX elemental maps: C (red), Se (green).

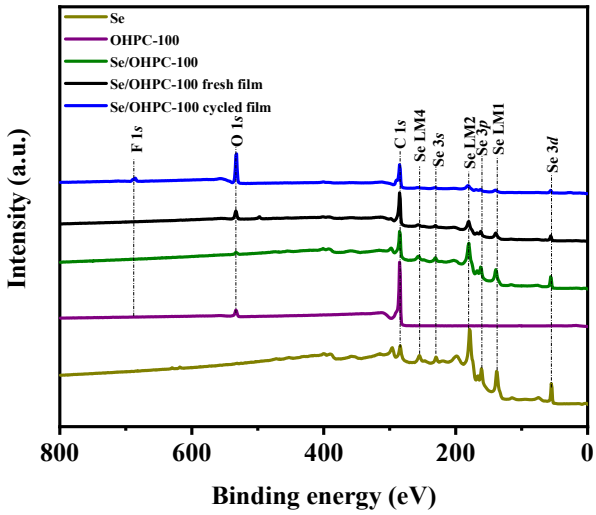

Fig. S10. XPS spectra of Se, OHPC-100, Se/OHPC-100, and corresponding fresh/cycled cathode film.

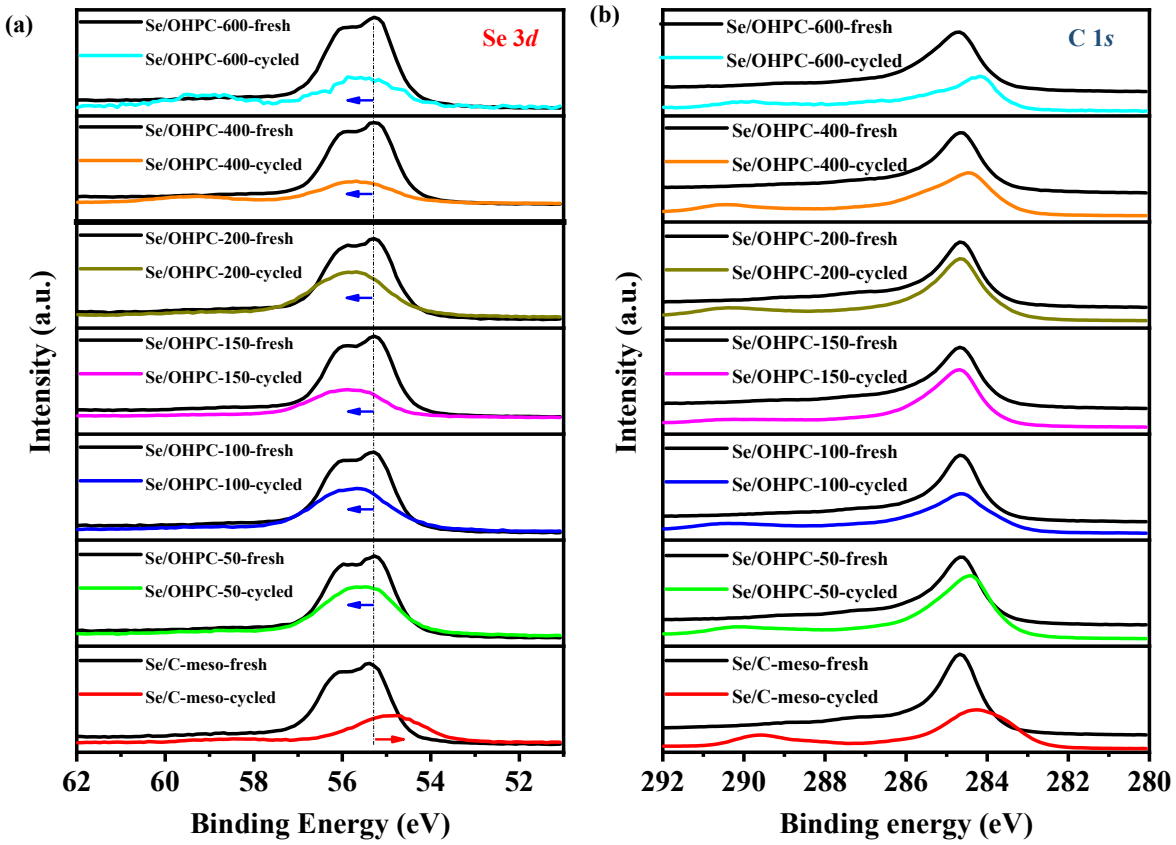

Fig. S11. Comparative XPS spectra of Se/C-meso and series of Se/OHPC: (a) Se 3*d*, (b) C 1*s* spectra of fresh cathode film and 200 cycles later.

Table S1. Variation in polymerization parameters for the preparation of polystyrene spheres with different sizes.

Samples	Deionized water (ml)	Styrene (g)	Sodium laurylsulfonate (g)	Potassium persulfate (g)	Temperature (°C) and time (h)	Average diameter (nm)
PS-50	360	20	0.8	0.6	75, 4.5	50
PS-100	360	30	0.8	0.6	75, 4.5	100
PS-150	360	40	0.6	0.54	75, 4.5	150
PS-200	360	47	0.6	0.5	75, 4.5	200
PS-400	400	47	0	0.43	80, 5	400
PS-600	430	49	0	0.51	70, 11	600

Table S2. Chemical compositions and the template diameter of different carbon host materials.

Samples	Carbon source	Mesopores template and Diameter (nm)	Macropores template and Diameter (nm)	KOH activation
C-micro	Sucrose	without	without	yes
C-meso	Sucrose	SiO_2 (22)	without	no
C-macro	Sucrose	without	PS (100)	no
OHPC-50	Sucrose	SiO_2 (22)	PS (50)	yes
OHPC-100	Sucrose	SiO_2 (22)	PS (100)	yes
OHPC-150	Sucrose	SiO_2 (22)	PS (150)	yes
OHPC-200	Sucrose	SiO_2 (22)	PS (200)	yes
OHPC-400	Sucrose	SiO_2 (22)	PS (400)	yes
OHPC-600	Sucrose	SiO_2 (22)	PS (600)	yes

Table S3. Nitrogen BET adsorption measurements textural properties of carbon host materials and Se/C composites.

Sample	S_{BET} ($m^2 g^{-1}$)	V_P ($cm^3 g^{-1}$)	V_{micro} ($cm^3 g^{-1}$)	D_P (nm)
C-micro	446	0.2	0.21	0.5
C-meso	1004	2.5	-	18
C-macro	180	1.0	-	90
OHPC-50	1363	3.2	0.60	0.5/15/62
OHPC-100	1391	3.2	0.62	0.5/15/85
OHPC-150	1286	1.9	0.55	0.5/16/150*
OHPC-200	1265	2.5	0.55	0.5/16/200*
OHPC-400	1277	2.0	0.57	0.5/16/400*
OHPC-600	1137	1.5	0.50	0.5/15/600*
Se/C-micro	-	0.003	-	-
Se/C-meso	116	0.6	-	18
Se/C-macro	8	0.2	-	89
Se/OHPC-50	50	0.4	0.02	53
Se/OHPC-100	81	0.6	0.03	17/72
Se/OHPC-150	82	0.4	0.03	17/150*
Se/OHPC-200	120	0.6	0.05	16/200*
Se/OHPC-400	99	0.3	0.04	16/400*
Se/OHPC-600	51	0.2	0.02	16/600*

The value with "*" is detected by SEM. There are some "windows" at the size of 60-80 nm in the OHPC host materials, because of their no contribution to the surface area and porous volume, which are not mentioned in the table.

Table S4. The stability and rate capacity of Se/C composite cathodes.

Samples	2nd discharge capacity at 0.2 C (mA h g^{-1})	The capacity of the 200th cycle at 0.2 C (mA h g^{-1})	Rate capacity at 5 C (mA h g^{-1})
Se/C-micro	188	93.9	7.5
Se/C-meso	591	311.6	77.3
Se/C-macro	596	254.6	71.5
Se/OHPC-50	607	325.0	151.6
Se/OHPC-100	651	361.2	155.4
Se/OHPC-150	622	329.6	136.4
Se/OHPC-200	627	318.4	129.8
Se/OHPC-400	617	316.1	115.8
Se/OHPC-600	596	276.1	110.2

Table S5. Charge-transfer resistance (R_{ct}) and D of Li-Se batteries with different Se/C cathodes.

Sample	R_{ct} (Ω)	D ($cm^2 s^{-1}$)
Se/C-micro	49.4	7.5×10^{-15}
Se/C-meso	31.1	4.2×10^{-12}
Se/C-macro	34.6	3.9×10^{-13}
Se/OHPC-50	24.2	1.2×10^{-11}
Se/OHPC-100	18.4	1.3×10^{-11}
Se/OHPC-150	24.1	1.1×10^{-11}
Se/OHPC-200	24.6	8.3×10^{-12}
Se/OHPC-400	29.7	6.2×10^{-12}
Se/OHPC-600	30.4	5.9×10^{-12}

Chapter V

Boosting reaction kinetics and shuttle effect suppression by single-crystal MOF-derived N-doped ordered hierarchically porous carbon for high performance Li-Se battery

The work described in this chapter has been published in:

H.Y. Li, W.D. Dong, C. Li, Sci. China Mater., 2022, 2:8.

Abstract

Maximizing the fixing ability of polyselenides to reduce the shuttle effect in Li-Se battery remains highly challenging. Single-crystal metal-organic framework (MOF)-derived N-doped ordered hierarchically porous carbon (S-NOHPC) synthesized by confined crystal growth and template-assistant method demonstrates excellent electrochemical performance as a host material for Li-Se battery. The large number of micropores inherited from the MOF structure provides large space and surface for Se loading and reaction sites, ensuring the high energy density of the battery. The *in-situ* X-ray diffraction (XRD) technique is used to understand the reaction mechanism. The synergy of the interconnected three-scale-level micro-meso-macroporous structure and N-doped polar sites can buffer the volume expansion, shorten the ions transportation with a very high diffusion coefficient of 4.44×10^{-10} cm^2 s^{-1} and accelerate the lithiation/delithiation reaction. Selenium is sufficiently reactive and the polyselenide intermediates are tightly fixed inside the carbon host material, thereby achieving excellent specific capacity, stability and rate capability. Such a cathode exhibits a very high 2nd discharge/charge capacity of 658 and 683 mA h g^{-1}, respectively, and retains a very high capacity of 367 mA h g^{-1} after 200 cycles at the current of 0.2 C. Even at the high current of 5 C, a very high discharge capacity of 230 mA h g^{-1} is obtained. This work provides a new kind of high-performance porous materials with rational pore arrangement applicable for highly efficient energy storage.

Keywords: Single-crystal MOF, N-doped ordered hierarchically porous carbon, shuttle effect, diffusion coefficient, Li-Se battery

1. Introduction

Lithium-selenium (Li-Se) battery is a prospective candidate for the future energy storage system owing to its small volume, high energy density, and much higher conductivity of Se (1 $\times 10^{-3}$ S m^{-1}) than that of S (5 $\times$ 10^{-28} S m^{-1})[1,2]. Generally, active selenium is confined into the conductive porous structure framework[3,4]. This not only further strengthens its conductivity to improve the utilization of selenium but also enhances the ion transfer, leading to a high performance of Li-Se battery. Among the commonly used frameworks of oxide, nitride, sulfide, and carbon-based materials[5–9], carbon host materials have attracted the most extensive attention owing to their high conductivity, various nanostructures, and easy design of porous systems[10]. However, due to the limitation of the liquid-solid-liquid reaction mechanism, dissolved polyselenides shuttle between the cathode and anode during the discharge/ charge process and will directly react with lithium, resulting in a serious loss of active Se and thus the important capacity decay and poor stability[11].

A series of strategies have been developed to suppress the shuttle effect[12–14]. The strategies of blocking polyselenide shuttle have been applied at each step of the polyselenides' travel path, from tightly confining the polyselenides within the frameworks[15,16], adding a protective layer to prevent their diffusion out of the cathode[17], to introducing an interlayer between the cathode and separator to reduce the diffusion of polyselenides to the anode[18]. Confining the polyselenides inside the frameworks by increasing the adsorption ability to restrict them from traveling out of the cathode is the most remarkable technology to solve the shuttle problem from the sources. Carbonaceous matrixes such as microporous carbon[19], mesoporous carbon[20], hierarchically porous carbon[21, 22], hollow carbon[23], and carbon fibers[24, 25] were designed to increase the physical adsorption of polyselenides by the enlarged surface area and designed porous systems. However, it is well recognized that it is insufficient to suppress the dissolution only by the confinement via the weak physical interaction between the nonpolar carbon host and polar polyselenides. Polar sites such as heteroatom doping (e.g., B, S, N, or P) have a strong interaction with polyselenides[26]. Therefore, introducing heteroatom doping sites into carbon host materials has become another attractive approach to confine polyselenides via chemisorption. For instance, Lv *et al.*[27] proved that the introduced N doping atoms can not only effectively confine the active selenium, but also prevent the dissolution of polyselenides by enhanced interaction between the host material and polyselenides. Zhao *et al.*[28] synthesized hierarchically porous carbon with dual-

doping heteroatoms (N and O) that strongly anchor the Se-containing species by strong chemisorption to reduce the shuttle effect. Mendes *et al.*[29] synthesized a N, S, O tri-doped mesoporous carbon host and achieved good stability. Thus, heteroatom doping is a promising strategy to realize high-performance Li-Se batteries.

Metal-organic framework (MOF) is a kind of organic-inorganic hybrid material with intramolecular pores formed by self-assembly of organic ligands and metal ions or clusters through coordination bonds[30, 31]. The organic ligands are typically multidentate molecules with N- or O-donor atoms, such as pyridyl, polyamines, and carboxylates[32]. However, the original MOFs are insulating, impeding their direct utilization as host materials[33, 34]. The transformation of the low conductive MOFs to well-organized porous and conductive carbon has been largely studied. Moreover, such treatment can simultaneously achieve the in-situ heteroatom doping[35, 36]. For example, Wu *et al.*[37] synthesized ZIF-8-derived carbon polyhedrons for sulfur embedding, which exhibited good cycling stability owing to the dual-physical confinement and strong chemisorption. Liu *et al.*[38] applied the ZIF-8-derived microporous carbon polyhedra in the Li-Se battery. He *et al.*[39] synthesized N-doped graphitic C-Co scaffold (C-Co-N) derived from MOF to immobilize Se via physical/chemical molecular interactions. All of the above host materials delivered superior electrochemical performance. However, as reported, the diameters of most of the pores of MOF materials are within the range of micropores (less than 2 nm), which impedes the efficient Se infiltration and ion transfer in the derived carbon host materials[40, 41]. Thus, constructing a well-organized hierarchically porous system with interconnected mesopores and macropores in N-doped MOF-derived carbon host to break through the limitation of micropore diffusion is essential to improve the battery performance.

We here report the synthesis of a highly ordered N-doped three-dimensional (3D) hierarchically micro-, meso-, and macro-porous carbon host (S-NOHPC) derived from the single-crystal MOF and its excellent electrochemical performance as the host material of Li-Se battery. Owing to the synergy of physical adsorption because of well-controlled porous system and chemisorption induced by N doping, the polyselenides as intermediate products are tightly fixed in the pores of the carbon host material, leading to the highly stable performance in terms of capacity and cycle recoverability of the Li-Se battery. Moreover, the hierarchical pathways constructed by interconnected micro-, meso-, and macro-pores accelerate the transfer of electrolyte and lithium ions, resulting in an improved rate capability. Thus, the Li-Se battery with the Se@S-NOHPC

cathode achieves a very high value of the 2nd discharge capacity of 658 mA h g^{-1} and remains at 367 mA h g^{-1} at 0.2 C after 200 cycles. Even at a high current of 5 C, the discharge capacity can achieve a very high level of 230 mA h g^{-1}. The results indicate that introducing the interconnected hierarchically micro-meso-macroporous structure inside the MOF-derived carbon host material combining N-doped sites has obvious advantages than carbon directly derived from the MOF with sole micropores. Such innovative single-crystal MOF-derived N-doped highly ordered and interconnected hierarchically porous carbon materials have all the characteristics required for high-efficiency surface reaction sites and the rapid mass transfer.

2. Experimental section

2.1 Chemicals: Polyvinyl pyrrolidone (PVP K30, Tokyo Chemical Industry Co. Ltd.), sodium hydroxide (NaOH, 98%, Carl Roth), styrene (C_8H_8, 99%, Aladdin Industrial Corporation), ammonium persulfate ($(NH_4)_2S_2O_8$, 99%, Sinopharm Chemical Reagent Co., Ltd.), silica sol (Ludox HS-30 colloidal silica, Sigma-Aldrich), methanol (CH_3OH, 99%, Carl Roth), zinc nitrate hexahydrate ($Zn(NO_3)_2{\cdot}6H_2O$, 99%, Sigma-Aldrich), 2-methylimidazole ($C_4H_6N_2$, 99%, Acros Organics), ammonia solution ($NH_3.H_2O$, 35%, Fisher scientific), selenium (-100 mesh, ≥99.5%, Sigma-Aldrich). All the chemicals involved in this work were of analytical grade and were used without further purification.

2.2 Preparation of ZIF-8: ZIF-8 was synthesized by using the following procedure[42]. Typically, 3.13 mmol of $Zn(NO_3)_2{\cdot}6H_2O$ and 12.5 mmol of 2-methylimidazole were dissolved in 25 ml of methanol, respectively. The two solutions were mixed and stirred continuously for 1 min, and then aged at room temperature for 24 h. ZIF-8 particles that precipitated in the solution were centrifuged and washed with methanol for several times. The collected powder was dried at 50 °C overnight.

2.3 Synthesis of 3D ordered macro and mesopores (PS/SiO_2) template: The PS/SiO_2 template was fabricated by self-assembly method. The polystyrene (PS) and silica (SiO_2) spheres work as templates for macropores and mesopores, respectively. The synthesis details and the scanning electron microscopy (SEM) image of monodispersed PS spheres (Fig. S1) are displayed in the Supporting information[43]. For the template precursor preparation, 3.75 g of silica sol was added to 100 ml of the synthesized milk-like PS suspension and stirred for 1 h. The dispersion was sonicated for 30 min, and then it was subsequently dried at 60 °C overnight.

2.4 Preparation of ZIF-8@PS/SiO_2 composite: The ZIF-8@PS/SiO_2 composite was synthesized *via* a confined crystal growth method. First, a ZIF-8 precursor solution was prepared by mixing 8.15 g of $Zn(NO_3)_2 \cdot 6H_2O$ and 6.75 g of 2-methylimidazole in 45 ml of methanol and stirring for 15 min. Then, a large piece of PS/SiO_2 template was immersed in the above ZIF-8 precursor solution and kept for 1 h. After that, the mixture was degassed under vacuum pressure of 150-300 hPa for 30 min to ensure that the precursor penetrates the entire template. The obtained ZIF-8 precursor@PS/SiO_2 composite was transferred to a beaker and dried at 50 °C overnight. To induce the growth of the single-crystal ZIF-8, the dried precursor@PS/SiO_2 were soaked into a mixed solution of $CH_3OH/NH_3 \cdot H_2O$ (v/v=1:1) at room temperature. Then, the solution was degassed in vacuum (300-450 hPa) for 10 min to guarantee the adequate permeation of solvent into precursor@PS/SiO_2. After that, the mixture was left at room temperature and atmospheric for 24 h. The obtained ZIF-8@PS/SiO_2 composite was then filtrated, washed with methanol and dried in air. As a reference, the ZIF-8@PS composite where ZIF-8 grows in the inter-space of the ordered macropores template was synthesized with the same process of ZIF-8@PS/SiO_2, except that the immersed template contained only PS spheres.

2.5 Preparation of single-crystal MOF-derived N-doped ordered hierarchically micro-meso-macroporous carbon (S-NOHPC): The S-NOHPC host was obtained by the calcination and etching process. The ZIF-8@PS/SiO_2 composite was calcined at 450 °C for 4 h and then at 800 °C for 3 h under argon atmosphere with a heating rate of 2 °C min^{-1} to achieve PS template removal and ZIF-8 carbonization. After cooling down to room temperature, the obtained black powder was etched by hydrofluoric acid to remove the SiO_2 mesopores template and then washed with deionized water until a neutral pH value was achieved. After drying overnight at 60 °C, the S-NOHPC with the designed structure was obtained. Two reference samples, single-crystal MOF-derived N-doped microporous carbon (S-NMC) and single-crystal MOF-derived N-doped micro-macroporous carbon (S-NOMMC), without addition of SiO_2 colloids to create mesoporosity, were prepared after the calcination of ZIF-8 and ZIF-8@PS, respectively. The template used in the synthesis process and the pores inside the different carbon host materials are shown in Table S1.

2.6 Synthesis of Se@S-NOHPC composites: The Se@S-NOHPC composite was fabricated by the melting-diffusion method. The as-prepared S-NOHPC host material and Se powder were mixed by mortar grinding with a mass ratio of 1:2. Subsequently, the mixture was heated at 260 °C for 20 h at a ramp rate of 2 °C min^{-1} under an argon atmosphere in a tubular furnace. The temperature was

further increased to 300 °C and purged for another 2 h in order to remove the residual Se on the surface of carbon host materials. After cooling down to room temperature, the Se@S-NOHPC composite was obtained. For comparison, S-NMC and S-NOMMC were treated with the same process, and the corresponding products were named Se@S-NMC and Se@S-NOMMC, respectively.

2.7 Visualized Li_2Se_6 adsorption experiments: First, the Li_2Se_6 solution (2 mmol L^{-1}) was prepared by mixing Li_2Se and Se with a molar ratio of 1:5 in 1,3-dioxolane/1,2-dimethoxyethane (DOL/DME) mixture (*v:v* = 1:1) and magnetic stirring at 60 °C for 24 h. Then, 20 mg of host materials (S-NOHPC, S-NOMMC and S-NMC) that dried at 60 °C for overnight were separately added to 10 ml Li_2Se_6 solution. After stirring for 2 min, the mixtures were stewing 24 h in glovebox.

2.8 Materials characterization

The morphology of the synthesized carbon host materials and their corresponding Se/C composites was investigated by field emission scanning electron microscopy (FESEM, JSM-7500F) and transmission electron microscopy (TEM, Tecnai 10). Microstructure and crystallization were studied by high-resolution transmission electron microscopy (HRTEM, talos F200s) and selected area electron diffraction (SAED). Energy-dispersive X-ray spectroscopy (EDX) was used to detect the elemental distribution states of the samples. The crystalline phase were investigated by X-ray diffraction (XRD, PANalytical X'pert Pro) with Cu Kα radiation (λ=1.5418 Å). The *in-situ* XRD was carried out in STOE STADI-MP powder diffractometer with Cu $K\alpha_1$ radiation (λ=1.54056 Å) in Bragg–Brentano geometry. The thermogravimetric analysis (TGA, SDT Q600) measurements were carried out to measure the Se content in the Se/C composites, where the temperature rose from 25 to 800 °C at a heating rate of 2 °C min^{-1} under nitrogen atmosphere. N_2 physisorption was carried out (ASAP 2420 apparatus, Micromeritics Instrument Corp., USA) at 77 K to analyze the Brunauer-Emmett-Teller (BET) surface area and pore size distribution. The pore size distribution ranges of micropores and mesopores were calculated by the analysis methods of Barrett-Joyner-Halenda (BJH) and Horvath-Kawazoe (H-K), respectively. X-ray photoelectron spectroscopy (XPS) analysis was performed in an Axis Ultra DLD (Kratos Analytical Ltd., UK) with a monochromatic Al Kα X-ray radiation to study the species and chemical states of the main elements in the synthesized samples. The absorbance of Li_2Se_6 was detected by an ultraviolet-visible (UV–vis) spectrophotometer (Shimadzu UV-1700, Japan) with the wavelength of 250-700 nm.

2.9 Electrochemical measurements

The CR2032 coin-type cells were assembled in an Ar-filled glove box (O_2 and H_2O<1 ppm, Vigor-SG1200/750TS, LTD, Suzhou) for the electrochemical measurements. The cell was constructed with lithium foil anode, selenium cathode, Whatman glass microfiber filters (GF/D) separator, and commercial 1.0 mol L^{-1} LiTFSI in DME/DOL (1:1, v/v by volume) with 1.0% $LiNO_3$ electrolyte. The Se cathode was prepared by coating the slurry that was prepared by mixing Se/C composite, carbon black (Super P, Timcal) and water-soluble binder sodium alginate (SA, Sigma-Aldrich) at a mass ratio of 8:1:1 on the aluminum current collector and vacuum drying overnight at 60 °C. Then, the obtained Se cathode was cut into discs with a diameter of 14 mm. The cyclic voltammetry (CV) experiments were performed on an LK 2005A electrochemical workstation at 0.1 mV s^{-1} in the voltage range of 1.5–2.6 V *vs.* Li^+/Li. The electrochemical impedance spectroscopy (EIS) was carried out on the same workstation in the frequency range of 100 kHz–0.01 Hz with an alternating current (AC) voltage amplitude of 5 mV. Galvanostatic discharge/charge measurements were conducted on a Land CT2001A multi-channel battery testing system in the voltage range of 1.5–2.6 V (*vs.* Li^+/Li) at different constant current densities. The galvanostatic intermittent titration technique (GITT) measurement was also carried out on the Land CT2001A multi-channel battery testing system. In detail, after 5 cycles of activation and stabilization, the battery was discharged at 0.1 C for 10 min, following by 40 min relaxing, and the process was repeated until the voltage drops to 1.5 V. Afterwards, the battery was charged to 2.6 V with the same process. All the electrochemical measurements were carried out at room temperature.

3. Results and discussion

3.1 Structural analysis

The preparation procedure of the highly ordered S-NOHPC and corresponding Se@S-NOHPC is shown in Scheme 1. First, the prepared macropore template of monodispersed PS spheres and commercial silica spheres used as mesopore template are self-assembled to form a 3D ordered template (Step 1). The ZIF-8 precursor is infiltrated in the voids of the face-centred cubic (fcc) PS and SiO_2 of the 3D ordered PS/SiO_2 template (Step 2). After adding the mixture of ethanol and ammonia, the single-crystals start to grow along the template and ZIF-8@PS/SiO_2 with the size of 100 nm. The ammonia deprotonates the ligand and induces rapid crystallization of ZIF-8.

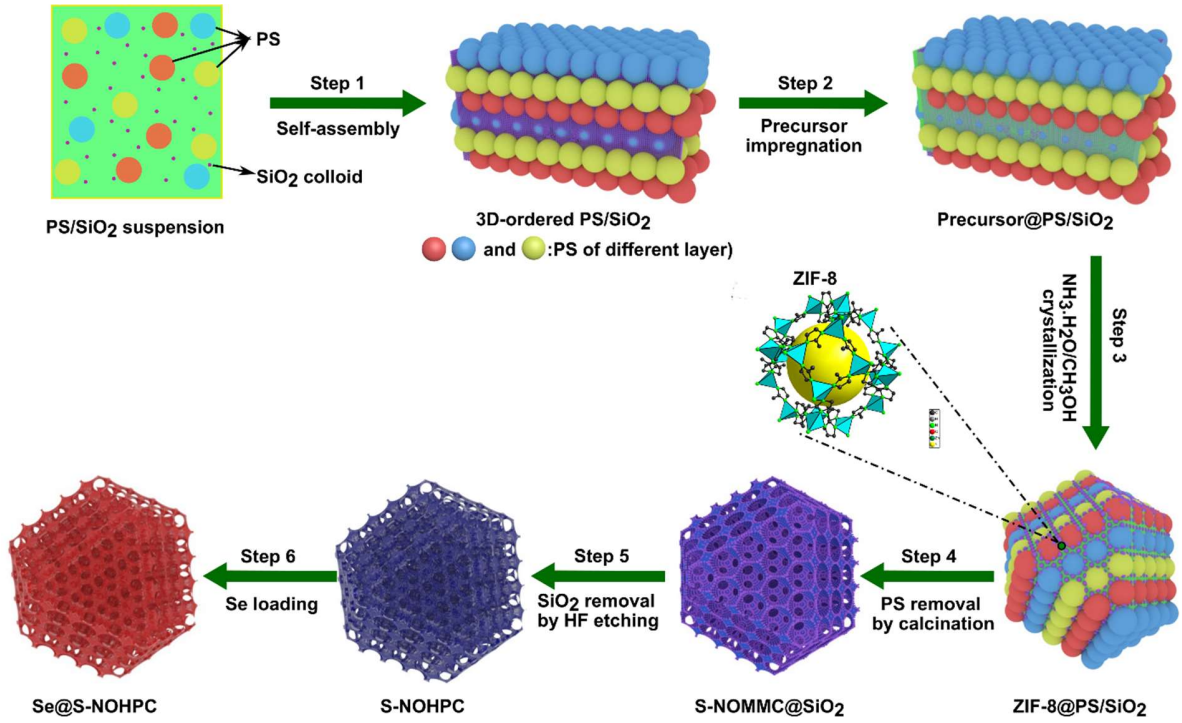

Scheme 1 Schematic illustration of Se@S-NOHPC synthesis process (PS: Polystyrene).

The ethanol is used to stabilize the precursor and adjust the balance between nucleation and growth (Step 3). After the PS removal by calcination, the ZIF-8 derived S-NOMMC containing SiO_2 (S-NOMMC@SiO_2) is obtained (Step 4). By etching the SiO_2, the S-NOHPC material with a 3D interconnected micro-meso-macroporous structure is synthesized (Step 5). Finally, active Se is infiltrated into the carbon host material by the melting-diffusion method. The Se@S-NOHPC cathode material is obtained (Step 6). Two reference samples of S-NMC and S-NOMMC are also prepared. Their preparation procedure is detailed in EXPERIMENTAL SECTION part and also in Table S1.

The SEM and TEM images show the porous structures and morphologies of S-NMC, S-NOMMC, S-NOHPC, and the corresponding Se@S-NOHPC composite. As shown in Fig. 1a, SNMC exhibits well-shaped ZIF-8 single-crystals, with a typical rhombic dodecahedron morphology and a particle size in the range of 400–500 nm. Fig. 1b, c and Fig. S2 show the tetrakaidecahedral structure of S-NOMMC with a uniform particle size of ~2 μm, which is composed of six triangles and eight squares. It can be seen that the highly ordered macropores are successfully generated throughout the tetrakaidecahedral after the removal of the PS template (Fig. 1c). The morphology of SNOMMC is different from that of S-NMC due to the growth advantage

of [111] and [100] faces in the PS template, resulting in the maximum oriented macropore arrangement structure[43]. The large-scale image of S-NOHPC is shown in Fig. 1d, with a uniform particle size of ~1.5 μm. The SEM image of single-crystal MOF-derived S-NOHPC in Fig. 1e shows similar morphology to that of S-NOMMC. However, due to the removal of SiO_2 template, the thickness of the interconnected walls became thinner, as shown in Fig. 1f. In the magnified

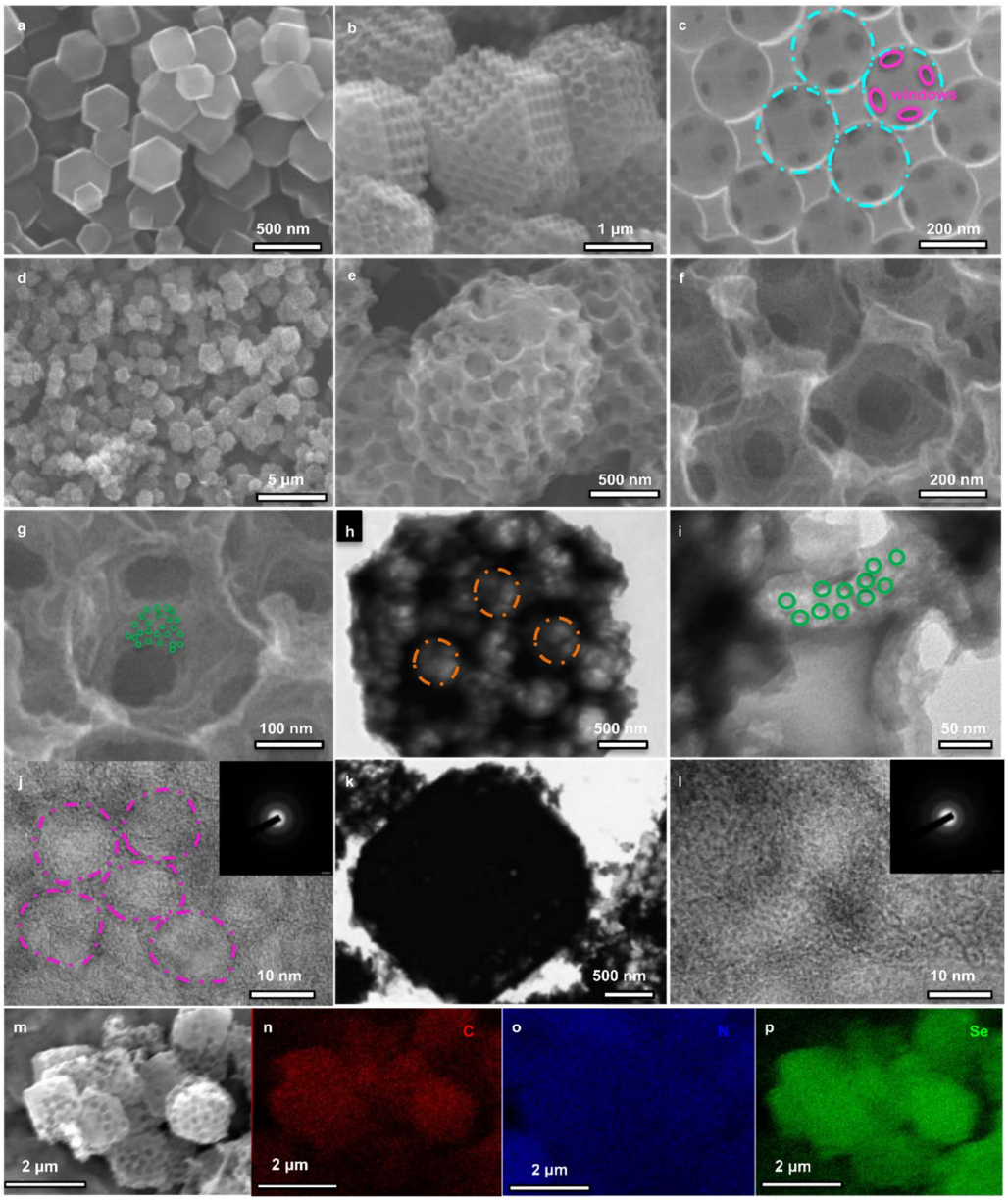

Figure 1 SEM images of (a) S-NMC, (b, c) S-NOMMC, and (d-g) S-NOHPC. TEM images of (h, i) S-NOHPC and (k) Se@S-NOHPC, (j, l) HR-TEM and SAED of S-NOHPC and Se@S-NOHPC composite, respectively. (m–p) SEM images of Se@ S-NOHPC and corresponding EDX mapping results.

image of S-NOHPC (Fig. 1g), the mesopores can be clearly seen in the thin walls where the SiO_2 spheres are removed. TEM images of S-NOHPC in Fig. 1h, i confirm the existence of macropores and mesopores that constructed the interconnected thin walls. The macropores with a size of 400 nm (orange cycles) are detected due to the removal of PS spheres. Moreover, a large number of mesopores with a size of ~12 nm (green cycles) and interconnected with macropores appear inside the thin walls after the removal of SiO_2 colloidal templates. The HRTEM image of S-NOHPC in Fig. 1j clearly displays a few layers of graphene-like carbon around the mesopores (pink cycles), which is beneficial to the transportation of electrons. The inserted SAED reflects that the host carbon of S-NOHPC is generally in an amorphous state. After Se infiltration into the S-NOHPC host, the obtained Se@S-NOHPC composite in Fig. 1k well maintains the original morphology. Compared with S-NOHPC, the HR-TEM of Se@SNOHPC in Fig. 1l shows a more disordered carbon phase and a darker color for the reason of the infiltration of Se into the pores. The SAED of Se@S-NOHPC indicates that Se stays in an amorphous nature. The EDX mapping measurement was applied to analyze the elemental compositions and their specific distribution in the Se@S-NOHPC composite. The good overlap of the SEM and the mapping images in Fig. 1m–p indicate that N and Se are homogeneously dispersed in the carbon host material.

N_2 adsorption-desorption was used to analyze the surface area and pore size distribution of the materials. The isotherms and BJH pore size distributions (1–200 nm) of all the carbon host materials and their corresponding Se/C composites are depicted in Fig. 2a and b, respectively. Their micropore size distributions obtained by the H-K method are given in Fig. 2c. S-NMC gives a type I isotherm, characteristic of microporous materials principally[44, 45]. This carbon host directly derived from ZIF-8 contains micropores with a size at around 0.5 nm (Fig. 2c). The very slight increase in N_2 uptake at a very high $P/P_0 > 0.9$ indicates the presence of a few macropores, stemming from the aggregation of S-NMC particles. S-NOMMC sample also exhibits a type I isotherm with a strong N_2 uptake at high P/P_0, indicating the presence of micropores and macropores. Fig. 2b, c confirm that S-NOMMC contains micropores of 0.5 nm coming from the ZIF-8 and macropores with a distribution centred at around 150 nm due to the removal of PS spheres. The isotherm of S-NOHPC is of type IV, characteristic of mesoporous materials[46, 47]. The mesopores are provided by the silica colloidal templates. The sharp N_2 uptake at high P/P_0 clearly indicates the presence of important macropores. The pore size distributions in Fig. 2b, c confirm the presence of micropores of 0.5 nm (Fig. 2c), mesopores of 12 nm, and macropores of 150 nm

(Fig. 2b), proving that S-NOHPC is a hierarchically porous carbon with micro-meso-macroporosity. After inclusion of Se into those carbon host materials, the N_2 adsorption capacity is drastically

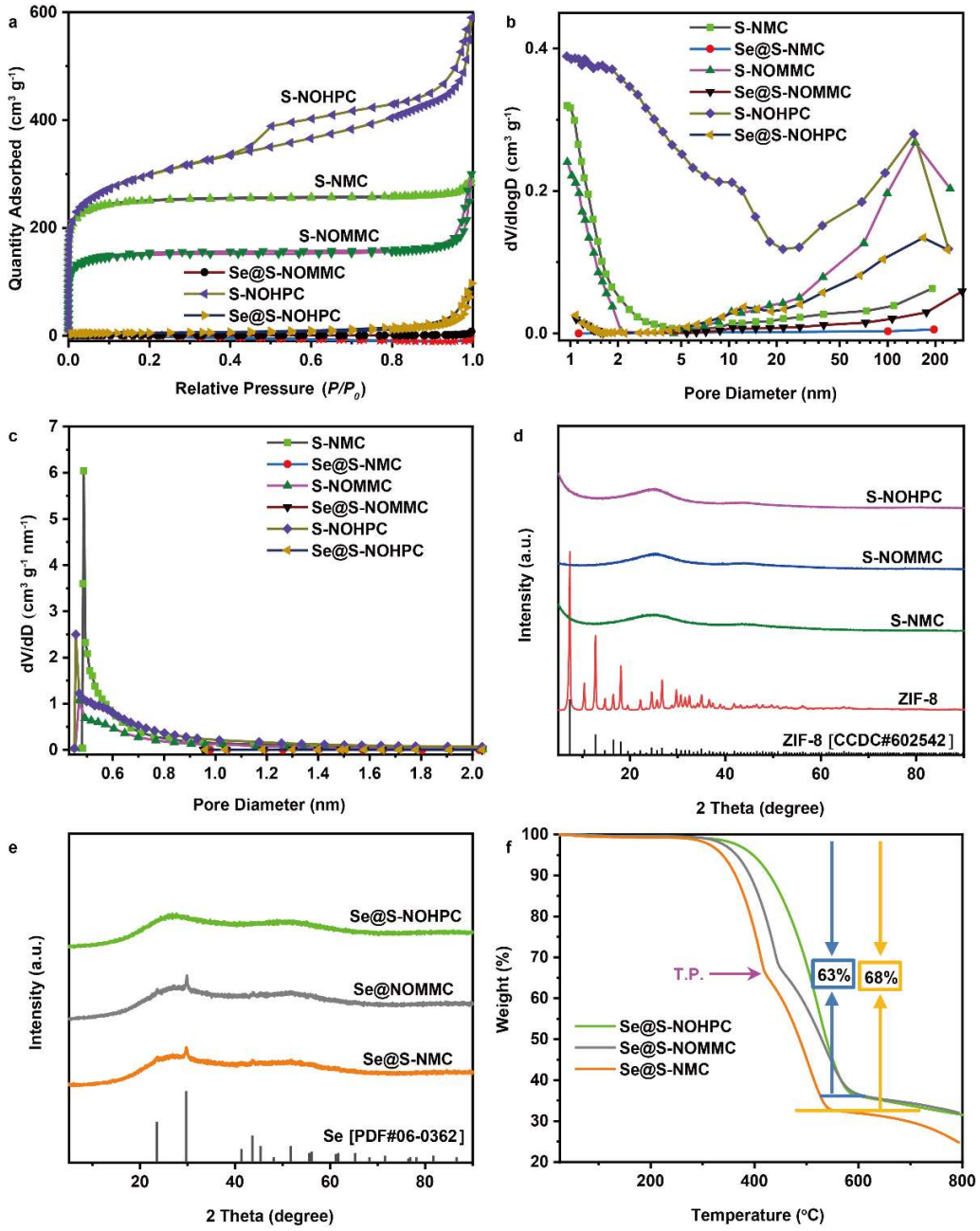

Figure 2 (a) N_2 adsorption-desorption isotherms, (b, c) Pore size distribution of S-NMC, S-NOMMC, S-NOHPC and corresponding Se@C composites, respectively. XRD patterns of (d) ZIF-8, S-NMC, S-NOMMC, S-NOHPC and (e) Se, Se@S-NMC, Se@S-NOMMC and Se@S-NOHPC, respectively. (f) TGA plots of prepared Se@S-NMC, Se@S-NOMMC and Se@S-NOHPC composites (T.P.: Turning point).

reduced to practically zero (Fig. 2a), suggesting the full occupation of pores of these carbon host materials. The surface areas and pore volumes of all the prepared host samples and corresponding Se@C composites are listed in Table S2. S-NOHPC containing micro-, meso-, and macro-pores achieves the highest specific surface area and pore volume of 1009 $m^2 g^{-1}$ and 0.9 $cm^3 g^{-1}$, respectively. Compared with microporous S-NMC (822 $m^2 g^{-1}$), the specific surface area of micro-macroporous S-NOMMC (493 $m^2 g^{-1}$) is reduced due to the presence of important macropores. The S-NOHPC also contains the highest micropore volume. The surface area and porous volume of all the Se/C composites are reduced to insignificant values after infiltration of Se, indicating the successful and full filling of Se in the pores of S-NMC, S-NOMMC, and S-NOHPC.

The crystalline structures of all the synthesized materials were analyzed by XRD measurements. ZIF-8 in Fig. 2d exhibits its typical crystalline structure (CCDC#602542)[48, 49]. Compared with PS and PS/SiO_2 templates in Fig. S3, the peaks belonging to ZIF-8 are detected in the patterns of ZIF-8@PS and ZIF-8@PS/SiO_2, indicating the formation of ZIF-8 in the voids of the templates. The carbon hosts (S-NMC, S-NOMMC, and SNOHPC) in Fig. 2d show two broad peaks at ~25° and 44°, which belong to amorphous carbon[50]. After Se is infiltrated into the pores of those carbon hosts, some small peaks of Se [PDF#06-0362] are still present in the prepared Se@S-NMC and Se@S-NOMMC composites (Fig. 2e), reflecting that a small amount of Se is present in a crystalline state. This may be due to the lack of diffusion pathways inside S-NMC particles and the low surface area of S-NOMMC. While the peaks belonging to selenium completely disappear in the obtained Se@S-NOHPC composite, which means that Se is completely dispersed into the pores of S-NOHPC and stays in a well-dispersed state[51]. The presence of the interconnected micro-meso-macroporosity in SNOHPC favors the facile diffusion and dispersion of Se in the core and throughout S-NOHPC particles. The presence of only micropores or micro-macropores is not favorable for the deep penetration of Se in S-NMC and S-NOMMC particles, and some Se crystals are thus found at the external surface of S-NMC and S-NOMMC particles. The uniform distribution of Se throughout the S-ONHPC is beneficial for electrochemical reactions.

TGA was performed to measure the selenium proportion in the as-synthesized composites and the results are shown in Fig. 2f. With the increase in temperature, the evaporation of Se in the composites occurs in the range of 300–580 °C. Se@S-NMC gives the lowest evaporation temperature. The evaporation temperature is related to the adsorption strength of Se in the pores. It is interesting to note that there has a turning point (T.P., where evaporation rate changes) in the

TG curves of Se@S-NMC and Se@S-NOMMC while the Se in the Se@S-NOHPC evaporates at the highest temperature without the turning point. The presence of the turning point for Se@S-NMC and Se@S-NOMMC can be explained as follows: Se located at the external surface of S-NMC and S-NOMMC will evaporate first at a lower temperature, and Se located in the pores of S-NMC and S-NOMMC will evaporate at the higher temperature. The presence of crystalline Se at the external surface of Se@S-NMC and Se@S-NOMMC has been revealed by XRD (Fig. 2e). The Se evaporation temperature of Se@S-NOMMC is higher than that of Se@S-NMC, indicating that the adsorption strength of Se within S-NOMMC is higher than that in S-NMC. The highest evaporation temperature found in Se@S-NOHPC illustrates the strongest interaction strength between Se and S-NOHPC. The absence of the turning point in Se@S-NOHPC suggests that Se is homogeneously dispersed in this sample without the presence of Se crystalline phase, in excellent agreement with XRD (Fig. 2e) and EDX mapping (Fig. 1n–p). The Se loading amounts in the Se@S-NMC, Se@S-NOMMC, and Se@S-NOHPC were calculated by the weight loss of the evaporation, being 68 wt%, 63 wt%, and 63 wt%, respectively. The highest Se loading in Se@S-NMC is due to the presence of external surface Se crystals.

XPS measurements were carried out to analyze the chemical nature of the synthesized carbon host and corresponding Se@C composites. After Se loading, the Se peaks were detected in the overall XPS (Fig. 3a), indicating that Se is well present in the Se@C composites. Besides, C, N, and O elements in S-NOHPC host material are present with the contents of 82.05 at%, 11.83 at% and 5.65 at%, respectively. N elements originate from the ligand of ZIF-8. The presence of N element in S-NOHPC sample indicates that the in-situ N doping in S-NOHPC occurs. The N 1s high-resolution spectrum of S-NOHPC in Fig. 3b could be deconvoluted into three peaks, corresponding to graphitic-N (404.1 eV), pyrrolic-N (399.6 eV), and pyridinic-N (398.1 eV), respectively[52, 53]. It is reported that the pyrrolic-N and pyridinic-N have a stronger binding with soluble polyselenides, and pyridinic-N plays an effective role in anchoring the polyselenides[54]. The C 1s spectra in Fig. 3c can be deconvoluted into three peaks at 284.6, 285.6, and 289.7 eV, which are associated with the C–C sp^2-hybridized graphitic carbon, C–N/C–C, and C=O/C=N, respectively.[55] This indicates that the elements of N are tightly doped in the carbon host material. The Se 3d spectrum in Fig. 3d shows a typical nature of Se, and the three peaks at 55.1, 56.0 and 58.1 eV correspond to Se $3d_{5/2}$, Se $3d_{3/2}$, and Se–O/Se–C, respectively. The existence of Se–O and C=O may be originated from the oxidation reaction of the Se/C composite material with the surface

adsorbed O_2. The high-resolution spectrum of N 1s, C 1s, and Se 3d in Se@S-NMC and Se@S-NOMMC are similar to that of Se@S-NOHPC.

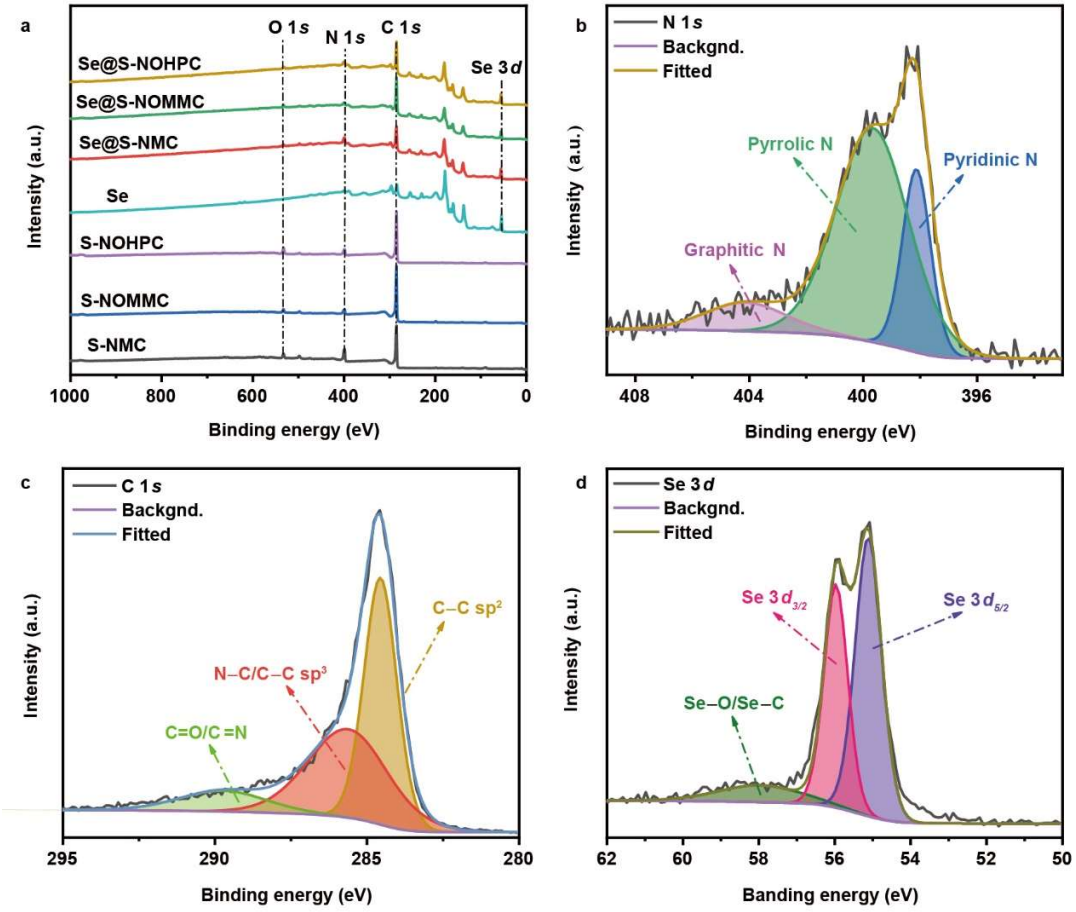

Figure 3 (a) The overall XPS of Se, S-NMC, S-NOMMC, S-NOHPC, and corresponding Se@C composites. The high-resolution spectrum of S-NOHPC: (b) N 1s, (c) C 1s, and (d) Se 3d, respectively.

3.2 Electrochemical properties

Selenium cathodes based on the obtained composite materials were prepared and assembled in CR2032 type-coin cells for electrochemical evaluation. Fig. S4a–c display the typical CV curves of Se@S-NOHPC, Se@S-NOMMC, and Se@S-NMC electrodes, respectively. Two characteristic cathodic peaks can be observed in all three CV curves, indicating that the discharge process follows a solid-liquid-solid conversion mechanism[56]. The first cathodic peak at the high voltage corresponds to the reaction of Se to dissoluble intermediate of Li_2Se_n ($4 \leqslant n \leqslant 8$), and the second cathodic peak at lower voltage is ascribed to the production of Li_2Se[57]. Only one anodic peak at

~2.23 V appears in the charging process of Se@S-NOHPC and Se@S-NOMMC due to the overlap of two peaks of Li_2Se to Li_2Se_n and Li_2Se_n to Se. Besides the peak at 2.23 V, another anodic peak at 2.05 V appears in Se@S-NMC and may be due to the slow intermediate polyselenide transformation solely in the micropores. Moreover, a small cathodic peak (at ~1.7 V in Se@S-NOHPC and Se@S-NOMMC and ~1.56 V in Se@S-NMC) in the first cycle appears because the electrolyte reduction at the low voltage forms an insulating SEI layer on the carbon host. The cathodic peak at 1.7 V in the CV curve of the pure S-NOHPC (Fig. S4d) confirms that its appearance is due to SEI formation rather than Se reaction. With the formation of SEI layer and Se activation of the Se@S-NOHPC in the first few cycles, the cathodic/anodic peaks undergo a shift. Afterwards, the obtained stable SEI layer and the accomplishment of most Se activation in Se@S-NOHPC cathode lead to the good overlap of the curves, meaning that the reaction keeps a good reproducibility. While the first-plateau-voltage saltation in Se@S-NMC still persists in the 10^{th} cycle, which is due to the fact that solely the micropores structure is not good for the transfer of electrolyte and ions. The comparison of those three cathodes in the 10^{th} cycle is shown in Fig. 4a. The Se@S-NMC electrode has a low current density and a large potential difference between cathodic and anodic peaks (ΔV of 0.17 V) due to the unfavorable ion transfer solely in micropores. The value of current density and ΔV (0.13 V) of SNOMMC have some degree of improvement owing to the internal micro-/macroporous electrolyte pathways. The Se@S-NOHPC electrode exhibits the highest current and the smallest ΔV of 0.04 V, indicating its superior electrochemical performance, faster redox kinetics, and decreased polarization during cell operation compared with the other two electrodes[21]. This is due to the presence of the interconnected hierarchical micro-meso-macropores and polar N-doped sites of S-NOHPC which can enhance the ion transfer and entrapping ability of polyselenides, and accelerate the solid-liquid-solid electrochemical conversion[58]. The galvanostatic discharge/charge profiles of all the electrodes are displayed in Fig. S5. Se@S-NOHPC demonstrates the lowest voltage hysteresis of 0.123 V and exhibits minimal growth in the subsequent cycling, while Se@S-NMC and Se@S-NOMMC give the much higher values of 0.186 and 0.211 V, respectively. This indicates that Se@S-NOHPC cathode possesses the fastest electrochemical reaction kinetics and the lowest resistance[59]. The two platforms of the discharge curve correspond to the two cathodic peaks of the CV plot, ascribed to the conversion of Se to Li_2Se, with the intermediate Li_2Se_n.

The phase-conversion process of the Se@S-NOHPC cathode was investigated by the in situ XRD characterization, as shown in Fig. 4b and Fig. S6. The broad peak at ~25° is due to the amorphous carbon. The peaks of Se (100) at 23.5° and Se (101) at 29.7° are detected at the beginning of the first discharge. With the time going, these peaks gradually disappear at the end of the first discharge plateau (Fig. S6) and no other diffraction peaks are detected. This is due to the fact that the products in this period are soluble polyselenides[60, 61]. Then, the peak of Li_2Se (PDF#23-0072)[1] at 25.7° appears and increases to the maximum value at the end of the first discharge. The phenomenon indicates that Se has already completely transformed to Li_2Se with the intermediate soluble polyselenides. During the first charge process, a reverse reaction undergoes, the Li_2Se goes back to Se, and the peaks belonging to Se are detected again. The second cycle will repeat the reaction of the first cycle. Compared with the first cycle, the peaks of the second cycle become weaker, which reflects that Se is gradually present in the state of chain Se rather than cyclic crystal Se_8. This is beneficial for the further delithiation/lithium reaction.

The EIS measurement was performed to investigate the internal resistance of the battery. The raw and the 5th cycled cathode impedance spectra of the as-prepared Se@C composites are shown in Fig. 4c. The Nyquist plot of the raw cathode consists of a semicircle in the high-frequency region and a sloped line in the low-frequency region. The semicircle is associated with the charge transfer resistance (R_{ct}), while the linear slope refers to the Warburg impedance reflecting the ion diffusion[62, 63]. For raw Se@S-NOMMC, the value of R_{ct} is 38.8 Ω, which is lower than that of Se@S-NMC (42.9 Ω) due to the introduction of interconnected micro-/macro-porous channels accelerating the transportation of the ions. The battery with Se@S-NOHPC cathode has a further decrease, achieving the smallest R_{ct} value of 34.4 Ω for the reason of interconnected micro-, meso-, and macro-pores leading to even faster ion/electron transfer. It is interesting to find that the second semicircle in extra high-frequency region of the spectra appears, which is due to the existence of the formed SEI layer (RSEI)[64]. The Nyquist plots are established by the equivalent circuit given in the inset of Fig. 4c and the fitted parameters are summarized in Table S3. The Se@S-NMC has a high value of RSEI of 23.6 Ω because the volume expansion causes uneven destroyed surface, which is not beneficial to the ion diffusion and further reaction. Compared with Se@S-NMC, the SEI resistance value of Se@S-NOMMC decreases to 16.6 Ω and that of S-NOHPC is as low as 11.5 Ω for its uniform SEI layer on the surface of the structurally stable S-NOHPC[65]. Notably, the R_{ct} values of Se@S-NOHPC and Se@S-NOMMC decrease after first 5 cycles of activation,

while that of Se@S-NMC increases to 50.7 Ω, owing to the structural damage caused by the volume expansion. Because of the preserved structural stability in the interconnected micro-meso-macroporous structure and rapid mass transfer, Se@SNOHPC possesses the smallest value of R_{ct} and R_{SEI}, reflecting its good charge transferability, thereby leading to much better electrochemical performance.

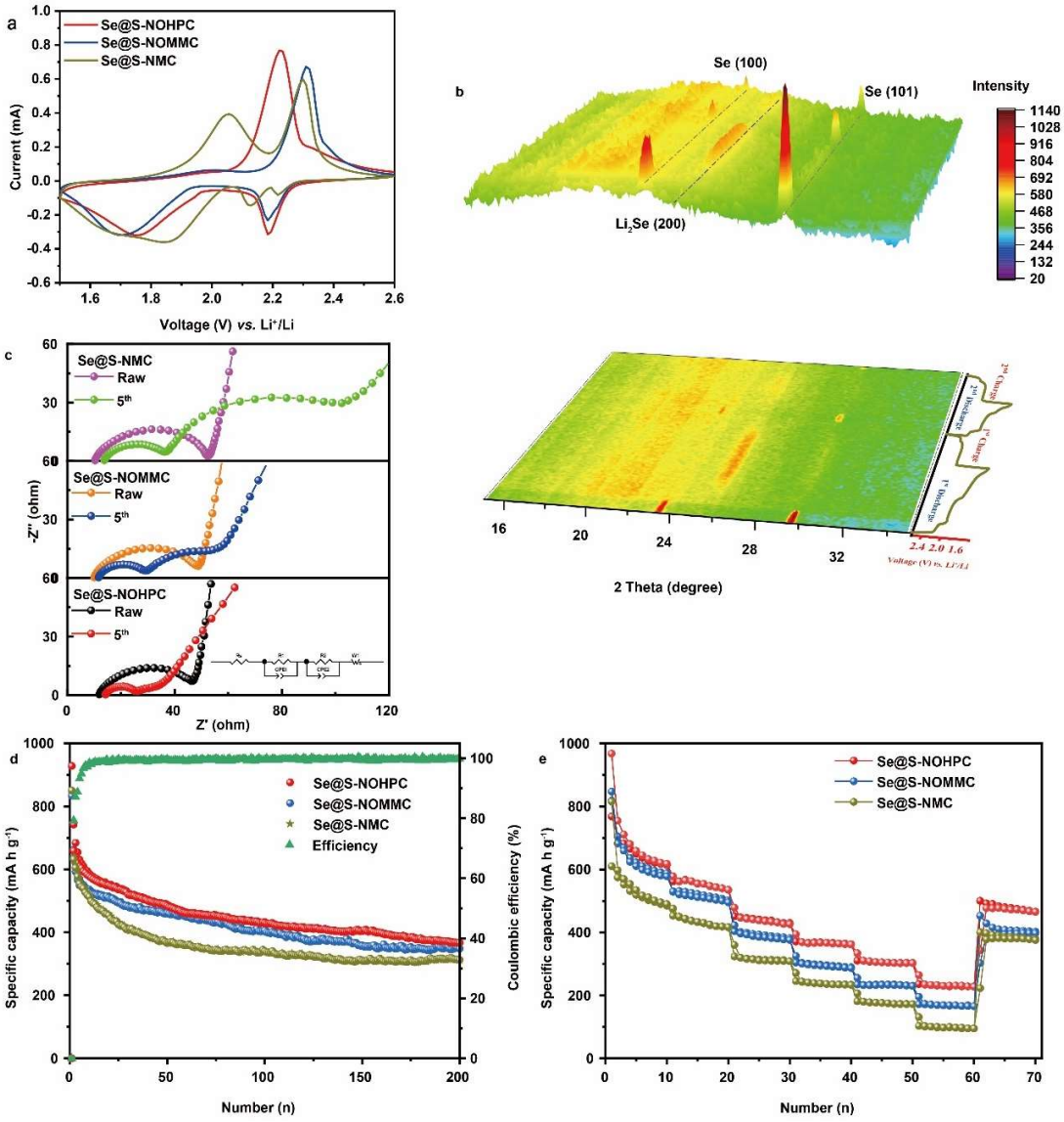

Figure 4 (a) CV curves of Se@C cathodes at 0.1 mV s^{-1}, (b) The in situ XRD characterization of the Se@S-NOHPC cathode in 2 discharge/charge cycles, (c) Nyquist plots and the equivalent circuit model (inset), (d) Cycling performance at 0.2 C and (e) Rate performance at different current densities of the Se@C cathodes.

The formed SEI layer on the surface of the cycled Se@S-NOHPC cathode material was further studied by XPS measurement and the result is shown in Fig. S7. Compared with Se@S-NOHPC fresh cathode, the intensity of the O 1s has an obvious increase and a new peak of F 1s appears in Fig. S7a. These two elements are the main components of the SEI layer, clearly indicating the formation of the SEI layer on the surface of the cathode. The high-resolution Li 1s and F 1s spectra of cycled Se@S-NOHPC are shown in Fig. S7b, c. The Se 3d and Li 1s are in the same range of binding energy; besides the three peaks of Se, a new peak of Li_2CO_3 appears at 52.8 eV due to the side reaction between the electrolyte and lithium species[66, 67]. Also, in the F 1s spectrum, two peaks belonging to LiF (684 eV) and C–F (688 eV) are convoluted, confirming the formation of the important SEI layer[68].

The stability of the three as-prepared Se@C composites was tested at the current density of 0.2 C and the results are shown in Fig. 4d. The capacity of Se@S-NMC quickly decays and reaches a value of 312 mA h g^{-1} after 200 cycles. This poor performance is due to the presence of partially crystalline selenium at the external surface and the small micropores preventing the good transfer of the lithium species as well as the structural failure due to volume expansion. Benefiting from the introduction of macropores to accelerate the ion transfer, and the enhanced adsorption of polyselenides by N doping, the capacity retention of Se@S-NOMMC reaches an improved value of 348 mA h g^{-1}. Importantly, Se@S-NOHPC exhibits the highest initial and 2nd discharge capacity of 927.7 and 658 mA h g^{-1} and remains 367 mA h g^{-1} after 200 cycles, with a Coulombic efficiency (CE) of almost 100%. The highly improved capacity and stability are owing to the uniformly distributed amorphous selenium, further accelerated ion transfer in the interconnected hierarchically micro-meso-macroporous channels, N-doping-enhanced adsorption of the polyselenides and their rapid transformation. The galvanostatic discharge/charge profiles of Se@S-NOHPC in 200 cycles are shown in Fig. S8. The initial discharge and charge capacities are 927.7 and 742 mA h g^{-1}, with the CE value of 80%. The higher capacity than theoretical value (675 mA h g^{-1}) and the lower CE are due to the generation of the SEI layer and the Se activation process in the first cycle. The cycling performance of the pure S-NOHPC was tested to investigate the capacity from the contribution by the SEI formation. From the result of Fig. S4e and f, the capacity produced by the pure S-NOHPC host can reach a value of 262 mA h g^{-1} in the first cycle owing to the electrolyte undergoing a decomposition at low voltage and the formation of an SEI layer on the surface of the carbon host. Then, the formed SEI layer separates the carbon host from electrolyte,

avoiding further decomposition of the electrolyte. Thus, the capacity offered by pure S-NOHPC rapidly drops to a low level, and Se makes the main contribution to the capacity of the Se@S-NOHPC in the following cycles.

Rate capability and its restoration ability were tested to analyze battery operation under different current densities. As presented in Fig. 4e, Se@S-NOHPC possesses the best rate performance with the highest capacity of 658, 554, 438, 367, 305, and 230 mA h g^{-1} at current densities of 0.1, 0.2, 0.5, 1, 2, 5 C, respectively. When the current restores to 0.1 C, the capacity soon recovers to 477 mA h g^{-1}, achieving 72% of the initial value, indicating superior reversibility. While the discharge values of the Se@S-NOMMC and Se@S-NMC at 5 C are 158 and 49 mA h g^{-1}, respectively. The best rate capability of Se@S-NOHPC is due to the synergy of the hierarchical structure constructed by interconnected channels that accelerates the transfer of ions, and the strong interaction between N-doped sites and polyselenides that inhibits the shuttle effect and boosts the reaction kinetics.

The lithium species (Li^+ and Li_2Se_n) diffusion coefficient (D) was analyzed by the GITT measurement[69, 70]. The test was conducted on five cycles of activated cells at a current density of 0.1 C with 10 min discharging/charging and then 40 min relaxing. The ion diffusion coefficients were calculated based on Fick's second law. The specific method is shown in the Supplementary information (Fig. S9). The calculated D results of different cathodes are summarized in Table S3[71].

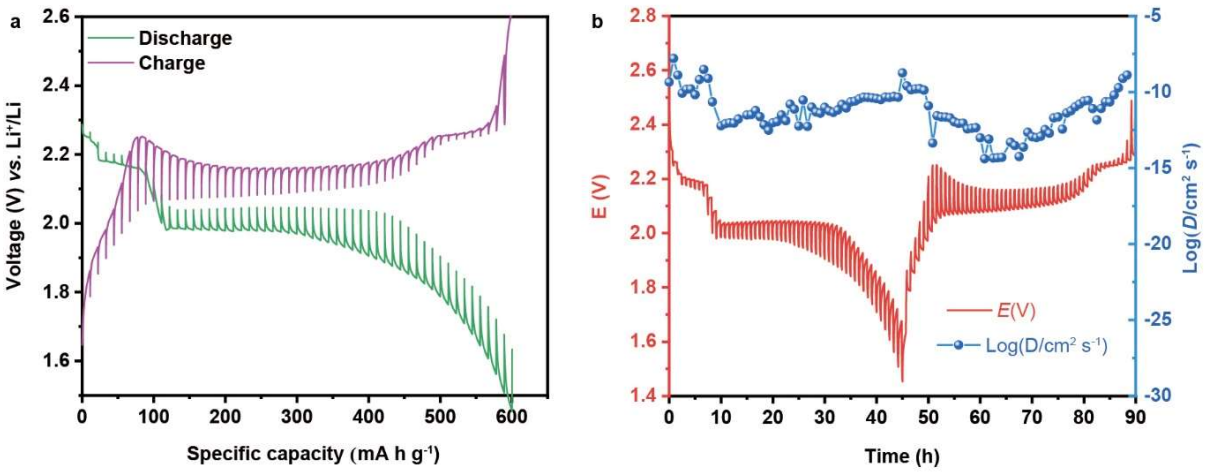

Figure 5 (a) Potential response of GITT measurement in the range of 1.5–2.6 V vs. Li^+/Li at 0.1 C and (b) Calculated D from the GITT data of Se@S-NOHPC.

The GITT potential response and calculated D values of Se@S-NOHPC as the representative sample are shown in Fig. 5. Se@S-NOHPC achieves the highest ion diffusion coefficient of 4.44 × 10^{-10} cm^2 s^{-1}, meaning the fast diffusion of Li^+ as well as Li_2Se_n on the surface of host material. Such fast ion diffusion combined with the polar N-doped sites that enhance strong adsorption of polyselenides results in the quick transformation of polyselenides, thus reducing the dissolution of Li_2Se_n and subsequent diffusion out of the cathode. The D value of Se@S-NOMMC has a little decrease at 4.25 × 10^{-10} cm^2 s^{-1} and Se@S-NMC possesses a D value of 4.59 × 10^{-11} cm^2 s^{-1}, being ten times lower than the other two cathodes. That indicates the most importance of the synergy of the quick ion transfer and strong adsorption of polyselenides. Only with the strong adsorption of N doping in S-NMC but the absence of interconnected channels for ion transfer, the N-doped sites will soon be fully occupied by polyselenides and the accumulated polyselenides soon diffuse out of the cathode. The accelerated ion transfer by the interconnected micro-meso-macroporous channels of S-NOHPC fully demonstrates the synergistic advantages of the strong adsorption by N-doped polar sites.

The stability is firmly dependent on the adsorption strength of the host to the polyselenides. The strong interaction between Se species and carbon host materials was further demonstrated through visualized Li_2Se_6 adsorption experiments. Compared with the pure polyselenides (Li_2Se_6) solution with a brown color, the solution with soaked S-NMC and S-NOMMC shows a redyellow and very light yellow color, respectively, while the solution with the presence of S-NOHPC almost turns to colorless. The result indicates that the S-NOHPC possesses the strongest adsorption ability to selenium species. The obtained supernatants were collected and diluted for further analysis by UV-vis absorption measurements, and the test results are shown in Fig. 6a. The characteristic peak at ~340 nm refers to the absorption of Li_2Se_6. The higher the absorption of the solution, the higher the intensity of Li_2Se_6. The spectrum of blank shows a high intensity of Li_2Se_6, the solution from the S-NMC and S NOMMC displays a sharp drop and the intensity of S-NOHPC exhibits the lowest value. This indicates that the S-NOHPC possesses stronger adsorption ability to soluble polyselenides due to its rational hierarchical structure and N doping, which is beneficial to preventing the shuttle effect and could also catalyze the subsequent conversion of polyselenides[72]. XPS measurement of the precipitation after Li_2Se_6 adsorption experiment was subsequently conducted to investigate the chemical interaction mechanism between Se species and post-adsorbed S-NOHPC. Compared with the raw S-NOHPC host material, the XPS spectrum of the

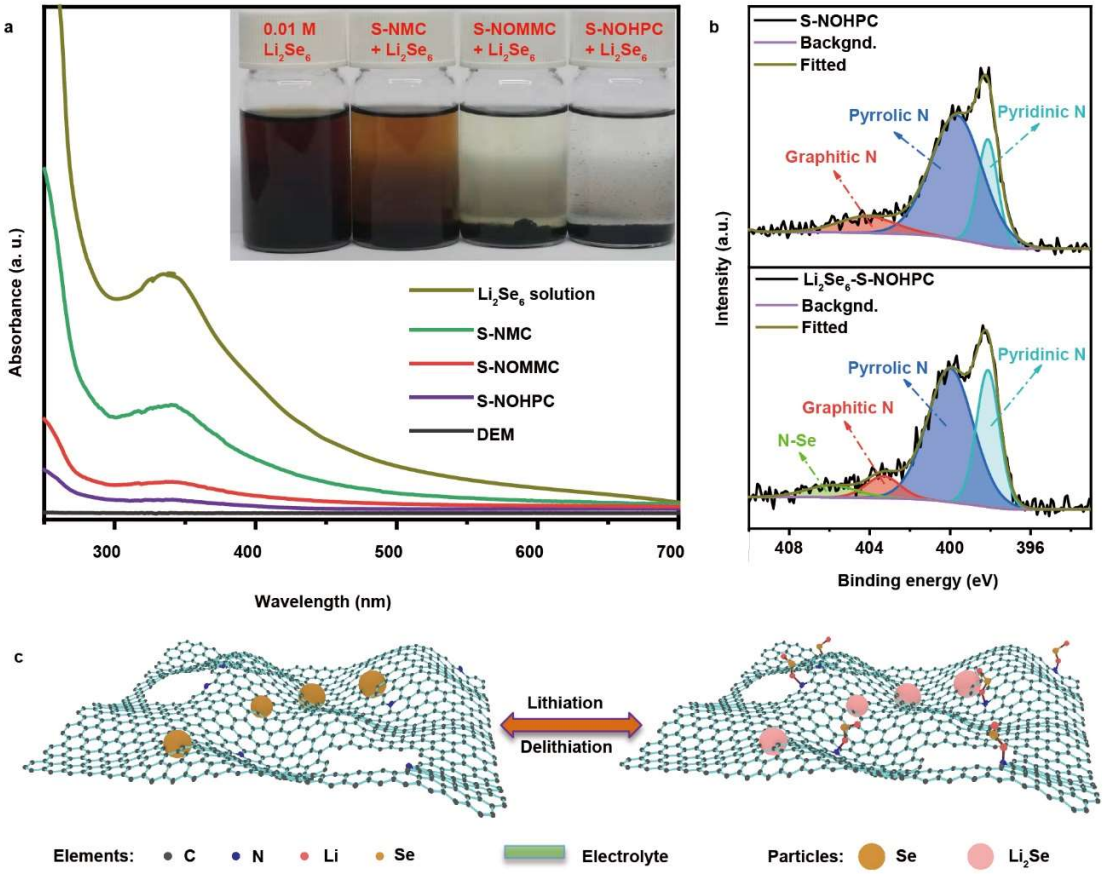

Figure 6 (a) Visualized Li_2Se_6 adsorption experiments and UV-vis spectra of Li_2Se_6 solution adsorbed by S-NMC, S-NOMMC, and S-NOHPC, (b) N 1s high-resolution XPS spectra of pristine S-NOHPC and S-NOHPC adsorbed by Li_2Se_6 (Li_2Se_6-S-NOHPC), (c) Schematic illustration for reaction process in the Se@S-NOHPC composites.

post-adsorbed S-NOHPC shows a new peak corresponding to N–Se[73]. This result suggests that there is strong chemical adsorption between S-NOHPC and Se species through N–Se bonds. Thus, the enhanced adsorption ability of S-NOHPC is due to the physical adsorption from the rational design of three-scale pores and the chemisorption from N-doping.

To better illustrate the advantages of the structure design for the superior battery performance, a schematic illustration is shown in Fig. 6c. The introduction of the interconnected mesoporous and macroporous channels in addition to micropores is beneficial to the quick ion transfer and can alleviate the volume expansion. The interconnected carbon framework accelerates the electron transfer. When the Li^+ and electrons reach the micropores and mesopores loaded with Se, the reaction happens in the rich sites. The produced polyselenide intermediate is rapidly transferred

and adsorbed on the surface of the S-NOHPC host material by the physical adsorption provided by micropores and the strong chemisorption brought by the *in-situ* doped N, thereby accelerating the conversion kinetics of the battery and inhibiting the shuttle effect. Thanks to the rational design of S-NOHPC integrating all the characteristics required for the superior electrochemistry, Se@S-NOHPC realizes the best performance in the Li-Se battery.

Conclusions

Single-crystal MOF-derived N-doped ordered hierarchically porous carbon with three scale pores of micro-, meso- and macro-porosity was successfully prepared with the help of templates and a saturated solution-based double-solvent-assisted strategy. The micropores from the nature of ZIF-8 and the introduced mesopores provide the loading space for active Se. The interconnected mesoporous and macroporous channels shorten the ion transfer pathways and effectively buffer volume expansion. Owing to the advantages of the three length scales of pore sizes and N-doping enhanced polyselenides adsorption strength, Se@S-NOHPC achieves the highest 2nd discharge capacity of 658 mA h g^{-1} and retains 367 mA h g^{-1} after 200 cycles at 0.2 C. The capacity of Se@S-NOHPC can reach 230 mA h g^{-1} at the high current density of 5 C. Our work provides a novel method to introduce mesopores and ordered macropores inside a single-crystal MOF-derived carbon host. The excellent electrochemical performance fully shows the advantages of the hierarchically porous structure design and heteroatom doping, which maybe give an important guideline for the applications in other fields.

Acknowledgements

Li H thanks the financial support from the China Scholarship Council (201809370046) and a scholarship from the Laboratory of Inorganic Materials Chemistry, Université de Namur. The authors thank Prof. Alexandru Vlad for his UV-vis absorption test supporting. We thank the PC2 technological platform at the University of Namur for access to Power X-ray diffractometer and TGA/DSC. This research used resources of Electron Microscopy Service located at the University of Namur. This service is member of the "Plateforme Technologique Morphologie-Imagerie". This work was supported by the National Postdoctoral Program (2020M672782), the National Natural Science Foundation of China (U1663225), Changjiang Scholars and Innovative Research Team in University (IRT_15R52), the Program of Introducing Talents of Discipline to Universities-Plan 111 (B20002) from the Ministry of Science and Technology and the Ministry of Education of China, and the National Key R&D Program of China (2016YFA0202602).

References

[1] Lu CW, Zhang WK, Fang RY, *et al.* Facile and efficient synthesis of Li_2Se particles towards high-areal capacity Li_2Se cathode for advanced Li–Se battery. Sustainable Materials and Technologies, 2021, 29: e00288

[2] Qi XQ, Jin Q, Yang FY, *et al.* A long-life and safe lithiated graphite-selenium cell with competitive gravimetric and volumetric energy densities. J. Energy Chem., 2021, 60: 556-563

[3] Qi XQ, Yang Y, Jin Q, *et al.* Two-Plateau Li-Se Chemistry for High Volumetric Capacity Se Cathodes. Angew. Chem., 2020, 132: 14012-14018

[4] Zhang Q, Cai LT, Liu GZ, Li Q, *et al.* Selenium-Infused Ordered Mesoporous Carbon for Room-Temperature All-Solid-State Lithium–Selenium Batteries. with Ultrastable Cyclability. ACS Appl. Mater. Interfaces, 2020, 12: 16541-16547

[5] Jin ZS, Liang ZM, Zhao M, *et al.* Rational design of MoNi sulfide yolk-shell heterostructure nanospheres as the efficient sulfur hosts for high-performance lithium-sulfur batteries. Chem. Eng. J., 2020, 394: 124983

[6] Sun TT, Huang C, Shu HB, *et al.* Porous $NiCo_2S_4$ Nanoneedle Arrays with Highly Efficient Electrocatalysis Anchored on Carbon Cloths as Self-Supported Hosts for High-Loading Li–S Batteries. ACS Appl. Mater. Interfaces, 2020,12: 57975-57986

[7] Angamuthu G, Bosubabu D, Ramesha K, *et al.* The Si_3N_4/MoS_2 hetero-structure as an effective polysulfide regulator for high-performance lithium-sulfur battery. Applied Materials Today, 2021, 22: 100916

[8] Zhao XS, Jiang L, Ma CH, *et al.* The synergistic effects of nanoporous fiber TiO_2 and nickel foam interlayer for ultra-stable performance in lithium-selenium batteries. J. Power Sources, 2021, 490: 229534

[9] Dong W-D, Yu W-B, Xia F-J, *et al.* Melamine-based polymer networks enabled N, O, S Co-doped defect-rich hierarchically porous carbon nanobelts for stable and long-cycle Li-ion and Li-Se batteries. J. Colloid Interface Sci., 2021, 582: 60-69

[10] Lin SX, Chen YH, Wang YF, *et al.* Three-Dimensional Ordered Porous Nanostructures for Lithium–Selenium Battery Cathodes That Confer Superior Energy-Storage Performance. ACS Appl. Mater. Interfaces, 2021, 13: 9955-9964

[11] Hao JW, Xu XK, You HR, *et al.* The free-standing cathode fabricated with nano-$CoSe_2$ embedded in mesoporous carbon nanosheets towards high performance Li/SeS_2 batteries, Chem. Eng. J., 2021, 418: 129475

[12] Bui HT, Jang H, Ahn D, *et al.* High-performance Li–Se battery: Li_2Se cathode as intercalation product of electrochemical in situ reduction of multilayer graphene-embedded 2D-$MoSe_2$. Electrochim. Acta, 2021, 368: 137556

[13] Cao YQ, Lei FF, Li YL, *et al.* A MOF-derived carbon host associated with Fe and Co single atoms for Li–Se batteries. J. Mater. Chem. A, 2021, 9: 16196-16207

[14] Jin J, Tian XC, Srikanth N, Kong LB, Zhou K. Advances and challenges of nanostructured electrodes for Li–Se batteries. J. Mater. Chem. A, 2017, 5: 10110-10126

[15] Babu DB, Ramesha K. Constraining polyselenide formation in ether based electrolytes through confinement of Se in microporous carbon matrix for Li-Se batteries. Electrochim. Acta, 2016, 219: 295-304

[16] Song J-P, Wu L, Dong W-D, *et al.* MOF-derived nitrogen-doped core–shell hierarchical porous carbon confining selenium for advanced lithium–selenium batteries. Nanoscale, 2019, 11: 6970-6981

[17] Wang BW, Zhang JJ, Xia ZG, *et al.* Polyaniline-coated selenium/carbon composites encapsulated in graphene as efficient cathodes for Li-Se batteries. Nano Res., 2018, 11:2460-2469

[18] Peng X, Wang L, Zhang XM, *et al.* Reduced graphene oxide encapsulated selenium nanoparticles for high-power lithium–selenium battery cathode. J. Power Sources, 2015, 288: 214-220

[19] Wang XW, Tan YQ, Liu ZX, *et al.* New insight into the confinement effect of microporous carbon in Li/Se battery chemistry: a cathode with enhanced conductivity. Small, 2020, 16:2000266

[20] Luo C, Xu YH, Zhu YJ, et al. Selenium@mesoporous carbon composite with superior lithium and sodium storage capacity. ACS nano, 2013, 7: 8003-8010

[21] Zhao P, Shiraz MHA, Zhu HZ, *et al.* Hierarchically porous carbon from waste coffee grounds for high-performance Li–Se batteries. Electrochim. Acta, 2019, 325: 134931

[22] Li HY, Dong WD, Li C, *et al.* Three-dimensional ordered hierarchically porous carbon materials for high performance Li-Se battery. J. Energy Chem., 2022,.68: 624-636

[23] Zhang JJ, Fan L, Zhu YC, *et al.* Selenium/interconnected porous hollow carbon bubbles composites as the cathodes of Li–Se batteries with high performance. Nanoscale, 2014, 6: 12952-12957

[24] Feng NX, Xiang KX, Xiao L, *et al.* Se/CNTs microspheres as improved performance for cathodes in Li-Se batteries. J. Alloys Compd., 2019, 786: 537-543

[25] Chen L-F, Feng Y, Liang H-W, *et al.* Macroscopic-scale three-dimensional carbon nanofiber architectures for electrochemical energy storage devices. Adv. Energy Mater., 2017, 7: 1700826

[26] Xia Q, Hu JL, Chen QQ, *et al.* N/S Co-doped microporous carbon derived from PSSH-Melamine salt solution as cathode host for Lithium-Selenium batteries. J. Colloid Interface Sci., 2022,.610: 643-652

[27] Lv HL, Chen RP, Wang XQ, *et al.* High-performance Li–Se batteries enabled by selenium storage in bottom-up synthesized nitrogen-doped carbon scaffolds. ACS Appl. Mater. Interfaces, 2017, 9: 25232-25238

[28] Zhao XS, Yin LC, Zhang T, *et al.* Heteroatoms dual-doped hierarchical porous carbon-selenium composite for durable Li–Se and Na–Se batteries. Nano Energy, 2018, 49: 137-146

[29] Mendes TC, Nguyen C, Barlow AJ, *et al.* A safe Li–Se battery in an ionic liquid-based electrolyte operating at 25–70 °C by using a N, S, O tri-doped mesoporous carbon host material. Sustain. Energy Fuels, 2020, 4: 2322-2332

[30] Xie LS, Skorupskii G, Dincă M. Electrically conductive metal–organic frameworks. Chem. Rev., 2020, 120: 8536-8580

[31] Ashworth DJ, Foster JA. Metal–organic framework nanosheets (MONs): a new dimension in materials chemistry. J. Mater. Chem. A, 2018, 6: 16292-16307

[32] Xu GY, Nie P, Dou H, *et al.* Exploring metal organic frameworks for energy storage in batteries and supercapacitors. Mater. Today, 2017, 20: 191-209

[33] Hu AQ, Pang QQ, Tang C, *et al.* Epitaxial growth and integration of insulating metal–organic frameworks in electrochemistry. J. Am. Chem. Soc., 2019, 141: 11322-11327

[34] Shrivastav V, Sundriyal S, Goel P, *et al.* Metal-organic frameworks (MOFs) and their composites as electrodes for lithium battery applications: Novel means for alternative energy storage. Coord. Chem. Rev., 2019, 393: 48-78

[35] Li C, Wang YY, Li HY, *et al.* Weaving 3D highly conductive hierarchically interconnected nanoporous web by threading MOF crystals onto multi walled carbon nanotubes for high performance Li–Se battery. J. Energy Chem., 2021, 59: 396-404

[36] Jin J, Zheng Y, Kong LB, *et al.* Tuning ZnSe/CoSe in MOF-derived N-doped porous carbon/CNTs for high-performance lithium storage. J. Mater. Chem. A, 2018, 6: 15710-15717

[37] Wu HB, Wei SY, Zhang L, *et al.* Embedding sulfur in MOF-derived microporous carbon polyhedrons for lithium–sulfur batteries. Chem. Eur. J., 2013, 19: 10804-10808

[38] Liu YX, Si L, Zhou XS, *et al.* A selenium-confined microporous carbon cathode for ultrastable lithium–selenium batteries. J. Mater. Chem. A, 2014, 2: 17735-17739

[39] He JR, Lv WQ, Chen YF, *et al.* Three-dimensional hierarchical C-Co-N/Se derived from metal-organic framework as superior cathode for Li-Se batteries. J. Power Sources, 2017, 363: 103-109.

[40] Hong H, Liu JL, Huang HW, *et al.* Ordered Macro–Microporous Metal–Organic Framework Single Crystals and Their Derivatives for Rechargeable Aluminum-Ion Batteries. J. Am. Chem. Soc., 2019, 141: 14764-14771

[41] Stassin T, Verbeke R, Cruz AJ, *et al.* Porosimetry for Thin Films of Metal–Organic Frameworks: A Comparison of Positron Annihilation Lifetime Spectroscopy and Adsorption-Based Methods. Adv. Mater., 2021, 33: 2006993

[42] Enomoto T, Ueno S, Hosono E, *et al.* Size-controlled synthesis of ZIF-8 particles and their pyrolytic conversion into ZnO aggregates as photoanode materials of dye-sensitized solar cell. CrystEngComm, 2017, 19: 2844-2851

[43] Shen K, Zhang L, Chen XD, *et al.* Ordered macro-microporous metal-organic framework single crystals. Science, 2018, 359: 206-210

[44] Li ZQ, Yin LW. MOF-derived, N-doped, hierarchically porous carbon sponges as immobilizers to confine selenium as cathodes for Li–Se batteries with superior storage capacity and perfect cycling stability. Nanoscale, 2015, 7: 9597-9606

[45] Krishnaveni K, Subadevi R, Raja M, *et al.* Sulfur/PAN/acetylene black composite prepared by a solution processing technique for lithium-sulfur batteries. J. Appl. Polym. Sci., 2018, 135: 46598

[46] Ye ZQ, Jiang Y, Li L, *et al.* A High-Efficiency CoSe Electrocatalyst with Hierarchical Porous Polyhedron Nanoarchitecture for Accelerating Polysulfides Conversion in Li–S Batteries. Adv. Mater., 2020, 32: 2002168

[47] Shi J-L, Tang C, Huang J-Q, *et al.* Effective exposure of nitrogen heteroatoms in 3D porous graphene framework for oxygen reduction reaction and lithium–sulfur batteries. J. Energy Chem., 2018, 27: 167-175

[48] Jiang XW, Jin H, Sun YJ, *et al.* Assembly of black phosphorus quantum dots-doped MOF and silver nanoclusters as a versatile enzyme-catalyzed biosensor for solution, flexible substrate and latent fingerprint visual detection of baicalin. Biosens. Bioelectron., 2020, 152: 112012

[49] Ren LP, Yu Y, Yang Y, Q. *et al.* Efficient removal of formaldehyde with ZIF-8 growth on TiO_2-coated activated carbon fiber felts prepared via atomic layer deposition. Journal of Materials Science, 2020, 55: 3167-3180

[50] Ma C, Fan QC, Dirican M, *et al.* Porous carbon nanosheets derived from expanded graphite for supercapacitors and sodium-ion batteries. Journal of Materials Science, 2020, 55: 16323-16333

[51] Aboonasr Shiraz MH, Zhu HZ, Liu YL, *et al.* Activation-free synthesis of microporous carbon from polyvinylidene fluoride as host materials for lithium-selenium batteries. J. Power Sources, 2019, 438: 227059

[52] Park S-K, Park J-S, Kang YC, Selenium-infiltrated metal–organic framework-derived porous carbon nanofibers comprising interconnected bimodal pores for Li–Se batteries with high capacity and rate performance. J. Mater. Chem. A, 2018, 6: 1028-1036

[53] Park S-K, Park J-S, Kang YC. Metal-organic-framework-derived N-doped hierarchically porous carbon polyhedrons anchored on crumpled graphene balls as efficient selenium hosts for high-performance lithium–selenium batteries. ACS Appl. Mater. Interfaces, 2018, 10: 16531-16540

[54] Yin L-C, Liang J, Zhou G-M, *et al.* Understanding the interactions between lithium polysulfides and N-doped graphene using density functional theory calculations. Nano Energy, 2016, 25: 203-210

[55] Yang M-X, Yan R-Z, Chen L-J and Lin S., Five 3D Co(ii)-MOFs constructed from 5-(2-methylimidazol-1-yl) isophthalic acid and different bis(imidazole) ligands and one of their derivatives as an efficient electrocatalyst for ORR. Dalton Trans., 2022, 10.1039/D2DT02383K

[56] Cui YJ, Abouimrane A, Lu J, *et al.* (De) Lithiation mechanism of Li/SeS_x (x=0–7) batteries determined by in situ synchrotron X-ray diffraction and X-ray absorption spectroscopy. J. Am. Chem. Soc., 2013, 135: 8047-8056

[57] Gu XX, Tong C-J, Rehman S, *et al.* Multifunctional nitrogen-doped loofah sponge carbon blocking layer for high-performance rechargeable lithium batteries. ACS Appl. Mater. Interfaces, 2016, 8: 15991-16001

[58] Xiao ZB, Yang Z, Zhou LJ, *et al.* Highly conductive porous transition metal dichalcogenides via water steam etching for high-performance lithium–sulfur batteries. ACS Appl. Mater. Interfaces, 2017, 9: 18845-18855

[59] Jiang ZP, Zeng ZQ, Hu W, *et al.* Diluted High Concentration Electrolyte with Dual Effects for Practical Lithium-Sulfur Batteries. Energy Stor. Mater., 2021, 36: 333-340

[60] Zhao J, Guo W, Fu Y. Performance enhancement of Li-Se batteries by manipulating redox reactions pathway. Mater. Today Energy, 2020, 17: 100442

[61] Cañas NA, Wolf S, Wagner N, *et al.* In-situ X-ray diffraction studies of lithium-sulfur batteries. J. Power Sources, 2013, 226: 313-319

[62] Mukkabla R, Deshagani S, Meduri P, *et al.* Selenium/graphite platelet nanofiber composite for durable Li–Se batteries. ACS Energy Lett., 2017, 2: 1288-1295

[63] Li Z, Yuan LX, Yi ZQ, *et al.* Confined selenium within porous carbon nanospheres as cathode for advanced Li–Se batteries, Nano Energy, 2014, 9: 229-236

[64] Zhang Q, Wang DF, Yang BW, *et al.* Electrochemical model of lithium-ion battery for wide frequency range applications. Electrochim. Acta, 2020, 343: 136094

[65] Orsini F, Dollé M, Tarascon J-M. Impedance study of the Li/electrolyte interface upon cycling, Solid State Ionics, 2000, 135: 213-221

[66] Lee S, Lee J, Kim W, *et al.* Selenium-infiltrated mesoporous carbon composite cathode for a high-capacity lithium-chalcogen battery: Effects of carbon structure and dopant on the rate-capability and cyclic stability. J. Power Sources, 2018, 408: 111-119

[67] Riegger LM, Schlem R, Sann J, *et al.* Lithium-Metal Anode Instability of the Superionic Halide Solid Electrolytes and the Implications for Solid-State Batteries. Angew. Chem. Int. Ed., 2021, 60: 6718-6723

[68] Zhou JJ, Yang J, Xu ZX, *et al.* A high performance lithium–selenium battery using a microporous carbon confined selenium cathode and a compatible electrolyte. J. Mater. Chem. A, 2017, 5: 9350-9357

[69] Wang P, Sun FH, Xiong SL, *et al.* WSe_2 Flakelets on N-doped Graphene for Accelerating Polysulfide Redox and Regulating Li Plating, Angew. Chem., 2022, 134: e202116048

[70] Qian J, Xing Y, Yang Y, *et al.* Enhanced Electrochemical Kinetics with Highly Dispersed Conductive and Electrocatalytic Mediators for Lithium–Sulfur Batteries, Adv. Mater., 2021, 33: 2100810

[71] Deiss E. Spurious chemical diffusion coefficients of Li^+ in electrode materials evaluated with GITT. Electrochim. Acta, 2005, 50: 2927-2932

[72] Cui GL, Li GR, Luo D, *et al.* Three-dimensionally ordered macro-microporous metal organic frameworks with strong sulfur immobilization and catalyzation for high-performance lithium-sulfur batteries. Nano Energy, 2020, 72: 104685

[73] Zhang Y, Guo Y, Wang BY, *et al.* An integrated hybrid interlayer for polysulfides/selenides regulation toward advanced Li–SeS_2 batteries. Carbon, 2020, 161: 413-422

Supplementary information

Boosting reaction kinetics and shuttle effect suppression by single-crystal MOF-derived N-doped ordered hierarchically porous carbon for high performance Li-Se battery

Synthesis polystyrene spheres (PS): Monodisperse polystyrene spheres with a diameter of 400 nm were synthesized in emulsion polymerization method. In typical, 59 ml of styrene without polymerization inhibitor (clean with 1 M NaOH solution and deionized water) was added into 500 ml of deionized water containing 0.6 g of sodium laurylsulfonate. After bubbling with the nitrogen gas for 15 min, the mixture was raised to 74 °C under stirring and kept for half an hour. Subsequently, 0.2 g of potassium persulfate solution was quickly dumped into the mixture under stirring and continue to react for 24 h under a nitrogen atmosphere. After cooling down to room temperature, a milk-like product containing monodispersed PS spheres were obtained.

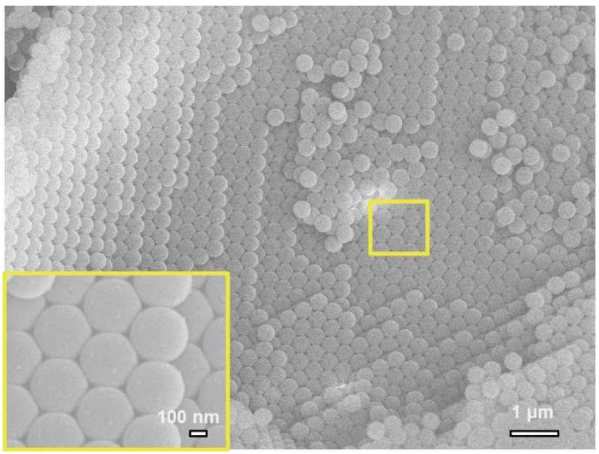

Figure S1 SEM image of ordered PS template.

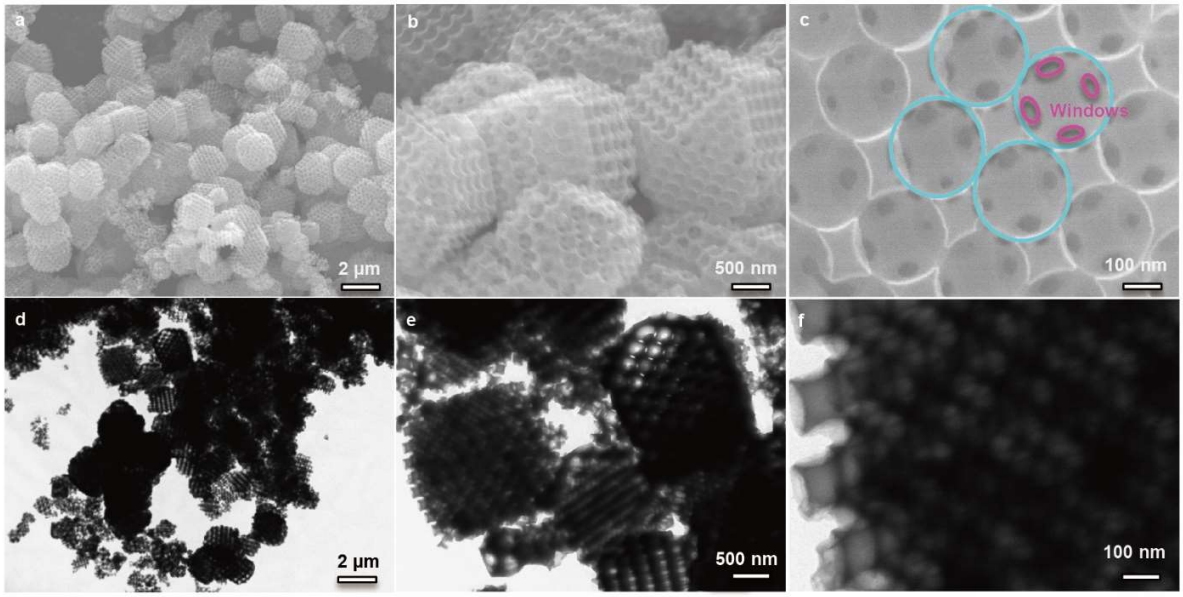

Figure S2 (a-c) SEM images and (d-f) TEM images of S-NOMMC.

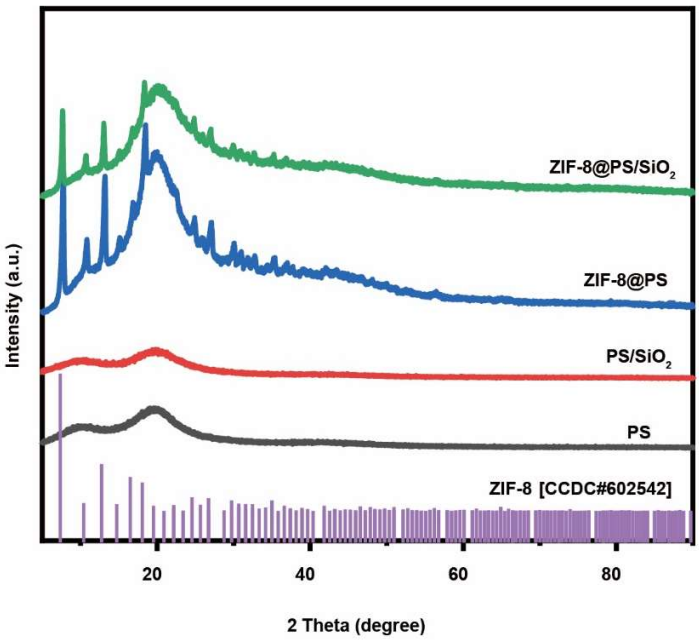

Figure S3 XRD patterns of ZIF-8, PS, PS/SiO_2, ZIF-8@PS and $ZIF-8@PS/SiO_2$.

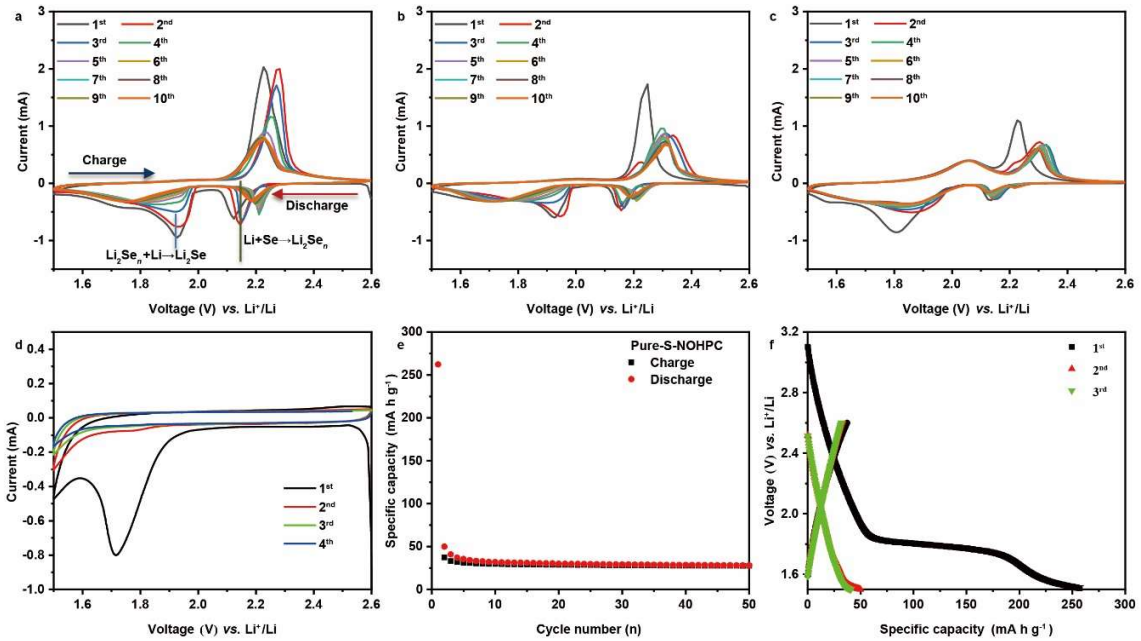

Figure S4 CV curves of (a) Se@S-NOHPC, (b) Se@S-NOMMC, (c) Se@S-NMC and (d) pure S-NOHPC cathode, Cycling performance (e) and the galvanostatic discharge/charge profiles (f) of pure NOHPC at 0.2 C.

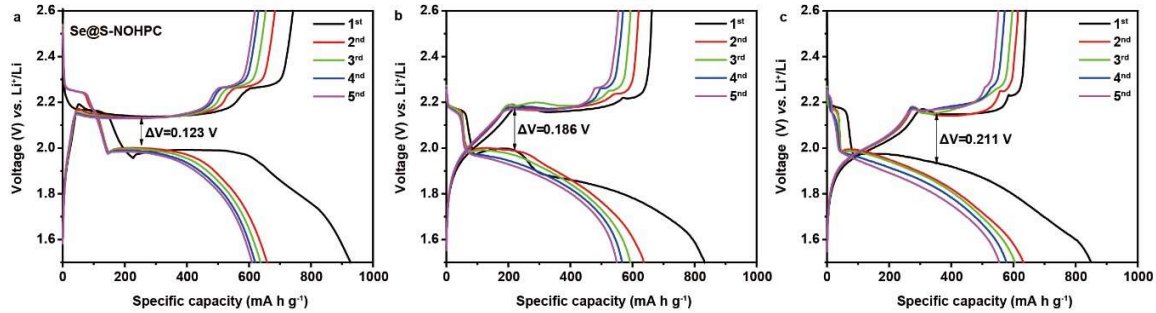

Figure S5 The galvanostatic discharge/charge profiles of Se@S-NOHPC, Se@S-NOMMC, and Se@S-NMC cathodes.

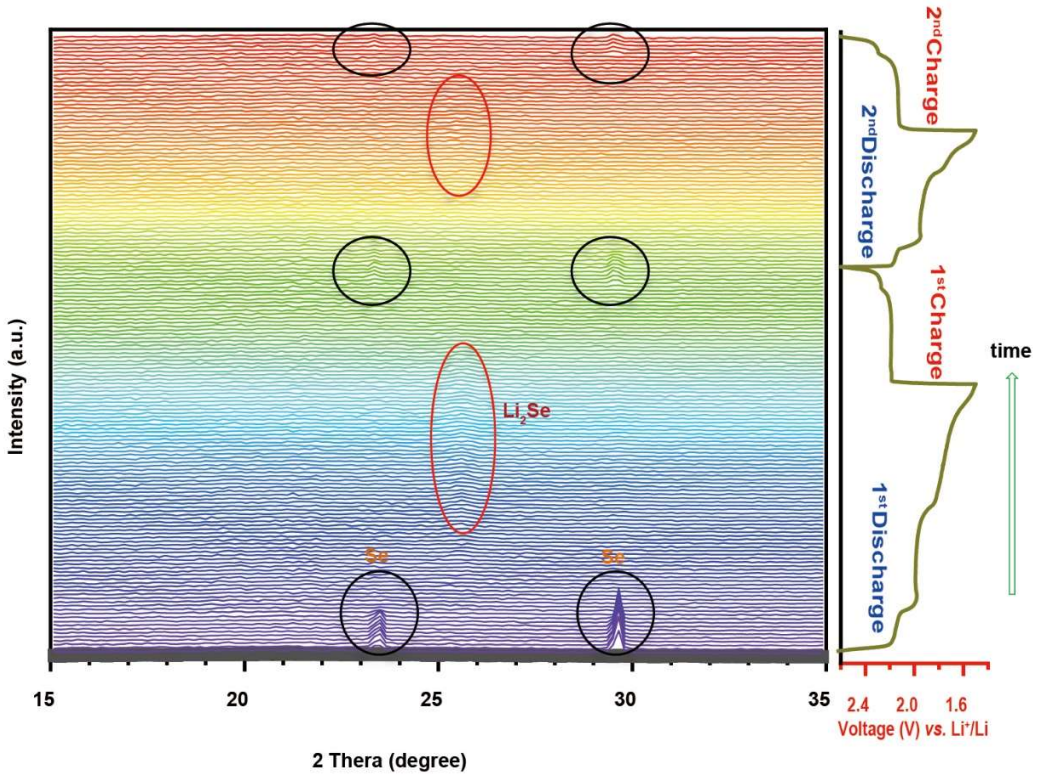

Figure S6 The in situ XRD characterization (2θ: 15–35°) of the Se@S-NOHPC cathode.

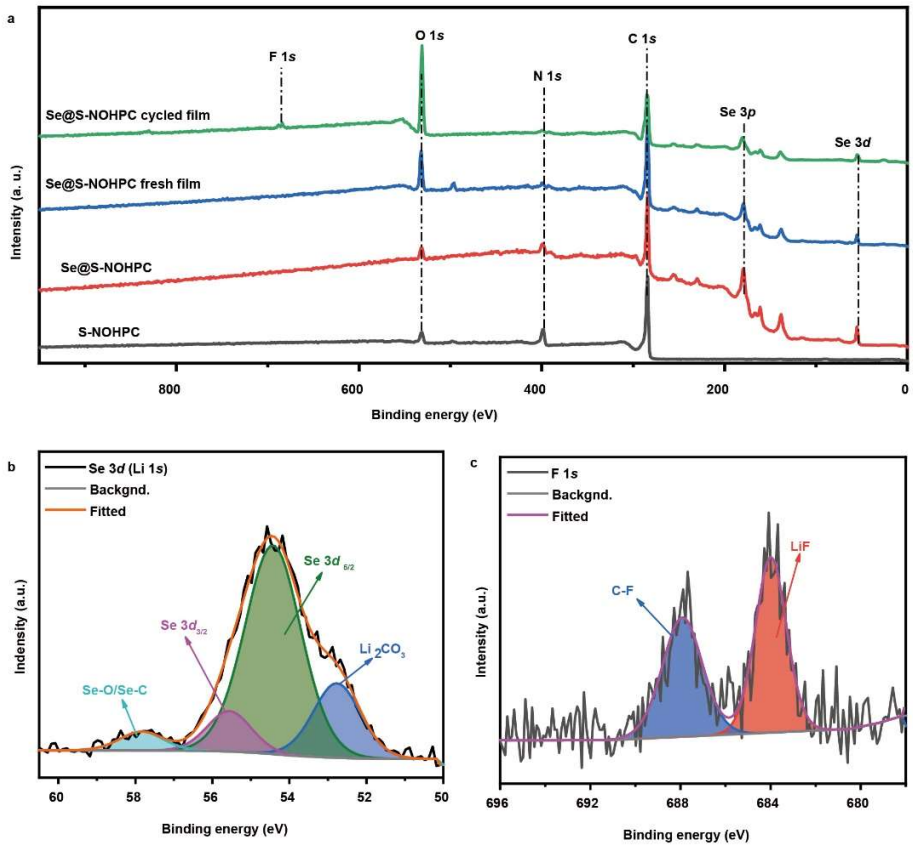

Figure S7 (a) XPS spectra of S-NOHPC, Se@S-NOHPC and corresponding fresh/cycled cathode film, High-resolution spectrum of cycled Se@S-NOHPC: (b) Se3*d* (Li 1*s*), (c) F 1*s*.

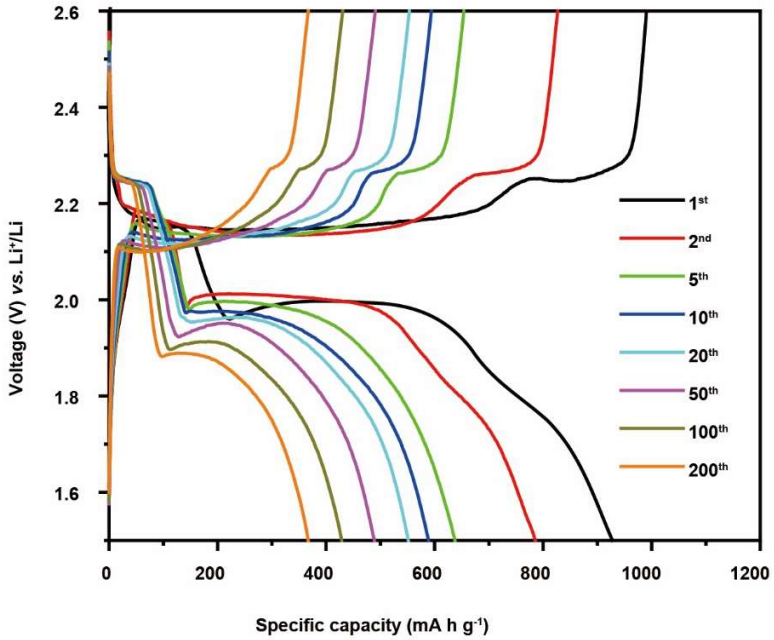

Figure S8 The galvanostatic charge/discharge profiles of Se@S-NOHPC in 200 cycles at the current of 0.2 C.

The lithium species diffusion coefficients D are obtained from the potential response to a small constant current pulse via the formula[1, 2]:

$$D = \frac{4}{\pi\tau}\left(\frac{m_B V_M}{M_B S}\right)^2\left(\frac{\Delta E_S}{\Delta E_t}\right)^2$$

where τ is the constant current pulse time, m_B, V_M, and M_B denote the mass, the molar volume, and the molar mass of the active material, respectively, S is the contact area between electrode and electrolyte, ΔE_s the change of the steady-state voltage during a single-step GITT experiment, and ΔE_t the total change of cell voltage during a constant current pulse τ of a single-step GITT experiment neglecting the IR-drop, as shown in **Fig. S8**. The GITT method allows the evaluation of D as a function of the potential. Because of the change of the concentration of ions and the polarization during the different charge/discharge states, the calculated value of D is varied. Thus, the average value is used to evaluate the chemical diffusion coefficient inside the battery.

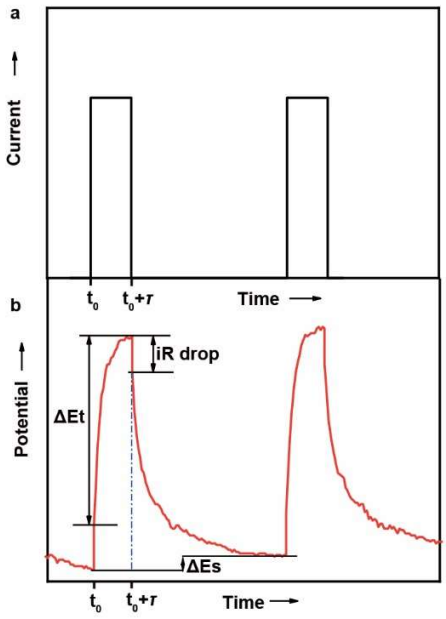

Figure S9 Scheme for GITT experiment: (a) the constant current pulse, (b) Corresponding potential response.

Table S1 Template used in the synthesis process and the pores include in the different carbon host materials.

samples	Method	Pores included
S-NMC	Without template	Micropores
S-NOMMC	PS template	Micro-, mesopores
S-NOHPC	PS/SiO_2 template	Micro-, meso-, macropores

Table S2 Porosity of different carbon host materials and the corresponding Se@C composites.

Samples	S_{BET} ($m^2 g^{-1}$)	Pore volume ($cm^3 g^{-1}$)	Micropore volume ($cm^3 g^{-1}$)
S-NMC	822	0.44	0.38
Se@S-NMC	-	-	-
S-NOMMC	493	0.46	0.23
Se@S-NOMMC	6	-	-
S-NOHPC	1009	0.91	0.44
Se@S-NOHPC	17	0.12	-

Table S3 Value of resistance of EIS (R_{EIS}), charge transfer resistance (R_{ct}) and lithium species diffusion coefficient (D).

Samples	R_{ct} of raw (Ω)	R_{EIS} at 5th (Ω)	R_{ct} at 5th (Ω)	D ($cm^2 s^{-1}$)
Se@S-NOHPC	34.4	11.5	7.2	4.44×10^{-10}
Se@S-NOMMC	38.8	16.6	19.7	4.25×10^{-10}
Se@S-NMC	42.9	23.6	50.7	4.59×10^{-11}

Reference

[1] Deiss E. Electrochim. Acta, Spurious chemical diffusion coefficients of Li^+ in electrode materials evaluated with GITT. 2005, 50: 2927-2932.

[2] Dibden J W, Meddings N, Owen J R, et al. Quantitative Galvanostatic Intermittent Titration Technique for the Analysis of a Model System with Applications in Lithium−Sulfur Batteries. ChemElectroChem, 2018, 5: 445-454.

Chapter VI

Polar adsorption and catalytic bifunctional particles suppress the shuttle effect by dual-adsorption catalysis to achieve high performance Li-Se battery

Abstract

Li-Se batteries have attracted increasing attention owing to their high energy density. However, limited by the shuttle effect of the soluble lithium polyselenides (LiPSes: Li_2Se_n, $4 \leq n \leq 8$), there are still certain challenges for their commercialization. Realizing the rapid transformation of LiPSes to Li_2Se and reducing their diffusion out of the cathode are critical issues for achieving both the high specific capacity and long term stability of the battery. In this work, $CoSnO_3$ nanoparticles *in-situ* decorated in interconnected porous multi-walled carbon nanotubes (CNTs) network functionalized with oxyphilic groups and synthesized $CoSnO_3$/CNTs composite. $CoSnO_3$ nanoparticles worked as redox accelerator for the first time to promote the bidirectional conversion of polyselenides by decreasing the reaction energy barrier and accelerating electrochemical kinetics. The interconnected high conductive three dimensional porous structure of CNTs possesses a high surface area is favorable for the fast transfer of electrons and ions, as well as the confinement of Se species. While $CoSnO_3$ nanoparticles tightly rivet the dissolved polar polyselenides by strong chemisorption. Compared with Se@CNTs cathode, the Se@$CoSnO_3$/CNTs cathode achieves a great improvement, exhibiting a high initial discharge capacity of 730 mA h g^{-1} which remains at 330 mA h g^{-1} after 200 cycles. At the high current density of 2 C, the capacity of the Se@$CoSnO_3$/CNTs can reach a value as high as 153 mA h g^{-1}. This work demonstrates the positive effects of introducing polar particles into the porous host materials and reveals their catalytic functional mechanism, giving a clear guiding for suppressing the shuttle effect for the future high-performance batteries.

Keywords: Shuttle effect; Polar particles; Porous $CoSnO_3$; Interconnected carbon nanotubes (CNTs); Chemisorption; Li-Se battery

1. Introduction

Lithium-selenium (Li-Se) batteries, as one of the competitive candidates of energy storage devices, have attracted much attention owing to their higher gravimetric capacity (675 mA h g^{-1}) than that of Li-ion battery (274 mA h g^{-1}). The high volume specific capacity (3253 mA h cm^{-3}) of Se cathode is comparable to that of Li-S batteries (3467 mA h cm^{-3}) but with a much higher electrical conductivity of Se (1×10^{-3} S m^{-1}) than S (5×10^{-28} S m^{-1})[1-3]. However, same with Li-S battery, the shuttle effect also exists in Li-Se batteries. That is due to the solid-liquid-solid electrochemical transformation during discharge/charge process. The dissolved intermediate lithium polyselenides (Li_2Se_n, $4\leq n\leq8$) shift between cathode and anode, leading to the loss of active Se species and the deposition of non-conductive Li_2Se on the anode surface by direct reaction with Li[4, 5]. In addition, due to the low density of the Li_2Se discharge products, the cathode undergoes a volume expansion, resulting in its peeling off[6-8]. The shuttle effect and volume expansion eventually lead to the short lifespan and rapid capacity decay of the Li-Se battery.

To achieve high performance Li-Se batteries, confining lithium polyselenides inside the Se cathode is a promising technology to solve these problems[9]. Porous carbon frameworks that possess strong adsorption towards polyselenides have been largely used[10]. For example, Lei *et al.* and Yan *et al.* respectively dispersed Se into microporous carbon spheres and porous monodisperse carbon spheres, and the obtained electrode materials achieved stable cycling performances[6, 11]. 2D micro-mesoporous carbon nanosheets with high graphitization degree of carbon as Se host material have been proven beneficial for fast Li^+/e^- transfer and high Se utilization[12]. Carbon nanotubes (CNTs) have been studied as host materials in Li-Se batteries due to their unique advantages[13]. Firstly, one-dimensional interconnected CNTs with high degree graphitization can achieve fast electron transport, which is indispensable for rapid Lithiation/Delithiation reactions[14]. Besides, the hollow tube in CNTs provides space for Se loading. Moreover, the interconnected mesh structure is beneficial for ions transfer and also buffers volume expansion caused by the low density of Li_2Se products[15]. Most importantly, CNTs can be easily decorated by oxygen-containing functional groups, which provide sites for *in-situ* growth of target particles on their surfaces[16, 17]. Given these advantages, considerable materials such as CNTs@graphene/CNTs[18], CNTs/MXene[19] and CNTs microspheres[20] were synthesized and applied in batteries.

However, the weak adsorption strength of the non-polar carbon material is insufficient to ensure that the polar polyselenides are anchored inside[21-23]. Density functional theory (DFT) calculations indicate that oxygen-rich, nitrogen-rich and sulfur-rich groups have high affinity for lithium species and exhibit high adsorption strength to polyselenides[24, 25]. Thus, introducing polar sites with these lithiophilic groups in carbon host materials is a promising strategy to enhance the adsorption of lithium polyselenides[26]. Doping carbon host with heteroatom is proved to be one of the effective ways to achieve the strong chemisorption. Song *et al.* fabricated N-doped core-shell hierarchically porous carbon frameworks, the binding energy between Li_2Se and substrate was increased from 1.66 eV on graphene to 4.49 eV on the N doped carbon host, which relieved the shuttle effect to some extent[27]. Mendes *et al.* dispersed Se in the N, S, O tri-doped mesoporous carbon and the battery with obtained composite performed a good cycle stability[28]. However, the very limited adsorption sites and reduced conductivity due to doping-induced breakage of the conjugation structure motivate researchers to seek more effective selenium fixation strategies. Introducing the polar particles into the cathode framework, such as metal oxides, nitrides and sulfides, where the elements of N, O, S have a strong affinity with lithium polyselenides, have become a simple and promising method to suppress the shuttle effect. Due to the high electronegativity of oxygen, the binding energy contribution of Li–O is higher than that of Li–N and Li-S[29-31]. Thus, oxides such as TiO_2[32], Al_2O_3[33], CeO_2[34] have been introduced into the carbon frameworks. It is proven that these polar particles have strong adsorption to the polar polyselenides and could tightly fix them inside of the cathode.

Besides of strong chemisorption to polyselenides, it proved that the transition metal oxides (TMO) can well work as catalyst to reduce the reaction energy barrier in the discharge/charge process[35]. Transition metal oxides such as MnO_2[36], V_2O_5[37], MoO_3[38, 39] have been used in batteries and performed the functions of adsorption and catalytic. Besides their appropriate adsorption strength to polyselenides, increasing the surface area of these low conductive polar particles is essential to ensure quick Li^+ transfer capability. Amorphous $CoSnO_3$ with porous structure is very well suitable for its higher density of catalytically active sites[40]. Moreover, the diffusion limitations in conventional heterogeneous catalysis no longer exists due to its porous structure[41]. Since the two types of metal elements have different expansion coefficients, the binary transition-metal oxides could function as a soft matrix to buffer the volume expansion[42, 43]. Regarding to the $CoSnO_3$, Co is used as a conductive parts, and Sn is used as a buffer matrix

parts[44]. These $CoSnO_3$ polar nanoparticles can therefore more efficiently confine the dissolved polyselenides and catalyze the lithiation/delithiation reaction. Due to its numerous advantages, the amorphous $CoSnO_3$ was applicated in fields of Li-ion battery[45-47], Li-S battery[48], Na-ion battery[49, 50], Li-O_2 battery[51] and photocatalysis[52].

In this work, $CoSnO_3$ decorated oxyphilic groups functionalized CNTs porous framework was synthesized by a facile co-precipitate method. The obtained $CoSnO_3$/CNTs composite was used as advanced Se host in Li-Se battery to suppress the shuttle effect. The excellent electrical conductivity and porous structure of interconnected CNTs and the enhanced chemisorption and transformation of LiPSes by polar $CoSnO_3$ particles is beneficial the electrochemical reaction. The Se@$CoSnO_3$/CNTs cathode thus achieves a great improvement in battery performance with a high specific capacity of 730 mA h g^{-1}, remains at 330 mA h g^{-1} after 200 cycles. Even at a high rate of 2 C, the capacity can reach 153 mA h g^{-1}. The higher value of Binding Energy (E_B) of $CoSnO_3$/CNTs to polyselenides than CNTs reflects the enhanced adsorption. The reduced free energy in the lithiation process reveals the catalytic function of $CoSnO_3$ by loosening some bonds inside of polyselenids to be easily opened. The result reflects combining polar particles with the conductive carbon frameworks is a simple and effective method to improve the electrochemical performance of Li-Se battery.

2. Experimental

2.1. Chemicals: Tin (IV) chloride ($SnCl_4$, 98%, Sigma-Aldrich), cobalt (II) chloride ($CoCl_2$, 97%, Alfa Aesar), trisodium citrate dihydrate ($C_6H_5Na_3O_7 \cdot 2H_2O$, 99%, Roth), ethanol (absolute, ≥ 99.8%, Fisher Chemical), sodium hydroxide (NaOH, ≥ 98%, Roth), carbon nanotubes (CNTs, >96%, Nanografi Nano Technology), lithium selenide (Li_2Se, 99.95%, Xian function material group Co. Ltd.) and selenium (~100 mesh, ≥ 99.5%, Sigma-Aldrich). All the chemicals involved in this work were of analytical grade and were used without further purification.

2.2. Preparation of functionalized CNTs: 1 g CNTs were dispersed in a 200 ml mixture of H_2SO_4 and HNO_3 with a volume ratio of 1:3 and refluxed at 70 °C for 4 h. The mixture was then diluted and washed with deionized water until pH 7 was reached. Finally, the functionalized CNTs rich with -COOH group were obtained by filtration and overnight drying at 60 °C.

2.3. Synthesis of $CoSn(OH)_6$/CNTs: 200 mg of functionalized CNTs were dispersed in 175 ml deionized water and sonicated for 30 min. Then, 1.19 g $CoCl_2$ and 1.47 g sodium citrate dihydrate

were dissolved in the above CNTs dispersion and marked as solution A. 1.75 g $SnCl_4$ was dissolved in 25 ml ethanol and marked as solution B. Solution B was then poured into solution A under stirring. After 30 min, 25 ml of a NaOH (2 M) aqueous solution was added dropwise and kept stirring for 2 h. The $CoSn(OH)_6$/CNTs was obtained by centrifugation and washed with deionized water and ethanol for three times, respectively. Finally, the obtained sample was dried overnight at 50 °C. As a comparison, $CoSn(OH)_6$ nanocubes without CNTs were synthesized using the same process, except for the absence of CNTs in solution A.

2.4. Preparation of $CoSnO_3$/CNTs: The obtained $CoSn(OH)_6$/CNTs composite was placed in a tubular furnace and calcined stepwise at each temperature of 150 °C, 300 °C and 500 °C for 2 h under argon atmosphere at a ramp rate of 2 °C min^{-1}. After cooling, the $CoSnO_3$/CNTs composite was obtained. The reference $CoSnO_3$ was obtained by annealing $CoSn(OH)_6$ in the same process.

2.5. Synthesis of Se@$CoSnO_3$/CNTs composite: The Se@$CoSnO_3$/CNTs composite was fabricated by melting-diffusion method. Specifically, the as-prepared $CoSnO_3$/CNTs and Se powder were fully mixed by mortar grinding at a mass ratio of 1:2. Subsequently, the mixture was moved to a tubular furnace and heated at 260 °C for 20 h at a ramp rate of 2 °C min^{-1} under argon atmosphere. The temperature was further increased to 300 °C and purged for another 2 h for surface Se removal. After cooling to room temperature, the Se@$CoSnO_3$/CNTs composite was obtained. For comparison, CNTs and $CoSnO_3$ were treated in the same way and the products were named as Se@CNTs and Se@$CoSnO_3$, respectively.

2.6. Preparation of Li_2Se_6 solution: Li_2Se and Se powder with the molar ratio of 1:5 were added into a mixed solution of 1,3-dioxolane (DOL)/1,2-dimethoxyethane (DME) (v/v = 1/1). After stirring at 60 °C for 12 h in the glovebox, the red brown Li_2Se_6 solution was obtained. The concentration of Li_2Se_6 solution was 0.01 M.

2.7. Visualized Li_2Se_6 absorption measurement: 20 mg of the dried host materials ($CoSnO_3$, CNTs, and $CoSnO_3$/CNTs) were added to 20 mL of a Li_2Se_6 solution (2 mM) and stirred for 10 min followed by stewing in the glovebox. After 20 h of polyselenides (Li_2Se_6) adsorption by the host materials, the supernatant was extracted and diluted for UV-vis measurement. The precipitate was collected and washed with DME for further XPS analysis.

2.8. Li_2Se_6 based symmetric cell assembly and electrochemical test: The electrodes were fabricated by coating the slurry of host materials ($CoSnO_3$, CNTs, or $CoSnO_3$/CNTs), Super P, and

sodium alginate (SA, Sigma-Aldrich) with a mass ratio of 8:1:1 with an appropriate amount of deionized water as solvent on aluminum foil and dried under vacuum at 60 °C for 12 h. The obtained 14 mm disc electrodes served as working and counter electrodes at the same time, glass microfiber filters (GF/D, Whatman #1823-150) as separator and Li_2Se_6 solution (0.01 M) as electrolyte. Then, the cyclic voltammetry (CV) and Electrochemical impedance spectroscopy (EIS) of the assembled symmetric cells were tested.

2.9. Materials characterization

The morphology of the synthesized host materials and their corresponding Se/host composites was investigated by field emission scanning electron microscopy (FESEM, JSM-7500F) at 5 kV and transmission electron microscopy (TEM, Tecnai 10) at 100 kV. High-angle annular dark-field scanning transmission electron microscopy (HAADF-STEM), high-resolution transmission electron microscopy (HRTEM), and selected-area diffraction (SAED) were performed using a Thermo Fisher Talos microscope fitted with a Super-X energy-dispersive X-ray spectroscopy (EDX) system operated at 200 kV. The crystalline phase were investigated by X-ray diffraction (XRD, PANalytical X'pert Pro) with Cu K_α radiation (λ=1.5418 Å). The *in-situ* XRD was carried out in STOE STADI-MP powder diffractometer with Cu $K\alpha_1$ radiation (λ=1.54056 Å) in Bragg–Brentano geometry The thermogravimetric analysis (TGA) measurements were carried out on Mettler Toledo TGA/DSC3+ analytical instrument to determine the Se percentage in the Se/host composites from 25 to 800 °C with a heating rate of 2 °C min^{-1} under nitrogen atmosphere. The Brunauer-Emmett-Teller (BET) was employed by N_2 physisorption using ASAP 2420 apparatus (Micromeritics Instrument Corp., USA) at 77 K to analyze the surface area and pore size distribution. X-ray photoelectron spectroscopy (XPS) analysis was performed in an Thermo Scientific K-Alpha XPS system (Thermo Fisher Scientific, UK) with a monochromatic Al Kα X-ray radiation to study the surface chemical states of the samples. The UV–vis analysis was performed on Perkin Elmer 750s UV/Vis/NIR spectrophotometer.

2.10. Electrochemical measurements

The CR2032 coin-type cells were assembled in an Ar-filled glove box (O_2 and H_2O<1 ppm, Vigor-SG1200/750TS, LTD, Suzhou) to measure the electrochemical performance of the synthesized cathodes. The Se/host composite, Super P and sodium alginate with a mass ratio of 8:1:1 were mixed and ball-milled with deionized water as solvent to get the slurry. Then the

obtained slurry was coated on an aluminium foil and dried overnight under vacuum at 60 °C. The Se cathode was obtained by cutting the coated aluminium foil into discs with a diameter of 14 mm. The cell was layer constructed with selenium cathode, Whatman glass microfiber filters (GF/D) separator, and lithium foil anode. Commercial 1.0 M LiTFSI in DME/DOL (1:1, *v/v* by volume) with 1.0% $LiNO_3$ additive was used as the electrolyte. The CV and EIS measurements of the Li-Se cells and symmetric cells were performed on an LK 2005A electrochemical workstation at 0.1 mV s^{-1} in the voltage range of 1.5–2.6 V (*vs.* Li^+/Li) and frequency range of 100 kHz–0.01 Hz with an AC voltage amplitude of 5 mV, respectively. Galvanostatic discharge/charge performance was conducted on a Land CT2001A multi-channel battery testing system in the voltage range of 1.5–2.6 V (*vs.* Li^+/Li) at different current densities. The galvanostatic intermittent titration technique (GITT) measurement was also carried out on the Land CT2001A multi-channel battery testing system with a repeat of 10 min discharge at the current of 0.1 C and 40 min relax until the voltage reached 1.5 V, followed by charging to 2.6 V in the same process. All the electrochemical measurements were carried out at room temperature.

3. Results and discussion

3.1. Structural analysis

The synthesis process of the Se@$CoSnO_3$/CNTs composite is illustrated in **Fig. 1a**. Firstly, the CNTs were treated in an acid solution (H_2SO_4/HNO_3=1:3 in volume) as to functionalize CNTs by introducing the oxygen-containing functional group $–COO^-$ at their surface[53, 54] (Step 1). The carbon elements at the tips of the CNTs are composed of high curvature pentagonal ring and the defects generated in the CNTs growth have high energy and much more active, they undergo an easier reaction with the acid, resulting in the opening up of the CNTs tips and introduction of –COO- group during the oxidation treatment. The opened bare hollow tubes inside of CNTs are accessible for Se infiltration. When the Co^{2+} and Sn^{2+} were introduced into functionalized CNTs solution, the metal cations would be tightly fixed on the CNTs surface due to their strong interaction with $–COO^-$, where the $CoSn(OH)_6$ crystal seeds started to *in-situ* grow when the dissolution environment is adjusted to alkaline (Step 2). After calcination, $CoSn(OH)_6$ dehydrates to $CoSnO_3$, leaving some pores inside the $CoSnO_3$ nanocubes (Step 3). Finally, Se is loaded in $CoSnO_3$/CNTs by melting-diffusion method and the Se@$CoSnO_3$/CNTs composite is obtained (Step 4).

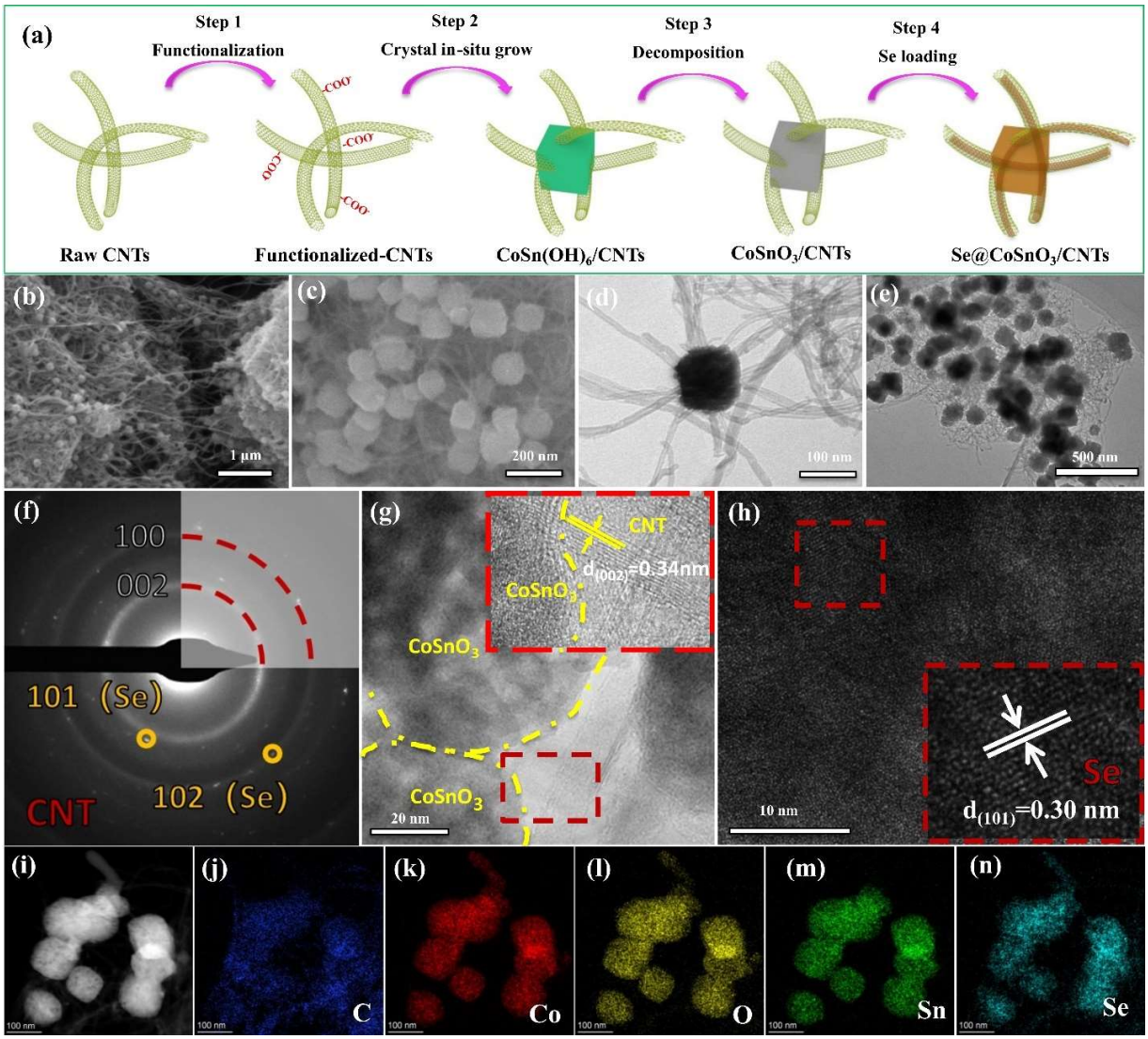

Fig. 1 (a) Schematic illustration of Se@$CoSnO_3$/CNTs synthesis process. (b, c) SEM images of $CoSnO_3$/CNTs, (d) TEM image of $CoSnO_3$/CNTs, (e) TEM image of the Se@$CoSnO_3$/CNTs and (f) corresponding SAED pattern, (g, h) HRTEM image of Se@$CoSnO_3$/CNTs, the enlarged HRTEM image of the area indicated by the red box, (i) HAADF-STEM image of Se@$CoSnO_3$/CNTs and corresponding EDX elemental maps of: (j) C (blue), (k) Co(red), (l) O (yellow), (m) Sn (green) and (n) Se (indigo).

SEM images of the $CoSn(OH)_6$ nanocubes with a uniform size of ~100 nm are shown in **Fig. S1a** and **b**. After calcination, $CoSn(OH)_6$ nanocubes lose bound water to form $CoSnO_3$ particles (**Fig. S1c** and **d**), which maintain the original morphological characteristics while generating pores inside. The SEM images in **Figs. 1b** and **c** show the morphologies of $CoSnO_3$/CNTs at different magnifications. The CNTs are interconnected to form a loose sponge structure, which not only facilitates the electronic transmission but also accelerates the transfer of the electrolyte and the ions.

Moreover, the $CoSnO_3$ particles with the uniform size of 100 nm are *in-situ* grown and homogeneously distributed on the surface of the interconnected CNTs. In the TEM image of $CoSnO_3$/CNTs (**Fig. 1d**), several CNTs penetrate one $CoSnO_3$ particle, which ensures that the particle is tightly fixed in its position. Therefore, the $CoSnO_3$/CNTs composite with interconnected CNTs and *in-situ* grown porous $CoSnO_3$ was obtained. The Se@$CoSnO_3$/CNTs composite in **Fig. 1e** indicates that the morphology of the $CoSnO_3$/CNTs was well maintained after Se was infiltrated and dispersed into the structure. In **Fig. 1f**, two diffraction ring of typical CNTs and slight Se ring were detected in the inserted SAED pattern of the entire area of **Fig. 1e** but absence of any diffraction ring of $CoSnO_3$, which reflect that the $CoSnO_3$ is in amorphous and also some Se in crystalline state. HRTEM image in **Fig. 1g** shows the porous $CoSnO_3$ particles and the pass through CNTs. The enlarged HRTEM image of the area indicated by the red box displays the lattice fringe values of 0.34 nm corresponding to (002) crystal plane of CNT and the $CoSnO_3$ is further confirmed in amorphous phase by the disordered range. The HRTEM image of $CoSnO_3$/CNTs in **Fig. 1h** shows some ordered atoms area. By the enlarged HRTEM image of the area indicated by the red box, (101) plane of crystalline Se is detected with the lattice fringe values of 0.3 nm, indicating there have Se in amorphous state. The HAADF-STEM image in **Fig. 1i** and corresponding EDX elemental maps in **Fig. 1j**–**n** are well overlapped, indicating that the elements of the particles of $CoSnO_3$ is uniformly distributed in the interconnected CNTs and the Se is well dispersed in the $CoSnO_3$/CNTs host.

XRD was used to investigate the phase structure of the synthesized materials. The XRD patterns of $CoSn(OH)_6$, $CoSnO_3$, CNTs and the $CoSnO_3$/CNTs composite are shown in **Fig. S2a**. The diffraction peaks of $CoSn(OH)_6$ are fitted well with its typical perovskite hydroxide crystal structure (PDF#13-0356), which reflects the successful synthesis of $CoSn(OH)_6$ crystals[55]. After calcination, the $CoSn(OH)_6$ is dehydrated to $CoSnO_3$[48, 56]. The XRD pattern of the obtained $CoSnO_3$ shows two broad peaks centered at 34 and 52° instead of its characteristics peaks (PDF#28-1236), suggesting the $CoSnO_3$ nanocubes are in amorphous state[57]. It is important to note that the amorphous $CoSnO_3$ is different from the mechanical mixture of CoO and SnO_2 crystals, as shown in **Fig. S2b**. The XRD pattern of CNTs exhibits its typical peak pattern[58]. The strong (002) peak located at 26.4° depicts a typical graphitic feature with a high degree of crystallinity, whereas the diffraction peak located at 42.8° is associated with the (100) diffraction peak from hexagonal graphite[59, 60]. For $CoSnO_3$/CNTs, broad peaks belonging to $CoSnO_3$ (34 and 52°) and CNTs (26.4

and 42.8°) are detected in the same pattern, indicating that the $CoSnO_3$ particles are successfully grown on the surface of CNTs. In **Fig. 2a**, the characteristic peaks corresponding to the standard XRD pattern of trigonal-phase selenium are observed in different Se@host composites, indicating that selenium was successfully loaded in the host materials of $CoSnO_3$, CNTs, and $CoSnO_3$/CNTs[61].

The surface area and porosity of CNTs, $CoSnO_3$, $CoSnO_3$/CNTs, and their corresponding Se@host composites are analyzed by the N_2 adsorption-desorption experiment. The isotherms and pore size distribution are shown in **Fig. 2b** and **Fig. S2c-d**, respectively. The N_2 adsorption-desorption isotherm of CNTs (**Fig. 2b** in red color) exhibits a typical type II shape, with a rapid N_2 uptake at a very low p/p_0 (about 0.01), indicating the presence of micropores in the CNTs[62, 63]. The adsorption curve displays a sharp increment at p/p_0 of 0.9, a characteristic of large mesopores in functionalized CNTs. A small closed adsorption/desorption hysteresis loop is observed due to the mesopores with a capillary condensation[64]. The mesopores size distribution was analyzed by Barrett–Joyner–Halenda (BJH) method. The pore size distribution in **Fig. S2c** indicates that CNTs display a bimodal distribution of mesopores centered around 3 and 40 nm**,** which corresponds to the size of the inner CNT diameter and the pores generated by the aggregated CNTs[65, 66], respectively. The micropore size distribution was calculated using the Horvath–Kawazoe (HK) model. The pore size distribution in **Fig. S2d** shows that the micropores in CNTs are centered at 0.7 nm, which mainly come from the exposed innerpores of tip-opened CNTs[67, 68]. The presence of significant micropore reflects the successful opening of the nanotube tips by acid functionalization, which is beneficial for the active Se loading. The isotherm of $CoSnO_3$ in **Fig. 2b** (green color) performs a typical type IV shape with a hysteresis loop at p/p_0 of 0.8–0.9, characteristic of mesoporosity. The continuous N_2 uptake at p/p_0 high p/p_0 of 0.9–1.0 indicates the existence of macropores[69]. The pore size distribution of $CoSnO_3$ in **Fig. S2c** confirms that the mesopore size is 18 nm. The existence of mesopores is induced by the loss of bound water by the transformation of $CoSn(OH)_6$ to $CoSnO_3$ during high temperature calcination. The presence of the macropores can be attributed to the aggregation of the $CoSnO_3$ nanoparticles. The isotherm of $CoSnO_3$/CNTs in **Fig. 2b** (black color) is a type II shape with a high N_2 uptake at low p/p_0 of 0.01 and high p/p_0 of 0.9, characteristic of micro- and mesoporosity. The micropores and bimodal distributed mesopores are centered at ~0.7 nm (**Fig. S2d**) and ~3, ~40 nm (**Fig. S2c**), respectively. Due to the introduction of $CoSnO_3$ into interconnected CNTs, the mesopores formed by the

aggregation (centered around 40 nm in **Fig. S2c**) are increased to some extent. Moreover, the $CoSnO_3$ particles are uniformly dispersed in the interconnected sponge-like CNTs, thus the macropores caused by the $CoSnO_3$ particles aggregation (range of over 100 nm in **Fig. S2c**) disappear in the $CoSnO_3$/CNTs composite. After Se was located in the host materials, the N_2 uptake is greatly reduced due to voids being occupied and the Se@CNTs and Se@$CoSnO_3$/CNTs exhibit type II isotherm. The surface area and pore volume information of the different host materials and corresponding Se@host composites are shown in **Table 1**. $CoSnO_3$ has a low surface area and pore volume of 44 m^2 g^{-1} and 0.3 cm^3 g^{-1}, respectively. Owing to the loose sponge structure and the hollow pores inside, CNTs achieve high specific surface area and pores volume of 265 m^2 g^{-1} and 1.3 cm^3 g^{-1}, respectively. The surface area and pores volume of $CoSnO_3$/CNTs are 308 m^2 g^{-1} and 1.7 cm^3 g^{-1}, respectively. The best porosity is due to the effective combination of CNTs and $CoSnO_3$. The surface area and pore volume of the Se@host composites decreased sharply to a lesser value, reflecting that the Se is successfully infiltrated into the pores of the host materials[70].

The Se (0) content of the Se@host composites was analyzed by TGA measurement. **Fig. 2c** shows that the Se evaporation occurs at the temperature of 350 to 480 °C. The Se evaporation start and end temperature are related to the interaction strength between host materials and Se. Se@CNTs has the lowest start/end evaporation temperature due to the weak interaction between Se and non-polar pure carbon. While, the Se evaporation in Se@$CoSnO_3$ starts and ends at higher temperature than Se@CNTs owing to the strong chemisorption of the oxygen-rich $CoSnO_3$ to the selenium[4, 71]. Benefiting from the introduction of polar $CoSnO_3$ particles, selenium is well confined inside the $CoSnO_3$/CNTs composites. The Se@$CoSnO_3$/CNTs composites also achieve improved evaporation temperature due to the enhanced interaction brought by the $CoSnO_3$ polar particles. From the weight loss of the TG curves, the Se contents of Se@$CoSnO_3$, Se@CNTs and Se@$CoSnO_3$/CNTs are calculated to be 62, 68 and 60 wt.%, respectively. The highest value of the Se proportion in Se@CNTs is due to the much higher surface area and pores of CNTs.

The chemical composition and surface chemical state of $CoSnO_3$/CNTs and Se@$CoSnO_3$/CNTs composites were investigated by XPS. The overall XPS spectrum is shown in **Fig. 2d**. The peaks of Co, Sn and O belonging to $CoSnO_3$ are identified in the survey spectrum of $CoSnO_3$/CNTs, which match well with the elements of the composites. After infiltration of Se, the peaks corresponding to Se were detected in the survey spectrum of Se@$CoSnO_3$/CNTs, indicating

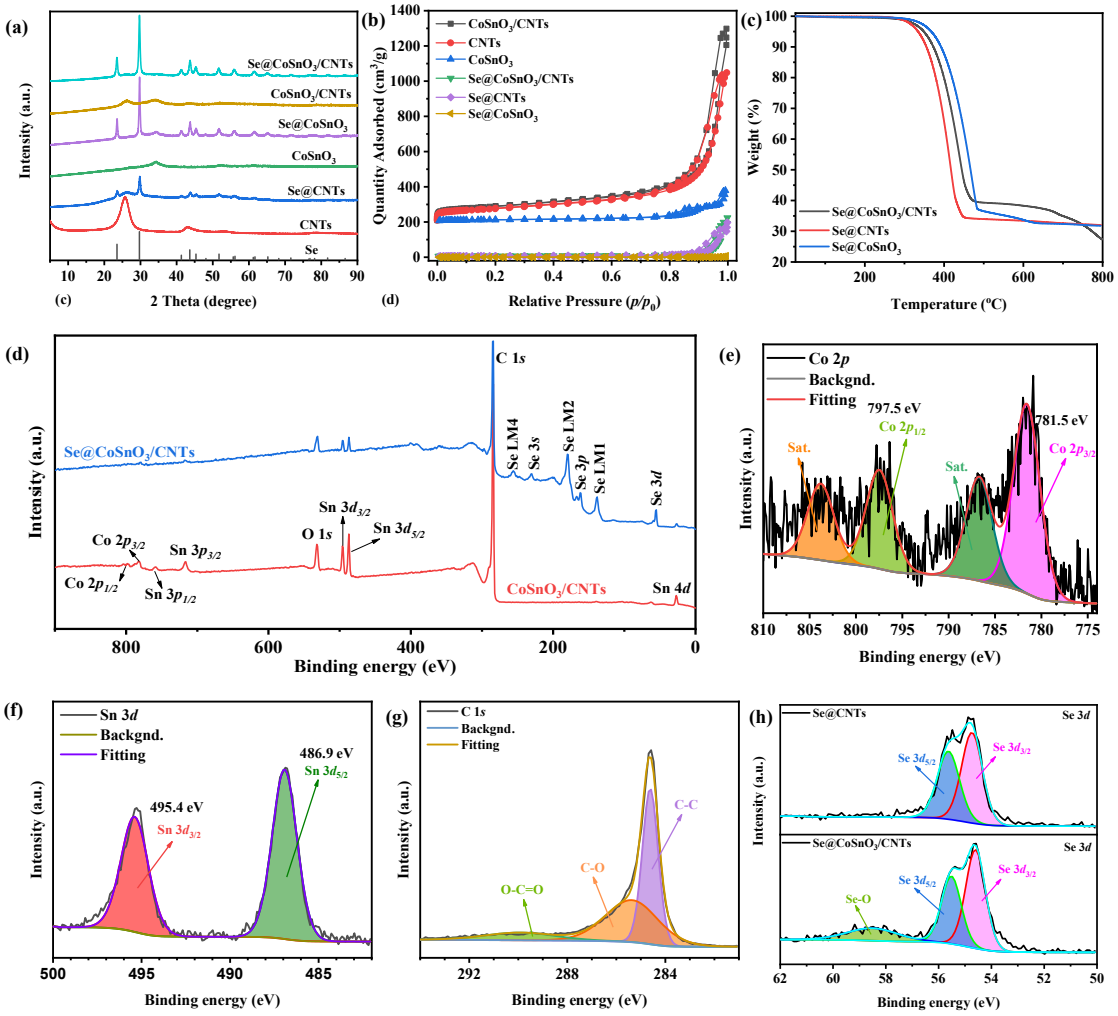

Fig. 2 (a) XRD patterns of Se, host materials and corresponding Se@host composites. (b) N_2 adsorption-desorption isotherms. (c) TGA plots of prepared Se@$CoSnO_3$, Se@CNTs and Se@$CoSnO_3$/CNTs, respectively. (d) The overall XPS spectra of $CoSnO_3$/CNTs and Se@$CoSnO_3$/CNTs. (e–g) The high-resolution spectrum of Co 2*p*, Sn 3*d*, C 1*s* in $CoSnO_3$/CNTs, respectively. (h) The high-resolution spectrum comparison of Se 3*d* in Se@CNTs and Se@$CoSnO_3$/CNTs.

the successful introduction of Se into the host material. The peaks of the high-resolution spectrum of Co 2*p* in **Fig. 2e** is deconvoluted into 4 peaks, which are Co $2p_{3/2}$ (781.5 eV), Co $2p_{1/2}$ (797.5 eV) and two satellite peaks at 786.7 and 803.8 eV, respectively, indicating unique presence of Co^{2+} species[72]. The peaks located at 486.9 and 495.4 eV of Sn 3*d* in **Fig. 2f** are characteristic of Sn $3d_{5/2}$ and Sn $3d_{3/2}$, respectively, which are in accordance with the electronic state of Sn^{4+} [47]. The convolution peak at 284.6, 285.4 and 289.9 eV of C 1*s* in **Fig. 2g** are attributed to C–C, C–O and O–C=O, respectively[73]. In **Fig. 2h**, a new peak of Se–O appears at 58.2 eV in Se@$CoSnO_3$/CNTs

compared with Se@CNTs. This may be due to the strong interaction between Se and $CoSnO_3$ particles.

3.2. Electrochemical properties

The obtained Se@$CoSnO_3$, Se@CNTs and Se@$CoSnO_3$/CNTs cathodes were assembled into CR3032 cells for electrochemical performance testing. To analyze the reaction in the discharge/charge process, CV measurement of Se@$CoSnO_3$/CNTs as the representative of the Se@host cathodes was conducted and the result is shown in **Fig. S3a**. Two reduction peaks at 2.12 and 1.93 V are observed, corresponding to the conversion of Se (0) to Li_2Se_n ($4 \leq n \leq 8$) and Li_2Se_n to Li_2Se, respectively[74]. A broad oxidation peak centered at 2.25 V results from the oxidation from the gradual oxidation of Li_2Se to Se. In addition, a small reduction peak appears at the voltage of 1.74 V in the first cycle. This is attributed to the reaction between electrolyte and electrode at low voltage and the formation of a solid electrolyte interphase (SEI) layer[75]. The CV curve of pure-$CoSnO_3$/CNTs was measured to analyze the reaction that occurs in the absence of active Se in the cell. The apparent peak at 1.74 V in pure-$CoSnO_3$/CNTs (**Fig. S3b**) is in good agreement with the CV result of Se@$CoSnO_3$/CNTs, proving that the peak at 1.74 V in Se@$CoSnO_3$/CNTs is produced by SEI formation rather than Se. The appearance of the F 1*s* and the much more increased intensity of the O 1*s* in the XPS spectrum (**Fig. S4a**) of the cycled Se@$CoSnO_3$/CNTs than raw Se@$CoSnO_3$/CNTs, which confirms the production of the SEI layer since these two elements are the main components of SEI layer. The high resolution of Se 3*d* of the cycled Se@$CoSnO_3$/CNTs in **Fig. S4b** has much higher intensity of Se–O due to the strong interaction between Se species and $CoSnO_3$. Moreover, a peak belonging to Li_2CO_3 appears also after the battery running. The high resolution of F 1*s* in **Fig. S4c** can be convoluted into two peaks, corresponding to F–C and LiF, respectively. In CV curves of Se@$CoSnO_3$/CNTs (**Fig. S3a**), the voltage position and the current density of the redox peaks undergo a shift in the first three cycles, which may be also due to the effects of the SEI formation and activation of Se cathode. After that, the curves overlap very well and the reduction peak at 1.74 V disappears as well, which means that the SEI remains stable and the cathode performs excellent electrochemical reversibility and stability[76]. The 5th cycle CV curves of the different composite cathodes are presented in **Fig. 3a**. In the first reduction peak, the Se@$CoSnO_3$ cathode shows the smallest current density and the lowest reduction potential. It indicates the Se@$CoSnO_3$ cathode has the lowest reaction kinetics due to the low conductivity of the $CoSnO_3$ (10^{-8} S cm^{-1})[77]. Owing to the participation of high conductivity of CNTs, the current

density and the value of reduction potential of Se@CNTs and Se@$CoSnO_3$/CNTs have some degree of improvement. Compared with Se@CNTs and Se@$CoSnO_3$, Se@$CoSnO_3$/CNTs shows a higher current density, higher reduction potential and lower oxidation potential. This indicates that Se@$CoSnO_3$/CNTs has the fastest electrochemical reaction kinetics and the lowest reaction resistance due to the synergy effects of CNTs and $CoSnO_3$[78]. It is interesting to note that the Se@$CoSnO_3$ has a higher current density and easier reaction potential at the second reduction and oxidation peaks than Se@CNTs, which is due to the revealing of the catalytic function of $CoSnO_3$ for the control reaction step of polyselenides to Li_2Se. Combining the high conductivity of CNTs and catalytic function of $CoSnO_3$, Se@$CoSnO_3$/CNTs cathode shows fast reaction kinetics and small reaction energy barrier.

The galvanostatic discharge/charge profiles of Se@$CoSnO_3$/CNTs were tested at 0.2 C and the result is shown in **Fig. 3b**. In the discharge profiles, two plateaus are observed at the voltage of ~2.18 and 2.01 V. The first one at 2.18 V is attributed to the conversion of Se to Li_2Se_n intermediate and the second at lower voltage is due to the transformation of Li_2Se_n to Li_2Se. The capacity greatly increases at the second plateau, indicating this step makes the most achievements to the capacity of Li-Se battery. The plateau at 2.25 V in the charge profiles is due to the inverse reaction from Li_2Se back to Se. Similar to the CV result, the first discharge plateau of the galvanostatic discharge/charge profiles also shifts to a higher voltage and the second plateau shifts to lower voltage. The phenomenon may be due to the cells running, when Se activation and SEI formation are finished, the rate-control step of the transformation of Li_2Se_n to Li_2Se is revealed. Moreover, a small bending of the curve at the voltage of 1.74 V appears in the first cycle discharge profile due to the formation of the SEI layer, which is consistent with the CV results in **Fig. 3a**. The plateau change trend of discharge/charge profiles fits well with the CV results, confirming the reaction in the discharge/charge process again.

To further investigate the reactions taking place in the different stages, the *in situ* XRD of cell with Se@$CoSnO_3$/CNTs cathode was measured, as shown in **Fig. 3c**. At the beginning of the discharge, there has an obvious peak of Se. With the lithiation going, the Se gradually disappears and instead the peak of Li_2Se appears. The battery undergoes an inverse reaction in the charge process compared with discharge. Thus, the intensity of the Li_2Se peak decreases and the lithium polyselenides species come back to Se at the end of the charge process. In detail, the discharge process can be derived into three stages (**Fig. S5**). The first stage at the 0–0.2 depth of discharge

(DOD), the peak of crystalline Se is detected and its peak intensity gradually decreases and completely disappears at the DOD of 0.2, which corresponds to the first discharge platform of the discharge curve. With the further depth of discharge, no peak of Se is detected due to all the Se has already transformed to chain polyselenides. This stage is in the DOD range of 0.2–0.6, which occurs at the second platform of the discharge curve, where the Li_2Se_n are transformed from long chain to short chain. After that, the polyselenides are gradually transformed to Li_2Se at the third stage of 0.6–1.0 DOD and the peaks being to Li_2Se are detected. The 1st charge process also can be divided into three stages at depth of charge of 0–0.4, 0.4–0.8 and 0.8–1, corresponding to the reaction Li_2Se to Li_2Se_n, Li_2Se_n shortening and Li_2Se_n back to Se again. Compared with the first discharge/charge cycle, the peaks intensity of Se and Li_2Se in the second cycle become weak because the Se species do not come back to crystalline Se but chain Se, which facilitates further lithiation/delithiation reaction.

The cycle stability performance of Se@$CoSnO_3$/CNTs, Se@CNTs and Se@$CoSnO_3$ is shown in **Fig. 3d**. The initial specific discharge capacity of Se@$CoSnO_3$/CNTs, Se@CNTs and Se@$CoSnO_3$ are 729.9, 898.8 and 605.3 mA h g^{-1}, respectively. The obtained capacity exceeds the theoretical value (675 mA h g^{-1}) because of the formation of the SEI layer and activation of Se. In order to quantify the capacity contributed by the SEI formation, the cell with pure-$CoSnO_3$/CNTs was assembled and tested at the current of 0.2 C, the result is shown in **Fig. S3c**. In the first cycle, the discharge capacity reaches to 232 mA h g^{-1}. Correspondingly, the capacity increases greatly in the platform of 1.8 V also in **Fig. S3d**, the voltage value being consistent with the peak position in **Fig. S3b**. After that, the formed SEI separates the electrolyte and cathode preventing further electrolyte decomposition. The capacity of pure-$CoSnO_3$/CNTs sharply drops to 23 mA h g^{-1} after the first cycle, thus the capacity of Se@$CoSnO_3$/CNTs cathode battery almost comes from the active Se after then. The 2nd cycle capacity of Se@$CoSnO_3$ is 528 mA h g^{-1} and drops to 226.6 mA h g^{-1} at the 200th cycle. The poor electrochemical performance is due to the poor conductivity of the $CoSnO_3$, shortage of space for Se loading and Se pealing caused by volume expansion. Compared with Se@$CoSnO_3$, the 2nd cycle capacity of Se@CNTs improved to 605.6mA h g^{-1} due to better conductivity and porous structure of CNTs for accelerated electrons transfer and Se dispersion. But limited by the weak physical adsorption to polyselenides, the capacity of Se@CNTs decreases to 257.1 mA h g^{-1} after 200 cycles. Combining the advantages of better Se loading and excellent conductivity provided by CNTs as well as the strong chemisorption of polyselenides by

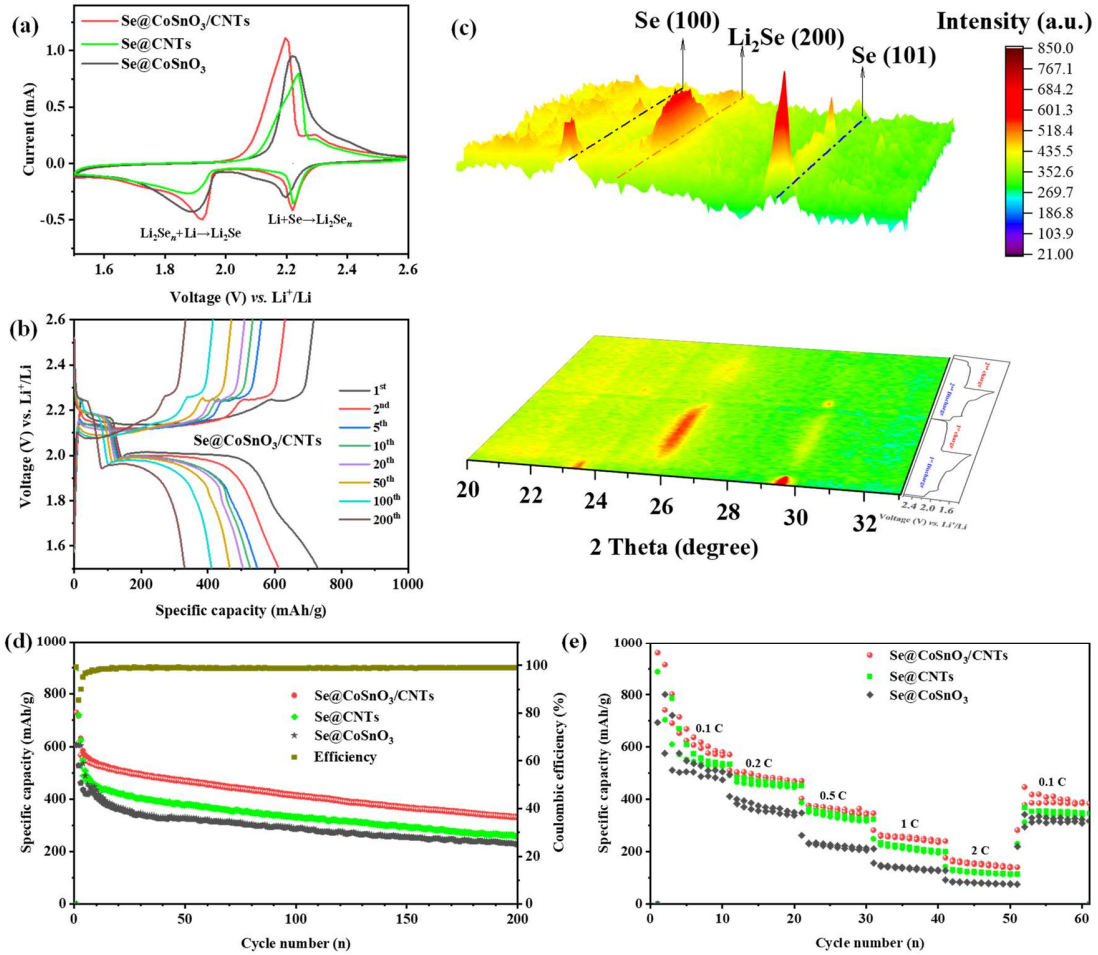

Fig. 3 (a) The CV performance and (b) The galvanostatic discharge/charge profiles of Se@$CoSnO_3$/CNTs. (c) The *in situ* XRD characterization of the Se@$CoSnO_3$/CNTs cathode in 2 discharge/charge cycles. (d) The cycle stability at 0.2 C and (e) Rate capacity at different current densities of Se@$CoSnO_3$, Se@CNTs, Se@$CoSnO_3$/CNTs, respectively.

the polar $CoSnO_3$, the Se@$CoSnO_3$/CNTs cathode exhibits an competitive performance in these three cathodes. The 2nd discharge/charge capacity and 200th capacity of Se@$CoSnO_3$/CNTs are 612/630 and 330.4 mA h g^{-1}, respectively, accompanied with almost 100% Coulombic efficiency. The result reflects that the introduction of $CoSnO_3$ particles in the interconnected CNTs framework formed $CoSnO_3$/CNTs suppresses the shuttle effect by enhancing the adsorption of polyselenides, resulting in a good electrochemical performance of the Li-Se battery.

The rate performance of a series of the designed cathodes at different current densities is shown in **Fig. 3e**. With the increase of the current, the capacity of the battery became lower due to the polarization of electrolyte and the limitation of the rate-control step of the transformation from Li_2Se_n to Li_2Se[79]. The capacity of Se@$CoSnO_3$/CNTs is 578, 485, 366, 254 and 153 mA h g^{-1} at the current of 0.1 C, 0.2 C, 0.5 C, 1 C and 2 C, respectively, while the capacity of Se@$CoSnO_3$ at 2 C is only 83 mA h g^{-1}. The low capacity is due to the slow lithiation/delithiation caused by the poor conductivity of $CoSnO_3$. The capacity of Se@CNTs at high rate (2 C) increase to 121 mA h g^{-1} beneficial from the good electrical conductivity of CNTs, but without the catalytic function of $CoSnO_3$, the polyselenides transformation as the rate-control step is limited. When the current comes back to the current of 0.1 C, the capacity quickly recovers to 418 mA h g^{-1}, indicating the Se@$CoSnO_3$/CNTs has a good rate capability and high reversibility.

The electrochemical performance is related to the charge transfer of the battery. The EIS measurements were investigated to analyze the electron and ion transferability. The Nyquist plots of the raw cathodes in **Fig. 4a** consist of a semicircle in the high-frequency and a straight line in the low-frequency, which correspond to the resistance of charge transfer (R_{ct}) and Warburg impedance (R_w), respectively[80, 81]. The Se@$CoSnO_3$ exhibits the largest R_{ct} value of 48.9 Ω. The poor charge transfer is due to the low electronic conductivity of $CoSnO_3$. The Se@CNTs cathode has a decreased R_{ct} value of 41.6 Ω due to the fast electron transportation of CNTs. While the Se@$CoSnO_3$/CNTs has the smallest R_{ct} (29.4 Ω), the superior charge transferability is due to the good conductivity of interconnected CNTs and the rapid reaction catalysis of $CoSnO_3$. With the battery running, the R_{ct} values of Se@CNTs and Se@$CoSnO_3$/CNTs undergo a decrease because of the activation of the cathode. At the same time, another semicircle at extra high frequency appears for the reason of the resistance brought from the SEI layer (R_{SEI}) that formed on the surface of the cathode material. However, the R_{ct} value of Se@$CoSnO_3$ has an increase due to the $CoSnO_3$ cathode destruction caused by the volume expansion. In the following cycles, the R_{SEI} value of $CoSnO_3$/CNTs and CNTs remains stable, as shown in **Fig. S6a** and **b**, reflecting the formation of the stable SEI on the surface. However, the R_{SEI} of Se@$CoSnO_3$ undergoes a gradual increase, as shown in **Fig. S6c**. That is for the reason that the SEI layer on $CoSnO_3$ electrode surface cracks and reforms due to the volume expansion in the lithiation process, leading to the SEI layer being thicker and thicker. This hinders the electrical contact between the current collector and the active material, increases the diffusion distance of lithium ions, and blocks the smooth deintercalation of

lithium ions, resulting in rapid capacity decay. At the same time, a thicker SEI generates great mechanical stress, which further damages the electrode structure. Combining the CNTs and polar $CoSnO_3$ particles solves the problem of expansion and achieves a stable SEI layer with small impedance. Fast ion transfer and rapid transformation are essential to achieve good electrochemical performance. The ion transfer can be estimated by the GITT measurement, and the transfer of Se_n^{2-} in the system can be reflected in some extent[82, 83]. The ion transfer is related to the response rate to the current given, which can be used to reflect the value of Li species diffusion coefficients (D). The detailed calculation method is described in the Supply Information. The GITT plot and Li species diffusion coefficients from GITT of Se@$CoSnO_3$/CNTs as a representative are shown in **Fig. 4b** and **c**. The average lithium diffusion coefficients D of Se@$CoSnO_3$, Se@CNTs and Se@$CoSnO_3$/CNTs are calculated to be 1.6×10^{-13}, 1.7×10^{-12} and 8.1×10^{-12} cm^2 s^{-1}, respectively. The highest D value of Se@$CoSnO_3$/CNTs indicates the fast Li^+ and Se_n^{2-} transfer. Thus, the fast electron and the ion transfer ensures the improved electrochemical performance of Se@$CoSnO_3$/CNTs cathode.

The adsorption ability of the host materials is analyzed by visualized Li_2Se_6 absorption measurement. As shown in **Fig. 4d inset**, the pure Li_2Se_6 solution has a red brown color. The color of the solution adsorbed by $CoSnO_3$ and CNTs host materials changes slightly. In contrast, the solution adsorbed by $CoSnO_3$/CNTs becomes almost colorless. The supernatants after the adsorption experiments were collected, diluted and the absorption of supernatants were measured by UV-vis spectrometry. As shown in **Fig. 4d**, the peak centered at ~340 nm in the absorption spectrum is attributed to the absorption of Se_6^{2-}[84]. The peak intensity of the solution with CNTs addition is lower than that of the initial Li_2Se_6 solution, which could be attributed to the physical adsorption to the polyselenides. The peak intensity of the solution with $CoSnO_3$ also decreases greatly due to the strong chemisorption between the polar particles and polyselenides. Because of the much higher surface area of $CoSnO_3$ than CNTs, $CoSnO_3$ achieves more adsorption of polyselenides on its surface. For the sample of $CoSnO_3$/CNTs, there is almost no absorption from Se_6^{2-}, which is beneficial from the synergistic effects of the physical adsorption of CNTs and chemisorption of $CoSnO_3$. The enhanced adsorption confines polyselenides inside of pores and their subsequent catalytic conversion, as well as the rapid redox kinetics. To verify the chemisorption of Se_6^{2-} by $CoSnO_3$/CNTs, XPS measurement was performed on $CoSnO_3$/CNTs composite before and after the adsorption experiment. The high resolution Co 2*p* XPS spectrum of

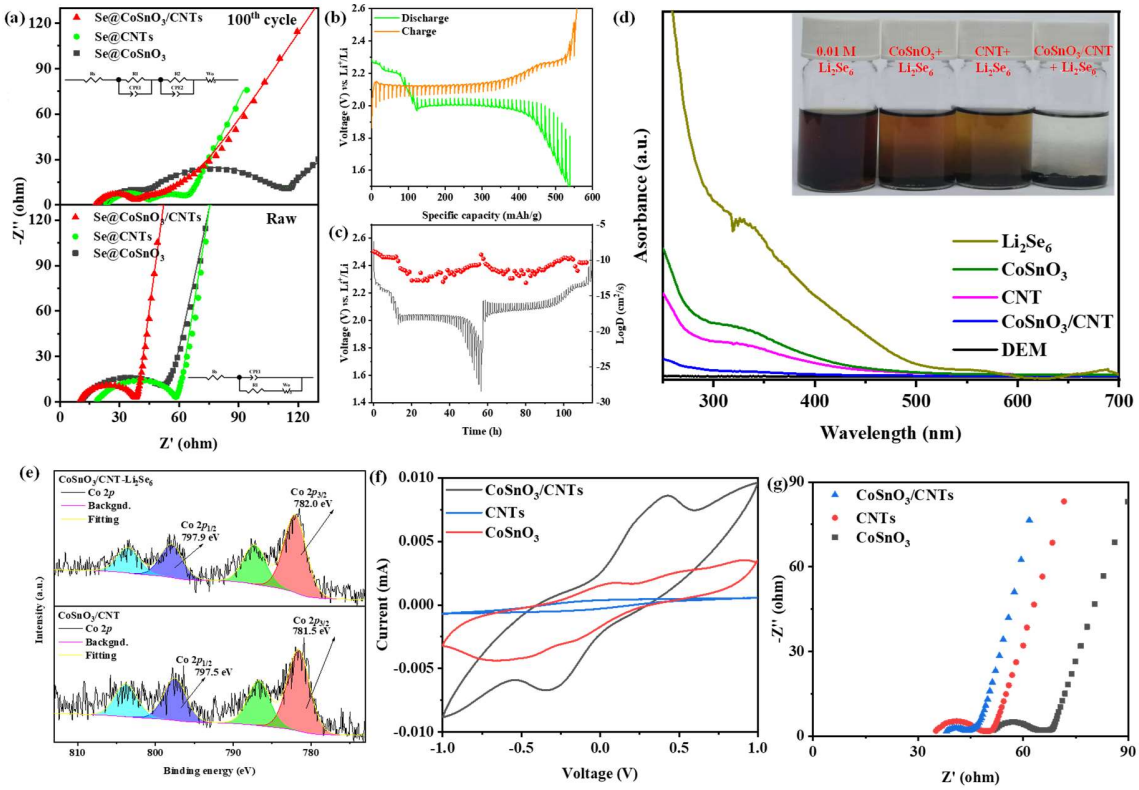

Fig. 4 (a) The Nyquist plots of $CoSnO_3$, CNTs and $CoSnO_3$/CNTs (bottom: raw, top: 100th cycle). (b) GITT plot and (c) Li species diffusion coefficients from GITT of Se@$CoSnO_3$/CNTs. (d) Visualized Li_2Se_6 adsorption experiments of $CoSnO_3$, CNTs, and $CoSnO_3$/CNTs and UV−vis absorption spectroscopy of corresponding supernatants. (e) High-resolution Co 2*p* XPS spectra of pristine $CoSnO_3$/CNTs and $CoSnO_3$/CNT adsorbed by Li_2Se_6 (Li_2Se_6-$CoSnO_3$/CNTs). (f) CV and (h) EIS of symmetrical cells with different electrodes.

$CoSnO_3$/CNTs composite is presented in **Fig. 4e**. After the Li_2Se_6 adsorption, the Co $2p_{3/2}$ peak of $CoSnO_3$/CNTs shifts to higher binding energy, indicating the electrons transfer from Li_2Se_6 to Co due to the interaction between polar $CoSnO_3$ particle and polyselenides[85].

In addition to inhibiting the shuttle effect by enhanced adsorption to polyselenides, another crucial factor is the rapid transformation of Li_2Se_n to Li_2Se[86]. To evaluate the catalytic ability of $CoSnO_3$, the symmetrical cells of $CoSnO_3$, CNTs and $CoSnO_3$/CNTs were assembled and tested. The CV result of different symmetrical cells are shown in **Fig. 4f**. Compared with the CNT symmetrical cell, the $CoSnO_3$ symmetrical cell with Li_2Se_6 electrolyte possesses high current, confirming the catalytic performance of $CoSnO_3$[61, 87]. The $CoSnO_3$/CNTs symmetrical cell achieves further improvement in current density due to the existence of CNTs that increases the

conductivity of the cathode. Further, the EIS of these symmetrical cells was explored and the result is shown in **Fig. 4g**. The $CoSnO_3$ symmetrical cell displayed a smaller charge transfer impedance than the CNTs, indicating the low energy barrier for electron and ion transfer brought by catalytic function of $CoSnO_3$ particles. After adding CNTs, the impedance of $CoSnO_3$/CNTs symmetrical cell had a further decrease due to the synergy of the high conductivity of CNTs and the catalytic function of $CoSnO_3$ particles.

The anchoring effect and the catalytic to the polyselenides resulted from introduction of transition metal oxides of $CoSnO_3$ in the system. To further verify the strong interaction between substrates and LiPSes, the binding energy (E_b) of substrate of CNTs and $CoSnO_3$ between different species of polyselenides (Li_2Se_8, Li_2Se_6, Li_2Se_4 Li_2Se_2 and Li_2Se) were calculated by the density functional theory (DFT) using first-principles approach, the results are shown in **Fig. 5a and Fig. S8**. The detailed calculation method is shown in the Supporting information. The E_b of CNTs and selenium species of Se_8, Li_2Se_8, Li_2Se_6 Li_2Se_4, Li_2Se_2 and Li_2Se are calculated to be 1.248, 1.421, 1.285, 1.608, 1.957, and 1.503 eV respectively. Compared with the pure non-polar carbon CNTs, the E_b value of Se_8 and Li_2Se_n (n=8, 6, 4, 2, 1) on $CoSnO_3$ are 1.656, 2.619, 3.012, 3.5, 3.7, and 3.047 eV, respectively, reflecting much enhanced binding strength. In the case of the selenium species of Li_2Se_4, the electron charge transfer between substrates of CNTs, $CoSnO_3$, and Li_2Se_4 is shown in **Fig. 5b**. Compared with CNTs, the charge transfer is obviously increased between $CoSnO_3$/CNTs and Li_2Se_4, especially Li atom and O atom, which induces strong chemical bonds of Li−O, reflecting the main interaction is between the elements of O in $CoSnO_3$ and Li in Li_2Se_n. Moreover, the Se–Co binding is observed also between polyselenides and $CoSnO_3$/CNTs. The same phenomenon is observed between Li_2Se and the substrate of $CoSnO_3$/CNTs. Due to the strong chemisorption of Li_2Se_4 and $CoSnO_3$, the distance of the Li_2Se_4 on $CoSnO_3$ (2.15 Å) is shorter than that of CNTs (2.064 Å), as shown in **Fig. 5c and Fig. S9**. It is worth noting that the Se−Se bridged bond (Se3−Se4) is the most stretched on the surface of $CoSnO_3$ (2.693 Å) compared with that of graphene (2.23 Å) and pristine Li_2Se_4 (2.126 Å), indicating that the substrate of $CoSnO_3$ could more effectively weaken the Se−Se bridged bond inside of polyselenides, which facilitates the further lithiation reaction. In the case of the selenium species of Li_2Se, charge is lost along the Li−Se bond inside Li_2Se (green part) and internal Li−Se bond softens (**Fig. 5b**). The Li−Se bond inside of Li_2Se on the surface of $CoSnO_3$ grows longer (2.205 Å) than with that of CNTs (2.074 Å) and pristine Li_2Se (1.983 Å) as the binding energy grows larger. The stretched and weakened bond

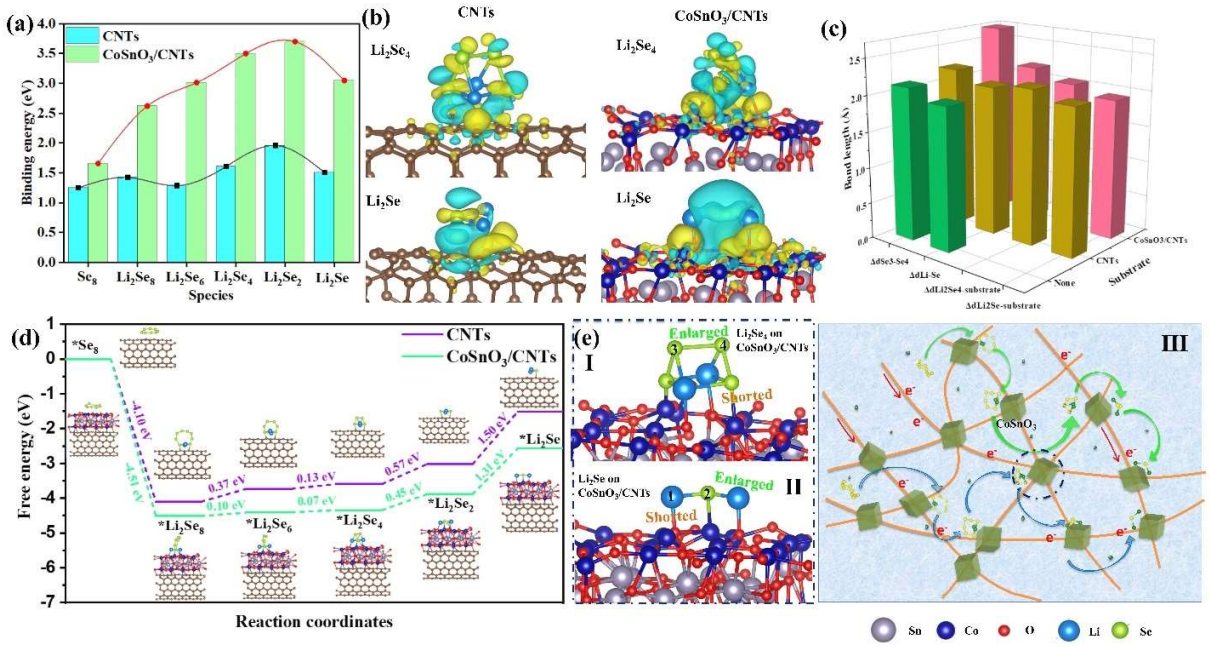

Fig. 5 (a) Binding energies of Se_8 and Li_2Se_n on CNTs and $CoSnO_3$/CNTs. (b) Charge transfers when Li_2Se_4 or Li_2Se adsorbs on the substrate of CNTs or $CoSnO_3$/CNTs. (c) The detailed bond lengths inside Li_2Se_4 and Li_2Se, and the distance between the two adsorbates and CNTs or $CoSnO_3$ when their adsorption. (d) The Free energy plots of conversion reactions of Se species activated by CNTs and $CoSnO_3$/CNTs. (e) I: Schematic illustration of the discharge process in Se@$CoSnO_3$/CNTs cathode, II and III: the $CoSnO_3$ function of strong adsorption and catalytic effect in the discharge and charge process, respectively.

of Li–Se is beneficial for the Li_2Se broken to LiSe and Li and finally gradually converted back to selenium. For evaluating the catalytic effect of $CoSnO_3$/CNTs on Se species conversion, the free energies of conversion reactions of Se_8/Li_2Se_n activated by $CoSnO_3$/CNTs and CNTs were calculated. The corresponding free energy plots are shown in **Fig. 5d**. The Se transformation reaction on $CoSnO_3$/CNTs has the lower Gibbs free energy compared to that of CNTs. Moreover, the free energy undergoes the most considerable decrease on the last two rate-determining steps of Li_2Se_4 to Li_2Se. Thus, the introduction $CoSnO_3$ to the framework host has great helpful in terms of anchoring effect and catalytic effect for Se species transformation.

The strong adsorption of $CoSnO_3$ particles for the polyselnides strengthens the bond between $CoSnO_3$ and Li_2Se_4, which at the same time weakens the bond of Se–Se inside of the Li_2Se_4 (**Fig. 5eI**), leading to the rapid transformation of polyselenides to Li_2Se. In particular, the strong interaction between Li_2Se and $CoSnO_3$ stretches and weakens the bond of Li–Se in Li_2Se (**Fig.**

5eII), accelerating the charge reaction. To better illustrate the talents of the $CoSnO_3$/CNTs composite for Se host material, the schematic illustration of the discharge process in Se@$CoSnO_3$/CNTs cathode is shown in **Fig. 5eIII**. During the discharge process, active Se reacts with Li^+ to form Li_2Se on the surface of the host with the dissolved intermediate muti-polyselenides. The high conductivity of CNTs ensures the fast electron transfer in the cathode. Moreover, the polar $CoSnO_3$ particles have a strong chemisorption to the polar polyselenides, combined with the physical adsorption provided by CNTs. The polyselenides that dissolved in the electrolyte will be riveted on the host framework surface again. Then, the adsorbed polyselenides have rapid transformation with $CoSnO_3$ catalysis. Thus, the strong adsorption and rapid transformation of the polyselenides decrease the polyselenides diffusion out of cathode, thereby inhibiting the shuttle effect, resulting in excellent stability of the Li-Se battery.

4. Conclusion

In summary, polar $CoSnO_3$ particles were *in-situ* grown on the interconnected CNTs network and the obtained $CoSnO_3$/CNTs served for Se host material in the Li-Se battery. The introduced $CoSnO_3$ particles were tightly fixed in the interconnected CNTs. The specific design enables quick transfer of electrons to $CoSnO_3$ along with the interconnected CNTs, where the rate-control step reaction of Li_2Se_n to Li_2Se is accelerated due to the catalytic function of the $CoSnO_3$. Thus, compared with solely $CoSnO_3$ and CNTs host materials, the electrochemical performance of $CoSnO_3$/CNTs as the Se host is significantly improved. The initial specific capacity of Se@$CoSnO_3$/CNTs was 730 mA h g^{-1} and remained at 330 mA h g^{-1} after 200 cycles, with a Coulomb efficiency of almost 100%. Even at the current of 2 C, the capacity can be reached to 153 mA h g^{-1}. The high capacity and excellent stability of the battery are due to the high conductivity and internally accommodated volume expansion of interconnected CNTs and the enhanced polyselenides adsorption and accelerated transformation by porous $CoSnO_3$. This work provides an easy method to solve the problems of shuttle effect and increase the reaction kinetics at the same time.

Acknowledgements

H.Y. Li thanks the financial support from the China Scholarship Council (201809370046) and a scholarship from the Laboratory of Inorganic Materials Chemistry, Université de Namur. The authors thank Prof. Olivier Deparis and Dr. Sebastien Mouchet for the UV-vis absorption test supporting. This research used resources of Electron Microscopy Service is carried out on "Plateforme Technologique Morphologie-Imagerie" at University of Namur. We thank the PC2 technological platform at the University of Namur for access to Power X-ray diffractometer and TGA/DSC. This work was supported by the National Postdoctoral Program (2020M672782), the National Natural Science Foundation of China (U1663225), Changjiang Scholars and Innovative Research Team in University (IRT_15R52), the Program of Introducing Talents of Discipline to Universities-Plan 111 (B20002) from the Ministry of Science and Technology and the Ministry of Education of China, and the National Key R&D Program of China (2016YFA0202602).

References

[1] X. Wang, Y. Tan, Z. Liu, Y. Fan, M. Li, H.A. Younus, J. Duan, H. Deng, S. Zhang, New insight into the confinement effect of microporous carbon in Li/Se battery chemistry: a cathode with enhanced conductivity, Small, 16 (2020) 2000266.

[2] X. Zhou, L. Wang, Y. Yao, Y. Jiang, R. Xu, H. Wang, X. Wu, Y. Yu, Integrating Conductivity, Captivity, and Immobility Ability into N/O Dual-Doped Porous Carbon Nanocage Anchored with CNT as an Effective Se Host for Advanced K-Se Battery, Adv. Funct. Mater., 30 (2020) 2003871.

[3] H. Wang, Design and modification of cathode materials for high-performance lithium-sulfur and lithium-selenium batteries, (2016).

[4] C. Li, Y. Wang, H. Li, J. Liu, J. Song, L. Fusaro, Z.-Y. Hu, Y. Chen, Y. Li, B.-L. Su, Weaving 3D highly conductive hierarchically interconnected nanoporous web by threading MOF crystals onto multi walled carbon nanotubes for high performance Li–Se battery, J. Energy Chem., 59 (2021) 396-404.

[5] X. Qi, Y. Yang, Q. Jin, F. Yang, Y. Xie, P. Sang, K. Liu, W. Zhao, X. Xu, Y. Fu, Two-Plateau Li-Se Chemistry for High Volumetric Capacity Se Cathodes, Angew. Chem., 132 (2020) 14012-14018.

[6] Z. Lei, Y. Lei, X. Liang, L. Yang, J. Feng, High stable rate cycling performances of microporous carbon spheres/selenium composite (MPCS/Se) cathode as lithium–selenium battery, J. Power Sources, 473 (2020) 228611.

[7] W.-D. Dong, C.-Y. Wang, C.-F. Li, F.-J. Xia, W.-B. Yu, L. Wu, H. Mohamed, Z.-Y. Hu, J. Liu, L.-H. Chen, The free-standing N-doped Murray carbon framework with the engineered quasi-optimal Se/C interface for high–Se-loading Li/Na–Se batteries at elevated temperature, Materials Today Energy, 21 (2021) 100808.

[8] Y. Wang, H. Hao, S. Hwang, P. Liu, Y. Xu, J.A. Boscoboinik, D. Datta, D. Mitlin, Selenium infiltrated hierarchical hollow carbon spheres display rapid kinetics and extended cycling as lithium metal battery (LMB) cathodes, J. Mater. Chem. A, 9 (2021) 18582-18593.

[9] L. Sun, K. Li, J. Fu, B. Tian, C. Wang, H. Li, L. Wang, Cerium Oxysulfide with O–Ce–S Bindings for Efficient Adsorption and Conversion of Lithium Polysulfide in Li–S Batteries, Inorg. Chem., 60 (2021) 12847-12854.

[10] L.-C. Zeng, W.-H. Li, Y. Jiang, Y. Yu, Recent progress in Li–S and Li–Se batteries, Rare metals, 36 (2017) 339-364.

[11] Y. Jun, W.-f. Liu, C. Cheng, C.-h. Zhao, K.-y. Liu, Synthesis and characterization of porous monodisperse carbon spheres/selenium composite for high-performance rechargeable Li-Se batteries, Transactions of Nonferrous Metals Society of China, 28 (2018) 1819-1827.

[12] S.-F. Zhang, W.-P. Wang, S. Xin, H. Ye, Y.-X. Yin, Y.-G. Guo, Graphitic nanocarbon–selenium cathode with favorable rate capability for Li–Se batteries, ACS Appl. Mater. Interfaces, 9 (2017) 8759-8765.

[13] D. Dutta, S. Gope, D.S. Negi, R. Datta, A. Sood, A.J. Bhattacharyya, Pressure-induced capillary encapsulation protocol for ultrahigh loading of sulfur and selenium inside carbon

nanotubes: application as high performance cathode in Li–S/se rechargeable batteries, J. Phys. Chem. C, 120 (2016) 29011-29022.

[14] X. Gu, C. Lai, One dimensional nanostructures contribute better Li–S and Li–Se batteries: progress, challenges and perspectives, Energy Stor. Mater., 23 (2019) 190-224.

[15] J. Ge, Q. Zhang, Z. Liu, H. Yang, B. Lu, Solvothermal synthesis of graphene encapsulated selenium/carboxylated carbon nanotubes electrode for lithium–selenium battery, J. Alloys Compd., 810 (2019) 151894.

[16] N. Sezer, M. Koç, Oxidative acid treatment of carbon nanotubes, Surfaces and Interfaces, 14 (2019) 1-8.

[17] Z. Wen, Q. Wang, Q. Zhang, J. Li, In situ growth of mesoporous SnO_2 on multiwalled carbon nanotubes: A novel composite with porous-tube structure as anode for lithium batteries, Adv. Funct. Mater., 17 (2007) 2772-2778.

[18] J. Li, C. Zhang, C.-J. Wu, Y. Tao, L. Zhang, Q.-H. Yang, Improved performance of Li–Se battery based on a novel dual functional CNTs@ graphene/CNTs cathode construction, Rare Metals, 36 (2017) 425-433.

[19] N. Li, W. Cao, Y. Liu, H. Ye, K. Han, Impeding polysulfide shuttling with a three-dimensional conductive carbon nanotubes/MXene framework modified separator for highly efficient lithium-sulfur batteries, Colloids Surf. Physicochem. Eng. Aspects, 573 (2019) 128-136.

[20] N. Feng, K. Xiang, L. Xiao, W. Chen, Y. Zhu, H. Liao, H. Chen, Se/CNTs microspheres as improved performance for cathodes in Li-Se batteries, J. Alloys Compd., 786 (2019) 537-543.

[21] Z. Ye, Y. Jiang, L. Li, F. Wu, R. Chen, A High-Efficiency CoSe Electrocatalyst with Hierarchical Porous Polyhedron Nanoarchitecture for Accelerating Polysulfides Conversion in Li–S Batteries, Adv. Mater., 32 (2020) 2002168.

[22] Y. Dong, P. Lu, Y. Ding, H. Shi, X. Feng, Z.S. Wu, Advanced design of cathodes and interlayers for high-performance lithium-selenium batteries, SusMat, 1 (2021) 393-412.

[23] S. Tang, C. Liu, W. Sun, J. Zhang, S. Bai, X. Zhang, S. Yang, Unraveling the superior anchoring of lithium polyselenides to the confinement bilayer C 2 N: an efficient host material for lithium–selenium batteries, PCCP, 23 (2021) 26981-26989.

[24] J. Yang, H. Gao, X. Kang, Nanomaterials application in Li–Se and Na–Se batteries, in: Advanced Nanomaterials for Electrochemical-Based Energy Conversion and Storage, Elsevier, 2020, pp. 69-114.

[25] Z.W. Seh, Y. Sun, Q. Zhang, Y. Cui, Designing high-energy lithium–sulfur batteries, Chem. Soc. Rev., 45 (2016) 5605-5634.

[26] J. Jin, X. Tian, N. Srikanth, L.B. Kong, K. Zhou, Advances and challenges of nanostructured electrodes for Li–Se batteries, J. Mater. Chem. A, 5 (2017) 10110-10126.

[27] J.-P. Song, L. Wu, W.-D. Dong, C.-F. Li, L.-H. Chen, X. Dai, C. Li, H. Chen, W. Zou, W.-B. Yu, MOF-derived nitrogen-doped core–shell hierarchical porous carbon confining selenium for advanced lithium–selenium batteries, Nanoscale, 11 (2019) 6970-6981.

[28] T.C. Mendes, C. Nguyen, A.J. Barlow, P.V. Cherepanov, M. Forsyth, P.C. Howlett, D.R. MacFarlane, A safe Li–Se battery in an ionic liquid-based electrolyte operating at 25–70° C by

using a N, S, O tri-doped mesoporous carbon host material, Sustain. Energy Fuels, 4 (2020) 2322-2332.

[29] T.Z. Hou, X. Chen, H.J. Peng, J.Q. Huang, B.Q. Li, Q. Zhang, B. Li, Design principles for heteroatom-doped nanocarbon to achieve strong anchoring of polysulfides for lithium–sulfur batteries, Small, 12 (2016) 3283-3291.

[30] X. Chen, H.-J. Peng, R. Zhang, T.-Z. Hou, J.-Q. Huang, B. Li, Q. Zhang, An analogous periodic law for strong anchoring of polysulfides on polar hosts in lithium sulfur batteries: S-or Li-binding on first-row transition-metal sulfides?, ACS Energy Lett., 2 (2017) 795-801.

[31] L. Ma, L.-J. Yu, J. Liu, Y.-Q. Su, S. Li, X. Zang, T. Meng, S. Zhang, J. Song, J. Wang, Construction of Ti4O7/TiN/carbon microdisk sulfur host with strong polar N–Ti–O bond for ultralong life lithium–sulfur battery, Energy Stor. Mater., 44 (2022) 180-189.

[32] H. Wu, Y. Wu, X. Chen, Y. Ma, M. Xu, W. Wei, J. Pan, X. Xiong, Rational design and preparation of few-layered MoSe 2 nanosheet@ C/TiO 2 nanobelt heterostructures with superior lithium storage performance, RSC Adv., 6 (2016) 23161-23168.

[33] M.H.A. Shiraz, H. Zhu, J. Liu, Nanoscale Al2O3 coating to stabilize selenium cathode for sodium–selenium batteries, J. Mater. Res., 35 (2020) 747-755.

[34] F. Zhu, M. Zhang, L. Wang, X. Cao, Synthesis and electrochemical performance of CeO2@ CNTs/S composite cathode for Li–S batteries, J. Solid State Electrochem., (2021) 1-13.

[35] B. Hammer, J.K. Norskov, Why gold is the noblest of all the metals, Nature, 376 (1995) 238-240.

[36] W. Ye, W. Li, K. Wang, W. Yin, W. Chai, Y. Qu, Y. Rui, B. Tang, ZIF-67@ Se@ MnO2: a novel Co-MOF-based composite cathode for lithium–selenium batteries, J. Phys. Chem. C, 123 (2018) 2048-2055.

[37] M. Liu, Q. Li, X. Qin, G. Liang, W. Han, D. Zhou, Y.B. He, B. Li, F. Kang, Suppressing self-discharge and shuttle effect of lithium–sulfur batteries with V2O5-decorated carbon nanofiber interlayer, Small, 13 (2017) 1602539.

[38] K. Wu, J. Wang, C. Xu, X. Jiao, X. Hu, W. Guan, Hollow Spherical α-MoO3: An Effective Electrocatalyst of Polyselenides for Lithium–Selenium Batteries, ACS Applied Energy Materials, (2021).

[39] D. Chen, X.-Y. Yue, X.-L. Li, J. Bao, Q.-Q. Qiu, X.-J. Wu, X. Zhang, Y.-N. Zhou, Freestanding Double-Layer MoO3/CNT@ S Membrane: A Promising Flexible Cathode for Lithium–Sulfur Batteries, ACS Appl. Mater. Interfaces, 12 (2019) 2354-2361.

[40] W. Cai, R. Chen, H. Yang, H.B. Tao, H.-Y. Wang, J. Gao, W. Liu, S. Liu, S.-F. Hung, B. Liu, Amorphous versus crystalline in water oxidation catalysis: a case study of NiFe alloy, Nano Lett., 20 (2020) 4278-4285.

[41] J. Van Wonterghem, S. Mørup, C.J. Koch, S.W. Charles, S. Wells, Formation of ultra-fine amorphous alloy particles by reduction in aqueous solution, Nature, 322 (1986) 622-623.

[42] R. Zhang, X. Huang, D. Wang, T.K. Hoang, Y. Yang, X. Duan, P. Chen, L.C. Qin, G. Wen, Single-phase mixed transition metal carbonate encapsulated by graphene: facile synthesis and improved lithium storage properties, Adv. Funct. Mater., 28 (2018) 1705817.

[43] Y. Zhao, X. Li, B. Yan, D. Xiong, D. Li, S. Lawes, X. Sun, Recent developments and understanding of novel mixed transition-metal oxides as anodes in lithium ion batteries, Adv. Energy Mater., 6 (2016) 1502175.

[44] S. Guo, M. Liu, H. Yang, X. Feng, Y. Bai, C. Wu, $CoSnO_3$/C nanocubes with oxygen vacancy as high-capacity cathode materials for rechargeable aluminum batteries, Green Energy & Environment, (2021).

[45] Z. Wang, Z. Wang, W. Liu, W. Xiao, X.W.D. Lou, Amorphous $CoSnO_3$@ C nanoboxes with superior lithium storage capability, Energy Environ. Sci., 6 (2013) 87-91.

[46] Y. Cao, L. Zhang, D. Tao, D. Huo, K. Su, Facile synthesis of CoSnO3/Graphene nanohybrid with superior lithium storage capability, Electrochim. Acta, 132 (2014) 483-489.

[47] X. Zhao, G. Wang, Y. Zhou, H. Wang, Flexible free-standing ternary CoSnO3/graphene/carbon nanotubes composite papers as anodes for enhanced performance of lithium-ion batteries, Energy, 118 (2017) 172-180.

[48] J. Chen, Z. Bian, M. Wu, M. Gao, J. Shi, M. Duan, X. Guo, Y. Liu, J. Zhang, Q. Kong, Preparation of $CoSnO_3$/CNTs/S and its Electrochemical Performance as Cathode Material for Lithium-Sulfur Batteries, ChemElectroChem, 7 (2020) 4209-4217.

[49] G. Zou, H. Hou, G. Zhao, P. Ge, D. Yin, X. Ji, N-rich carbon coated $CoSnO_3$ derived from in situ construction of a Co–MOF with enhanced sodium storage performance, J. Mater. Chem. A, 6 (2018) 4839-4847.

[50] S. Dou, X. Li, L. Fan, D. Xiong, H.M.K. Sari, B. Yan, W. Liu, J. Li, J. Xu, D. Li, Novel amorphous CoSnO3@ rGO nanocomposites highly enhancing sodium storage, Electrochim. Acta, 316 (2019) 236-247.

[51] G. Yue, J. Liu, J. Han, D. Qin, Q. Chen, J. Shao, Amorphous $CoSnO_3$@ rGO nanocomposite as an efficient cathode catalyst for long-life Li-O2 batteries, Chinese Journal of Catalysis, 39 (2018) 1951-1959.

[52] L. Zhang, Y. Hu, J. Zheng, Fabrication of 3D hierarchical $CoSnO_3$@ CoO pine needle-like array photoelectrode for enhanced photoelectrochemical properties, J. Mater. Chem. A, 5 (2017) 18664-18673.

[53] C. Dong, A.S. Campell, R. Eldawud, G. Perhinschi, Y. Rojanasakul, C.Z. Dinu, Effects of acid treatment on structure, properties and biocompatibility of carbon nanotubes, Appl. Surf. Sci., 264 (2013) 261-268.

[54] M.A. Turgunov, J.O. Oh, S.H. Yoon, Surface modification of multiwall carbon nanotubes by sulfuric acid and nitric acid, Materials, 64 (2014) 22-25.

[55] B. Li, G.-X. Zhang, K.-S. Huang, L.-F. Qiao, H. Pang, One-step synthesis of $CoSn(OH)_6$ nanocubes for high-performance all solid-state flexible supercapacitors, Rare Metals, 36 (2017) 457-464.

[56] W. Cui, F. Wang, J. Wang, C. Wang, Y. Xia, Nanostructural CoSnC anode prepared by $CoSnO_3$ with improved cyclability for high-performance Li-ion batteries, Electrochim. Acta, 56 (2011) 4812-4818.

[57] F. Fan, G. Fang, R. Zhang, Y. Xu, J. Zheng, D. Li, Influences of carbon content and coating carbon thickness on properties of amorphous $CoSnO_3$@C composites as anode materials for lithium-ion batteries, Appl. Surf. Sci., 311 (2014) 484-489.

[58] M. Kazazi, Z.A. Zafar, M. Delshad, J. Cervenka, C. Chen, TiO_2/CNT nanocomposite as an improved anode material for aqueous rechargeable aluminum batteries, Solid State Ionics, 320 (2018) 64-69.

[59] K. Wang, X. Zhang, J. Han, X. Zhang, X. Sun, C. Li, W. Liu, Q. Li, Y. Ma, High-performance cable-type flexible rechargeable Zn battery based on MnO_2@ CNT fiber microelectrode, ACS Appl. Mater. Interfaces, 10 (2018) 24573-24582.

[60] Z. Mo, R. Yang, D. Lu, L. Yang, Q. Hu, H. Li, H. Zhu, Z. Tang, X. Gui, Lightweight, three-dimensional carbon Nanotube@ TiO2 sponge with enhanced microwave absorption performance, Carbon, 144 (2019) 433-439.

[61] K. Wu, J. Wang, C. Xu, X. Jiao, X. Hu, W. Guan, Hollow Spherical α-MoO_3: An Effective Electrocatalyst of Polyselenides for Lithium–Selenium Batteries, ACS Applied Energy Materials, 4 (2021) 10203-10212.

[62] H. Zhang, L. Zhong, J. Xie, F. Yang, X. Liu, X. Lu, A COF-Like N-Rich Conjugated Microporous Polytriphenylamine Cathode with Pseudocapacitive Anion Storage Behavior for High-Energy Aqueous Zinc Dual-Ion Batteries, Adv. Mater., 33 (2021) 2101857.

[63] J. Zheng, Y. Sun, Y. Wu, J. Rong, Z. Wang, H. Li, L. Niu, Ultralong cycle life and high rate potassium ion batteries enabled by multi-level porous carbon, J. Power Sources, 492 (2021) 229614.

[64] R. Reyhani, A. Zadhoush, N.S. Tabrizi, H. Nazockdast, M. Naeimirad, Synthesis and characterization of powdered CNT-doped carbon aerogels, J. Non-Cryst. Solids, 571 (2021) 121058.

[65] F. Su, C. Lu, S. Hu, Adsorption of benzene, toluene, ethylbenzene and p-xylene by NaOCl-oxidized carbon nanotubes, Colloids Surf. Physicochem. Eng. Aspects, 353 (2010) 83-91.

[66] C. Lu, F. Su, S. Hu, Surface modification of carbon nanotubes for enhancing BTEX adsorption from aqueous solutions, Appl. Surf. Sci., 254 (2008) 7035-7041.

[67] G. Viswanathan, D.B. Kane, P.J. Lipowicz, High efficiency fine particulate filtration using carbon nanotube coatings, Adv. Mater., 16 (2004) 2045-2049.

[68] C.-J.M. Chin, L.-C. Shih, H.-J. Tsai, T.-K. Liu, Adsorption of o-xylene and p-xylene from water by SWCNTs, Carbon, 45 (2007) 1254-1260.

[69] L. Wang, Z. Du, X. Bai, Y. Lin, Constructing macroporous C/Co composites with tunable interfacial polarization toward ultra-broadband microwave absorption, J. Colloid Interface Sci., 591 (2021) 76-84.

[70] W. Dong, H. Chen, F. Xia, W. Yu, J. Song, S. Wu, Z. Deng, Z.-Y. Hu, T. Hasan, Y. Li, Selenium clusters in Zn-glutamate MOF derived nitrogen-doped hierarchically radial-structured microporous carbon for advanced rechargeable Na–Se batteries, J. Mater. Chem. A, 6 (2018) 22790-22797.

[71] S. Lee, J. Lee, W. Kim, H.-J. Kim, C. Pak, J.T. Lee, K. Eom, Selenium-infiltrated mesoporous carbon composite cathode for a high-capacity lithium-chalcogen battery: Effects of carbon

structure and dopant on the rate-capability and cyclic stability, J. Power Sources, 408 (2018) 111-119.

[72] L. Su, Y. Xu, J. Xie, L. Wang, Y. Wang, Multi-yolk–shell SnO2/Co3Sn2@ C nanocubes with high initial coulombic efficiency and oxygen reutilization for lithium storage, ACS Appl. Mater. Interfaces, 8 (2016) 35172-35179.

[73] L. Wu, S. Huang, W. Dong, Y. Li, Z. Wang, H.S. Mohamed, Y. Li, B.-L. Su, Alkoxide hydrolysis in-situ constructing robust trimanganese tetraoxide/graphene composite for high-performance lithium storage, J. Colloid Interface Sci., 594 (2021) 531-539.

[74] Y. Cui, A. Abouimrane, J. Lu, T. Bolin, Y. Ren, W. Weng, C. Sun, V.A. Maroni, S.M. Heald, K. Amine, (De) Lithiation mechanism of Li/SeS x (x= 0–7) batteries determined by in situ synchrotron X-ray diffraction and X-ray absorption spectroscopy, J. Am. Chem. Soc., 135 (2013) 8047-8056.

[75] C. Luo, J. Wang, L. Suo, J. Mao, X. Fan, C. Wang, In situ formed carbon bonded and encapsulated selenium composites for Li–Se and Na–Se batteries, J. Mater. Chem. A, 3 (2015) 555-561.

[76] L. Sha, P. Gao, X. Ren, Q. Chi, Y. Chen, P. Yang, A Self-Repairing Cathode Material for Lithium–Selenium Batteries: Se− C Chemically Bonded Selenium–Graphene Composite, Chem. Eur. J., 24 (2018) 2151-2156.

[77] A. Aparnev, N. Uvarov, A. Loginov, B. Bokhonov, Synthesis of mixed cobalt (II)-tin (IV) hydroxide and study of its dehydration products, Materials Today: Proceedings, 31 (2020) 551-554.

[78] T. Sun, C. Huang, H. Shu, L. Luo, Q. Liang, M. Chen, J. Su, X. Wang, Porous NiCo2S4 Nanoneedle Arrays with Highly Efficient Electrocatalysis Anchored on Carbon Cloths as Self-Supported Hosts for High-Loading Li–S Batteries, ACS Appl. Mater. Interfaces, 12 (2020) 57975-57986.

[79] X. Zhou, R. Meng, N. Zhong, S. Yin, G. Ma, X. Liang, Size-Dependent Cobalt Catalyst for Lithium Sulfur Batteries: From Single Atoms to Nanoclusters and Nanoparticles, Small Methods, 5 (2021) 2100571.

[80] A. Guo, X. Zhang, B. Shao, S. Sang, F. Cui, X. Yang, The Pseudo-capacitance of Graphitic Nanoribbons Aerogel with Encapsulated Fe Nanoparticles, J. Alloys Compd., (2021) 160742.

[81] T. Zhu, Z. Song, J. Lin, L. Fan, J.-Y. Lin, J. Wu, Ion-pore size match effects and high-performance cucurbit [8] uril-carbon-based supercapacitors, Electrochim. Acta, 405 (2022) 139827.

[82] W. Peng, F. Sun, S. Xiong, Z. Zhang, B. Duan, C. Zhang, J. Feng, B. Xi, WSe2 Flakelets on N-doped Graphene for Accelerating Polysulfide Redox and Regulating Li Plating, Angew. Chem., (2021).

[83] J. Qian, Y. Xing, Y. Yang, Y. Li, K. Yu, W. Li, T. Zhao, Y. Ye, L. Li, F. Wu, Enhanced Electrochemical Kinetics with Highly Dispersed Conductive and Electrocatalytic Mediators for Lithium–Sulfur Batteries, Adv. Mater., (2021) 2100810.

[84] Y. Zhang, Y. Guo, B. Wang, Y. Wei, P. Jing, H. Wu, Z. Dai, M. Wang, Y. Zhang, An integrated hybrid interlayer for polysulfides/selenides regulation toward advanced Li–SeS2 batteries, Carbon, 161 (2020) 413-422.

[85] B. Guan, Y. Zhang, L. Fan, X. Wu, M. Wang, Y. Qiu, N. Zhang, K. Sun, Blocking Polysulfide with Co_2B@ CNT via "Synergetic Adsorptive Effect" toward Ultrahigh-Rate Capability and Robust Lithium–Sulfur Battery, ACS nano, 13 (2019) 6742-6750.

[86] X. Tao, J. Wang, C. Liu, H. Wang, H. Yao, G. Zheng, Z.W. Seh, Q. Cai, W. Li, G. Zhou, Balancing surface adsorption and diffusion of lithium-polysulfides on nonconductive oxides for lithium–sulfur battery design, Nat. Commun., 7 (2016) 1-9.

[87] Y. Lu, J.L. Qin, T. Shen, Y.F. Yu, K. Chen, Y.Z. Hu, J.N. Liang, M.X. Gong, J.J. Zhang, D.L. Wang, Hypercrosslinked Polymerization Enabled N-Doped Carbon Confined Fe_2O_3 Facilitating Li Polysulfides Interface Conversion for Li–S Batteries, Adv. Energy Mater., 11 (2021) 2101780.

Supply information

Polar adsorption and catalytic bifunctional particles suppress the shuttle effect by dual-adsorption catalysis to achieve high performance Li-Se battery

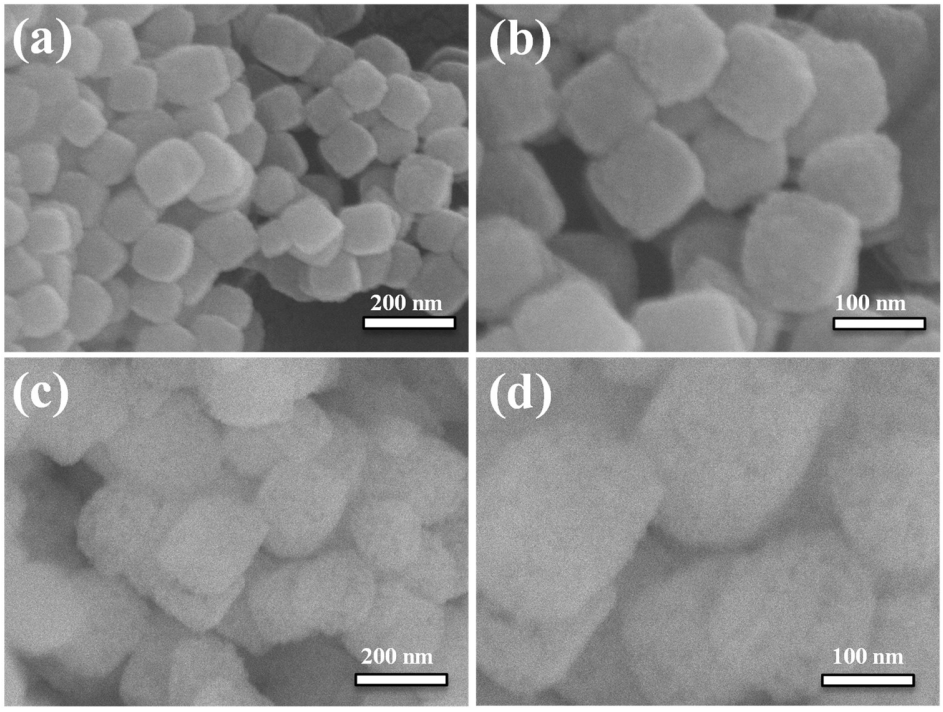

Fig. S1. SEM images of (a, b) $CoSn(OH)_6$ and (c, d) $CoSnO_3$.

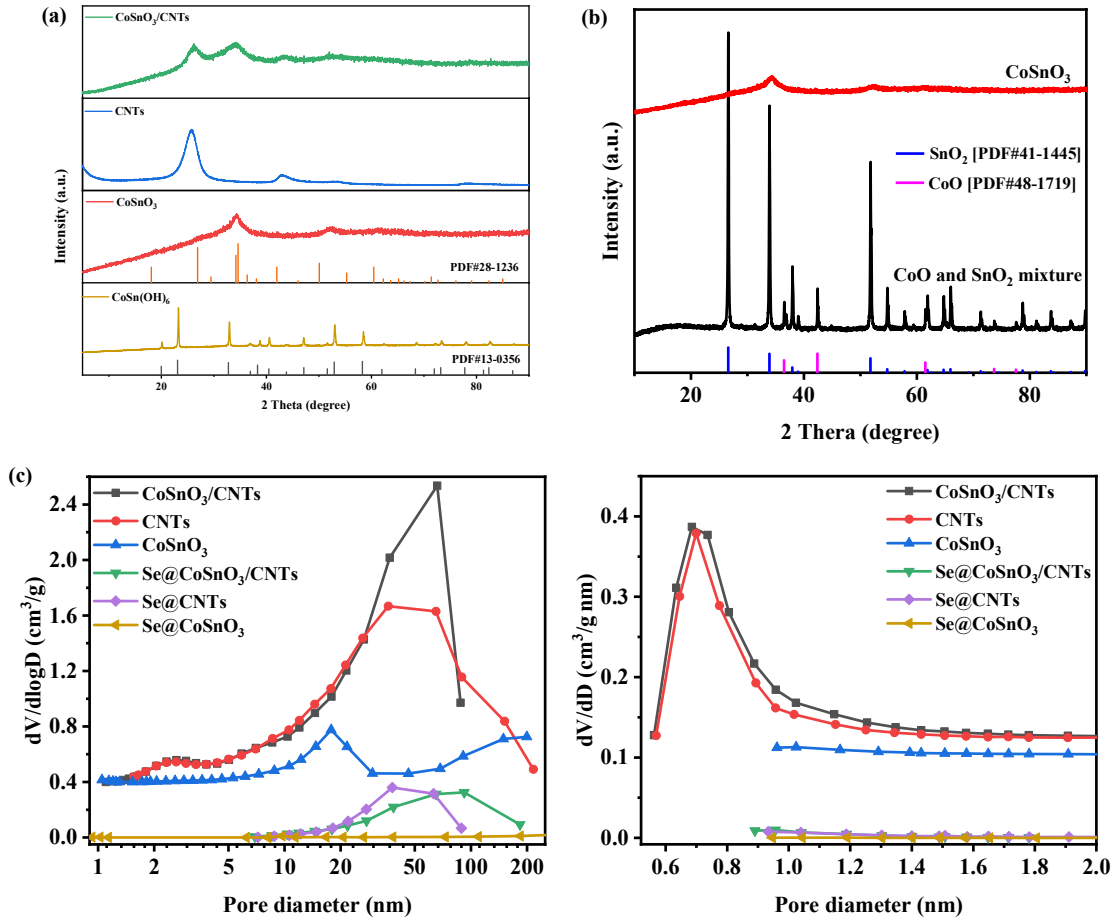

Fig. S2. XRD patterns of (a) $CoSn(OH)_6$, CNTs, $CoSnO_3$ and $CoSnO_3$/CNTs and (b) the mixture of CoO and SnO_2 (molar ratio of 1:1) and $CoSnO_3$, respectively. (c, d) BJH and H-K pore size distribution of CNTs, $CoSnO_3$, $CoSnO_3$/CNTs and corresponding Se@host composites.

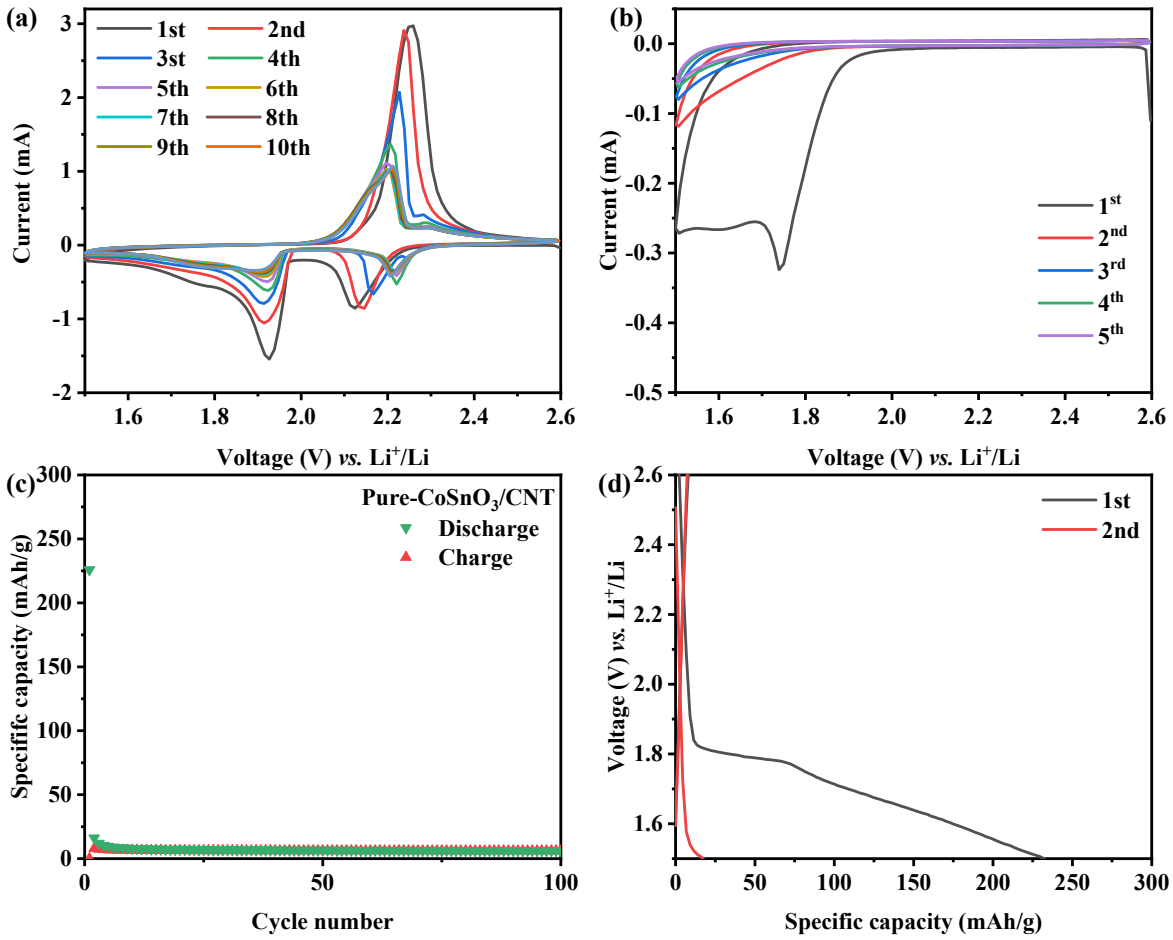

Fig. S3. (a) CV curves of Se@$CoSnO_3$/CNTs cathode at 0.1 mV/s. (b) CV curves, (c) cycling performance and (d) discharge/charge profiles of pure-$CoSnO_3$/CNTs.

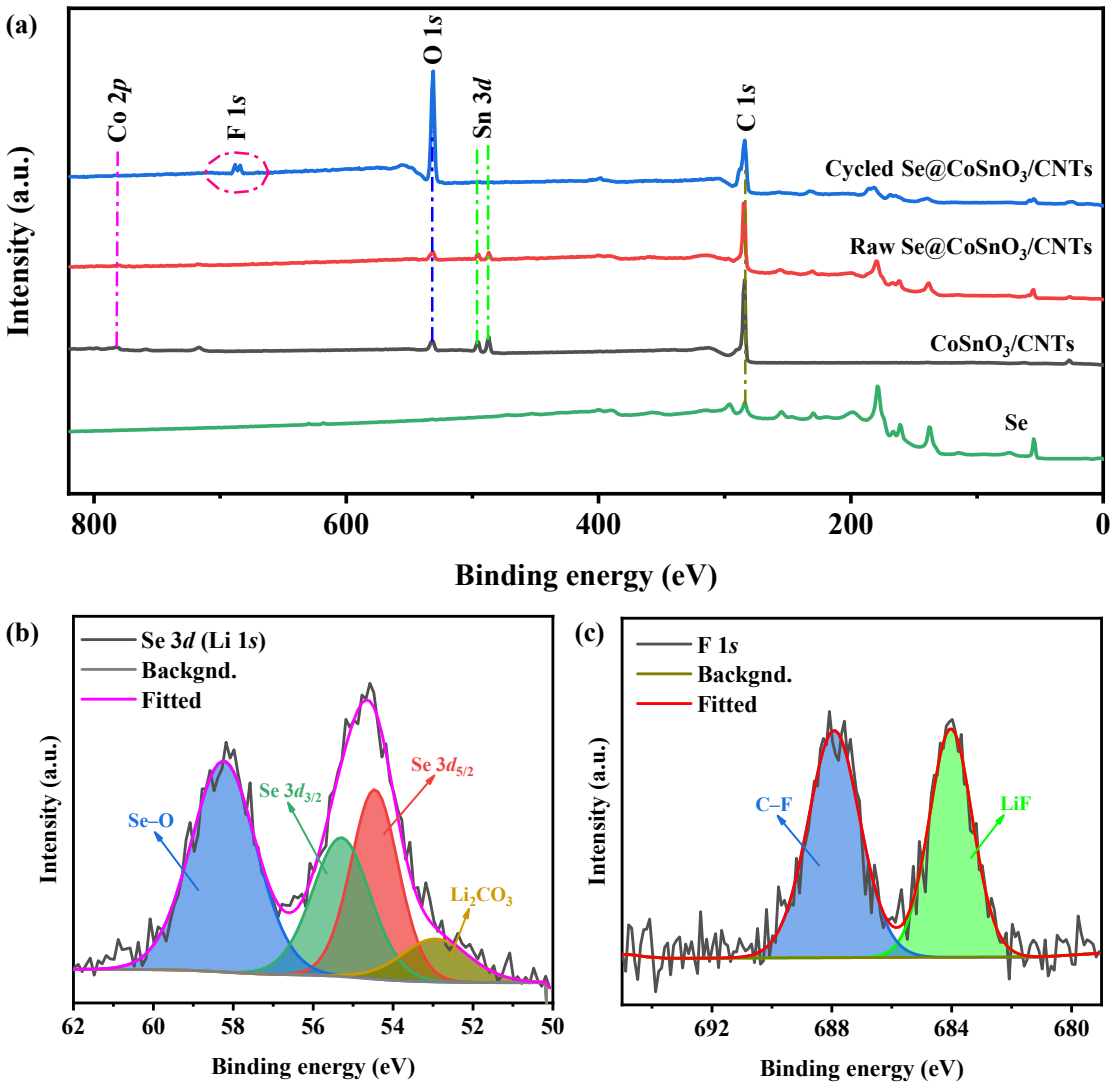

Fig. S4. (a) XPS spectra of Se, $CoSnO_3$/CNTs, corresponding fresh and cycled Se@$CoSnO_3$/CNTs cathode materials, High-resolution spectrum of cycled Se@$CoSnO_3$/CNTs: (b) Se 3*d* and (c) F 1*s*.

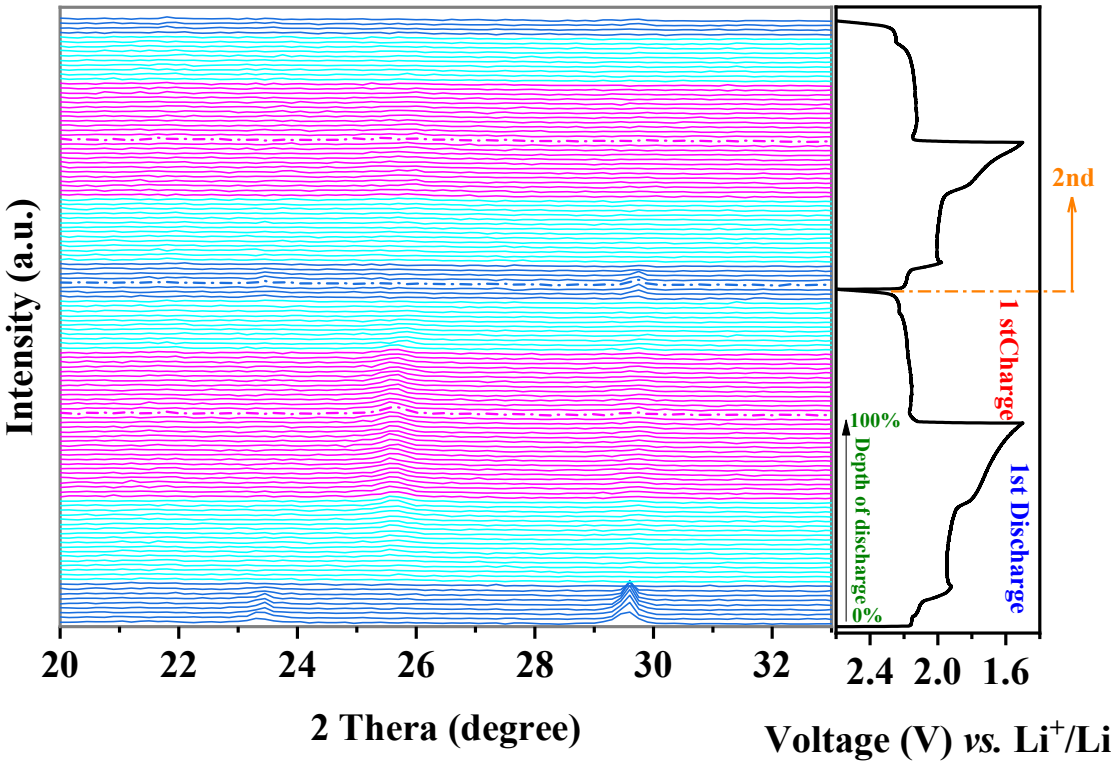

Fig. S5. The in situ XRD characterization of the Se@$CoSnO_3$/CNTs cathode in 2 discharge/charge cycles.

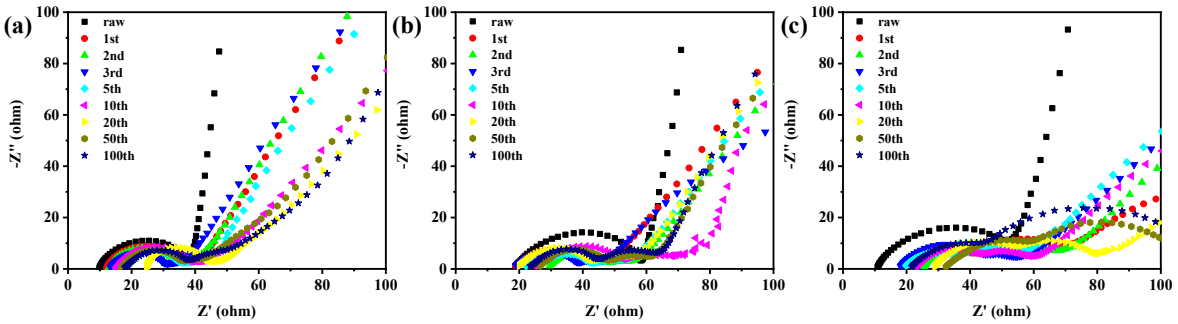

Fig. S6. The Nyquist plots of (a) $CoSnO_3$/CNTs, (b) CNTs and (c) $CoSnO_3$.

GITT is a stand method to measure the Li^+ transfer in Li-ion battery. Due to the different lithium species (Li^+, Li_2Se_n) include in the cell, the calculated value of D not only reflect the transfer of Li^+ but also Li_2Se_n, which is important to rate-control step reaction. The D value is calculated by the following equation:

$$D = \frac{4}{\pi\tau}\left(\frac{m_B V_M}{M_B S}\right)^2\left(\frac{\Delta E_S}{\Delta E_t}\right)^2$$

where τ is the constant current pulse time, m_B, V_M, and M_B denote the mass, the molar volume, and the molar mass of the active material, respectively, S is the contact area between electrode and electrolyte, ΔEs the change of the steady-state voltage during a single-step GITT experiment, and ΔE_t the total change of cell voltage during a constant current pulse τ of a single-step GITT experiment neglecting the IR-drop, as shown in **Fig. S3**.

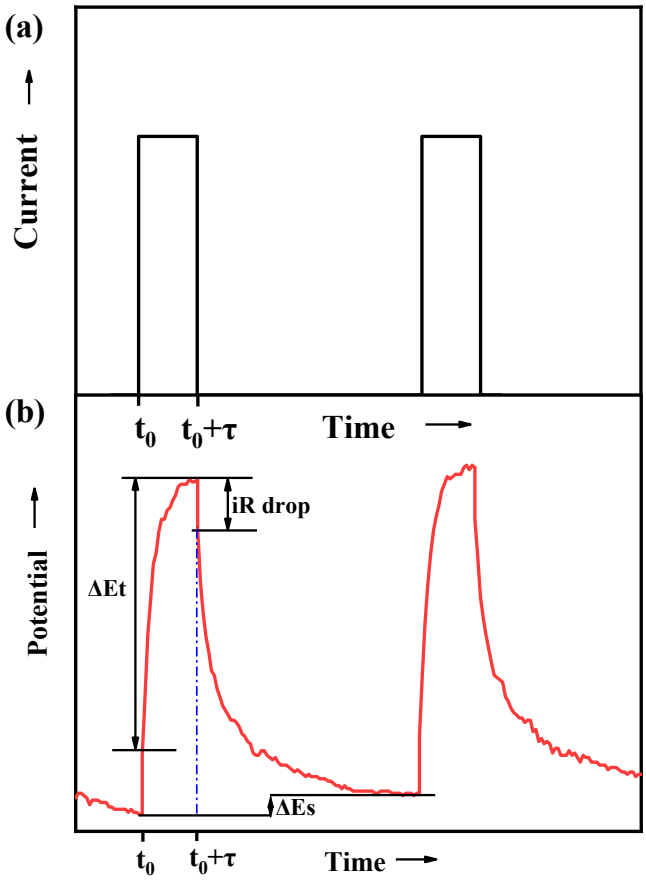

Fig. S7. Scheme for GITT experiment: (a) the constant current pulse, (b) Corresponding potential response.

The first-principles [1,2] perform all spin-polarization density functional theory (DFT) calculations within the generalized gradient approximation (GGA) using the Perdew-Burke-Ernzerhof (PBE) [3] formulation. The projected augmented wave (PAW) potentials [4,5] was applied to describe the ionic cores and take valence electrons into account using a plane wave basis set with a kinetic energy cutoff of 450 eV. Partial occupancies of the Kohn−Sham orbitals were allowed using the Gaussian smearing method and a width of 0.05 eV. The electronic energy was considered self-consistent when the energy change was smaller than 10^{-4} eV. A geometry optimization was considered convergent when the energy change was smaller than 0.05 eV $Å^{-1}$. In our structure, the U correction is used for Co atoms. The vacuum spacing in a direction perpendicular to the plane of the structure is 20 Å form the surfaces. The Brillouin zone integration is performed using 3×3×1 Monkhorst-Pack k-point sampling for a structure.

Finally, the binding energy, E_b, is computed to measure the binding strength between these Li_2Se_n species and the different substances. It is calculated with the following formula:

$$E_b = E_{Li_2Se_n} + E_{sub} - E_{Li_2Se_n+su} \quad (1)$$

For the substance of graphene, the E_b with graphene and Li_2Se_4 is:

$$E_b = E_{Li_2Se_4} + E_{graphene} - E_{Li_2Se+graphene} \quad (2)$$

For the substance of $CoSnO_3$, the E_b is:

$$E_b = E_{Li_2Se_4} + E_{CoS\ \ _3} - E_{Li_2Se_4+CoSnO_3} \quad (3)$$

The free energy was calculated using the equation:

$$G = E_{ads} + ZPE - TS \quad (4)$$

where G, E_{ads}, ZPE and TS are the free energy, total energy from DFT calculations, zero point energy and entropic contributions, respectively.

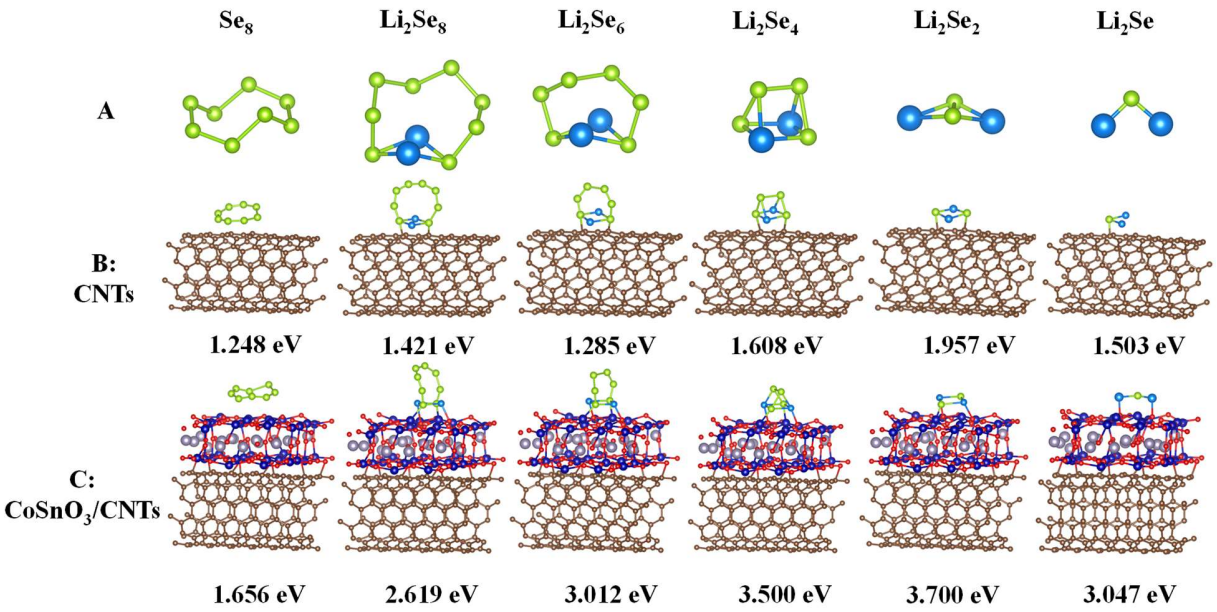

Fig. S8 (A) Structures of Se_8 and series of polyselenides (Li_2Se_n, n=8, 6, 4, 2, 1). Binding energy of different Se species on the substrate of (B) CNTs and (C) $CoSnO_3$/CNTs.

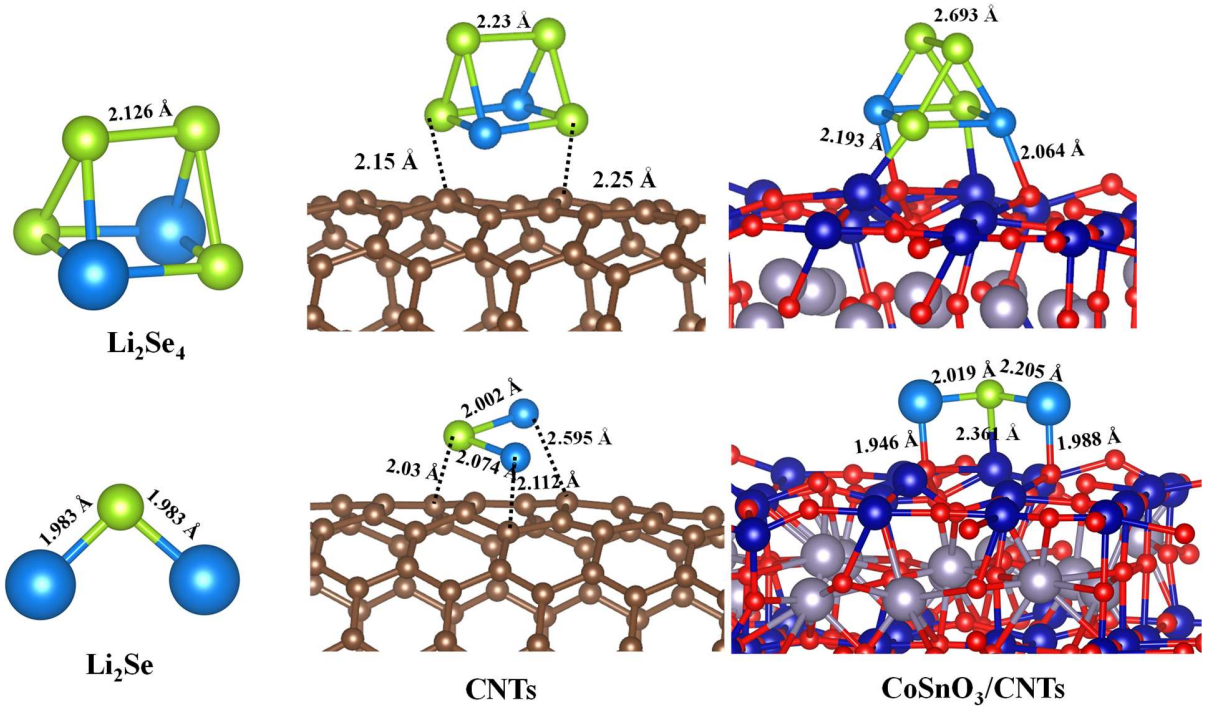

Fig. S9 Bond length of isolate Li_2Se_4 and Li_2Se and their adsorption on the substrate of CNTs and $CoSnO_3$/CNTs.

Table S1: Nitrogen BET adsorption measurements textural properties of the different host materials and corresponding Se@host composites.

Samples	S_{BET} ($m^2 g^{-1}$)	Vp ($m^3 g^{-1}$)	Pore size (nm)
$CoSnO_3$/CNTs	308	1.7	0.7, 3, 13, 50
CNTs	265	1.3	0.7, 3, 50
$CoSnO_3$	44	0.3	18, 200
Se@$CoSnO_3$/CNTs	22.7	0.3	50
Se@CNTs	23.2	0.3	50
Se@$CoSnO_3$	0.5	0.01	13, 170

Table S2: Capacity of the batteries with Se@$CoSnO_3$/CNTs, Se@CNTs and Se@$CoSnO_3$, respectively.

Samples	Initial capacity (mA h g^{-1})	2nd capacity (mA h g^{-1})	200th capacity (mA h g^{-1})	Capacity at 2 C (mA h g^{-1})
Se@$CoSnO_3$/CNTs	729.9	612.4	330.4	153
Se@CNTs	898.8	605.6	257.1	121
Se@$CoSnO_3$	605.3	528.0	226.6	83

References

[1]. Kresse, G., Furthmüller, J. Efficiency of Ab-Initio Total Energy Calculations for Metals and Semiconductors Using a Plane-Wave Basis Set. Comput. Mater. Sci. 1996, 6, 15−50.

[2]. Kresse, G., Furthmüller, J. Efficient Iterative Schemes for Ab Initio Total-Energy Calculations Using a Plane-Wave Basis Set. Phys. Rev. B 1996, 54, 11169−11186.

[3]. Perdew, J. P., Burke, K., Ernzerhof, M. Generalized Gradient Approximation Made Simple. Phys. Rev. Lett. 1996, 77, 3865−3868.

[4]. Kresse, G., Joubert, D. From Ultrasoft Pseudopotentials to the Projector Augmented-Wave Method. Phys. Rev. B 1999, 59, 1758-1775.

[5]. Blöchl, P. E. Projector Augmented-Wave Method. Phys. Rev. B 1994, 50, 17953−17979.

Chapter VII

Conclusions and perspectives

1. Conclusions

This thesis focuses on dealing with the challenges of Li-Se batteries. At first, the mechanism of the battery, the parameters to evaluate, the problems were displayed. The research work on Li-Se was also summarized from cathode to anode. Based on these previous works, solving the problem of shuttle effect has become the priority task. Confining Se inside of the cathode and realizing its rapid transportation is an effective method to overcome the problem. To ensure the high loading of active Se, tight polyselenides fixing, high conductivity of the host system and release of the volume expansion, porous carbon materials become the ideal candidates for the host material. Focus on this criterion, three kinds of carbon host materials were synthesized and implemented in Li-Se batteries.

The research work is concluded in three parts:

1) Inspired by natural organisms, a series of 3D OHPC materials with micro-meso-macropores structure was synthesized. By tunable macropore size of the system, the optimized pores distribution that following the concept of the generalized Murray's law was explored. Compared to the Se confined in sole micropores, mesopores or macropores obtained cathodes, Se/OHPC composites with hierarchically porous structure perform much higher rate performance and ultra-long cyclic stability in Li-Se battery. Moreover, in this host system, when the size of the macropores is equal to 100 nm, the obtained Se/OHPC-100 cathode delivers the highest 2nd discharge capacity of 651 mA h g^{-1} at 0.2 C and a prolonged cycle life over 200 cycles, maintaining at 360 mA h g^{-1}. Even at the current of 5 C, it exhibits discharge capacity of 154 mA h g^{-1}. The high specific capacity and good stability of the Li-Se battery are due to this pores distribution that follows of the best generalized Murray's law. With enough micropores giving Se loading space, reaction site and physical adsorption and, at the same time, the interconnected meso-macroporous constructed the highways of electrolyte and ions transfer. With the best synergy of the different pore size ranges, the Se on OHPC-100 composite achieved a good electrochemical performance.

2) Introducing the optimized three-scale pore size into single-crystal MOF, the obtained carbon material of S-NOHPC not only maintains the appropriate pores distribution but also provides polar N-doping sites. Owing to the advantages of the three length scales of pore sizes and N-doping

enhanced polyselenides adsorption strength, Se@S-NOHPC achieves the highest 2nd discharge capacity of 658 mA h g^{-1} and retains 367 mA h g^{-1} after 200 cycles at 0.2 C. The capacity of Se@S-NOHPC can reach 230 mA h g^{-1} at the high current density of 5 C. With the optimized pores size design and heteroatom doping, the cycle stability and rate capability achieved some degrees of improvement.

3) In order to overcome the limitation of the polar sites by heteroatom doping, polar $CoSnO_3$ particles were *in-situ* grown on interconnected CNTs network and the obtained $CoSnO_3$/CNTs served for Se host material in the Li-Se battery. Compared with solely $CoSnO_3$ and CNTs host materials, the electrochemical performance of $CoSnO_3$/CNTs as the Se host is significantly improved. The initial specific capacity of Se@$CoSnO_3$/CNTs was 730 mA h g^{-1} and remained at 330 mA h g^{-1} after 200 cycles, with a coulomb efficiency of almost 100%. Even at the current of 2 C, the capacity can be reached to 153 mA h g^{-1}. The high capacity and excellent stability of the battery are due to the high conductivity and internally accommodated volume expansion of interconnected CNTs and the enhanced polyselenides adsorption and accelerated transformation by porous $CoSnO_3$.

2. Perspectives

In our third Se@$CoSnO_3$/CNTs system, the electrochemical performance of the cathode achieved much higher capacity compared with Se@CNTs and Se@$CoSnO_3$ cathodes. It fully proves the positive effect of the introduction of polar particles into the host material. However, compared with the first two Se@OHPC and Se@S-NOHPC systems, the capacity of Se@$CoSnO_3$/CNTs is lower. That is due to the lack of pore volume and lower surface area of $CoSnO_3$/CNTs cannot confine Se in an amorphous short link state, which limits the utilization of Se. To combine the advantages of the pore size design and polar particles, the polar particle can be tried to introduce a hierarchically porous carbon with a much higher surface area and porous volume, better with *in-situ* method. In this case, the capacity and cycle stability of the Li-Se battery maybe will have a further increase.

As described in the mechanism of the Li-Se battery, the Se confined in the pores of frameworks get electrons, it will have a reaction with around Li^+. Generally, the transfer of ions is slower than electrons, which leads the diffused polyselenides on the surface of cathode to easier capture the ions and finish the polyselenides transportation to Li_2Se first. The surface coated solid Li_2Se will increase the resistance of the ions movement, leading to a drop of the reaction kinetics. Moreover, the surface Li_2Se will be easier to lose in the following lithiation/ delithiation process. Polar particles, such as oxide, nitride, sulfide have a strong interaction with polyselenides. Designing a cathode with gradient distributed polar particles may be a feasible method to suppress the Se species out of the cathode. The high gradient of polar particles on the side away from the separator will keep the polyselenide always at the side away from the electrolyte and avoid the decay of the Li-Se battery.

In addition, the problems brought by Se cathode, other problems such as the leakage of electrolyte, characteristic of flammable and explosive and lithium dendrites also restrict the application of lithium selenium batteries. A lot of effects, such as solid electrolyte, high concentration lithium salt electrolyte and anode current collector and frameworks design have achieved considerable progress. Realizing the commercial application of the Li-Se battery has a long road to go.

List of publications

1. **Hongyan Li**, Polar particles suppress the shuttle effect by enhanced adsorption and catalytic function to achieve high performance Li-Se battery, submitted.

2. **Hongyan Li**, Wenda Dong, Chao Li, Yingying Wang, Ming-Hui Sun, Tarek Barakat, Yu Li, and Bao-Lian Su, Boosting reaction kinetics and shuttle effect suppression by single crystal MOF-derived N-doped ordered hierarchically porous carbon for high performance Li-Se battery, Sci. China Mater., 2022, 2:8. IF 8.64

3. Wen-Da Dong, Chao-Fan Li, **Hong-Yan Li**, Liang Wu, Hemdan S. H. Mohamed, Zhi-Yi Hu, Li-Hua Chen, Yu Li and Bao-Lian Su, The chain-mail Co@C electrocatalyst accelerating one-step solid-phase redox for advanced Li–Se batteries, J. Mater. Chem. A, 2022,10, 8059-8067. IF 14.511

4. **Hongyan Li**, Chao Li, Yingying Wang, Ming-Hui Sun, Wenda Dong, Yu Li, Bao-Lian Su, Selenium confined in ZIF-8 derived porous carbon@MWCNTs 3D networks: tailoring reaction kinetics for high performance lithium-selenium batteries, Chem. Synth., 2022, 2: 8.

5. **Hongyan Li**, Wenda Dong, Chao Li, Tarek Barakat, Minghui Sun, Yingying Wang, Liang Wu, Lang Wang, Lei Xia, Zhi-Yi Hu, Yu Li, Bao-Lian Su, Three-dimensional ordered hierarchically porous carbon materials for high performance Li-Se battery, J. Energy Chem., 2022, 68, 624-636. IF 13.599

6. Chao Li, Yingying Wang, **Hongyan Li**, Jing Liu, Jianping Song, Luca Fusaro, Zhi-Yi Hu, Yanxin Chen, Yu Li, Bao-Lian Su, Weaving 3D highly conductive hierarchically interconnected nanoporous web by threading MOF crystals onto multi walled carbon nanotubes for high performance Li–Se battery, J. Energy Chem., 2021, 59, 396-404. IF 13.599

Acknowledgments

I am so happy to finish my thesis with the help and guidance of my supervisor Prof. Su. The last four years is really memorable and fruitful for me.

First, I would like to thank Prof. Bao-Lian Su at the Laboratory of Inorganic Materials Chemistry (CMI), University of Namur, Belgium. He gives me the valuable opportunity to study here to carry out my research work. Prof. Su gave me a great help in guiding my research work and the scientific staff and let me a much more deeper understanding of the project of battery. Most important, Prof. Su also gives me meticulous care in my life, which is a beam of light for my foreign life.

I would like to thank Prof. Yu Li at State Key Laboratory of Advanced Techonology for Materials Synthesis and Processing, Wuhan University of Technology, China. He gave me a lot of professional guidance on my subject.

Then, I would like to thank the committee members of Prof. Alexandru Vlad at Institute of Condensed Matter and Nanosciences, Catholic University of Leuven, Belgium and Prof. Olivier Deparis at Unité de recherche en physique du solide (LPS), Department of Physics, University of Namur, Belgium. Prof. Vlad inspired me should consider the things comprehensive, but not just focus on my own project, which is really very important for my research work. I would like to thank Prof. Olivier Deparis at Department of Physics, University of Namur. He is enthusiastic, and he gave me some important suggestions for my research work. I would like to thank Prof. Laurencde Leherte at Department of Chemistry, University of Namur. She gives patient guidance on this thesis.

I would like to thank Prof. Arien Krief. His rigorous attitude in doing things is worth learning from. I would like to thank Mrs. Isabelle Virlet and Mrs. Valerie Charles. They give me warmth from the family and help a lot. I would like to thank Dr. Nikolay TUMANOV, Dr. Luca Fusaro, Dr. Corry Charlier, they always give me timely help in my technical experiment.

I would like to thank Dr. Chao Li, Dr. Tarek Barakat, Dr.Yingying Wang, Dr. Minghui Sun, Mr. Marvin Laboureur, and Mr. Wenda Dong, they gave me a lot of help in work and life. I would like to thank all the family number of CMI, all of you will become a very precious part of my life.

I would like to thank all of my friends, Dandan He, Dan Xie, Mingqi Wan, etc. Your concern makes me not feel so far away from you.

Last, I will thank my family members. No matter what decision I make, they always stand beside me and give me power. Thanks for their unprincipled support.

Thanks all of you, hope all of us enjoy our life.

Hongyan Li

November, 2022, Namur